Doctoral theses at NTNU, 2011:235

Zhenhui Liu

Analytical and numerical analysis of iceberg collisions with ship structures

ISBN 978-82-471-3030-8 (printed version)
ISBN 978-82-471-3031-5 (electronic version)
ISSN 1503-818

NTNU
Norwegian University of Science and Technology
Thesis for the degree of Philosophiae Doctor
Faculty of Engineering Science and Technology
Department of Marine Technology

NTNU – Trondheim
Norwegian University of
Science and Technology

Doctoral Thesis

Zhenhui Liu

Doctoral theses at NTNU, 2011:235

NTNU

NTNU – Trondheim
Norwegian University of
Science and Technology

Zhenhui Liu

Analytical and numerical analysis of iceberg collisions with ship structures

Thesis for the degree of philosophiae doctor

Trondheim, April 2011

Norwegian University of Science and Technology
Faculty of Engineering Science and Technology
Department of Marine Technology

NTNU – Trondheim
Norwegian University of
Science and Technology

NTNU
Norwegian University of Science and Technology

Thesis for the degree of philosophiae doctor

Faculty of Engineering Science and Technology
Department of Marine Technology

ISBN 978-82-471-3030-8 (printed version)
ISBN 978-82-471-3031-5 (electronic version)
ISSN 1503-8181

ITK Report 2011-72

Doctoral Theses at NTNU, 2011:235

Printed by Skipnes Kommunikasjon as

To my family

Abstract

The scope of the present Ph.D. thesis was to investigate the mechanics of collisions between icebergs and ship structures. Large reservoirs of oil and gas and new sailing routes in the Arctic area are two large motivations for the present research. Human activity in the Arctic demands well-designed naval architectures for facing different kinds of ice loads. According to modern design codes, ship and offshore structures are usually designed under the ultimate limit state (ULS) methods and checked with the accidental limit state (ALS) methods. The methods and assumptions presented in this thesis are only valid for ALS design.

This thesis considers three topics related to the iceberg collisions with ship structures: external mechanics, internal mechanics and residual strength assessments.

Collisions between icebergs and ship structures are quite complicated processes. For simplicity, this problem was split into its external and internal mechanics. External mechanics talks about the translational and rotational momentum balance. It is believed that the impact mechanics of iceberg collisions with ship structures should be presented in three dimensions. Thus, a new formulation of impact mechanics was proposed that describes the impact in three dimensions. All forces except for impact force are neglected. This new three-dimensional method degrades to existing two dimension (2D) method. It was successfully applied to the calculation of the demanded dissipated energy for iceberg and ship collisions.

Internal mechanics deal with both deformations of icebergs and ship structures. Nonlinear finite-element analysis (NLFEA) was used in this research. The commercial code LS-DYNA 971 was used to assess the internal mechanics of both icebergs and ship structures. Deformations of both icebergs and ship structures should be well captured by numerical simulations. However, due to the difficulties of simulating ice, NLFEA is not straightforward. To facilitate such simulations, a plasticity-based material model for icebergs was developed in this thesis. Iceberg crack propagation was simulated by element erosion. An empirical failure criterion for detecting those failed ice elements is proposed. Numerical examples showed that the new iceberg model gives good results. The model was successfully implemented in LS-DYNA 971 through a user-defined subroutine. Subsequently, the integrated numerical analysis of iceberg-ship collisions was then successfully performed. Efforts were made to investigate the internal mechanics of both icebergs and ship structures during collision, such as local structural behaviours and ice failure. Two scenarios of iceberg-ship collisions were investigated: iceberg collisions with foreship and side-ship structures. In the first scenario, efforts focused on the investigation of the detailed internal mechanics of the icebergs and ship structures. The strength of ship structures was varied by adjusting the parameters of the steel material model, thereby varying the relative strength of icebergs and ship structures. A comprehensive discussion is based on the simulation results. The discussion addresses contact pressure, iceberg shapes and collision locations. In the second scenario, investigations focused on the influences of the iceberg shapes. Simple

iceberg shapes representing “sharp” and “blunt” icebergs were used. The results show that “blunt” icebergs may behave as rigid bodies.

Finally, the residual strengths of the ship structures after impact, which may be caused by the icebergs, was assessed. A simple plasticity method and a single stiffener model were developed to quantify the residual strengths of the damaged ship structures. In the simple plasticity method, elastic and rigid-plastic methods were combined to derive the end-shortening curve for damaged stiffeners. In the single stiffener model, proper boundary conditions were proposed. Both methods were verified against numerical simulations. Generally, good results were obtained. From this work, a rapid method to assess the residual strength of damaged ship structures is suggested.

Acknowledgements

First of all, I would like to express my great thanks to my supervisor, Professor Jørgen Amdahl. He encouraged me to address this challenging topic. To be sure, this doctoral thesis could not have been completed without his professional perspective and intelligent guidance. I have enjoyed both my academic discussions and private talks with him. I was really fortunate to have the chance to work with Professor Jørgen Amdahl. Thank you very much for your kindly, patient supervision.

Thanks should also be given to my co-supervisor, Professor Sveinung Løset. He taught me everything I know about ice mechanics. Whenever I had questions and doubts, he found time to help me. This doctorial thesis was made possible by Professor Sveinung Løset's generous support, which started right from the beginning.

I am also heartily thankful to Professor Odd S. Hopperstad and Professor K. Høyland for their patience and constructive suggestions on material modelling and ice mechanics, respectively. Great thanks to Dr. H.S. Alsos for generously sharing his knowledge on developing user-defined material subroutines and the usage of LS-DYNA 971.

It is a pleasure to thank the experts I met on all kinds of occasions, including Professor P. Pedersen, Professor E. M. Schulson, Professor C. Daley, Dr. K. McKenna, Dr. R. Gagnon, Dr. Gus Gammert *et al.* Thank you very much for the interesting discussions regarding various perspectives of my doctoral studies.

I offer my regards and blessings to all my friends and fellow colleagues both at the department of Marine Technology and the department of Civil and Transport Engineering, though I do not have enough space to list all the names. I will never forget those days we spent together. Great thanks are assigned to my lovely team members from the most famous football club, "Kinesisk Fotball Klubb" (KFK).

Last but not least, I own my deepest gratitude to my family. Thanks you very much for your unconditional support and love. Especially, I am grateful to my beloved wife, Juan Wu, who has made her support available in a number of ways. I would like to give my special thanks to my little son, Haichen Liu. Thank you so much for bringing us so many enjoyable moments.

This doctoral thesis was carried out as a part of the Strategic University Programme, "ScenaRisC&G". The financial support from the Research Council of Norway for this programme is acknowledged.

Zhenhui Liu
April, 2011.
Trondheim, Norway

Appended Paper List

[Paper I]

Liu, Z. and Amdahl J., A new formulation of the impact mechanics of ship collisions and its application to a ship-iceberg collision, *Marine Structures*, 2010, 23(3): 360-384.

[Paper II]

Liu, Z., Amdahl J. and Løset S., Plasticity based material modelling of ice and its application to ship-iceberg impacts, *Cold Regions Science and Technology*, 2011, 65(3): 326-333.

[Paper III]

Liu, Z., Amdahl J. and Løset S., Integrated numerical analysis of an iceberg collision with a foreship structure. *Marine Structures* (in press), 2011.

[Paper IV]

Liu, Z., Amdahl J. and Løset S., Integrated numerical analysis of iceberg collision with ship side structures. *International Conference on Port and Ocean Engineering*, 2011. POAC11-004, July 10-14, Montréal, Canada.

[Paper V]

Liu, Z. and Amdahl J., Numerical and simplified methods for analysis of the residual strength of ship double bottoms. Submitted to *Ocean Engineering*, 2011.

[Other papers]

The author has also taken part in the following papers. They are, however, not included in the thesis.

Liu, Z., Amdahl J. and Løset S., Numerical simulation of collisions between ships and icebergs. In: *Proceedings of the 20th International Conference on Port and Ocean Engineering under Arctic Conditions,* POAC09-38, 9-12 June, 2009, Lulea, Sweden.

Liu, Z. and Amdahl J., Residual strength of damaged stiffened panel on double bottom ship. In: *Proceedings of the 2nd International Conference on Marine Structures*, MARSTRUCT, Lisbon, 16-18 March, 2009, p. 163-171.

Liu, Z., J. Amdahl and S. Løset, Application of plasticity theory on the simulation of iceberg impacts. In: *Proceedings of the 3rd International Conference on Computational Methods in Marine Engineering*, Trondheim, 15-17 June, 2009, p.109-114.

Liu, Z., Amdahl J. and Løset S., Integrated analysis of ship/iceberg collision. In: *Proceedings of the 5th International Conference on Collision and Grounding*, ICCGS, 14-16 June, 2010, Espoo, Finland.

Liu, Z., Amdahl J. and Løset S., A parametric study on the external mechanics of ship/iceberg collision. In: *Proceedings of the 29th International Conference on Ocean, Offshore and Arctic Engineering*, OMAE 2010-20064, 6-11 June, 2010, Shanghai, China.

Hu, Z., Liu Z. and Amdahl J., Collision character research for semi-submersible through model test, simplified analytical and numerical simulation method. In: *Proceedings of the 29th International Conference on Ocean, Offshore and Arctic Engineering*, OMAE 2010-20253, 6-11 June, 2010, Shanghai, China.

Liu, Z., Garee L. and Amdahl J., Analysis of foreship and iceberg impact loads based on Bayesian networks. In: *Proceedings of the 30th International Conference on Ocean, Offshore and Arctic Engineering*, OMAE 2011-50028, 19-24 June, 2011, Rotterdam, The Netherlands.

Contents

Chapter 1

Introduction

1.1 Background and motivation

> *"Considered as a whole, the formal economy of the Arctic is of fundamental geo-political importance. Indeed, it permits the production of raw materials that contribute to meeting the needs of the industrialized world."*
>
> *----Arctic Human Development Report, Duhaime, G. (2004)*

The Arctic Human Development Report (AHDR), which was signed by the leaders of all Arctic countries, states that oil and gas exploration, production and transportation would be the driving force behind the formal development of the Arctic economy in the coming decades.

According to assessments made by the U.S. Geological Survey (USGS) in 2008 (Figure 1-1), about 30% of the world's undiscovered gas and 13% of the word's undiscovered oil are stored in the North Arctic Circle (Gautier *et al.*, 2009). The Arctic is regarded as the Middle East of the future. Oil companies began to explore oil and gas in the Arctic area, such as the Hibernia field project, as early as the 1980s. Started more recently, the ongoing Shtokman project in the Barents Sea is one of the largest natural-gas projects in the world. It can be expected that human activity in the Arctic area will definitely increase in the near future.

However, the decreasing number of ice features in the Arctic makes sailing routes from Western European countries to East Asia or North America increasingly possible (Figure 1-2). The voyage made by MV Nordic Barents in July of 2010 was a historic breakthrough in Arctic shipping (see Nilse, 2010). With these new shipping routes, the distance of traditional routes can be reduced by one-third. If these routes become reliable, the Arctic may become one of the world's busiest shipping areas.

However, Arctic exploration is still in the early stages. One major reason is due to the harsh environment in this area. Ship structures need to be specially designed to withstand the ice loads they may meet. According to modern ship design codes, ship structures should be designed under the principles of an ultimate limit state (ULS) and verified with the principles of an accidental limit state (ALS). Accidents between naval structures and ice features may cause severe damage, such as penetration, flooding or even the sinking of ship structures. The biggest maritime disaster in history, the Titanic, is an example of a casualty that is frequently mentioned. In connection with the potential explorations of the Arctic discussed above, the probability of iceberg-ship

collisions is increasing, which makes the research on icebergs' impact loads to ship structure a necessity.

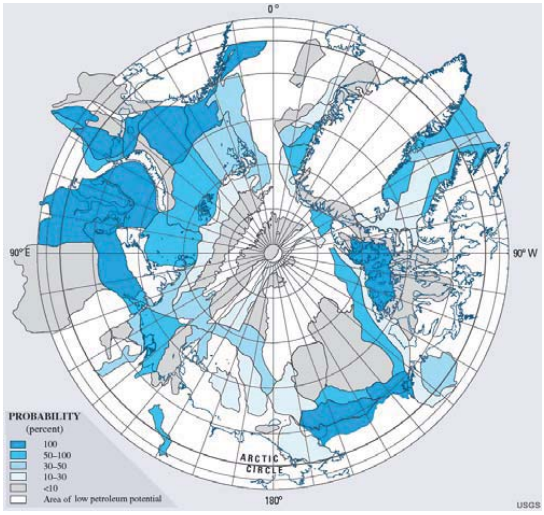

Figure 1-1 Assessment units (AUs) in the Circum-Arctic Resource Appraisal (CARA) color-coded by assessed probability of the presence of at least one undiscovered oil and/or gas field with recoverable resources greater than 50 million barrels of oil equivalent (MMBOE). Probabilities for AUs are based on the entire area of the AU, including any parts south of the Arctic Circle, from USGS (2008).

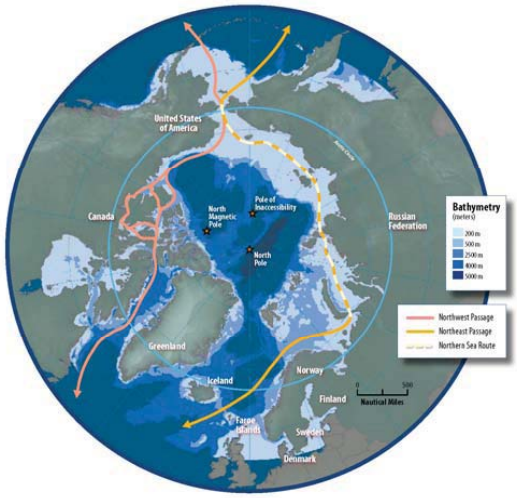

Figure 1-2 The Arctic Marine Area, from AMSA (2009).

Aside from the famous Titanic disaster, collisions between icebergs and ship structure have caused significant structural damage and economic costs. The Overseas Ohio directly hit an iceberg on the 2nd of Jan., 1994. The bulbous bow was ruptured and the

ballast tank was holed. The cost to repair the damage to ship, as shown in Figure 1-3, was at least $1 million.

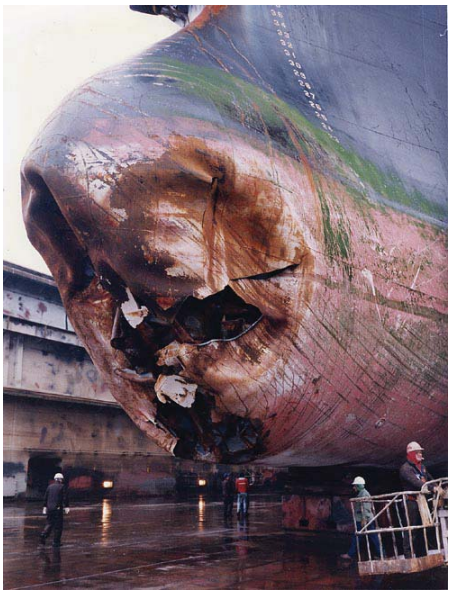

Figure 1-3 Damaged bow of Overseas Ohio after collision with iceberg, from Hill (2006).

On 21st of July, 1996, a bulk carrier Reduta Ordona was hit by an iceberg in Hudson Bay while heading for Churchill, Manitoba. Hull structure was severely damaged and cracks were observed (Figure 1-4).

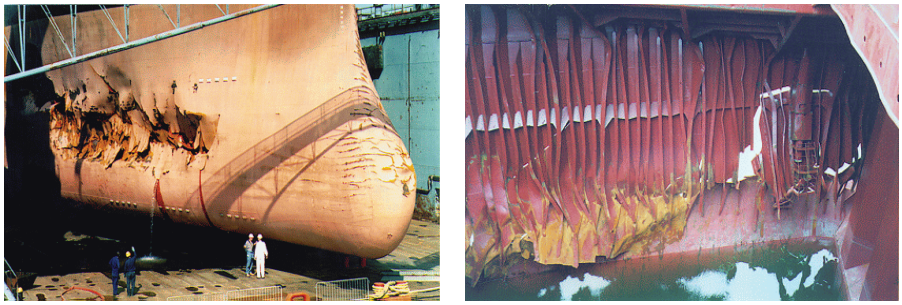

Figure 1-4 Structure damage of Reduta Ordona after collision with iceberg, from Hill (2006).

The ice features in both of these collisions were small icebergs, according to Hill (2006). After the Titanic disaster, collisions between ships and medium or bigger icebergs (with heights above sea level larger than 15 meters and an approximate mass larger than 2,000,000 tons) will be rare due to modern high-tech radar and satellite systems. However, smaller icebergs, also termed as bergy bits or growlers, are quite difficult to detect prior to collision, and bad weather conditions can make detection even more

difficult. These collisions may cause severe structural damage to ship structures, especially for ships that are not strengthened for ice loads.

1.2 An overview of research on iceberg collisions with marine structures

The research on collisions between icebergs and marine structures has been mainly motivated by the explorations of oil and gas fields in Arctic and sub-Arctic areas (e.g., the Shtokman field in the Barents Sea and four fields off the east coast of Canada (Hibernia, Terra Nova, Hebron, Whiterose)). The earliest related research appeared in the 1980s, including the work of Cammaert and Tsinker (1981), Curtis, *et al.* (1984), Kitami *et al.* (1984), Arockiasamy *et al.* (1984), Duthinh and Marsden (1986), Neve (1987) and Johnson and Prodanovic (1989). Although various collision scenarios were investigated, iceberg impact loads were usually simplified by analytical equations and were then implemented into equations of motion. Pressure-area relationships or the crushing strength of ice was often chosen to represent the iceberg impact load. Detailed studies on the structures of icebergs interactions were not possible at that time.

Kierkegaard (1993) made a comprehensive study on iceberg-ship collisions that focused on the deformations of ship structures. Icebergs were idealised as rigid objects due to their extremely complicated mechanical behaviours, as stated by the author in his thesis. Løset and Kvamsdal (1994) were the first to simulate icebergs' structural interactions with the commercial code LS-DYNA 971. In this software, the iceberg is simulated by a material with a so-called 'Tsai-Wu' yield surface. Fuglem *et al.* (1996) assessed iceberg impact loads using probabilistic methods. Again, the icebergs' mechanic behaviours were simply represented by a pressure-area relationship.

Brown and Daley (1999) did a computer simulation of the lateral collisions between icebergs and a moored structure in the Terra Nova oilfield. A pressure-area relationship was used to assess the icebergs' impact loads, and the loads were output to a computer code (Working Model 2D), which solved the equations of motion. Croasdale (2001) summarised the relevant local ice-load data with the aim of providing design guidance for severe ice-load events to offshore structures, such as icebergs and pack-ice impacts. However, the present experimental data are insufficient to fully describe the ice loads caused by iceberg impacts. Ideally, the pressure-area relationship should be considered together with an iceberg's aspect ratio. The pressure-area relationships obtained from aspect ratios that are not suitable for icebergs should be separated.

R. Gagnon has carried out both experimental and numerical work on iceberg impacts (e.g., Gagnon and Gammon, 1995; Gagnon, 1998; 2004; 2006; 2008; 2011). Together with his colleagues, he carried out bergy-bit impact trials on the CCGS Terry Fox off the northern tip of Newfoundland (Gagnon *et al.*, 2008). A comprehensive research study was made from these trials. However, no structure damage was reported in that experimental study, which may be due to the relatively small energy of the collision conducted (Figure 1-5). Gagnon also tried to do numerical simulations of iceberg impacts. His idea was to simulate ice by implementing a 'crushable foam' material

model in LS-DYNA 971. The results were promising but have not yet been applied to structure-iceberg interactions simulations. Researchers in Korea have shown interest in iceberg impact problems recently (e.g., Han *et al.,* 2008; Lee *et al.,* 2009; Oh, Kim and Lee, 2009). Those works deal with carriers of Liquefied Natural Gas (LNG) colliding with icebergs, which is a plausible scenario in the Arctic. Intensive attention was paid to the ship's global response due to iceberg impacts, but little work was done to investigate the local iceberg deformations.

Figure 1-5 Bergy bit impact trials, from Ritch *et al.* (2008)

With respect to the Shtokman field development, Eik (2009), Eik and Gudmestad (2010) and Eik and Marchenko (2010) performed comprehensive studies on iceberg management and its influences on iceberg impact loads to offshore structures. Probabilistic methods were used to assess the iceberg impact probability and its corresponding impact loads. However, no further studies on local structures and iceberg failures have been conducted.

To investigate iceberg and ship collisions, it is convenient to use a separation of external mechanics and internal mechanics to divide and describe the problem. External mechanics refers to translational and rotational momentum and energy balance. Internal mechanics refers to the local deformations of ship structures and ice. The literature review conducted above mainly obtains iceberg impact loads from the perspective of external mechanics. Little work has been done on the internal mechanics of such scenarios. The main reason for this is that the complex mechanical behaviours of ice demand significant efforts. Further, the coupling between icebergs and ship structures is even more complicated. However, this thesis attempted to take the first step forward. To the author's knowledge, this is the first work involving detailed discussions of both external and internal mechanics of iceberg-ship collisions.

1.3 Problem description and objectives

Based on the design principles of ALS, the research on iceberg and ship collisions can be categorised into following three aspects with respect to the distribution of strain energy dissipation (Figure 1-6).

- Strength design;
- Shared-energy design;
- Ductile design.

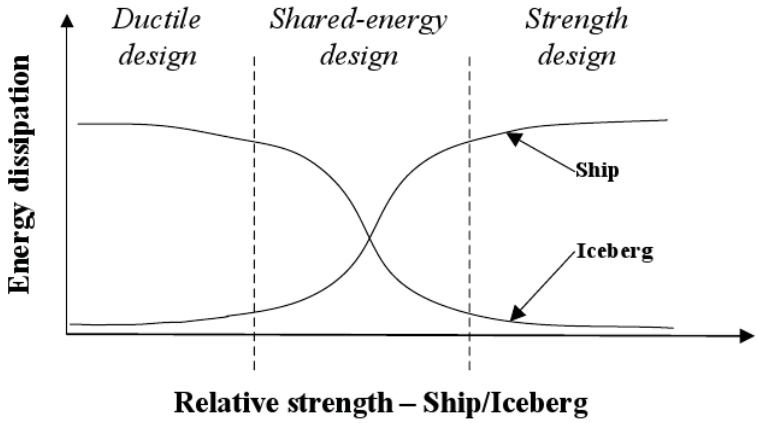

Figure 1-6 Energy dissipation for strength, ductile and shared-energy design, based on NORSOK (2004)

Ships operating in the Arctic regions have always been designed to resist ice. However, those design rules are traditionally fairly prescriptive; the actions and resistance variables are often mixed so that the design philosophy is somewhat disguised. Nevertheless, the resistance models used in design formulations were either elastic or based on plastic bending mechanisms. In either case, the acceptable deformations are small. The ice action is typically expressed by pressure-area relationships.

Modern codes for offshore structures typically require design checks carried out by ULS and ALS methods. The ULS check is typically based on actions with annual probabilities of occurrence in the range of 10^{-2}. The resistance is predominantly based on elastic resistance models. The ALS check is carried out for actions with annual frequencies in the range of 10^{-4}. The resistance may be assessed by nonlinear analysis methods; the structure may undergo yielding, buckling and large permanent deformations on its member and sub-structure levels, but the overall integrity will not be impaired.

In the ISO (2010), the ice actions associated with the ULS and ALS design checks were denoted as extreme level ice events (ELIE) and abnormal level ice events (ALIE). The ELIE corresponds roughly to the assumptions used in ship-design rules. In this case, it

is reasonable to base the design of the ship side on pressure-area relationships. The plating should be able to crush the ice and hence resist the maximal credible ice pressure for a given area, which depends on the layout of the shell panels (e.g., stiffeners and frame spacing). In the ALIE check, however, it is a matter of survival or of gross damage leading to the spill of cargo and associated pollution, *etc*. It is not natural to base the design on pressure-area relationships because the pressure experienced in a collision depends on the relative resistance of the ship, the iceberg and the damage evolution. This can only be assessed accurately if both the ship and the ice are modelled and if the interaction between the two structures is taken into account.

What is needed for realistic designs for accidental iceberg impact is, in addition to iceberg mass and speed, knowledge about iceberg shape and a continuum-mechanics model of icebergs. Both issues are associated with substantial challenges.

Icebergs may take on a variety of shapes (Figure 1-7). A few attempts have been made to characterise the shapes (e.g., Sanderson, 1988; McKenna, 2005), but so far, a common agreement on a set of standard shapes to be used for ALS design has not been established. An alternative approach to the characterisation of iceberg shapes on the basis of empirical surveys is to characterise the shapes with respect to structural resistance to icebergs impacts. In principle, a "spear-like" protrusion of an iceberg has a large puncturing potential (Figure 1-8 (a)). However, in such cases, the ship side may simply crush the ice. A vertical, planar-surface iceberg represents significant confinement of ice, which may become virtually rigid relative to the structure (Figure 1-8 (d)). However, the associated large contact area yields significant energy dissipation on the ship side and no penetration of the inner hull (unless the iceberg's kinetic energy is very large). Icebergs with intermediate shapes (Figure 1-8 (b, c)), will cause both deformations to the ship structure and the iceberg itself.

Figure 1-7 Different iceberg shapes.

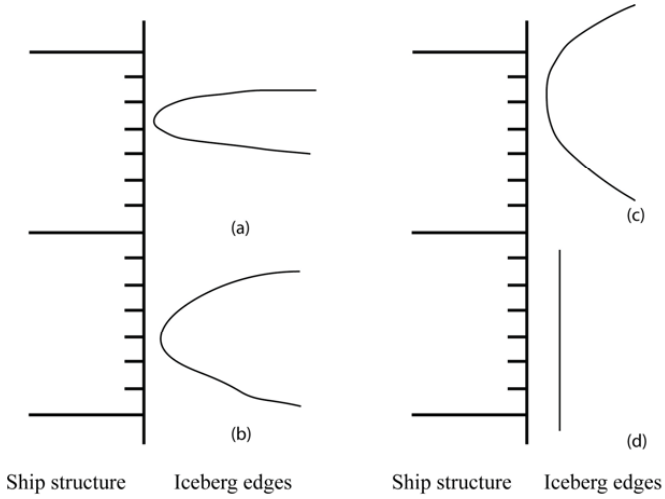

Figure 1-8 Illustration of ship structure scantlings and different shapes of iceberg edges

The present thesis attempted to assess iceberg impact loads by considering both ship and iceberg deformations and followed the principles of shared-energy design in ALS. The objectives of the present thesis were:

- To develop a new three-dimensional (3D) analytical method that describes the external mechanics of iceberg-ship collisions;
- To develop a new user-defined iceberg material model, which can be further applied to integrated numerical simulations;
- To perform integrated numerical simulations of iceberg-ship collisions and to discuss the results;
- To investigate the residual strength of ship structures after damage; such damage may be caused by grounding or iceberg impacts.

The icebergs discussed here were limited to small icebergs, say growlers or bergy bits, with heights above sea level of less than 5 meters. The approximate mass may be several thousand tons. For ship structures, both ice-strengthened oil-shuttle tankers and floating production, storage and offloading (FPSO) units were considered.

This thesis was carried out as a part of the Strategic University Programme Scenario-based Approach to Risk Analysis of Ship Collision and Grounding (ScenaRisC&G) funded by the Research Council of Norway.

1.4 Methodologies and assumptions

Iceberg-ship collisions are quite complicated processes. Due to this fact, reasonable simplifications were made in the present research. The main methodologies used are listed below:

- The split between external and internal mechanics for iceberg and ship

collisions and the coupling between them was linked by the total dissipated strain energy;
- Stronge's impact theory was applied in the external mechanics study; all forces except for the impact force were neglected;
- The iceberg material model was assumed to be strain-rate independent;
- Element erosion was used to simulate ice failure. Failed ice was numerically removed from the simulation, and thus, the force from the crushed ice was not considered;
- The rigid-plastic method was used to develop an end-shortening curve for damaged stiffeners, and all damaged stiffeners were assumed to have the same end-shortening curve.

1.5 Scope of work

Present thesis includes following chapters:

Chapter 1, the introduction;

Chapter 2, the external mechanics;

Chapter 3, the ice material modelling;

Chapter 4, the integrated numerical analysis;

Chapter 5, the residual strength assessment;

Chapter 6, the conclusions and recommendations for further work.

Chapter 2

External Mechanics

The external mechanics of ship and iceberg impact demands a three dimensional analytical solution. A new method was developed accordingly in Paper [I] by Liu and Amdahl (2010).

2.1 Introduction

A ship collision is a multi-physical and highly coupled process. However, in ALS, the analysis of collision may conveniently be split into two uncoupled processes: namely, external mechanics and internal mechanics, see Pedersen and Zhang (1998). The external mechanics deals with rigid body motions and determines the energy to be dissipated as strain energy. The internal mechanics is concerned with how the strain energy is dissipated in the striking and struck objects and involves the assessment of the structural resistance during large deformations, either by means of a plasticity theory or by using non-linear finite element analysis (NLFEA) method. The internal mechanics of iceberg and ship collision will be discussed in details in Chapter 3 and 4 of this thesis.

Experience has shown that iceberg and ship impacts, particularly oblique-type collisions, produce considerable motion in the components of sway, yaw and roll, see Johnston *et al.* (2008). Thus, modelling a ship and iceberg collision should take the six degree of freedom (6DOF) into account for each object involved. In particular, if the collision happens at the bow of a ship, the shape of the outer shell determines the contact force direction and has a significant influence on the final dissipated energy; this fact has not been taken into account in previous studies.

In this thesis, a fully 3D solution to the ship collision problem is proposed based on Stronge and Pedersen and Zhang's work (see Stronge, 2004 and Pedersen and Zhang, 1998). The two dimension (2D) case can be treated as a special case. The vertical geometry shape is taken into account. The main point of this approach is that all equations are formulated in a local coordinate system, which allows the dissipated energy along each axis in the local coordinate system to be obtained in a closed form.

In conjunction with iceberg and ship collisions, the shape and inertia properties of the iceberg are associated with significant uncertainty, notably because the major part of the iceberg is submerged. Ralph, McKenna and Gagnon (2008) carried out a series of investigations to characterise the underwater iceberg shapes using a sonar system. The mass of the iceberg can be estimated by empirical equations on the basis of iceberg's

main dimensions for the part above sea level. For the inertia properties, a calculation should be made based on the shapes detected. However, in order to illustrate the application of the present model, a simplified iceberg shape is considered.

2.2 Stronge impact theory

Stronge (2004) has done a comprehensive research work on the impact theory. The so-called local coordinate system is established to derive the equations of motion, e.g., $\vec{n}_1\vec{n}_2\vec{n}_3$ (Figure 2-1). The basic assumptions are:

- The impact duration is short, and the impact force is large, so all other external forces are neglected;
- The deformations are limited to a small area within the contact surface.

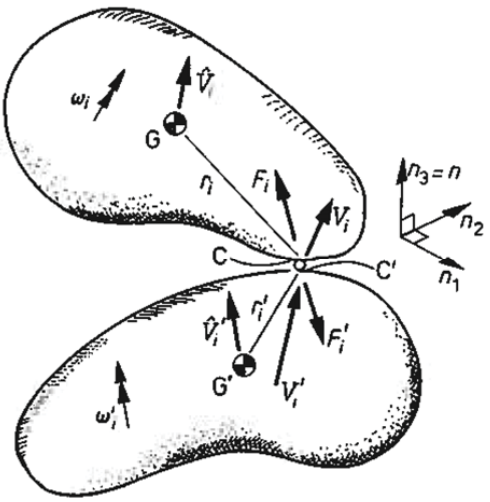

Figure 2-1 Collision between two rough bodies. The rigid bodies have contact pints C and C' that are separated by a deformable particle, after Stronge, W. J. (2004).

Consider two bodies that collide at contact point C. The bodies have no displacement constraints except that they are mutually impenetrable at C. If the surface of at least one of the bodies has a continuous curvature at C, there is a common tangent plane that constrains point C. First, define a common normal direction $\vec{n}$ that is perpendicular to the common tangent plane. Let $\vec{n}_i$, i=1, 2, 3, be a set of mutually perpendicular unit vectors with $\vec{n}_1$ and $\vec{n}_2$ at the tangent plane, while $\vec{n}_3 = \vec{n}$ is normal to this plane, as shown in Figure 2-1. A local coordinate system $\vec{n}_1\vec{n}_2\vec{n}_3$ is established. The bodies have masses M and M' and inertia tensors $\hat{I}_{ij}$ and $\hat{I}'_{ij}$ for the second moments of their masses at G and G', respectively. The diacritical mark $\wedge$ here indicates the variable is referring to the axes passing through the centre of gravity, and the prime mark $'$ over a symbol is used to distinguish variables for different collision objects. A direction vector r_i

connects G to the contact point C, while r_i' locates C' relative to G'. Let $\hat{V}_i$ and $\hat{V}_i'$ be the velocities of the centres of mass, while ω_i and ω_i' are the corresponding angular velocities for the bodies in $\vec{n}_i$ of the local coordinate system. At the contact points C and C', the bodies are subjected to forces F_i and F_i'. These contact forces are mutual reactions applying an impulse to each body. The impulses $P_i(t)$ and $P_i'(t)$ are given by

$$dP_i = F_i dt \tag{2.1}$$

$$dP_i' = F_i' dt \tag{2.2}$$

The equations of translational and rotational motion for each body can be expressed as

$$M d\hat{V}_i = dP_i \tag{2.3}$$

$$\hat{I}_{ij} d\omega_j = \varepsilon_{ijk} r_j dP_k \tag{2.4}$$

And

$$M' d\hat{V}_i' = dP_i' \tag{2.5}$$

$$\hat{I}_{ij}' d\omega_j' = \varepsilon_{ijk} r_j' dP_k' \tag{2.6}$$

where a repeated index (e.g., j or k) indicates summation, and the permutation tensor ε_{ijk} takes the values +1 if the indices are in cyclic order, -1 if the indices are in anticyclic order and 0 for repeated indices.

The velocity of each contact point, V_i and V_i', can be obtained from the velocity of the respective centre of mass and the relationship between the velocities of two points on a rigid body.

$$V_i = \hat{V}_i + \varepsilon_{ijk} \omega_j r_k \tag{2.7}$$

$$V_i' = \hat{V}_i' + \varepsilon_{ijk} \omega_j' r_k' \tag{2.8}$$

Let the relative velocity be

$$v_i = V_i - V_i' \tag{2.9}$$

Any incremental change in the reaction impulses acting on the rigid bodies is equal in magnitude but opposite in direction if the infinitesimally small deforming element has negligible mass.

$$dp_i = dP_i = -dP_i' \tag{2.10}$$

From the above equations, we find

$$dv_i = m_{ij}^{-1} dp_j \tag{2.11}$$

where the elements of the inverse inertia matrix m_{ij}^{-1} are given by

$$m_{ij}^{-1} = (M^{-1} + M'^{-1}) + \varepsilon_{ikm}\varepsilon_{jln}(I_{kl}^{-1} r_m r_n + I_{kl}'^{-1} r_m' r_n') \tag{2.12}$$

The inverse inertia matrix is symmetric, i.e., $m_{ij}^{-1} = m_{ji}^{-1}$. The following are representative elements:

$$m_{11}^{-1} = (M^{-1} + r_2^2 I_{33}^{-1} - 2r_2 r_3 I_{23}^{-1} + r_3^2 I_{22}^{-1}) + (M'^{-1} + r_2'^2 I_{33}'^{-1} - 2r_2' r_3' I_{23}'^{-1} + r_3'^2 I_{22}'^{-1}) \tag{2.13}$$

$$m_{12}^{-1} = (M^{-1} + r_1 r_3 I_{23}^{-1} - r_3^2 I_{21}^{-1} - r_1 r_2 I_{33}^{-1} + r_2 r_3 I_{31}^{-1}) + (M'^{-1} + r_1' r_3' I_{23}'^{-1} - r_3'^2 I_{21}'^{-1} - r_1' r_2' I_{33}'^{-1} + r_2' r_3' I_{31}'^{-1}) \tag{2.14}$$

$$m_{13}^{-1} = (M^{-1} + r_1 r_2 I_{32}^{-1} - r_2^2 I_{31}^{-1} - r_1 r_3 I_{22}^{-1} + r_2 r_3 I_{21}^{-1}) + (M'^{-1} + r_1' r_2' I_{32}'^{-1} - r_2'^2 I_{31}'^{-1} - r_1' r_3' I_{22}'^{-1} + r_2' r_3' I_{21}'^{-1}) \tag{2.15}$$

In these expressions, it should be noted that the matrix I_{ij} of moments and products of inertia has an inverse, which is denoted by I_{ij}^{-1}, e.g., $I_{21}^{-1} = (\hat{I}_{13}\hat{I}_{23} - \hat{I}_{12}\hat{I}_{33}) / det(\hat{I}_{ij})$.

2.3 The new formulation of external mechanics (Paper [I])

The impact theory developed by Stronge (2004) has been successfully applied to investigate the external mechanics of ship collision. A new formulation of the external mechanics of ship collision has been developed. This new method describes the impact mechanics of ship collision in three dimensions.

2.3.1 Transformation matrix

Two coordinate systems are used during the derivation of equations, namely the global and the local coordinate system. They are established as follows:

- Global coordinate system (XYZ, see Figure 2-2): The origin of the XYZ-system is placed at the centre of gravity (COG) of ship. The X-axis lies in the symmetry plane of the striking ship pointing towards the bow. The Z-axis is oriented out of water;
- Local coordinate system ($\vec{n}_1\vec{n}_2\vec{n}_3$, see Figure 2-3): The local coordinate system is similarly established as method described in section 2.2. It is further assumed that the hull shape at the collision point of ship determines the direction of the local frame.

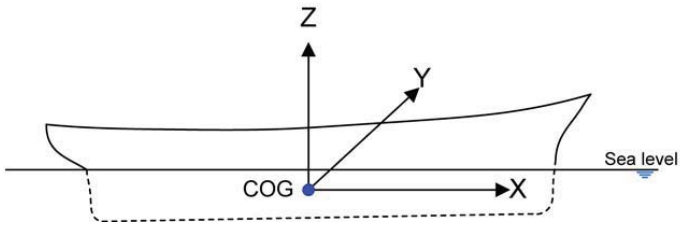

Figure 2-2 Global coordinate system of the ship

For simplicity, the influence of hydrodynamic forces is considered by introducing the added mass factors in both the mass and inertia matrices. Consequently, the mass M and M' in Stronge's theory should be replaced by the mass matrices M_{ij} and M'_{ij}. As discussed by Salvesen, Tuck, and Faltinsen (1970), the mass and inertia matrices are significantly simplified due to the lateral symmetry of the ship hull (symmetry about the X,Z-plane in the global coordinate system). If we put the origin of the coordinate system in the COG of the ship, then the mass and inertia matrices can be assumed to be diagonal matrices with reference to the global coordinate system, e.g., $\hat{M}_{ij}, \hat{M}'_{ij}$ and $\hat{I}_{ij}, \hat{I}'_{ij}$. However, it does not apply to the iceberg because its shape is usually irregular. Field measurements are necessary if accurate results are required. To begin, a simplified iceberg shape can be used. Then, the formation of M_{ij}, M'_{ij} and I_{ij}, I'_{ij} in the local coordinate system $\vec{n}_1\vec{n}_2\vec{n}_3$ can be generated if the transformation matrix is known.

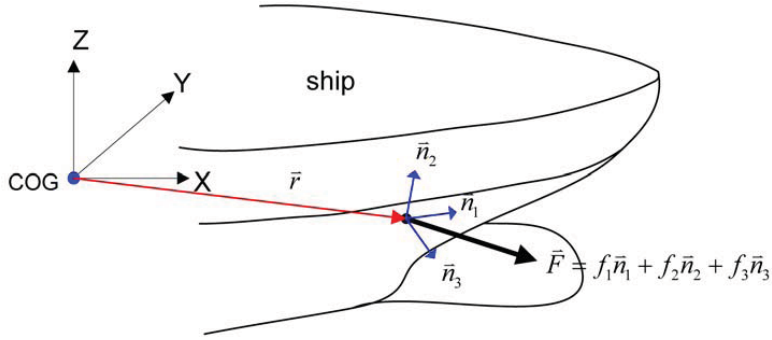

Figure 2-3 Collision point geometry and the local coordinate system, modified from Daley (1999).

The transformation matrix between local and global coordinate system is derived based on the definition of hull angles as defined by DNV (2009) (Figure 2-4).

- α : waterline angle
- β : frame angle
- β' : normal frame angle
- γ : sheer angle

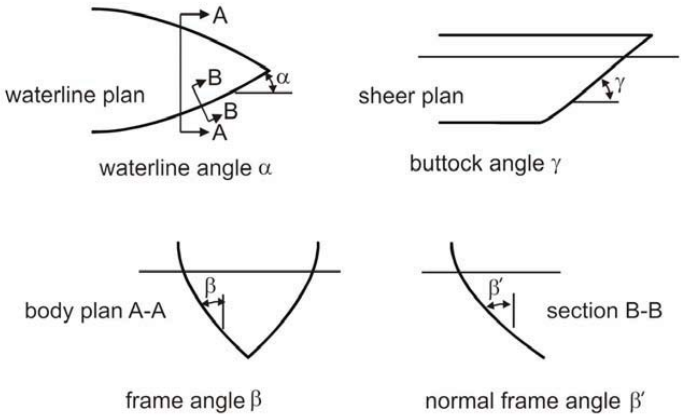

Figure 2-4 The definition of hull angles, DNV (2009)

The transformation matrix is as follows:

$$T_{lg} = \begin{bmatrix} cos(\alpha) & -sin(\alpha) & 0 \\ -sin(\alpha)sin(\beta') & -cos(\alpha)sin(\beta') & -cos(\beta') \\ sin(\alpha)cos(\beta') & cos(\alpha)cos(\beta') & -sin(\beta') \end{bmatrix} \tag{2.16}$$

2.3.2 Derivation of energy dissipation

The impulse in each direction, $\vec{n}_i \quad (i = 1,2,3)$, is given by

$$dp_i = f_i dt \tag{2.17}$$

where f_i is the *i*'th component of the interaction force acting on the infinitesimally small deforming element in the $\vec{n}_i$ direction.

The relative acceleration $\ddot{s}_i$ in each direction is

$$\ddot{s}_i = \frac{dv_i}{dt} \tag{2.18}$$

According to Eqs. (2.1) and (2.10),

$$f_i = F_i = -F_i' \tag{2.19}$$

By substitution of Eqs. (2.17) and (2.18) into Eq. (2.11), we obtain

$$\ddot{s}_i = m_{ij}^{-1} f_j \tag{2.20}$$

The acceleration can be written

$$\ddot{s}_i = \frac{d\dot{s}_i}{ds_i}\frac{ds_i}{dt} \tag{2.21}$$

Substituting Eq. (2.21) into Eq. (2.20) and integrating over the impact duration t, it can be seen that

$$\int_0^t m_{ij}^{-1} f_j ds_i = \int_0^t \dot{s}_i d\dot{s}_i = \frac{1}{2}((v_i^t)^2 - (v_i^0)^2) = \frac{1}{2}\Delta v_i^2 \tag{2.22}$$

where v_i^t, v_i^0 are the relative velocities before and after the collision in the $\vec{n}_i$-direction, and Δv_i^2 is the change of the squared relative velocities v_i^t and v_i^0. Note that it is not always positive.

$$\Delta v_i^2 = (v_i^t)^2 - (v_i^0)^2 = dv_i(dv_i + 2v_i^0) \tag{2.23}$$

where dv_i is the relative velocity change in the $\vec{n}_i$-direction:

$$dv_i = v_i^t - v_i^0 \tag{2.24}$$

Further,

$$\int_0^t m_{ij}^{-1} f_j ds_i = m_{ij}^{-1} \frac{f_j}{f_i} \cdot \int_0^t f_i ds_i = E_i \cdot m_{ij}^{-1} \frac{f_j}{f_i} \tag{2.25}$$

Substitution of Eq. (2.25) into Eq. (2.22) yields

$$E_i = abs(\int_0^t f_i ds_i) = \frac{1}{2} \cdot abs(\frac{1}{m_{ij}^{-1} \frac{f_j}{f_i}} \cdot \Delta v_i^2) \tag{2.26}$$

where 'abs' indicates to calculate the absolute value because the force f_i and ds_i may be not at the same direction. If we define an equivalent mass variable $\bar{m}_i$ as follows:

$$\frac{1}{\bar{m}_i} = m_{ij}^{-1} \frac{f_j}{f_i} \tag{2.27}$$

Then, the dissipated energy has the following form:

$$E_i = \frac{1}{2} abs(\bar{m}_i \Delta v_i^2) \tag{2.28}$$

Eq. (2.28) shows that the complicate 6DOF can be simplified to a *1DOF* problem in each direction if the equivalent mass $\bar{m}_i$ and change of the squared relative velocity Δv_i^2 can be derived. These can only be done by introducing proper boundary conditions, such as the friction definition, relative velocities. For detailed solutions, please refer to Paper [I] by Liu and Amdahl (2010).

2.4 Validation

The new method has been validated against existing method and experimental data available. It agrees excellently well with the 3DOF method developed by Pedersen and Zhang (1998) if the vertical eccentricity is not considered. And further, 3DOF method by Pedersen and Zhang (1998) will overestimate the dissipated energy level if the

vertical eccentricity exists, in which the roll motions for each collision objects are activated (Figure 2-5, 6). This feature can only be captured by present method.

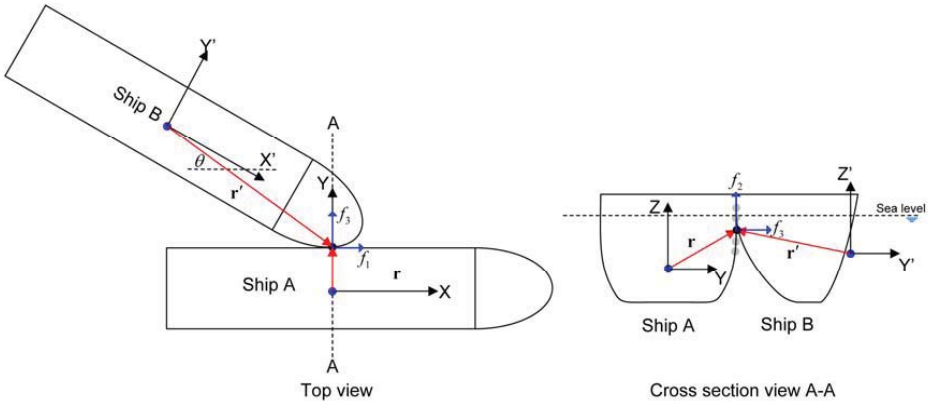

Figure 2-5 Scenario of numerical example

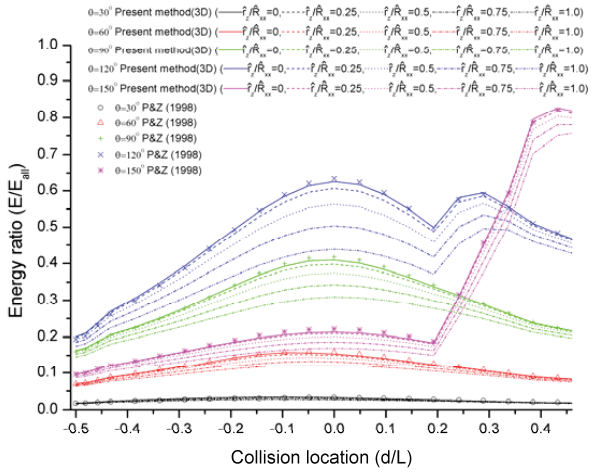

Figure 2-6 Energy ratio of total dissipated energy with $\hat{r}_z/\hat{R}_{xx}$.

2.5 Application example

One numerical example of ship and iceberg collision has been successfully performed. The iceberg was idealized as a cone shaped object (Figure 2-7). A parametric study was performed. The calculated energy dissipation was normalised versus the maximum possible energy dissipation E_0, associated with a central, plastic impact as following:

$$E_0 = \frac{1}{2} M_{iceberg} \hat{v}_{ship}^2 \frac{(1 - \frac{\hat{v}_{ice}}{\hat{v}_{ship}})^2}{1 + \frac{M_{iceberg}}{M_{ship}}} \tag{2.29}$$

where $\hat{v}_{ship}, \hat{v}_{ice}$ are velocities under the global coordinate system of ship and iceberg respectively, $M_{ship}, M_{iceberg}$ are the mass of ship and iceberg respectively. As seen from Figure 2-8, it is observed that a very large normal frame angle β' is favourable with respect to small energy dissipation for the given iceberg shape. As β' decreases, the energy dissipation increases and attains a maximum for $\beta' = 20^0$ to 30^0. Figure 2-8 shows that the 3D method produces a smaller energy ratio than the 2D method, which is expected because the 3D method allows transfer of the kinetic energy into motion components in all 6DOFs. The 2D method proposed by Pedersen and Zhang (1998) is quite conservative in this case.

However, large uncertainties still exist due to the lack of field data on iceberg dimensions, such as mass, added mass factors, location of COG and shapes. In this respect, probability methods may provide an meaningful approach. For instance, Liu, Garee and Amdahl (2011) used the so called Bayesian Network method to assess the iceberg impact loads.

Two additional works have been done regarding the further application of present method. The first one is the parametric study on the external mechanics of iceberg collision with ship structures (Liu, Amdahl and Løset, 2010). The second one is the application of present theory on calculating the dissipated energy level for a semi-submersible collision model test (Hu, Liu and Amdahl, 2010). Present new method has been proved to be an accurate and efficient tool on assessing the external mechanics of ship collision problems.

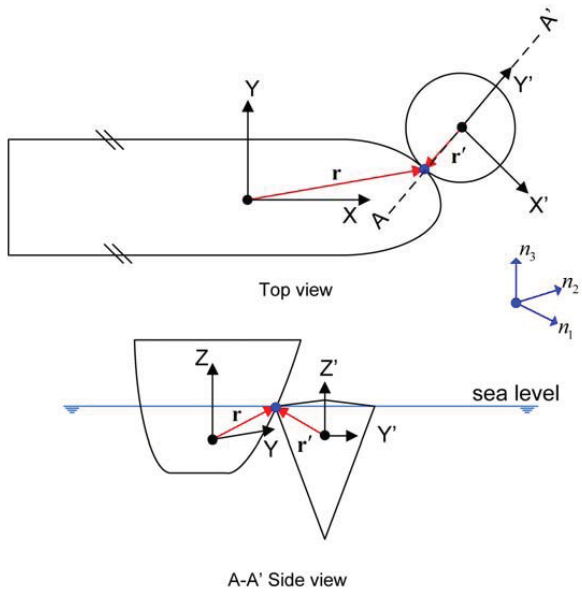

Figure 2-7 Proposed collision scenario of iceberg collision with ship, from Liu and Amdahl (2010).

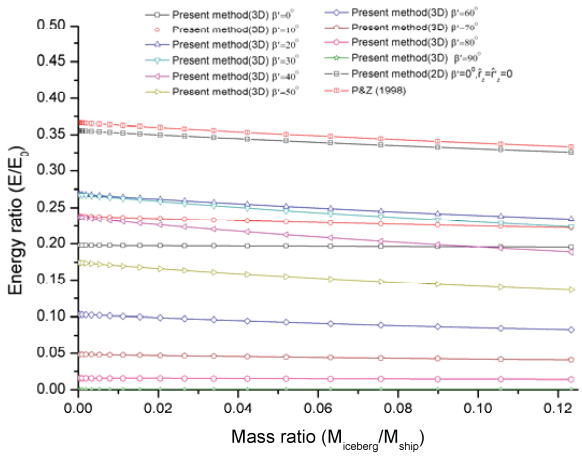

Figure 2-8 Energy ratio and mass ratio relationship, from Liu and Amdahl (2010).

Chapter 3

Ice Material Modelling

A new material model of ice was developed in this thesis. Ice-material modelling is used to facilitate the numerical simulations of iceberg and ship collisions. The ice material model in this thesis was presented in Paper [II] by Liu, Amdahl and Løset (2011a).

3.1 Introduction

Iceberg ice falls within the category of a multi-year ice, which has survived at least two summer seasons. It is composed of freshwater ice from land-based glaciers flowing off the land into the sea. Iceberg ice can be idealised as an isotropic material, as it shows no significantly different mechanical properties in each direction (Sanderson, 1988). In this sense, it is comparatively simpler than sea ice. However, iceberg ice is also influenced by temperature, porosity, grain size, strain rate and confinement. In general the ice becomes weaker and softer with increasing temperature, porosity and grain size. The effect of the strain rate (loading rate) was discussed by Schulson (2001) (Figure 3-1). Strength increases with increasing strain rate until brittle failure takes over after which strength decreases. There exists a transition from ductile to brittle, with a strain rate of 10^{-3} . In iceberg collisions, it is believed that the strain rate is greater than the transition value, as discussed by Liu *et al.* (2011a) and Derradji-Aouat (2005).

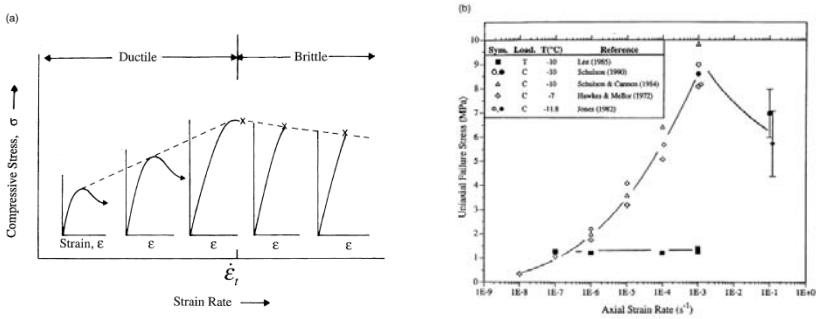

Figure 3-1 Ice strength plotted against strain rate, from Schulson (2001)

During a collision with structures, ice within the contact area undergoes large confinement and compression (Figure 3-2). High-pressure zones exist in these areas, which may be as high as 70 MPa. For ice features next to the edge, spall and extrusion are more likely. A phase change from ice to water is possible in these small areas. Thus, for high hydrostatic pressures, the ability of ice to resist deviatoric stresses is reduced.

Yield-surface techniques, such as von Mises, Drucker-Prager and Mohr-Coulomb, cannot model this phenomenon.

Researchers have tried to use proper yield surfaces to assess the maximum ice loads delivered to ship structures (e.g., Riska, 1980; Nadreau and Michel, 1986; Derradji-Aouat, 2000; 2003; Bjornar, 2001; Heinonen, 2004). It was concluded that a shear-cap yield surface, such as that of *"*Tsai-Wu*"* (e.g., Tsai and Wu, 1971) could simulate ice-impact behaviours.

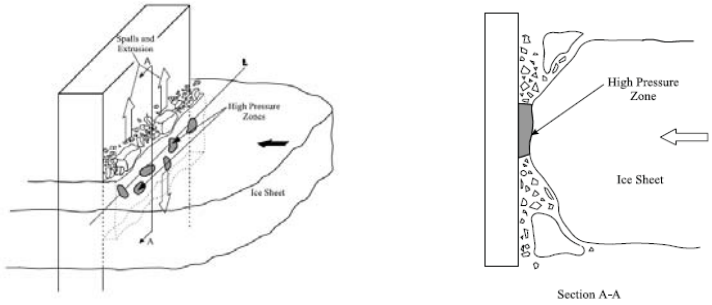

Figure 3-2 Schematic illustration of the main process of spalling, extrusion and high-pressure zone formation, from Jordaan (2001).

Numerical ice models for simulations are not well established. Carney *et al.* (2006) presented an ice model for high-strain-rate ice impacts that was designed for very high-velocity collisions (on the order of 100 m/s). Gagnon (2008) simulated growler impacts to ships with a 'crushable foam' material model to simulate the ice behaviour; the model was developed by Hallquist (2007). However, input for the "*crushable foam*" model suffered from the lack of a physical explanation. Further, ice cracks and damage were not considered.

In this thesis, a simple plastic model was proposed. This material model was based on plasticity theory and was strain-rate independent. The 'Tsai-Wu' yield surface and associated flow rule were combined to describe the constitutive behaviours of iceberg ice.

3.2 Yield surface of iceberg ice

The determination of yield function f for iceberg ice should be based on triaxial experimental data. Jones (1982) has done a series of experiments with polycrystalline ice under triaxial stress state. The strain rate ranges from $1.4\cdot10^{-6}\mathrm{s}^{-1}$ to $1.4\cdot10^{-2}\mathrm{s}^{-1}$ and the confining pressure varied from 0.1 to 85 MPa. All tests were performed at -12ºC. Nadreau and Michel (1986) summarized the data by Jones and proposed a *'Teardrop'* shaped yield surface which agrees quite well with Jones' data (Figure 3-3). Nadreau and Michel's yield surface can be written as a function of the stress invariants:

$$f(\sigma_{ij}) = aI_1^3 + bI_1^2 + cI_1 + dJ_2 - 1 = 0 \qquad (3.1)$$

with I_1 being the first invariant of the stress tensor and J_2 the second invariant of the deviatoric stress tensor, a, b, c, d are constants which are dependent on material tensile and compression strength. One of the main advantages of this formulation is its ability to account for the hydrostatic pressure at which ice can take no shear and may be treated as water. It is seen that the yield surface expands with increasing strain rate. However, this may not apply to iceberg ice.

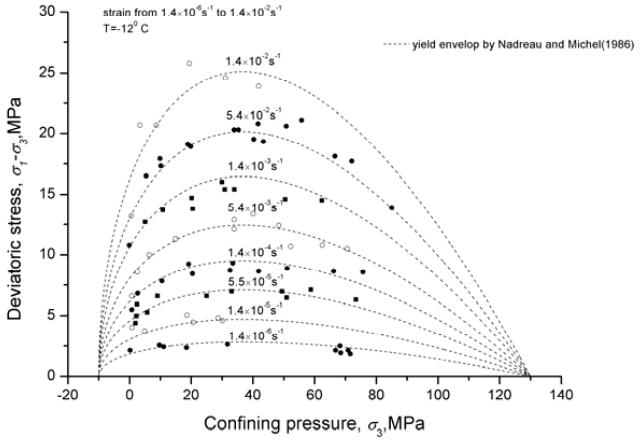

Figure 3-3. Teardrop yield surfaces and Jones' triaxial experiment data, reproduced after Jones (1985) and Nadreau (1986).

Gagnon and Gammon (1995) carried out the triaxial experiments with iceberg and glacier ice. Triaxial tests were conducted on cylindrical samples with strain rates ranging from $4 \cdot 10^{-5} \mathrm{s}^{-1}$ to $2.7 \cdot 10^{-1} \mathrm{s}^{-1}$, and confining pressure ranging from 0 to 13.8 MPa. The temperature varied: -1ºC, -6ºC, -11ºC and -16ºC. Even though the available experimental data cover a limited span of hydrostatic pressures (Figure 3-4), a similar elliptical yield envelop as Nadreau for the iceberg ice is proposed as by Derradji-Aouat (2000):

$$\left(\frac{\tau-\eta}{\tau_{\max}}\right)^2+\left(\frac{p-\lambda}{p_c}\right)^2=1 \tag{3.2}$$

where $\eta, q_{\max}, \lambda, p_c$ are constants. τ is the octahedral stress and p is the hydrostatic pressure. Figure 3-4 shows the yield surface proposed by Derradji-Aouat for the iceberg ice for a temperature of -1ºC.

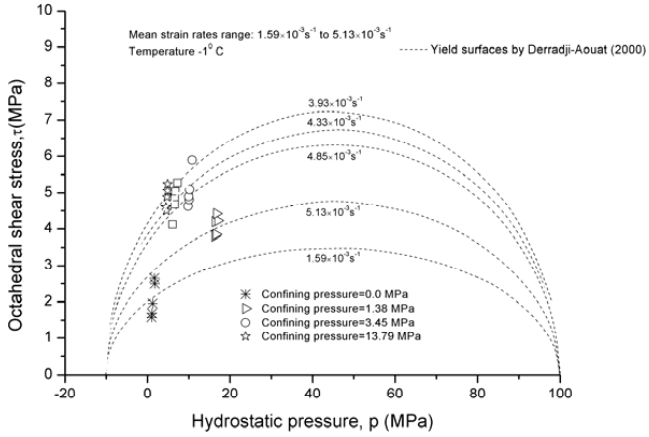

Figure 3-4. Elliptical yield surfaces for iceberg ice, reproduced after Derradji-Aouat (2000).

Mathematically, the yield surface proposed by Derradji-Aouat (2000) is the same as the so called "Tsai-Wu" yield surface for the condition $\eta = 0$. The Tsai-Wu yield surface has been used for modelling of ice mechanics for years, see Liukkonen and Kivimaa (1991), Riska and Frederking (1987), Løset and Kvamsdal (1994) and Kierkegaard (1993). However, its application to integrated FEM simulation of structure – iceberg impacts has not been done before.

The Tsai-Wu yield surface for isotropic material is usually written in following form:

$$f(p,q) = q - \sqrt{a_0 + a_1 p + a_2 p^2} \tag{3.3}$$

where p is the hydrostatic pressure, $p = \frac{\sigma_{kk}}{3} = \frac{I_1}{3}$ and q is the deviatoric stress, $q = \frac{3}{2}\sqrt{s_{ij} : s_{ij}}$, s_{ij} are the deviatoric stress components, a_2, a_1, a_0 are constants which should be fitted to triaxial experimental data. The elliptical yield surface is adopted in the present work to describe iceberg behaviour. In order to make the implementation convenient, the Tsai-Wu yield surface is rewritten in $p - J_2$ space as follows:

$$f(p,J_2) = J_2 - (a_0 + a_1 p + a_2 p^2) = 0 \tag{3.4}$$

where J_2 is the second invariant variable for deviatoric stress tensor, $J_2 = \frac{1}{2} s_{ij} : s_{ij}$. Figure 3-5 shows a comparison of the recommended inputs based on various data sources in $p - J_2$ space. It is seen that there are big differences existing which are due to the different data sources and the fitting methods used to approach the experimental data sets.

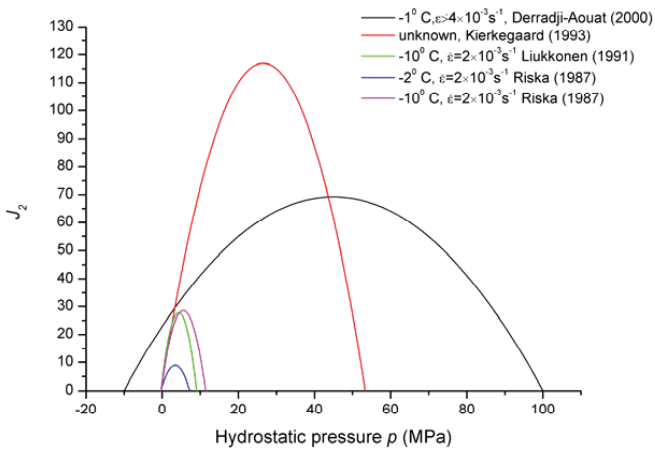

Figure 3-5 Illustration of Tsai-Wu yield surface in $p-J_2$ space.

3.3 The new numerical ice model (Paper [II])

The Tsai-Wu yield surface was chosen in the present research to describe the constitutive behaviour of iceberg ice in various loading conditions. The numerical material model with a Tsai-Wu yield surface was successfully implemented into the commercial code LS-DYNA 971 through a user-defined subroutine. A cutting-plane algorithm was employed to map the plasticity back to the yield surface in numerical simulations (Simo and Hughes, 1998). The yield surface was obtained from the curves fitted to the triaxial experimental data. The temperature and strain-rate influence on iceberg strength were discussed in detail by the authors; see Liu *et al.* (2011a). The difference in strength between the tensile and compression states was described with a cut-off pressure p_{cut}.

Numerical simulation of ice cracks is still a large challenge. A common way to simulate failure is to use an erosion technique in which elements violating the failure criterion are deleted. Erosion is an easy and efficient procedure and was employed in the present work. Prior experience has shown that erosion does not simulate elastic or brittle failures very well due to stress-wave issues (Liu, Amdahl and Løset, 2009). Therefore, the ice was assumed to be perfectly elastic and plastic. An empirical, user-defined element failure criterion based on the stress state and the effective plastic strain was introduced (Figure 3-6). In this manner, a quasi-brittle material model was proposed and successfully simulated using the commercial code LS-DYNA 971.

Unlike level ice-structure interactions, the ice in an iceberg impact is well confined. Hydrostatic pressure plays an important role during this process. As discussed by Schulson (2002) and Schulson and Duval (2009), hydrostatic pressure and friction may trigger different failure mechanisms, namely frictional or Coulombic faults and non-frictional or plastic faults (Figure 3-6).

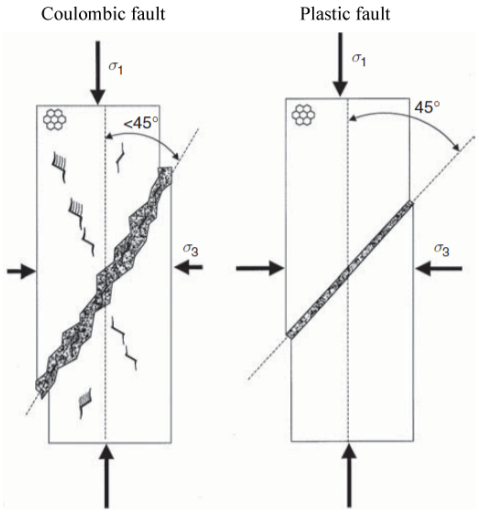

Figure 3-6 Schematic sketches of two kinds of compressive shear fault. Coulombic faults form under lower degrees of confinement. Plastic faults form under higher degrees of triaxial confinement, from Schulson and Duval (2009)

Coulombic faults are mainly due to shear forces at relatively low confinement pressures, while plastic faults develop under conditions where confinement is sufficient to suppress friction sliding. Taking iceberg impacts as an example, ice particles suffer shear forces at the very beginning. Numerically, ice elements should be kept during this phase until shear forces reach a certain value after which the ice elements may be ejected away as discussed by Schulson (2010). Thus, the failure criterion should become easier to satisfy, as pressure increases during Coulombic faults. However, the ice failure mechanism can also enter a plastic-fault phase. In a plastic-fault phase, the ice will be much stiffer due to the increasing hydrostatic pressure. Thus, the failure criterion should be more difficult to reach as pressure increases. This understanding of the failure criterion proposed in present study agrees the investigations carried out by Jordaan, Matskevitch and Meglis (1999). In that study, damage theory was used instead. Pioneering work done by Liu *et al*. (2009) proposed a U-shaped strain-based failure criterion to simulate ice-fracture mechanics and showed promising results.

Finally, an empirical failure criterion, as follows, was proposed in the present doctoral thesis; see Eqs. (3.5) and (3.6).

$$\varepsilon_{eq}^{p} = \sqrt{\frac{2}{3}\varepsilon_{ij}^{p} : \varepsilon_{ij}^{p}} \tag{3.5}$$

$$\varepsilon_{f} = \varepsilon_{0} + (\frac{p}{p_2} - 0.5)^2 \tag{3.6}$$

where ε_{eq}^{p} is the equivalent plastic strain; ε_{ij}^{p} is the plastic strain tensor; ε_{f} is the failure strain; ε_{0} is the initial failure strain, which should be adjusted according to

experimental data; and p_2 is the larger root of the yield function. If $\varepsilon_{eq}^{p} > \varepsilon_f$ or if the pressure is less than the cut-off pressure p_{cut}, erosion is activated. This failure criterion is based on trial-and-error and is purely empirical. Only one input parameter (ε_0) is needed (Figure 3-7).

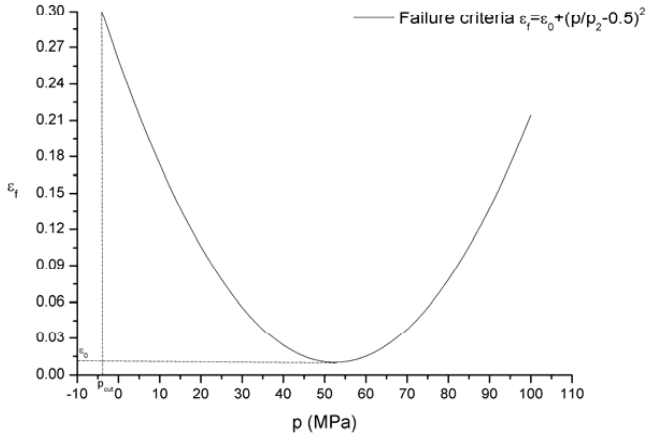

Figure 3-7 Illustration of the failure criteria curve (p_2=100 MPa).

3.4 Validation

The validation of the new ice model has been performed by conducting numerical examples. As one of the examples, the experiment carried out by Johnson (1987) was used to validate present iceberg model (Figure 3-8).

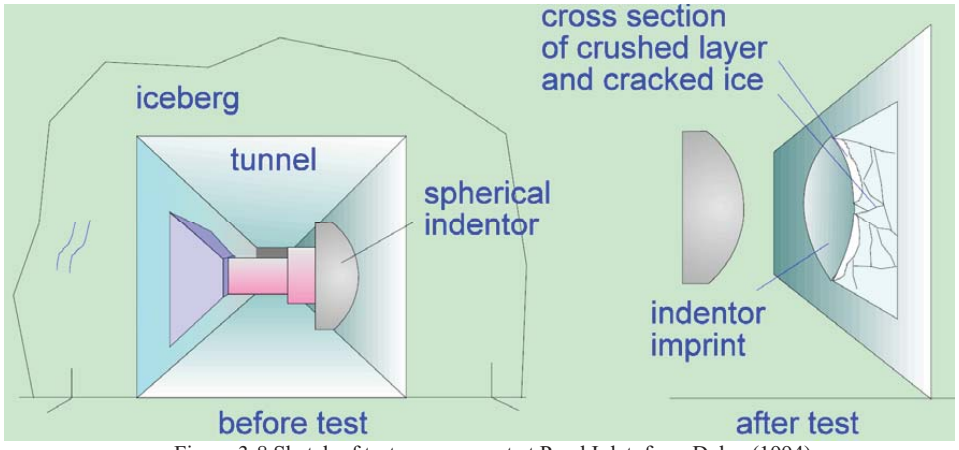

Figure 3-8 Sketch of test arrangement at Pond Inlet, from Daley (1994).

The pressure was calculated by dividing the contact force by the nominal contact area, which depends on the penetration distance. Good agreement between simulations and tests was obtained if the contact area is larger than 0.3 m^2 (Figure 3-9). Initially, the simulation predicted a significantly higher pressure than that recorded in the experiments (contact area less than 0.3 m^2). As discussed by Johnson (1987), significant noise in the experimental displacement curves caused difficulty in precisely locating the penetration distance in the beginning of denting. This may explain the large discrepancies for small contact areas. However, the simple iceberg material model yielded promising results and agrees reasonably with the ISO-ALIE design curve (ISO, 2010).

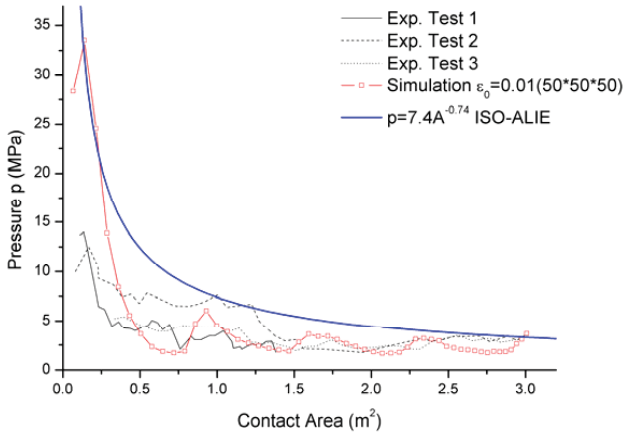

Figure 3-9 Numerical results and experimental data (pressure with nominal contact area).

3.5 Application example

Present iceberg material model has been successfully applied to simulate the head-on collision between iceberg and ship. The simulation was carried out in the same environment as that used in the previous validations. Figure 3-10 shows that the strain energy was dissipated in both the iceberg and the ship structure for the bow collision with iceberg and rigid wall. In scenario A, the penetration distance corresponding to an energy dissipation of 18.2 MJ is 1.5 m; the ship structure undergoes minor plastic deformations while the iceberg dissipates most of the energy (Figure 3-11(a)). In other words, the ship bow structure is strong enough to crush the iceberg. For scenario B, 75.5 MJ is dissipated for a penetration distance of 3.9 m. Both the ship bow and the iceberg experience large plastic deformations. Ice particles have been eroded extensively (Figure 3-11(b)), and the bow is subjected to significant crushing behaviour. It is interesting to see that there is a 'maximum crushing distance' for the ship bow corresponding to the present ice material model. From this point, the bow structure begins to undergo significant permanent deformation (see the turning point symbol (☆) in Figure 3-10). This takes place for a penetration of 1.7 m, which corresponds to an

internal energy dissipation of 25 MJ. Using the results of the external mechanics calculations, the associated iceberg mass is estimated to be 1,750 t. In other word, if the iceberg is heavier than 1,750 t in the present scenario, the bow will be crushed. In future studies, a failure criterion will be included for the steel material so that tearing of the shell plating can be accounted for as well (Chapter 4).

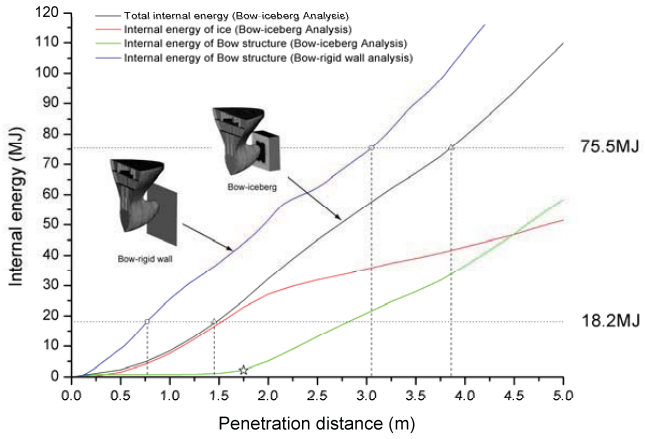

Figure 3-10 Internal Energy vs. Penetration distance

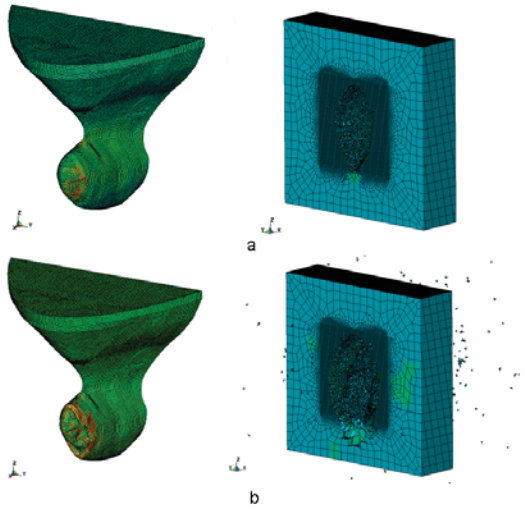

Figure 3-11 Bow and iceberg deformation (penetration distance=1.5 m (a), 3.9 m (b)).

Chapter 4

Integrated Numerical Analysis

The integrated numerical analysis of an iceberg collision with foreship and ship side structures has been successfully performed. The newly developed iceberg material model in Chapter 3 was used. This work was presented in Paper [III] by Liu, Amdahl and Løset (2011b) and Paper [IV] by Liu, Amdahl and Løset (2011c).

4.1 Introduction

Due to the complexity mechanical behaviours of iceberg ice, researches on simulating the iceberg and structure interactions are mainly conducted by neglecting the iceberg behaviours, as discussed by Liu *et al.* (2011a). For a realistic design against an accidental iceberg impact, we require knowledge about the iceberg shape and a continuum mechanics model of icebergs, in addition to iceberg mass and speed. Both issues are associated with substantial challenges.

The integrated analysis of ship-iceberg collisions in this chapter means that the deformations of both ship and iceberg are taken into consideration in the non-linear finite element simulations. This analysis corresponds to the shared-energy design method in the ALS design stage. To authors' knowledge, this was the first attempt to simulate both iceberg and structure deformations at the same time. A comprehensive discussion based on the results of numerical simulation was presented.

The demand for energy dissipation is another issue of importance. The iceberg with its associated added mass represents a kinetic energy, where the impact speed often is largely governed by the ship speed. Only a fraction of the kinetic energy must, however, be dissipated as strain energy. Depending on the collision geometry, a significant part of the impact energy will remain as kinetic energy. This determination is conveniently made by splitting the analysis into two tasks, namely, an assessment of i) external mechanics and ii) internal mechanics. The result of external mechanics is the demand for energy dissipation. This result provides a useful perspective on the amount of deformations that is to be expected in the structure and the ice. The distribution of damage and energy dissipation is determined in the integrated analysis of internal mechanics. A major objective of the present work was to study the distribution of damage in the ship and the iceberg as a function of the relative strength of the two structures. A further objective was to determine the size of iceberg impacts that a typical tanker can resist without jeopardising the acceptance criteria.

Two collision scenarios were proposed (Figure 4-1), namely the iceberg collision with foreship and ship side structures, which were presented in Paper [III] and [IV] respectively.

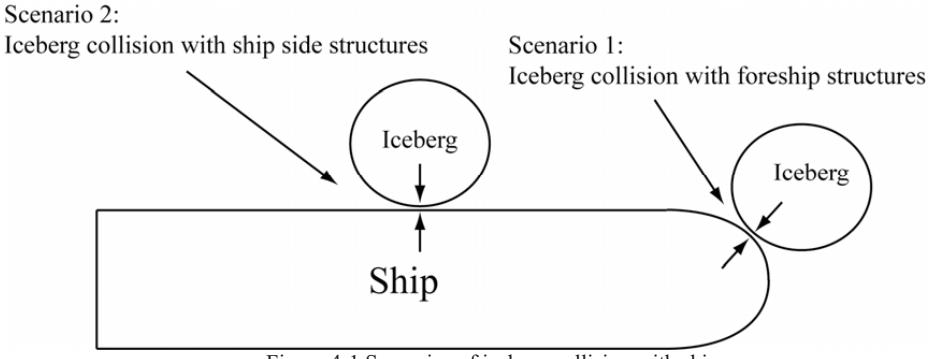

Figure 4-1 Scenarios of iceberg collision with ship.

4.2 Material models

The steel material model which used was developed by Aslos, Amdahl and Hopperstad (2009). The so called 'power law' relationship was used to simulate the stress-strain plastic behaviour. The *RTCL* damage criterion was employed in the integrated analysis in case steel fracture and crack happens in the simulation. Detailed information can be found in the paper by Aslos *et al.* (2009). The key data for the steel model are listed in Table 1. To investigate the relative stiffness between ship and iceberg, the yield stress σ_y has been varied from 75 MPa, 125 MPa, 150 MPa, 235 MPa and 285 MPa and K, n are adjusted accordingly.

Table 1. Steel material model inputs.

Items	Value
Density ρ	7.89×10^3 kg/m^3
Young's modulus E	210 GPa
Poisson ratio ν	0.3
Yields stress σ_y	285 MPa
Strength index K	740 MPa
Strain index n	0.24

The iceberg material model was developed by Liu, Z. *et al.* (2011a), which is based on the so called Tsai-Wu yield surface. Chapter 2 has presented details about this new ice model. The data obtained based on the work done by Derradji-Aouat (2000) can be used for simulation of local structure deformation. The data for the present iceberg material model are listed in Table 2.

Table 2. Iceberg material model inputs.

Items	Value (Derradji-Aouat, 2000)
Constant a_0	22.93 MPa^2
Constant a_1	2.06 MPa
Constant a_2	-0.023
Initial failure strain ε_0	0.01
Young's modulus E	9.5 GPa
Density ρ	900 kg/m^3

4.3 Iceberg collision with foreship structures (Paper [III])

4.3.1 Ship and iceberg models

A FPSO designed for abnormal ice condition was adopted for the numerical simulations (Figure 4-2).

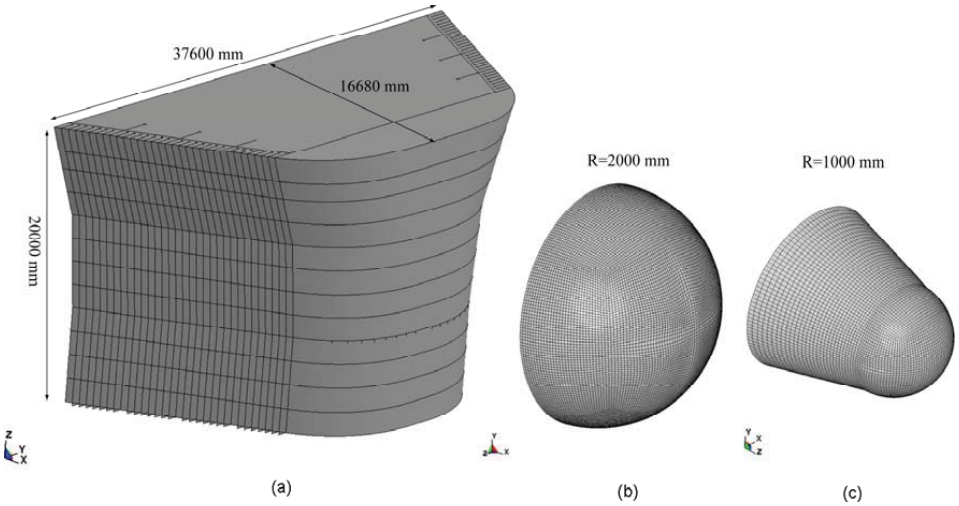

Figure 4-2 Proposed iceberg shapes. (a) Foreship model, (b) R=2000 mm, (c) R=1000 mm. Notice that (a,b,c) are not at the same scale level.

The end of the ship bow structure was fixed. The ship bow structure was big enough to minimize the boundary influences to the results. The iceberg was free to move against the ship bow with velocity of 4000 mm/s. Vertically, collision positions were placed at the middle of two vertical stringers (side view in Figure 4-3). Horizontally, two locations were considered, one was on the top of the web frame and the other was located in the middle of two web frames (top view in Figure 4-3)

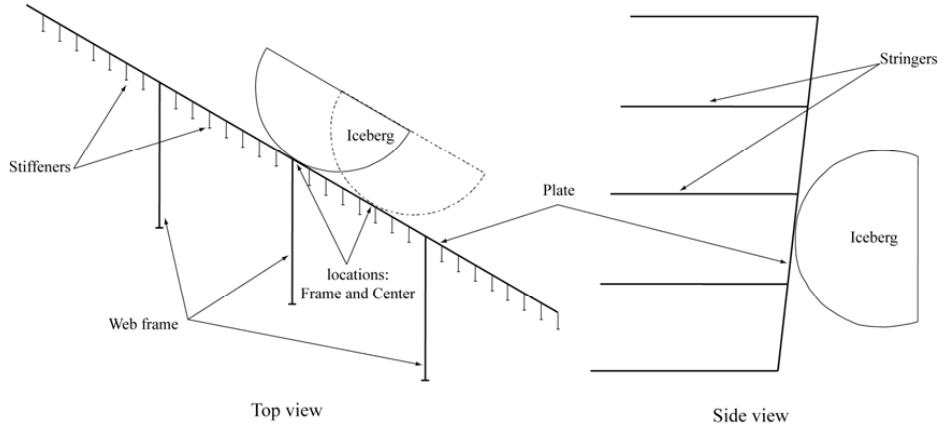

Figure 4-3 Illustration of collision location.

4.3.2 Results

Prior to the detailed discussion regarding to internal mechanics, the external mechanics of iceberg collision with foreship structures was discussed. According to Liu and Amdahl (2010), the maximum dissipated energy in a collision between ship and iceberg is reached if the impact is purely plastic and central (collision force through centre of gravity), as discussed in section 2.5 of Chapter 2 in present thesis. Eq.(2.29) can be rewritten as:

$$E_0 = \frac{1}{2}\chi M_{iceberg}\Delta v^2 \tag{4.1}$$

where $M_{ship}, M_{iceberg}$ are the mass of ship and iceberg respectively. Generally, the added mass factor should be considered, see the discussion in Liu and Amdahl (2010). However for simplicity, it was simply neglected in present discussion. $\chi = 1/(1+M_{iceberg}/M_{ship}) = M_{ship}/(M_{ship}+M_{iceberg})$, and χ is usually close to 1 in this research as focused was place on growler or bergy bits collisions with ship structures. Say a ship with 150,000 tons collides with an iceberg of 1,000 tons, then $\chi = 150/151$. $\Delta v = \hat{v}_{ship} - \hat{v}_{ice}$ is the relative velocity between ship and iceberg. The demand for energy dissipation in a ship-iceberg collision may therefore be expressed as follows based on Eq. (4.2):

$$E = \xi E_0 \tag{4.2}$$

where ξ is a factor that depends on a variety of parameters, such as the collision position, the water line angle, the frame angle of ship, the relative centre of gravity (COG) position and the velocity direction between the ship and iceberg. To quantify the value of ξ is a challenge. The work done by Fuglem, Muggeridge and Jordaan (1999) sheds light on how to assess ξ. As to the iceberg and ship collision case, if we consider the iceberg collision with the foreship structure as the most likely scenario, a factor of 0.3 may be conservatively assumed based on previous study by Liu and Amdahl (2010).

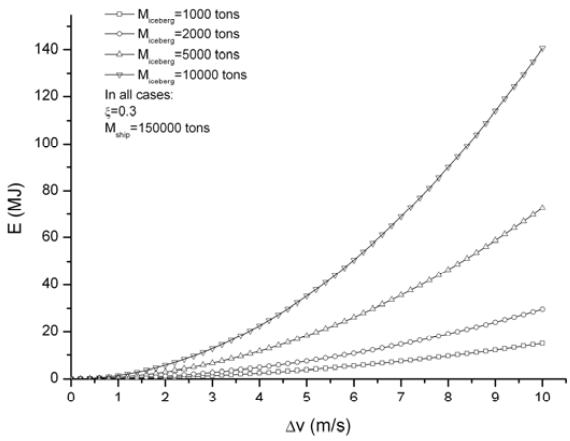

Figure 4-4 E versus Δv .

The demand for strain energy dissipation for foreship collisions with different iceberg sizes is plotted in Figure 4-4 as a function of the relative speed based on Eq. (4.2). For example, if an iceberg with a size of 5000 tons collides with the foreship of a 150000 tons vessel with a relative velocity of 5 m/s, then the estimated total dissipated energy is 18.2MJ. If the iceberg size is 10000 tons, the demand for energy dissipation becomes 35.2MJ. These values are comparable to present criteria for accidental collisions with platforms in the North Sea (14MJ for supply vessels, 40-60 MJ high energy collisions with passing vessels, see Moan, Amdahl, Wang *et al.* (2003)). The required energy can either be dissipated as strain energy in the vessel or by crushing of ice or both "structures". Such value gives a direct measurement on the damage extent if we connect it with the following internal mechanics analysis.

Prior to discussing how the deformation and energy dissipation are shared by the ice and the ship structure in the integrated analysis, it is interesting to investigate how ice pressures develop on the contact surface. The ice pressures were obtained by assessing the output data of contact pressure per node, which corresponds to a square mesh of size 0.014 m^2 (120 × 120 mm^2) in the present simulation (Hallquist, 2007). Gagnon, R. (2008) used a new impact panel to measure forces and pressures during collisions of a ship with bergy bits - and small icebergs. It was concluded that the contact zones consisted of relatively small regions of hard ice (pressure in the range of 8-20 MPa for contact areas varying from 0.002 m^2 to 0.03 m^2) usually surrounded by a larger area of softer pulverized ice, where the pressure was around 2.5 MPa. To compare with this finding, the contact pressures in the numerical simulation were investigated. Screenshots of the contact pressure at time 0.005 s and 0.15 s are presented in Figure 4-5(a, b). The contact pressure at the very beginning (at time 0.005 s) is in the range of 16-37 MPa. The maximum contact pressure at time 0.15 is 15.5 MPa (red colour in Figure 4-5(b)). The high contact pressure points in the range of 8-15.5 MPa at 0.15 s are distributed randomly within the contact surface. Several nodes are picked up for investigation, as shown by Figure 4-5(c). It is seen that the contact pressure in the centre

area is generally higher than that in the area close to the edge. This is as expected since the ice at the centre area is well confined. The failure criterion embedded in the material model which determines the "erosion" of ice elements plays an important role on inducing such big variation of contact pressure as Figure 4-5(b) presents. However, other reasons, e.g. the dynamic stress wave and the contact algorithm used by LS-DYNA may also exist. Anyway, it still provides a reasonable good ice impact loads to the ship structure.

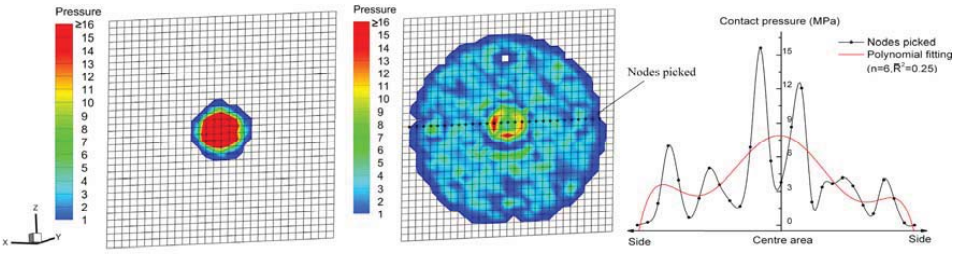

(a) t=0.005 s (b) t=0.15 s (c) t=0.15 s

Figure 4-5. (a) Screenshot of the contact pressure (unite: MPa) on the ship outer hull, at time 0.25 s. (b) Contact pressure variation for those nodes picked within contact area, at time 0.25s.

A comprehensive discussion based on simulation results has been performed afterwards. The discussions include the investigation of contact pressure to patches with different sizes (Figure 4-6), the load-deformation curve (Figure 4-7), iceberg shapes and also the collision locations. Some of the conclusions are as follows:

- Impacts with the icebergs with modelled properties will not cause severe damage to the ice strengthened foreship with the nominal yield strength of $\sigma_y = 285$ MPa studied, The maximum deflection of the side is 137 mm;
- If the ship structure is not designed as strong as the present model, then the iceberg impact may cause severe damage to the structure side. Severe penetration and fracture is observed in the case when $\sigma_y = 75$ MPa ;
- In all the simulations, the stiffeners beneath the contact area are subjected to significant folding and can not effectively support the forces created in the plating. If not hit directly the stringers and web frames may support the membrane forces produced in the side when it undergoes finite deformations;
- Icebergs may take on infinitely many shapes. Both on macroscopic and local level. Some few attempts have been made to characterize iceberg shapes, but accepted standards for iceberg shapes is far from being established by the engineering community, probably because the need for this has not even been recognized up to now. In ALS analysis the need for characterizing iceberg shapes can no longer be circumvented. In lieu of relevant data, it is proposed to approach the iceberg shape issue from the ship scantlings point of view. It is proposed to use the aspect ratio A_r to describe the shapes of the leading edges of icebergs. And it is further suggested that A_r can be defined in the structure damage point of view.

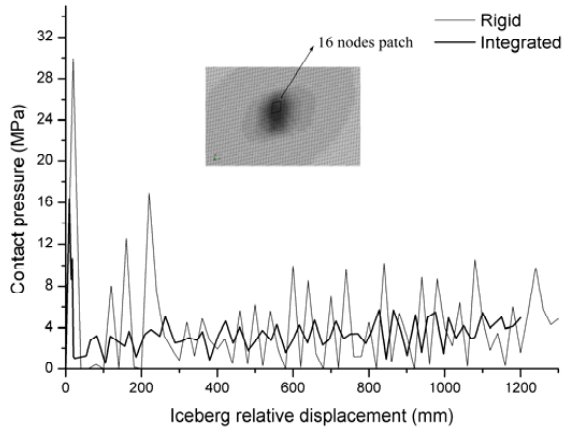

Figure 4-6 Contact pressure for a loading patch of 16nodes (0.22m2) located at the contact area centre. Rigid vs. Integrated.

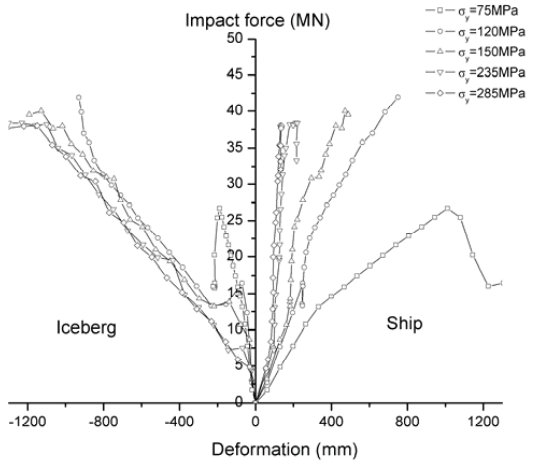

Figure 4-7 Load-deformation curves, R=2000mm.

4.4 Iceberg collision with ship side structures (Paper [IV])

4.4.1 Ship and iceberg models

The ship structure model here is based on the side scantlings of a FPSO tanker which has been designed for ice loads (Figure 4-8).

Generally speaking, two categories, namely “sharp” and “blunt” iceberg profiles are proposed. Both “sharp” and “blunt” can be simply represented by revolving a parabolic

or a circle profile line about its symmetry axis. The iceberg profiles based on different parabolic or circle lines are created. The 3D iceberg shapes can be easily obtained by revolving the profile lines with the X-axis for 360°. In this paper, the iceberg shapes are modelled based on the parabolic line $X = -\frac{1}{500}Y^2$, and half circle lines, $Y^2 + (X + r)^2 = r^2$, where r equals to 1000 mm, 2000 mm and 3000 mm. All the icebergs modelled have the same height of 2000 mm along the X-axis. Thus, a round platform is additionally attached to the half sphere when $r = 1000$ mm with an inclination angle of 25^0. The final iceberg shapes are presented in Figure 4-9.

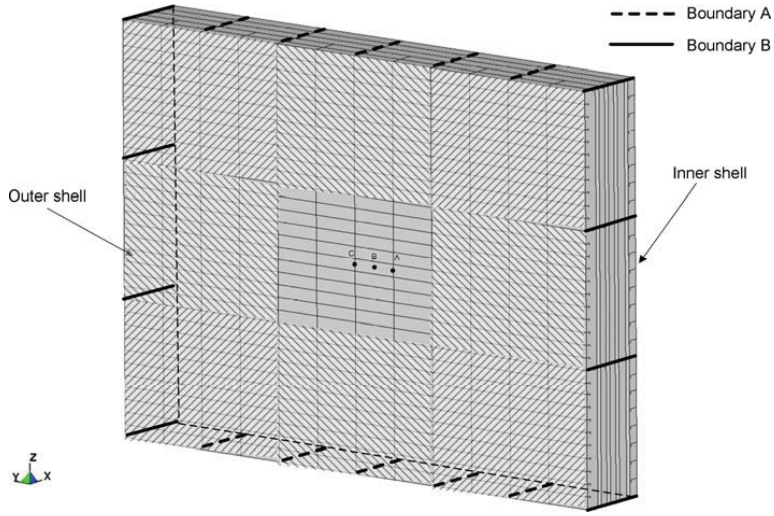

Figure 4-8 The side structure model with illustrations on boundary conditions and collision locations.

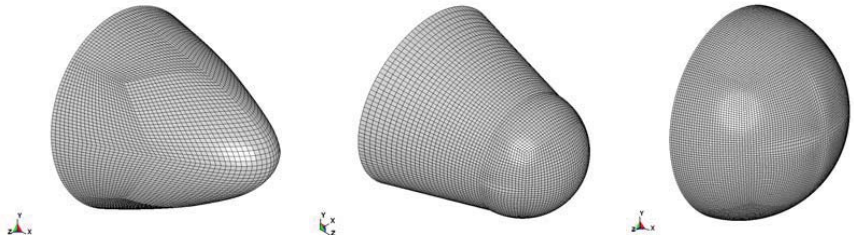

Figure 4-9 FEM models for local iceberg part (Parabola, round platform plus half sphere and sphere).

The locations of the initial contact during the ship-iceberg collision are assumed to be in the middle of the structure model, thus the influence of the boundary conditions' is minimized. Three typical locations are proposed, as seen in Figure 4-8. If we considering a grid (2215 mm×600 mm) between stringer/web frame and two longitudinal stiffeners, the three points A,B,C are distributed evenly along this grid.

4.4.2 Results

The iceberg and side ship collision has been simulated. Results are presented by the deflection of ship structure or the energy dissipation with iceberg displacement (Figure 4-10). The simulated iceberg damage patterns are illustrated in Figure 4-11. The collision location shows significant influence when both the iceberg and side structure endure large deformation. The web frame and stringer support in the cases of types A and C increases the side structure stiffness significantly compared to the case of type B where the location of collision is in the middle of spacing. The integrated analyses differ a lot from the rigid analyses in most cases. And the difference is highly dependent on the iceberg profiles. The iceberg with "sharp" profile has the biggest difference while the "blunt" has little. In the present study, when the radius of circle profile is bigger than 2000 mm, the iceberg will be stiff as rigid; thus, the rigid analysis is valid in such cases.

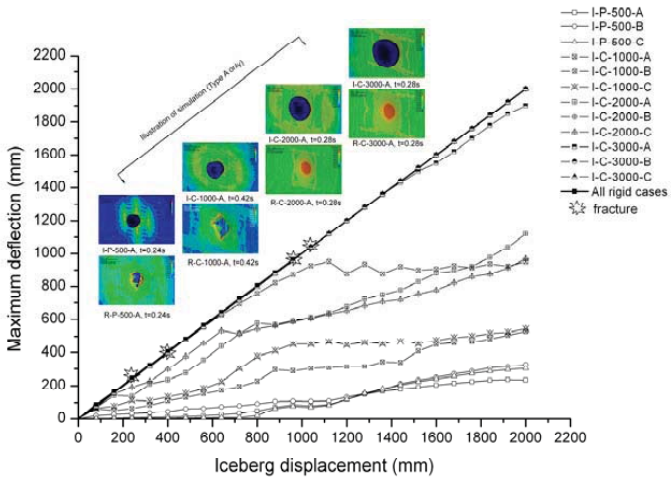

Figure 4-10. Maximum deflections of outer shell with the iceberg displacement.

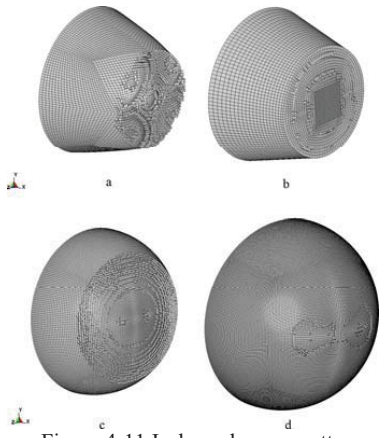

Figure 4-11 Iceberg damage patterns.

Chapter 5

Residual Strength Assessment

The residual strength of damaged ship structure has been analysed by analytical and numerical methods. The results was presented in Paper [V] by Liu and Amdahl (2011).

5.1 Introduction

Even not explicitly expressed in Paper [V], the method used here can be also applied to investigate the residual strength of ship after the collision with icebergs. As investigation performed in previous chapter, if the ice strengthened ship structure collides with bergy bits or growlers, the probably damaged caused will be only moderate dent. Fracture may not happen in such cases. Paper [V] presented both numerical and analytical methods on how to assess the residual strength of such damaged ship structures.

The double bottom structure of a 140,000 m^3 shuttle tanker was the subject of the present study (Figure 5-1). The damage was simulated by colliding the double bottom structure with rigid indentors in LS-DYNA 971. Subsequent to the introduction of the damage, the double bottom was subjected to compression created by forced inward displacement of the boundaries. The forced displacement should mimic global bending of the hull girder. In pure bending and in the elastic phase the displacement will vary linearly over the double bottom height

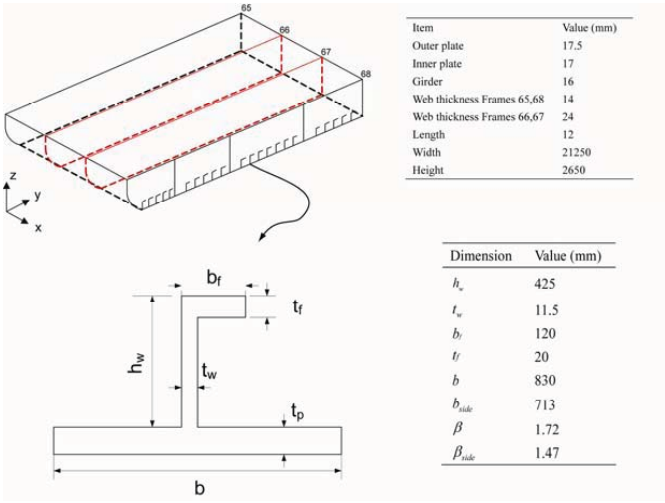

Item	Value (mm)
Outer plate	17.5
Inner plate	17
Girder	16
Web thickness Frames 65,68	14
Web thickness Frames 66,67	24
Length	12
Width	21250
Height	2650

Dimension	Value (mm)
h_w	425
t_w	11.5
b_f	120
t_f	20
b	830
b_{side}	713
β	1.72
β_{side}	1.47

Figure 5-1 Profile and dimensions of the double bottom model.

As shown in Figure 5-2, the boundary conditions were divided into three groups: the forward (FOR) frame, the afterward (AFT) Frame, and the centre nodes. The six-degree constraints for all three groups are also listed in Figure 5-2, in which 1 indicates fixed and 0 indicates free. The symmetry conditions were imposed on the centre line nodes. The nodes for the AFT and FOR frames were rigidly connected and behaved as a rigid section. The nodes for the AFT frame were fixed on the X, Y and Z displacements, and the rotation was free about the Y axis. A bending moment was applied. The nodes on the FOR frame had fixed displacement on the Y axis and fixed rotation about the Z axis. These conditions were due to the combined compression and bending loads added to these nodes in the simulation. These boundary conditions cause the membrane forces during the denting stage in the simulation to be balanced by the middle span of the total double bottom structure.

	X	Y	Z	RX	RY	RZ
AFT. Frame	1	1	1	1	0	1
FOR. Frame	0	1	1	1	0	1
Nodes Center	0	1	0	0	0	1

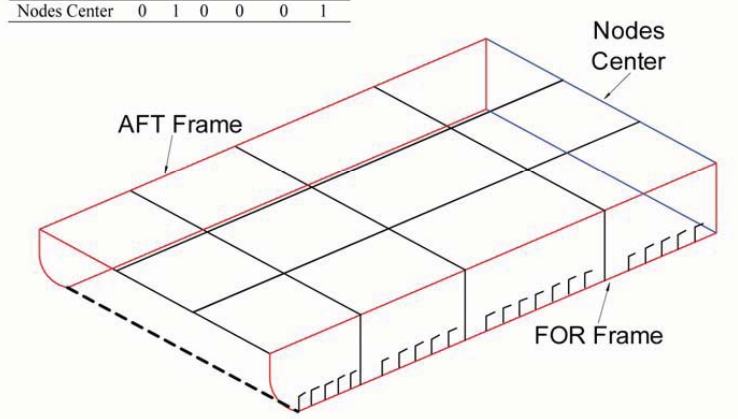

Figure 5-2 The boundary conditions.

Besides the numerical simulation, analytical method was developed. To obtain the residual strength of damaged ship structures, the end-shortening curves for damaged stiffeners are crucial. Two simplified models were proposed, namely the elastic and rigid-plastic method (purely analytical) and the 3-span single stiffener model (semi-analytical).

5.2 The new models (Paper [V])

5.2.1 Elastic and Rigid-plastic method

A new damage model for stiffener was proposed, as shown in Figure 5-3. The following relations apply:

$$h_w^e = h_w - \delta \tag{5.1}$$

$$cos(\alpha) = \frac{h_w - \delta}{h_w} \tag{5.2}$$

$$b_f^e = b_f cos(\alpha) \tag{5.3}$$

where h_w^e, b_f^e are effective web height and flange width after damage, α is the tripping angle. The effective web height and flange width is used instead of h_w, b_f when calculating the section properties in the $N-M$ relationship.

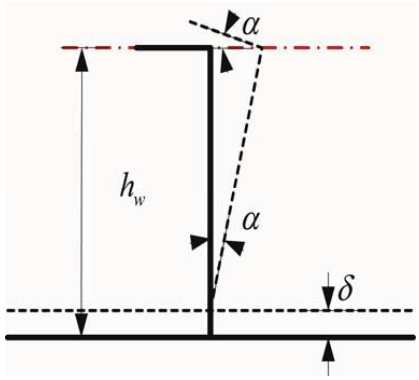

Figure 5-3 The simplified damage mechanics at the cross section of a stiffener

5.2.2 A 3-span single stiffener method

A 3-span single stiffener method was also developed. The boundary conditions were listed as seen in Figure 5-4.

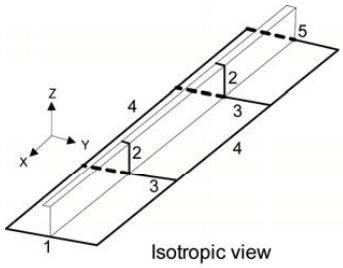

Nodes set No.	Freedom					
	x	y	z	rx	ry	rz
1	0	1	1	1	0	1
2	0	1	1	0	0	0
3	0	0	1	1	0	1
4	0	0	0	1	0	1
5	1	1	1	1	0	1

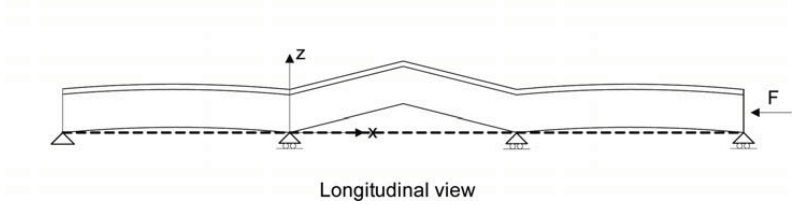

Figure 5-4 Illustration of the boundary conditions and the damage pattern for the single-stiffener model

5.3 Results

Firstly, the residual strength of damaged double bottom structure was presented based on the simulations, as seen in Figure 5-5. It was interesting to observe that for a given number of damaged stiffeners, the peak resistance B shows fairly small sensitivity to

level of indentation, while the resistance A at buckling of outer panels is significantly more sensitive. In other words, initial buckling is considerably influenced by the level of denting, while the resistance of the damaged stiffeners, which are well into the post-collapse region at point B, does not depend that much on the denting.

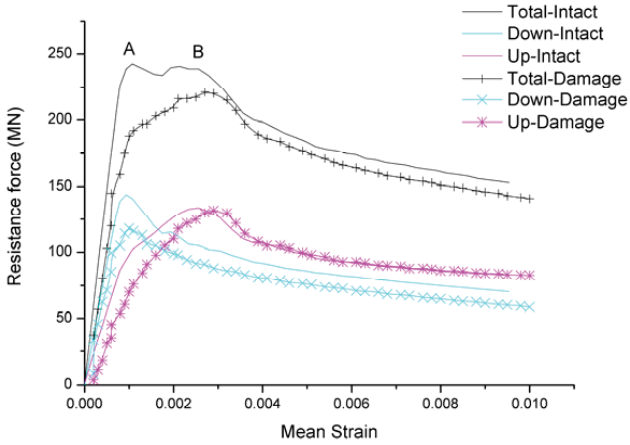

Figure 5-5 Ultimate strength of the bottom, Case intact and Case 150d.

Secondly, analytical and semi-analytical methods were developed to assess the residual strength of damaged stiffeners. The residual strength of damaged ship bottom structures was finally predicted, as seen in Figure 5-6 for the case of 50mm denting distance. Generally, good results were obtained.

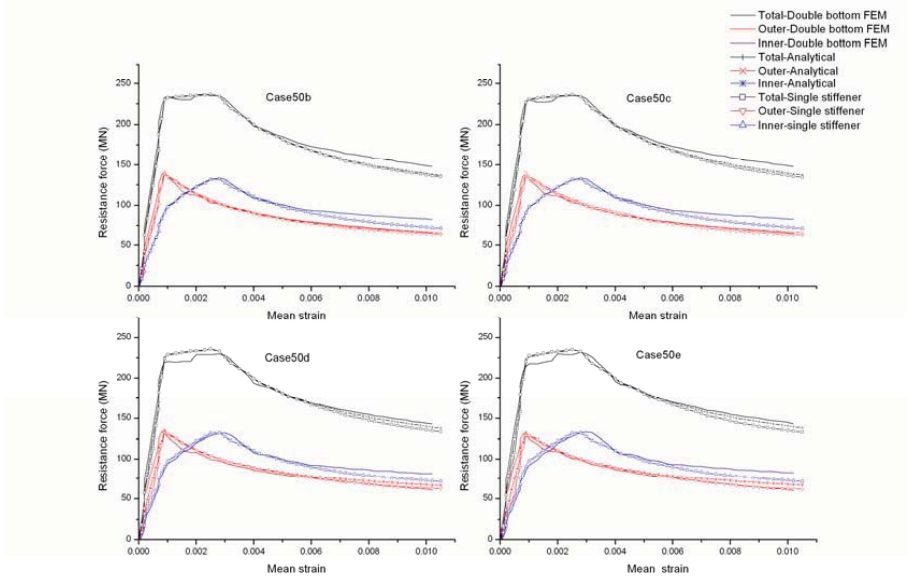

Figure 5-6 Results for the 50 mm denting cases.

Chapter 6

Conclusions and recommendations for future work

6.1 Conclusions

The present doctoral thesis represents comprehensive research regarding the external and internal mechanics of iceberg-ship collisions. The residual strength of damaged ship structures was assessed as well. These research results have been all published in journal and peer-reviewed conference articles. To give an overview of the present doctorial work, the following conclusions are summarised.

6.1.1 External mechanics

To investigate the external mechanics of iceberg-ship collisions, a 3D impact theory was developed (Paper [I]). Stronge's 3D impact theory was successfully applied to describe ship collision problems.

The new formulation of impact mechanics was developed under a "local frame" system, which is determined by the geometry of the ship at the contact point. All variables in the equations of motion were formulated under the local frame system. A transformation matrix from the global to the local frame system was established by introducing the definition of hull angles. The equations of motion were solved with proper boundary conditions, which included the definitions of friction and the slide and stick mechanisms during impact.

Numerical examples showed that the 3D method degenerates to the existing 2D method if the ship side is vertical and the vertical eccentricity is neglected. Excellent agreement between the present 3D method and the existing 2D method was obtained. However, the new 3D method shows that the energy to be dissipated as strain energy is significantly influenced by vertical eccentricity when the collision takes place amid ships, which means that the 2D method may overestimate impact energy by neglecting vertical eccentricity.

The new 3D impact theory was successfully applied to analyse ship-iceberg collisions. The results showed that the existing 2D theory may produce very conservative values for the energy ratio. The normal frame angle of the ship influences the energy ratio significantly. The worst frame angle for the iceberg collision is in the range of 20° to 30° .

6.1.2 Ice material modelling

To facilitate the research on the internal mechanics of iceberg-ship collisions, a numerical model of icebergs was developed (Paper [II]). The new ice material model is based on plasticity theory and is strain-rate independent. An erosion technique was adopted to simulate ice fractures. The present model provides a useful tool for ALS design of ship structures with respect to iceberg impact loads.

The material model consists of two parts: a perfectly elastic, plastic material model and a user-defined failure criterion. The difference in strength between the tensile and compression states is described by a cut-off pressure. The perfectly elastic, plastic material model is described by a yield surface called "Tsai-Wu*"* and the associated flow rule. The inputs of the "Tsai-Wu*"* yield surface should be derived from triaxial experimental test data from iceberg samples. The effects of a temperature gradient may also be taken into account. Although the present material model is strain-rate independent, a discussion regarding the strain-rate's influence on the mechanical properties of the ice was performed. It was concluded that the strain rate during an iceberg-ship collision is usually high, larger than $10^{-3}s^{-1}$, where the iceberg ice should be in brittle failure mode. The user-defined failure criterion is based on the hydrostatic pressure and an effective plastic strain. It was developed from ice-fracture mechanics and trial-and-error numerical simulations. The new ice material model was successfully implemented into the commercial code LS-DYNA 971 by user-defined subroutines. The "Cutting-plane*"* algorithm was adopted for the numerical calculations of plasticity development in the material model.

Numerical examples showed that the present model yields good results. The rigid-wall numerical example showed that the ice model may produce different pressure-area relationships based on various input parameters of the yield surface. The numerical denting test showed that the ice model can produce good results compared to experimental data. The simulation undergoes mesh convergence and the computational time is acceptable.

The application of the present material model to the simulation of a head-on iceberg-ship collision was successfully performed. During such a collision, the ship's bow and the iceberg share the total dissipated energy. The iceberg dissipates most of the energy initially. In the scenario analysed, the bow will be crushed if the iceberg is heavier than 1,750 tons.

6.1.3 Integrated numerical analysis

The internal mechanics of iceberg-ship collisions involve research on both ship structures and icebergs. Internal-mechanics research is extremely challenging due to the lack of proper numerical models for ice. With the developed model, detailed research on the internal mechanics of iceberg-ship collisions was performed by conducting integrated numerical analysis. Two collision scenarios were investigated, namely iceberg collisions with foreship structures (Paper [III]) and with ship-side structures (Paper [IV]).

Integrated numerical analysis of iceberg collisions with foreship structures (Paper [III]).

The integrated numerical analysis of iceberg collisions with foreship structures involves discussions of both the external and internal mechanics. The steel model of Aslos *et al.* (2009) and the iceberg model of Liu *et al.* (2011a) were applied successfully in numerical simulations. This represents the first recognition of equivalent importance for both iceberg and ship structural deformations in numerical simulations.

For external mechanics, the demanded dissipated energy in an iceberg-foreship collision is mainly determined by the iceberg and ship masses and the relative velocity between them. A fully plastic impact represents an upper bound for the required energy dissipation. Based on typical foreship geometries, it was found that the required energy dissipation is only 30% of the energy of plastic impact. Thus, a significant amount of energy is transferred into kinetic energy by deflecting the iceberg. Large icebergs represent the largest damage potential. However, they are more likely to be detected by radar. Presumably, icebergs in the range of 5,000 – 100,000 tons represent the largest risk from kinetic energy potential and detectability. If a 5000-ton iceberg collides with a 150,000-ton ship at a relative velocity of 5 m/s, the demand for energy dissipation is 18 MJ. This is not dramatic from an ALS point of view. The typical kinetic energy used for supplying vessel collisions in the North Sea is 11-14 MJ. *FPSO* has been shown to resist considerably larger energies before puncturing the inner tank.

For internal mechanics, discussions are mainly conducted based on the simulation results generated by LS-DYNA 971 in which the newly developed iceberg numerical model was used. The ice material model showed many good features in integrated analyses. It gave reasonably good contact pressure values for various sizes of patches. The contact pressure in the centre area was generally higher than in the area close to the edge. This was expected, as the ice at the centre area is well confined. The averaged contact pressure in the core area was around 3.5-4 MPa. Impacts with the icebergs as modelled will not cause severe damage to an ice-strengthened foreship with the nominal yield strength of $\sigma_y = 285$ MPa studied. The maximum deflection of the side is 137 mm. If the ship structure is not as strong as the present model, then the iceberg impact may cause severe damage to the structure's side. Severe penetration and fracture was observed when $\sigma_y = 75$ MPa. In all of the simulations, the stiffeners beneath the contact area were subjected to significant folding and could not effectively support the forces created in the plating. If hit indirectly, the stringers and web frames may support the membrane forces produced in the side for finite deformations. Icebergs may take on an infinite number of shapes, both on the macroscopic and local level. Few attempts have been made to characterise iceberg shapes; accepted standards for iceberg shape is far from being established by the engineering community, probably because the need has not yet been recognised. In ALS analysis, the need for characterising iceberg shapes can no longer be circumvented. In lieu of relevant data, it is proposed to approach the iceberg-shape issue from the ship scantlings point of view. We propose the use of the aspect ratio A_r to describe the shape of the leading edges of icebergs. It is further suggested that A_r can be defined in the structural damage point of view.

Integrated numerical analysis of iceberg collisions with ship side structures (Paper [IV]).

Similar to the previous subsection, an integrated numerical analysis of iceberg collisions with ship side structures was performed. The main focus of this research was to investigate the influences of different iceberg shapes and collision positions. For comparison, rigid analyses were also performed. In total, 24 numerical simulations were carried out.

The iceberg profiles in the present study were simplified by revolving a parabolic or a circular line about an axis. An iceberg with a parabolic profile ($y = 1/500\,x^2$) will be crushed by a ship, and an icebergs with a circular profile ($Y^2 + (X - r)^2 = r^2$, $r = 3000$ mm) is sufficiently stiff to crush the side structure. When $r = 1000\,mm$ or 2000 mm , the iceberg and side structure share the energy during the collision in the integrated analyses. In the rigid analyses, the "sharp" profiles represented by the first and second profiles ($y = 1/500\,x^2$ and $Y^2 + (X - 1000)^2 = 1000^2$) penetrate the side structure. In the integrated analyses, no fracture was observed in the side structure in any case.

The collision location showed significant influence on the outcome when both the iceberg and the side structure endured large deformations. The web frame and stringer provided support for types A and C and increased the side structure stiffness significantly compared to type B, where the location of collision was in the middle of the spacing.

The integrated analyses differed greatly from the rigid analyses in most cases. Moreover, the difference was highly dependent on the iceberg profiles. Icebergs with a "sharp" profile showed the greatest difference, whereas the "blunt" profiles showed little difference. In the present study, when the radius of the circle profile was greater than 2000 mm, the icebergs were as stiff as they were rigid; thus, the rigid analysis is valid in such cases.

6.1.4 Residual strength assessment

Numerical and analytical assessment of the residual strengths for damaged ship structures was carried out. The research object was the double-bottom structure of an oil tanker. The damage was simulated with rigid indenters colliding with the outer shell of the double-bottom structure. The residual strength was obtained by applying compressing forces to both ends of the double bottom, and the bending-moment influence was considered.

The damage caused by the indentation of the bottom stiffeners primarily affected the load-bearing capacity of the stiffeners directly subjected to damage. The bending moment and the double-bottom height substantially influenced the residual strength of the double bottom.

The peak resistance (buckling strength) of an individual stiffener was significantly affected by the indentation level but the pots-buckling resistance at the point of ultimate resistance of the entire double bottom was significantly less influenced. The method described in the *DNV* rules was verified again as an effective and accurate method to obtain the post-buckling strength of the ship hull.

The simplified damage mechanism for the tripping behaviour of stiffened plates was developed. Based on this, the shortening curve was obtained by an elastic and rigid analysis method, which showed reasonably good results. It provided a quick and efficient method to assess the residual strength of the ship structure.

A single stiffener *FEM* analysis model was proposed. Force-end shortening relationships obtained with the single stiffener model agreed well with those obtained from the double-bottom model.

Results from the analytical and single stiffener analysis may effectively be used to generate the residual strength of the double bottom with a large reduction in computation time. The application showed that the present method was able to estimate the buckling and post-buckling strengths of the double bottom, which provide an alternative way to the general Smith's method.

6.2 Contributions

In short, the main contributions of the present doctorial research were as follows.

- A new formulation of three-dimensional impact mechanics of iceberg and ship collisions was developed. The new method showed that the existing two-dimensional method overestimated the dissipated energy if vertical eccentricity exists in a collision. It provides an efficient tool for assessing the external mechanics of iceberg-ship collisions. The presented method was successfully applied to calculate the energy dissipation in iceberg-ship collisions;
- A new numerical material model of icebergs was developed and successfully implemented in the commercial code LS-DYNA 971. The pressure and area relationships recorded in numerical rigid-wall impact tests were comparable with the curve recommended by the international standard code. An experimental iceberg indenter test was simulated by the present material model, and good agreement was achieved. As an application example, the new material model successfully simulated a head-on iceberg-ship collision;
- Integrated numerical analyses of iceberg-ship collisions were successfully performed for the first time. The contact pressure was assessed. Good pressure-area relationships were obtained in the numerical simulation, which proved the validity of the present material model. A comprehensive discussion regarding the different structural strengths, iceberg shapes and collision locations was successfully performed;
- Different iceberg shapes were proposed and integrated into the numerical simulations. A ship structure will simply crush a "sharp" iceberg while suffering significant deformation if it meets a "blunt" iceberg. This pioneering work sheds the first light on the consideration of iceberg shape from the structural damage point of view;
- The residual strength of the damaged ship structure was assessed both numerically and analytically. A simple damage model and a three-span single stiffener model were both developed. These two models provided a quick and efficient tool for assessing the residual strength of a damaged ship structure.

6.3 Recommendations for future work

The topic of iceberg and ship collision is quite new and challenging. There are still some aspects of the present doctorial thesis that can be further investigated. For instance, following listed points may be recommended.

- The split of external and internal mechanics simplified the problem significantly. However, it is still questionable whether such a split reveals the true or the worst case scenario. The neglect of all forces except for the impact force may lead to an incorrect estimation of the extent of damage to ship structure; see the work done by Tabri, K. (2010);
- The simplified iceberg shapes in the external mechanics is not sufficient to derive useful conclusions. More iceberg shapes and sizes are needed, which may be created through Monte Carlo simulation. Thus, more convincing conclusions may be obtained;
- Iceberg material modelling is based on the plasticity theory. The "Tsai-Wu" yield surface was used to present the constitutive relationships of ice. However, the yield surface was not fully used due to the erosion technique adopted in the material modelling. Erosion also fails to simulate the crushed ice during an impact, which may play an important role. It is suggested that other numerical techniques may be alternatively used for this point of view;
- The integrated analysis of iceberg-ship collisions is a challenging topic. The simulation should be goal-oriented rather than general. For instance, in the investigation of iceberg shapes, more simulations of different iceberg shapes are absolutely necessary. Only from results based on sufficient simulations can general conclusions be made;
- As to the residual strength study, it is suggested that more simulations on the end-shortening curve of damaged stiffeners are needed. The proposed models can thus be verified in more detail.

References

AMSA (2009). Arctic Marine Shipping Assessment 2009 Report. *Technique Report*. Arctic Council. p.194.

Arockiasamy, M., El-Tahan H., Swamidas A. S. J., *et al*. (1984). Semisubmersible response to transient ice forces. *Ocean Engineering*, **11**(5): 463-490.

Aslos, H. S., Amdahl J. and Hopperstad O. S. (2009). On the resistance to penetration of stiffened plates Part II - Numerical analysis. *Int. J. of Impact Eng.*, **36**(6): 799-807.

Bjornar Sand, G. H. (2001). Simulations of ice ridge forces on conical structures. In: *Proc. of the 11th Int. Offshore and Polar Eng. Conf.*, June 17-22, Stavanger, Norway.

Brown, R. and Daley C. (1999). Computer simulation of transverse ship-ice collisions. *Tech. Rept*. Memorial of Newfoundland.

Cammaert, A. B. and Tsinker G. P. (1981). Impact of large ice floes and icebergs on marine structures. In: *Proc. of the 6th Int. Conf. on Port and Ocean Eng. under Arctic Conditions*, July 27-31, Quebec, Canada.

Carney, K. S., Benson D. J., DuBois P., *et al*. (2006). A phenomenological high strain rate model with failure for ice. *Int. J. of Solids and Structures*, **43**(25-26): 7820-7839.

Croasdale, K. R. (2001). Local ice load data relevant to Grand Banks structures. *PERD/CHC Report 20-61*.

Curtis, D. D., Cammaert A. B., Wong T. T., et al. (1984). NUMERICAL ANALYSIS OF IMPACT OF SMALL ICEBERGS ON SEMISUBMERSIBLES. In: *Proc. of the 3rd Int. Specialty Conf. - Cold Regions Eng., Northern Resource Development.*, Edmonton, Alberta, Can, Canadian Soc for Civil Engineering.

Daley, C. G. (1999). Energy based ice collision forces. In: *Proc. Of the 15th Int. Conf. on Port and Ocean Eng. under Arctic Conditions*, Espoo, Finland

Derradji-Aouat, A. (2000). A Unified failure envelope for isotropic fresh water ice and iceberg ice. In: *Proc. of the ETCE/OMAE-2000 Joint Conf., Energy for the New Millennium*, New Orleans, USA.

Derradji-Aouat, A. (2003). Multi-surface failure criterion for saline ice in the brittle regime. *Cold Reg. Sci. and Tech.*, **36**(1-3): 47-70.

Derradji-Aouat Ahmed, M. L. (2005). Ice loads on electric power generating stations in the bell isle strait. In: *Proc. Of the 18th Int. Conf. on Port and Ocean Eng. under Arctic Conditions*, June 26-30, Postdam, New York.

DNV (2009). Rules for classification of ships. Pt 5, Ch 1: Ships for navigation in ice. DNV.

Duhaime, G. (2004). Arctic Human Development Report. Chapter 3: Economic Systems. Universite Laval.

Duthinh, D. and Marsden S. (1986). ICEBERG IMPACT LOAD ON A GRAVITY BASED STRUCTURE. In: *Proc. of the 4th Int. Conf. on Cold Regions Engineering*, Anchorage, AK, USA, ASCE.

E.Nevel, D. (1987). Iceberg impact forces. In: *Working Group on Ice Forces 3rd State-of-the-Art Report*.

Eik, K. (2009). Iceberg drift modelling and validation of applied metocean hindcast data. *Cold Reg. Sci. and Tech.*, **57**(2-3): 67-90.

Eik, K. and Gudmestad O. T. (2010). Iceberg management and impact on design of offshore structures. *Cold Reg. Sci. and Tech.*, **63**(1-2): 15-28.

Eik, K. and Marchenko A. (2010). Model tests of iceberg towing. *Cold Reg. Sci. and Tech.*, **61**(1): 13-28.

Fuglem, M., Jordaan I., Crocker G., et al. (1996). Environmental factors in iceberg collision risks for floating systems. *Cold Reg. Sci. and Tech.*, **24**(3): 251-261.

Fuglem, M., Muggeridge K. and Jordaan I. (1999). Design load calculations for iceberg impacts. *Int. J. of Offshore and Polar Eng.*, **9**(4): 298-306.

Gagnon, R. (2004). Analysis of laboratory growler impact tests. *Cold Reg. Sci. and Tech.*, **39**(1): 1-17.

Gagnon, R. (2006). First results of numerical simulations of bergy bit collisions with the CCGS terry fox icebreaker. In: *Proc. of the 18th Int. Ass. for the Hydo-Enviroment Eng. and Research (IAHR) Symp. on ice*, Aug. 28- Sep. 1, Sapporo, Japan.

Gagnon, R. (2008a). Analysis of data from bergy bit impacts using a novel hull-mounted external Impact Panel. *Cold Reg. Sci. and Tech.*, **52**(1): 50-66.

Gagnon, R. (2011). A numerical model of ice crushing using a foam analogue. *Cold Reg. Sci. and Tech.*, **65**(3): 335-350.

Gagnon, R., Cumming D., Ritch R., et al. (2008b). Overview accompaniment for papers on the bergy bit impact trials. *Cold Reg. Sci. and Tech.*, **52**(1): 1-6.

Gagnon, R. E. (1998). Analysis of visual data from medium scale indentation experiments at Hobson's Choice Ice Island. *Cold Reg. Sci. and Tech.*, **28**(1): 45-58.

Gagnon, R. E. and Gammon P. H. (1995). Triaxial experiments on iceberg and glaciers ice. *J. of Glaciology*, **41**(139): 528-840.

Gautier, D. L., Bird K. J., Charpentier R. R., et al. (2009). Assessment of Undiscovered Oil and Gas in the Arctic. *Science*, **324**(5931): 1175-1179.

Hallquist, J. O. (2007). Ls-dyna Keyword User's Manual (version 971). Livermore Software Technology Corp. p.2206.

Han S., J.-Y. L., Y-I Park and J Che (2008). Structural risk analysis of an NO96 membrane-type liquefied natural gas carrier in Baltic ice operation. In: *Proc. of the Inst. of Mech. Eng. part M, Journal of engineering for the maritime environment*, **222**(4): 179-194.

Heinonen, J. (2004). Constitute Modeling of ice rubble in First year ridge keel. Doctorial thesis. VTT, Finland. p.146.

Hill, B. T. (2006). Ship Iceberg collision database V.1.13, National Research Council Canada.

Hu, Z., Liu Z. and Amdahl J. (2010). Collision character research for semi-submersible through model test, simplified analytical and numerical simulation method. In: *Proc. of the 29th Int. Conf. on Ocean, Offshore and Arctic Eng.*, Shanghai.

ISO (2010). Petroleum and natural gas industries - Arctic offshore structures. ISO TC 67/SC 7/WG 8.

Johnson R. C. and Prodanovic A. (1989). Calculation of iceberg impact forces. In: *Proc. of the 10th Int. Conf. on Port and Ocean Eng. under Arctic Conditions*, June 12-16, Lulea, Sweden.

Johnson, R. C. (1987). Iceberg impact strength. In: *Proc. of the Int. Offshore Tech. Conf.*, Houston.

Johnston, M., Timco G. W., Frederking R., et al. (2008). Measuring global impact forces on the CCGS Terry Fox with an inertial measurement system called MOTAN. *Cold Reg. Sci. and Tech.*, **52**(1): 67-82.

Jones, S. J. (1982). The confined compressive strength of polycrystalline ice. *J. of Glaciology*, **28**(98): 171-177.

Jordaan, I. J. (2001). Mechanics of ice-structure interaction. *Eng. Fracture Mech.*, **68**(17-18): 1923-1960.

Jordaan, I. J., Matskevitch D. G. and Meglis I. L. (1999). Disintegration of ice under fast compressive loading. *Int. J. of Fracture*, **97**(1-4): 279-300.

Kierkegaard, H. (1993). Ship Collisions with Icebergs. Doctorial thesis, Denmark Technology University.

Kitami E., K. F., Y. Taguchi, T. Navata, T. Kawasaki, F. Sakai (1984). Iceberg collision with semi-submersible drilling unit. In: *Proc. of the 7thInt. Ass. of Hydraulic Research Ice Symp.*. Hamburg. **II:** 45-53.

Løset, S. and Kvamsdal T. (1994). Iceberg/structure interaction-effects of ice temperature on the impact force. In: *Proceedings of the 12th Int. Ass. for Hydro-Environment Eng. and Research (IAHR) Ice Symp.*, Aug. 23-26, Trondheim, Norway.

Lee, S. G., Lee J. S., Baek Y. H., et al. (2009). Structural safety assessment in membrane-type CCS in LNGC under iceberg collisions. In: *Proc. of the Int. Conf. on Ship and Offshore Technology: Ice Class Vessels*, 28 - 29 September 2009, Busan, Korea.

Liu, Z. and Amdahl J. (2010). A new formulation of the impact mechanics of ship collisions and its application to a ship-iceberg collision. *Marine Structures*, **23**(3): 360-384.

Liu, Z. and Amdahl J. (2011). Numeric and analytical assessment of residual strength of damaged double bottom. *J. Ocean Engineering, submitted*.

Liu, Z., Amdahl J. and Løset S. (2009). Numeric simulation of collisions between ships and icebergs. In: *Proc. of the 20thInt. Conf. on Port and Ocean Eng. Under Arctic Conditions*, 9-12 June, Lulea, Sweden.

Liu, Z., Amdahl J. and Løset S. (2010). A parametric study on the external mechanics of ship/iceberg collision. In: *29th International Conference on Ocean, Offshore and Arctic Engineering*, Shanghai.

Liu, Z., Amdahl J. and Løset S. (2011a). Plasticity based material modelling of ice and its application to ship-iceberg impacts. *Cold Reg. Sci. and Tech.*, **65**(3): 326-334.

Liu, Z., Amdahl J. and Løset S. (2011b). Integrated Numerical Analysis of foreship and iceberg collision. *Marine Structures, submitted*.

Liu, Z., Amdahl J. and Løset S. (2011c). Integrated numerical analysis of iceberg collisions with ship side structure. In: *Proc. of the 21stInt. Conf. on Port and Offshore Eng. under Arctic Conditions, submitted*, Montreal, Canada.

Liu, Z., Garee L. and Amdahl J. (2011). Analysis of foreship and iceberg impact loads based on Bayesian networks. In: *Proc. of 30th International. Conf. on Ocean, Offshore and Arctic Eng.*, 19-24 June, Rotterdam, The Netherlands.

Liukkonen, S. and Kivimaa S. (1991). FE-modelling of ice failure load during ship bow indentation into multi-year ice. *Tech. Rept.* Technical Research Center of Finland. p.49.

McKenna, R. (2005). Iceberg shape characterization. In: *Proc.18th Int. Conf. on Port and Ocean Eng. Under Arctic Conditions.* Vol. 2:555-564.

Moan, T., Amdahl J., Wang X., et al. (2003). Risk assessment of FPSOs with emphasis on collision. In: *Society of Naval Architects and Marine Engineers (SNAME) Annual Meeting*, Boston, Society of Naval Architects and Marine Engineers.

Nadreau, J.-P. and Michel B. (1986). Yield and failure envelope for ice under multiaxial compressive stresses. *Cold Reg. Sci. and Tech.*, **13**(1): 75-82.

Nilse, T. (2010). ""MV Nordic Barents" makes historic voyage." from http://barentsobserver.com/mv-nordic-barents-to-make-historic-voyage.4812338-16175.html.

NORSOK (2004). Design of Steel Structures, Appendix A: Design against Accidental Actions. Standards Norway. p.287.

Oh, H., Kim W. and Lee J. (2009). Safety of membrane type cargo containment system in LNG carrier under accidental iceberg collision. In: *Proc. of the Int. conf. on Ship and offshore tech.: Ice class vessels*, 28 - 29 September 2009, Busan, Korea.

Pedersen, P. T. and Zhang S. (1998). On impact mechanics in ship collisions. *Marine Structures*, **11**(10): 429-449.

Ralph, F., McKenna R. and Gagnon R. (2008). Iceberg characterization for the bergy bit impact study. *Cold Reg. Sci. and Tech.*, **52**(1): 7-28.

Riska, K. (1980). On the role of failure criterion of ice in determining ice loads. Laivatekniikan laboratorio.

Riska, K. and Frederking R. (1987). Ice load penetration modelling. In: *Proceedings of the 9th Port and Ocean Eng. Under Arctic Conditions Conference*, Fairbanks, Alaska, USA.

Ritch, R., Frederking R., Johnston M., et al. (2008). Local ice pressures measured on a strain gauge panel during the CCGS Terry Fox bergy bit impact study. *Cold Reg. Sci. and Tech.*, **52**(1): 29-49.

Salvesen, N., Tuck E. O. and Faltinsen O. M. (1970). Ship motions and sea loads. In: *the Annual meeting of the Society of Naval Architects and Marine Engineers*, New York.

Sanderson, T. J. Q. (1988). Ice Mechanics-Risks to offshore Structures. London, Graham and Trotman.

Schulson, E. M. (2001). Brittle Failure of Ice. *Engineering Fracture Mechanics*, **68**: 1839-1887.

Schulson, E. M. (2002). Compressive shear faults in ice: plastic vs. Coulombic faults. *Acta Materialia*, **50**(13): pp.3415-3424.

Schulson, E. M. (2010). Personal communication, Trondheim, Norway.

Schulson, E. M. and Duval P. (2009). Creep and Fracture of Ice, Cambridge University Press.

Simo, J. C. and Hughes T. J. R. (1998). Computational Inelasticity, Springer.

Stronge, W. J. (2004). Impact mechanics. Cambridge, Cambridge University Press.

Tabri, K. (2010). Influence of coupling in the prediction of ship collision damage. In: *Proc. of 5th Int. Conf. on Collision and Grounding of Ships*, Espoo, Finland.

Tsai, S. and Wu E. (1971). A General theory of strength for anisotropic materials. *Composite Materials*, **5**(1):58-80.

USGS (2008). Estimates of Undiscovered Oil and Gas North of the Arctic Circle. *Tech. Rept*. the U.S. Geological Survey (USGS).

Appendix A: Appended Papers

PAPER I

Liu Z., Amdahl J.

A new formulation of the impact mechanics of ship collisions and its application to a ship-iceberg collision

Published in:

Marine Structures

Volume 23, Issue 3, Pages 360-384, 2010.

Marine Structures 23 (2010) 360–384

Contents lists available at ScienceDirect

Marine Structures

journal homepage: www.elsevier.com/locate/marstruc

A new formulation of the impact mechanics of ship collisions and its application to a ship–iceberg collision

Zhenhui Liu*, Jørgen Amdahl

Norwegian University of Science and Technology, Trondheim 7491, Norway

ARTICLE INFO

Article history:
Received 18 September 2009
Received in revised form 10 May 2010
Accepted 10 May 2010

Keywords:
Ship collisions
External mechanics
Iceberg impacts

ABSTRACT

A new formulation is proposed for the analysis of the impact mechanics of ship collisions that can be applied to both 2D and 3D cases. It is assumed that the impact force is large, and all other forces except the impact forces are neglected. The equations of motion are solved in a local coordinate system, and a transformation matrix between the global and the local coordinate system is proposed. The mass and inertia properties are formulated in the local coordinate system. The orientation of the local coordinate system is determined by the hull shape of the struck ship at the contact point. A closed form solution of the external mechanics of ship collisions is derived. Excellent agreement with an alternative 2D formulation for ship–ship collisions is achieved. The features of the proposed 3D method are demonstrated by numerical examples. An application of the method to estimate the required energy dissipation in ship–iceberg collisions is included. Results and discussions are presented and finally, conclusions are made.

1. Introduction

A ship collision is a multi-physical and highly coupled process. However, in the accidental limit state (ALS), the analysis of collision may conveniently be split into two uncoupled processes: namely, external mechanics and internal mechanics [1]. The external mechanics deals with rigid body motions and determines the energy to be dissipated as strain energy. The internal mechanics is concerned with

* Fax: +47 73 59 55 28.
E-mail address: zhenhui.liu@ntnu.no (Z. Liu).

0951-8339/$ – see front matter © 2010 Elsevier Ltd. All rights reserved.
doi:10.1016/j.marstruc.2010.05.003

how the strain energy is dissipated in the striking and struck objects and involves the assessment of the structural resistance during large deformations, either by means of a plasticity theory or by using nonlinear finite element analysis (NLFEA).

This paper focuses on the external mechanics, and a new formulation for the analysis of the impact mechanics of ship collisions is presented. The initial motivation for this work is to study ship–iceberg collisions. Actually, ship–iceberg impact modelling has been continuously developed over recent decades. Cammaert and Tsinker [2] used a single degree of freedom (1DOF) model to calculate head-on collisions between a structure and an iceberg. The structure is rigid and non-compliant. Matskevitch [3,4] presented a simple 3DOF model of ice–structure interaction, which is a two-dimensional (2D) model that describes the motion of an ice feature in the horizontal plane. The analysis shows that eccentric impacts decrease the maximum impact force significantly. One pioneering attempt to assess the 6DOF problem of ice impacts is made by Popov et al. [5] in the form of a three-dimensional (3D) model. The 6DOF of the ship is well considered, while the ice motion is limited to level ice, and heave, pitch and roll can be neglected. The friction has been ignored. Accordingly, this model can only be considered a semi-6DOF solution.

Experience has shown that ship–iceberg impacts, particularly oblique-type collisions, produce considerable motion in the components of sway, yaw and roll; see Johnston et al. [6]. Thus, modelling a ship and iceberg collision should take the 6DOF into account for each object involved. In particular, if the collision happens at the bow of a ship, the shape of the outer shell determines the contact force direction and has a significant influence on the final dissipated energy; this fact has not been taken into account in previous studies.

Pedersen and Zhang [1] developed an impact mechanics model of ship–ship collisions. In that model, the dissipated energy is obtained through the integration of the contact force and relative motion in each direction. Finally, a closed form for the dissipated energy is obtained. It is only valid for the 3DOF (2D) case. The formulation is somewhat complicated, and further development to the 6DOF (3D) case is difficult. Stronge [7] developed an advanced solution for 3D impacts, but attention is paid to the accelerations and velocities of the objects involved. In this paper, a fully 3D solution to the ship collision problem is proposed based on Stronge's work. The 2D case can be treated as a special case. The vertical contact geometry shape is taken into account. The main point of this approach is that all equations are formulated in a local coordinate system, which allows the dissipated energy along each axis in the local coordinate system to be obtained in a closed form.

In conjunction with ship–iceberg collisions, the shape and inertia properties of the iceberg are associated with significant uncertainty, notably because the major part of the iceberg is submerged. Ralph et al. [8] carried out a series of investigations to characterise the underwater iceberg shapes using a sonar system. The mass of the iceberg can be estimated by empirical equations on the basis of iceberg's main dimensions for the part above sea level. For the inertia properties, a calculation should be made based on the shapes detected. However, in order to illustrate the application of the present model, a simplified iceberg shape is considered in this paper.

In the following sections, a review of the impact mechanics models of Pedersen and Zhang (Section 2) and Stronge (Section 3) is presented. Section 4 describes the present theory in detail. Section 5 deals with the projection of the present method to the 2D case and its validation. Section 6 is concerned with numerical examples illustrating the characteristics of the present method. An application to the analysis of a ship–iceberg collision is included in the last part in this section. The conclusions are presented in Section 7. Appendix A and B show information on the usage of transformation matrices and the empirical equations proposed by Popov et al. [5].

2. Ship impact theory according to Pedersen and Zhang

Three different coordinate systems are established to derive the equations of motion; see Fig. 1. The XYZ and $X'Y'Z'$ coordinate systems are defined as global coordinate systems for ship A and ship B, respectively. (It is noted that the original expression in reference [1] was changed accordingly to keep the notations consistent in this paper.)

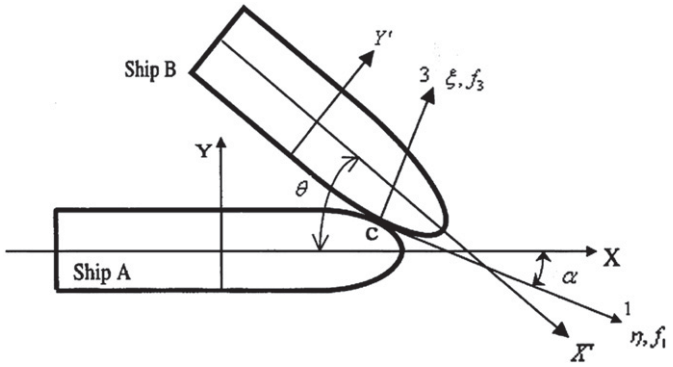

Fig. 1. The coordinate system used for analysis of a ship–ship collision, after Pedersen and Zhang [1].

- The *XYZ* coordinate system for ship A is fixed to the sea bed. The *Z*-axis is oriented out of water. The *X*-axis lies in the symmetry plane of the striking ship pointing towards the bow. The origin of the *XYZ*-system is placed so that the midship section is in the *YZ*-plane at the moment of contact;
- The *X′Y′Z′* coordinate system for ship B is established in the same way as the *XYZ* coordinate system is for ship A;
- The $\xi\eta$ coordinate system (corresponding to the $\vec{n}_1\,\vec{n}_3$ local coordinate system in this paper, please refer to Section 3) is located at the contact point C. The ξ-direction is normal to the impact surface. The angle between the X-axis and the η-axis is denoted α (the waterline angle, see Section 4), and the angle between the X-axis and the symmetry plane of the struck vessel is θ.

For example, the equations of motion of ship A are given by

$$M\left(1+\widehat{m}_x\right)\dot{\widehat{v}}_x = -f_3\sin\alpha - f_1\cos\alpha \tag{1}$$

$$M\left(1+\widehat{m}_y\right)\dot{\widehat{v}}_y = -f_3\cos\alpha + f_1\sin\alpha \tag{2}$$

$$M\widehat{R}_{zz}^2\left(1+\widehat{j}_{zz}\right)\dot{\widehat{\omega}} = f_3\left[\widehat{y}_c\sin\alpha - \left(\widehat{x}_c-\widehat{x}_a\right)\cos\alpha\right] + f_1\left[\widehat{y}_c\cos\alpha + \left(\widehat{x}_c-\widehat{x}_a\right)\sin\alpha\right] \tag{3}$$

where M is the mass of the ship, and $\widehat{m}_x$, $\widehat{m}_y$ are the added mass. The subscripts x, y represent the *X*-axis and *Y*-axis, respectively. If there is no explanation, the diacritical mark $\wedge$ over a symbol in this paper expresses that the quantity is formulated in the global coordinate system. $\dot{\widehat{v}}_x$, $\dot{\widehat{v}}_y$ are the accelerations. The dot over a symbol signifies time derivatives. f_1, f_3 are the impact forces in the local coordinate system, corresponding to the $\vec{n}_1$ and $\vec{n}_3$ direction, respectively, see Fig. 1. $\widehat{R}_{zz}$ is the radius of gyration for yaw motion, $\widehat{j}_{zz}$ is the added inertia factor of the ship, and $\dot{\widehat{\omega}}$ is the angular acceleration. $\widehat{x}_a$ is the coordinate of the centre of ship A on the *X*-axis, and $\widehat{x}_c, \widehat{y}_c$ give the contact point C in the *XYZ* coordinate system.

In order to determine the energy to be dissipated through the crushing of the ship structures at the contact point, Pedersen and Zhang further assume that the ratio between the collision forces parallel and perpendicular to the impacting surfaces, f_1 and f_3, are constant during the collision; that is, $f_1 = \mu_n \cdot f_3$, where μ_n is the ratio of the impact impulses. For more details, please see reference [1]. If $|\mu_0| < |\mu_n|$, the two ships will slide against each other, where μ_0 is the real friction factor between the two ships. If $|\mu_0| \geq |\mu_n|$, the ships will stick together during the collision. The expressions for the dissipated energy in these two cases are finally calculated as follows:

a) Sticking case:

$$E_3 = \frac{1}{2}\frac{1}{D_\xi + \mu\cdot D_\eta}\left(1-e^2\right)\left(v_3^0\right)^2 \tag{4}$$

$$E_1 = \frac{1}{2}\frac{1}{1/\mu \cdot K_\xi + K_\eta}\left(v_1^0\right)^2 \tag{5}$$

b) Sliding case:

$$E_3 = \frac{1}{2}\frac{1}{D_\xi + \mu_0 \cdot D_\eta}\left(1 - e^2\right)\left(v_3^0\right)^2 \tag{6}$$

$$E_1 = \frac{1}{2}\frac{1}{1/\mu_0 \cdot K_\xi + K_\eta}\left(v_1^0 - v_1^t\right)^2 \tag{7}$$

where D_ξ, D_η, K_ξ, K_η are expressions derived from equation of motions; please refer to section 2.1 in reference [1]. v_3^0, v_1^0 are the initial relative velocities in the local $\xi\eta(\vec{n}_1\,\vec{n}_3)$ coordinate system, ${v_1}^t$ is the final relative velocity in η-axis $(\vec{n}_1)$, and e $(0 \le e \le 1)$is the coefficient of restitution. For an entirely plastic collision, $e = 0$, and for a perfect elastic collision, $e = 1$.

3. Stronge's impact mechanics model

Unlike the previous method, one so-called local coordinate system is established to derive the equations of motion in Stronge's impact mechanics [7], e.g., $\vec{n}_1\,\vec{n}_2\,\vec{n}_3$; see Fig. 2. The basic assumptions are

- The impact duration is short, and the impact force is large, so all other external forces are neglected.
- The deformations are limited to a small area within the contact surface.

Consider two bodies that collide at contact point *C*. The bodies have no displacement constraints except that they are mutually impenetrable at *C*. If the surface of at least one of the bodies has a continuous curvature at *C*, there is a common tangent plane that constrains point *C*. First, define a common normal direction $\vec{n}$ that is perpendicular to the common tangent plane. Let $\vec{n}_i$, $i = 1, 2, 3$, be a set of mutually perpendicular unit vectors with $\vec{n}_1$ and $\vec{n}_2$ at the tangent plane, while $\vec{n}_3 = \vec{n}$ is

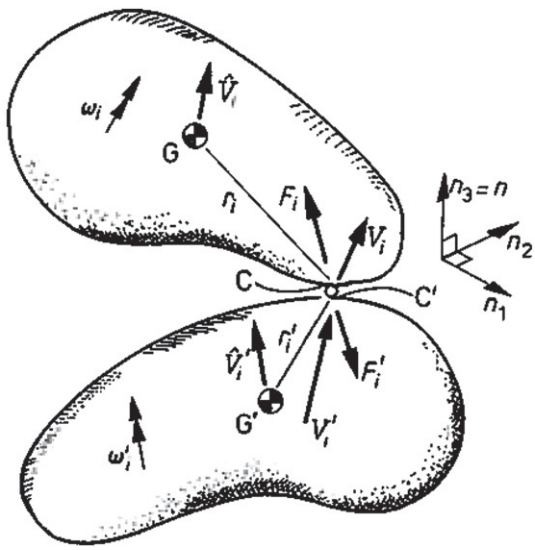

Fig. 2. Collision between two rough bodies. The rigid bodies have contact pints C and C′ that are separated by a deformable particle, after Stronge [7].

normal to this plane, as shown in Fig. 2. A local coordinate system $\vec{n}_1\,\vec{n}_2\,\vec{n}_3$ is established. The bodies have masses M and M' and inertia tensors $\widehat{I}_{ij}$ and $\widehat{I}'_{ij}$ for the second moments of their masses at G and G', respectively. The diacritical mark $\wedge$ here indicates the variable is referring to the axes passing through the centre of gravity, and the prime mark $'$ over a symbol is used to distinguish variables for different collision objects. A direction vector r_i connects G to the contact point C, while r'_i locates C' relative to G'. Let $\widehat{V}_i$ and $\widehat{V}'_i$ be the velocities of the centres of mass, while ω_i and ω_i' are the corresponding angular velocities for the bodies in $\vec{n}_i$ of the local coordinate system. At the contact points C and C', the bodies are subjected to forces F_i and F'_i. These contact forces are mutual reactions applying an impulse to each body. The impulses $P_i(t)$ and $P_i(t)$ are given by

$$\mathrm{d}P_i = F_i\,\mathrm{d}t \tag{8}$$

$$\mathrm{d}P'_i = F'_i\,\mathrm{d}t \tag{9}$$

The equations of translational and rotational motion for each body can be expressed as

$$M\,\mathrm{d}\widehat{V}_i = \mathrm{d}P_i \tag{10}$$

$$\widehat{I}_{ij}\,\mathrm{d}\omega_j = \varepsilon_{ijk} r_j\,\mathrm{d}P_k \tag{11}$$

and

$$M'\,\mathrm{d}\widehat{V}'_i = \mathrm{d}P'_i \tag{12}$$

$$\widehat{I}'_{ij}\,\mathrm{d}\omega'_j = \varepsilon_{ijk} r'_j\,\mathrm{d}P'_k \tag{13}$$

where a repeated index (e.g., j or k) indicates summation, and the permutation tensor ε_{ijk} takes the values $+1$ if the indices are in cyclic order, -1 if the indices are in anticyclic order and 0 for repeated indices.

The velocity of each contact point, V_i and V'_i, can be obtained from the velocity of the respective centre of mass and the relationship between the velocities of two points on a rigid body.

$$V_i = \widehat{V}_i + \varepsilon_{ijk}\omega_j r_k \tag{14}$$

$$V'_i = \widehat{V}'_i + \varepsilon_{ijk}\omega'_j r'_k \tag{15}$$

Let the relative velocity be

$$v_i = V_i - V'_i \tag{16}$$

Any incremental change in the reaction impulses acting on the rigid bodies is equal in magnitude but opposite in direction if the infinitesimally small deforming element has negligible mass; see Fig. 2.

$$\mathrm{d}p_i = \mathrm{d}P_i = -\mathrm{d}P'_i \tag{17}$$

From the above equations, we find

$$\mathrm{d}v_i = m_{ij}^{-1}\,\mathrm{d}p_j \tag{18}$$

where the elements of the inverse inertia matrix m_{ij}^{-1} are given by

$$m_{ij}^{-1} = \left(M^{-1} + M'^{-1}\right) + \varepsilon_{ikm}\varepsilon_{jln}\left(I_{kl}^{-1} r_m r_n + I'^{-1}_{kl} r'_m r'_n\right) \tag{19}$$

The inverse inertia matrix is symmetric, i.e.,$m_{ij}^{-1} = m_{ji}^{-1}$. The following are representative elements:

$$m_{11}^{-1} = \left(M^{-1} + r_2^2 I_{33}^{-1} - 2r_2 r_3 I_{23}^{-1} + r_3^2 I_{22}^{-1}\right) + \left(M'^{-1} + r'^2_2 I'^{-1}_{33} - 2r'_2 r'_3 I'^{-1}_{23} + r'^2_3 I'^{-1}_{22}\right) \tag{20}$$

$$m_{12}^{-1} = \left(M^{-1} + r_1 r_3 I_{23}^{-1} - r_3^2 I_{21}^{-1} - r_1 r_2 I_{33}^{-1} + r_2 r_3 I_{31}^{-1}\right) + \left(M'^{-1} + r_1' r_3' I_{23}'^{-1} - r_3'^2 I_{21}'^{-1} - r_1' r_2' I_{33}'^{-1} + r_2' r_3' I_{31}'^{-1}\right) \quad (21)$$

$$m_{13}^{-1} = \left(M^{-1} + r_1 r_2 I_{32}^{-1} - r_2^2 I_{31}^{-1} - r_1 r_3 I_{22}^{-1} + r_2 r_3 I_{21}^{-1}\right) + \left(M'^{-1} + r_1' r_2' I_{32}'^{-1} - r_2'^2 I_{31}'^{-1} - r_1' r_3' I_{22}'^{-1} + r_2' r_3' I_{21}'^{-1}\right) \quad (22)$$

In these expressions, it should be noted that the matrix I_{ij} of moments and products of inertia has an inverse, which is denoted by I_{ij}^{-1}, e.g., $I_{21}^{-1} = (\hat{I}_{13}\hat{I}_{23} - \hat{I}_{12}\hat{I}_{33})/\det(\hat{I}_{ij})$.

4. Present method

4.1. Equations of motion

The method is an application of previous studies to ship impacts. The global coordinate system originates from the COG (centre of gravity) of the ship at the moment when impact occurs. In this way, it minimises the effect of COG movement. The impact force is assumed to be much larger than other external forces, e.g., the restoring forces. Taking two ships in collision as an example; see Fig. 3.

The derivation of the equations of motion follows the principles described in Section 3. For simplicity, the influence of hydrodynamic forces is considered by introducing the added mass factors in both the mass and inertia matrices. Consequently, the mass M in Stronge's theory should be replaced by the mass matrices M_{ij} and M_{ij}'. As discussed by Salvesen et al. [9], the mass and inertia matrices are significantly simplified due to the lateral symmetry of the ship hull (symmetry about the X,Z-plane in the global coordinate system). If we put the origin of the coordinate system in the COG of the ship, then the mass and inertia matrices can be assumed to be diagonal matrices with reference to the global coordinate system, e.g., $\widehat{M}_{ij}, \widehat{M}_{ij}'$ and $\widehat{I}_{ij}, \widehat{I}_{ij}'$. However, it does not apply to the iceberg because its shape is usually irregular. Field measurements are necessary if accurate results are required. To begin, a simplified iceberg shape can be used. Then, the formation of M_{ij}, M_{ij}' and I_{ij}, I_{ij}' in the local coordinate system $\vec{n}_1\,\vec{n}_2\,\vec{n}_3$ can be generated if the transformation matrix is known; see the Appendix A. The

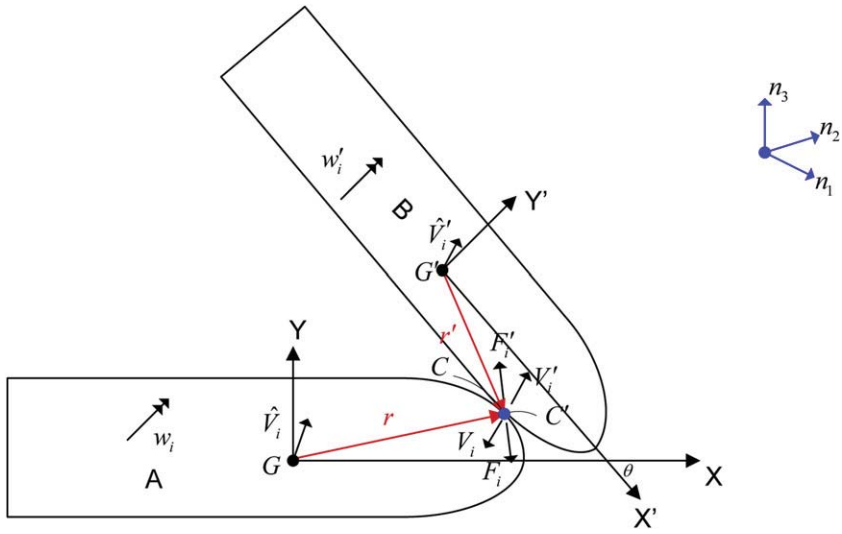

Fig. 3. Illustration of a ship–ship collision.

transformation matrix is presented in the following subsection. Based on the discussion above, Eq. (19) will be in the following form

$$m_{ij}^{-1} = \left(M_{ij}^{-1} + M_{ij}'^{-1}\right) + \varepsilon_{ikm}\varepsilon_{jln}\left(I_{kl}^{-1} r_m r_n + I_{kl}'^{-1} r_m' r_n'\right) \tag{23}$$

where, for example,

$$m_{11}^{-1} = \left(M_{11}^{-1} + r_2^2 I_{33}^{-1} - 2r_2 r_3 I_{23}^{-1} + r_3^2 I_{22}^{-1}\right) + \left(M_{11}'^{-1} + r_2'^2 I_{33}'^{-1} - 2r_2' r_3' I_{23}'^{-1} + r_3'^2 I_{22}'^{-1}\right) \tag{24}$$

$$\begin{aligned} m_{12}^{-1} = {} & \left(M_{12}^{-1} + r_1 r_3 I_{23}^{-1} - r_3^2 I_{21}^{-1} - r_1 r_2 I_{33}^{-1} + r_2 r_3 I_{31}^{-1}\right) \\ & + \left(M_{12}'^{-1} + r_1' r_3' I_{23}'^{-1} - r_3'^2 I_{21}'^{-1} - r_1' r_2' I_{33}'^{-1} + r_2' r_3' I_{31}'^{-1}\right) \end{aligned} \tag{25}$$

$$\begin{aligned} m_{13}^{-1} = {} & \left(M_{13}^{-1} + r_1 r_2 I_{32}^{-1} - r_2^2 I_{31}^{-1} - r_1 r_3 I_{22}^{-1} + r_2 r_3 I_{21}^{-1}\right) \\ & + \left(M_{13}'^{-1} + r_1' r_2' I_{32}'^{-1} - r_2'^2 I_{31}'^{-1} - r_1' r_3' I_{22}'^{-1} + r_2' r_3' I_{21}'^{-1}\right) \end{aligned} \tag{26}$$

Similarly, it should be noticed that the matrix M_{ij} has an inverse, which is denoted by M_{ij}^{-1}, e.g., $M_{21}^{-1} = (M_{13}M_{23} - M_{12}M_{33})/\det(M_{ij})$.

4.2. Transformation matrix

Generally, the ship motions are described in the global coordinate system XYZ (or $X'Y'Z'$), as defined in Section 2; see Fig. 4. The present subsection will demonstrate how to derive the transformation matrix between the global and the local coordinate system.

The local coordinate system is established according to the method discussed in Section 2; see Fig. 6. It is further assumed that the hull shape at the collision point of ship A determines the direction of the local frame. The following hull angles defined by DNV [10] are used; see Fig. 5:

- α: waterline angle
- β: frame angle
- β': normal frame angle
- γ: sheer angle

The various angles are related through the expressions

$$\tan(\beta) = \tan(\alpha)\tan(\gamma) \tag{27}$$

$$\tan(\beta') = \tan(\beta)\cos(\alpha) \tag{28}$$

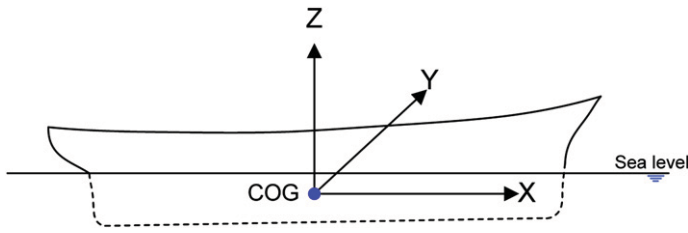

Fig. 4. Global coordinate system of the ship.

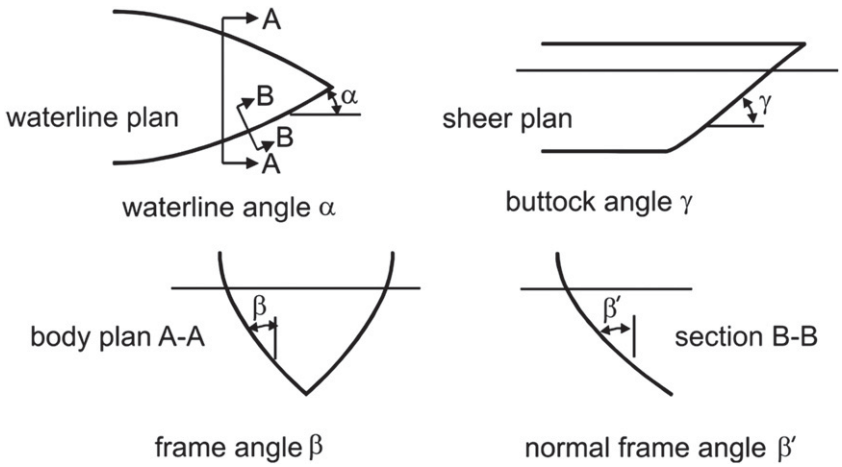

Fig. 5. Definition of hull angles.

Here, the angles α, β' are chosen as the independent variables because only two angles are independent.

The direction cosines of the normal direction $\vec{n}_3$ at the impact point are follows; see Daley [11]:

$$\cos(\vec{n}_3 X) = \sin(\alpha)\cos(\beta') \tag{29}$$

$$\cos(\vec{n}_3 Y) = \cos(\alpha)\cos(\beta') \tag{30}$$

$$\cos(\vec{n}_3 Z) = -\sin(\beta') \tag{31}$$

We define the intersection line of the collision plane (parallel to the water plane and passing through the impact point) and the tangential plane as one of the vectors in the tangential plane, say $\vec{n}_1$, heading forward as positive. The cosines are expressed as

$$\cos(\vec{n}_1 X) = \cos(\alpha) \tag{32}$$

$$\cos(\vec{n}_1 Y) = -\sin(\alpha) \tag{33}$$

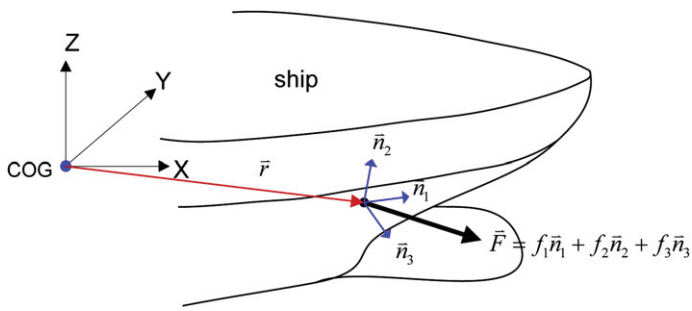

Fig. 6. Collision point geometry and local coordinate system, modified from Daley [11].

$$\cos(\vec{n}_1 Z) = 0 \tag{34}$$

$\vec{n}_2$ is obtained by taking the cross product of $\vec{n}_1$ and $\vec{n}_3$. Finally, the transformation matrix from the global to the local coordinate system of ship A can be written as

$$T_{lg} = \begin{bmatrix} \cos(\alpha) & -\sin(\alpha) & 0 \\ -\sin(\alpha)\sin(\beta') & -\cos(\alpha)\sin(\beta') & -\cos(\beta') \\ \sin(\alpha)\cos(\beta') & \cos(\alpha)\cos(\beta') & -\sin(\beta') \end{bmatrix} \tag{35}$$

Some special cases for the transformation matrix:

- For a symmetrical collision at the stem, the transformation matrix becomes $\alpha = 90^\circ$, $\beta' = \gamma$:

$$T_{lg} = \begin{bmatrix} 0 & -1 & 0 \\ -\sin(\gamma) & 0 & -\cos(\gamma) \\ \cos(\gamma) & 0 & -\sin(\gamma) \end{bmatrix}$$

- For collision at amidships, $\alpha = 0^\circ$, $\beta = \beta' = 0$:

$$T_{lg} = \begin{bmatrix} 1 & 0 & 0 \\ 0 & 0 & -1 \\ 0 & 1 & 0 \end{bmatrix}$$

As for ship B, the corresponding transformation matrix can be obtained by defining the angle θ in Fig. 3. The transformation matrix from ship B to ship A is

$$T_{ab} = \begin{bmatrix} \cos(\theta) & \sin(\theta) & 0 \\ -\sin(\theta) & \cos(\theta) & 0 \\ 0 & 0 & 1 \end{bmatrix} \tag{36}$$

Thus, the transformation matrix from the global to local coordinate system of ship B is given by

$$T'_{lg} = T_{lg} T_{ab} \tag{37}$$

After establishing the transformation matrix, the input parameters in the local coordinate system can be generated according to the method in Appendix A.

4.3. Derivations of energy dissipation

The impulse in each direction, $\vec{n}_i$ ($i = 1,2,3$), is given by

$$\mathrm{d}p_i = f_i \, \mathrm{d}t \tag{38}$$

where f_i is the ith component of the interaction force acting on the infinitesimally small deforming element in the $\vec{n}_i$ direction.

The relative acceleration $\ddot{s}_i$ in each direction is

$$\ddot{s}_i = \frac{\mathrm{d}v_i}{\mathrm{d}t} \tag{39}$$

According to Eqs. (8) and (17),

$$f_i = F_i = -F'_i \tag{40}$$

By substitution of Eqs. (38) and (39) into Eq. (18), we obtain

$$\ddot{s}_i = m_{ij}^{-1} f_j \tag{41}$$

The acceleration can be written

$$\ddot{s}_i = \frac{\mathrm{d}\dot{s}_i}{\mathrm{d}s_i}\frac{\mathrm{d}s_i}{\mathrm{d}t} \tag{42}$$

Substituting Eq. (42) into Eq. (41) and integrating over the impact duration t, it can be seen that

$$\int_0^t m_{ij}^{-1} f_j \,\mathrm{d}s_i = \int_0^t \dot{s}_i \,\mathrm{d}\dot{s}_i = \frac{1}{2}\left(\left(v_i^t\right)^2 - \left(v_i^0\right)^2\right) = \frac{1}{2}\Delta v_i^2 \tag{43}$$

where v_i^t, v_i^0 are the relative velocities before and after the collision in the $\vec{n}_i$-direction, and Δv_i^2 is the change of the squared relative velocities v_i^t and v_i^0. Note that it is not always positive.

$$\Delta v_i^2 = \left(v_i^t\right)^2 - \left(v_i^0\right)^2 = \mathrm{d}v_i\left(\mathrm{d}v_i + 2v_i^0\right) \tag{44}$$

where $\mathrm{d}v_i$ is the relative velocity change in the $\vec{n}_i$-direction:

$$\mathrm{d}v_i = v_i^t - v_i^0 \tag{45}$$

Further,

$$\int_0^t m_{ij}^{-1} f_j \,\mathrm{d}s_i = m_{ij}^{-1}\frac{f_j}{f_i}\cdot\int_0^t f_i \,\mathrm{d}s_i = E_i \cdot m_{ij}^{-1}\frac{f_j}{f_i} \tag{46}$$

Substitution of Eq. (46) into Eq. (43) yields

$$E_i = \mathrm{abs}\left(\int_0^t f_i \,\mathrm{d}s_i\right) = \frac{1}{2}\cdot\mathrm{abs}\left(\frac{1}{m_{ij}^{-1}\frac{f_j}{f_i}}\cdot\Delta v_i^2\right) \tag{47}$$

where 'abs' indicates to calculate the absolute value because the force f_i and $\mathrm{d}s_i$ may be not at the same direction. If we define an equivalent mass variable $\overline{m}_i$ as follows:

$$\frac{1}{\overline{m}_i} = m_{ij}^{-1}\frac{f_j}{f_i} \tag{48}$$

Then, the dissipated energy has the following form:

$$E_i = \frac{1}{2}\mathrm{abs}\left(\overline{m}_i\Delta v_i^2\right) \tag{49}$$

Eq. (47) shows that the complicate 6DOF can be simplified to a 1DOF problem in each direction if the equivalent mass $\overline{m}_i$ and change of the squared relative velocity Δv_i^2 can be derived.

To illustrate the usage of $\overline{m}_i$ and Δv_i^2, we can consider one simple case, the purely plastic head-on collision of two spheres. We have $\widehat{r}_y = \widehat{r}'_y = 0$, $\widehat{r}_z = \widehat{r}'_z = 0$ and $\alpha = 90^\circ$, $\beta' = 0$. Based on Appendix A, the transformation is made, and thus we obtain $r_1 = r'_1 = r_2 = r'_2 = 0$, $r_3 = \widehat{r}_x$ and $r'_3 = \widehat{r}'_x$ correspondingly. According to Eq. (23), we obtain

$$\overline{m}_3 = \frac{1}{M} + \frac{1}{M'} \tag{50}$$

with

$$\Delta v_3^2 = -\left(\widehat{V}_x - \widehat{V}'_x\right)^2 \tag{51}$$

The dissipated energy is calculated as follows through Eq. (47):

$$E_3 = \frac{1}{2}\frac{1}{\frac{1}{M} + \frac{1}{M'}}\left(\widehat{V}_x - \widehat{V}'_x\right)^2 \tag{52}$$

The dissipated energy in the other two directions can be obtained similarly. In this case, they are both zero; $E_1 = E_2 = 0$ (Fig. 7).

4.4. Boundary conditions and solutions

4.4.1. Effect of friction

In order to solve Eq. (47), boundary conditions are needed. First, the Amontons–Coulomb theory for friction is considered; see Johnson [12]. The theory assumes that the friction force is proportional to the normal component of the reaction. Two friction factors are introduced, namely the normal friction factor and the tangential friction factor μ_t.

$$\sqrt{f_1^2 + f_2^2} = \mu_n f_3 \tag{53}$$

$$f_2 = \mu_t f_1 \tag{54}$$

This yields the following relationships:

$$f_1 = \frac{\mu_n}{\sqrt{1+\mu_t^2}} f_3 \tag{55}$$

$$f_2 = \frac{\mu_t \mu_n}{\sqrt{1+\mu_t^2}} f_3 \tag{56}$$

μ_n is calculated by the impulse ratio in order to determine whether the sticking or sliding mechanism applies; see Eq. (57). Similarly, μ_t can be obtained through Eq. (58).

$$\mu_n = \operatorname{sign}(\mathrm{d}p_1)\frac{\sqrt{\mathrm{d}p_1^2 + \mathrm{d}p_2^2}}{\mathrm{d}p_3} \tag{57}$$

$$\mu_t = \frac{\mathrm{d}p_2}{\mathrm{d}p_1} \tag{58}$$

where 'sign' is defined as follows:

$$\operatorname{sign}(x) = \begin{cases} 1 & \text{if } x > 0 \\ 0 & \text{if } x = 0 \\ -1 & \text{if } x < 0 \end{cases} \tag{59}$$

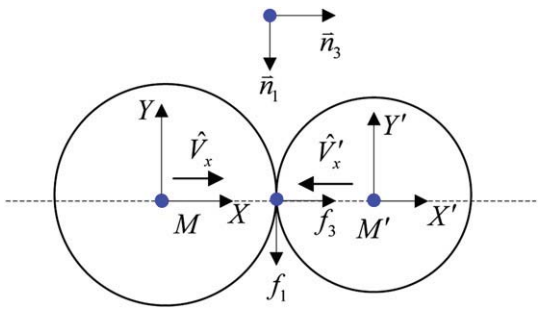

Fig. 7. Example of 1DOF problem.

4.4.2. Relative velocities

According to the definition in Section 2, we have

$$v_3^t = -ev_3^0 \tag{60}$$

Then, on the basis of Eq. (44),

$$\Delta v_3^2 = \left(v_3^t\right)^2 - \left(v_3^0\right)^2 = \left(e^2-1\right)\left(v_3^0\right)^2 \tag{61}$$

For the case where two objects stick together after collision, in which $v_i^t = 0$ $(i = 1,2)$ and $\mathrm{d}v_i = -v_i^0$ $(i = 1,2)$, we have

$$\Delta v_1^2 = \left(v_1^t\right)^2 - \left(v_1^0\right)^2 = -\left(v_1^0\right)^2 \tag{62}$$

$$\Delta v_2^2 = \left(v_2^t\right)^2 - \left(v_2^0\right)^2 = -\left(v_2^0\right)^2 \tag{63}$$

For the case where sliding occurs, Δv_1^2 and Δv_2^2 cannot be established because $\mathrm{d}v_1$ and $\mathrm{d}v_2$ are unknown. They should be calculated through the Eq. (18), which will be presented in following section.

4.4.3. Equations for $\mathrm{E_i}$

According to Eqs. (48), the equivalent mass is derived as follows:

$$\frac{1}{\overline{m}_1} = m_{11}^{-1} + m_{12}^{-1}\mu_t + m_{13}^{-1}\frac{\sqrt{1+\mu_t^2}}{\mu_n} \tag{64}$$

$$\frac{1}{\overline{m}_2} = m_{21}^{-1}\frac{1}{\mu_t} + m_{22}^{-1} + m_{23}^{-1}\frac{\sqrt{1+\mu_t^2}}{\mu_n\mu_t} \tag{65}$$

$$\frac{1}{\overline{m}_3} = m_{31}^{-1}\frac{\mu_n}{\sqrt{1+\mu_t^2}} + m_{32}^{-1}\frac{\mu_t\mu_n}{\sqrt{1+\mu_t^2}} + m_{33}^{-1} \tag{66}$$

As to the determination of μ_t, μ_n and Δv_i^2, two cases are considered.

a. Sticking case $|\mu_n| \le |\mu_0|$

By substituting Eqs. (61)–(63) into Eq. (18), $\mathrm{d}p_i$ $(i = 1,2,3)$ is obtained. Then μ_n and μ_t are determined by means of Eq. (57). Thus, both $\overline{m}_i$ and Δv_i^2 are known, and the dissipated energy in each direction is found for the sticking case:

$$E_1 = \mathrm{abs}\left(\int_0^t f_1\,\mathrm{d}s_1\right) = \frac{1}{2}\mathrm{abs}\left(\overline{m}_1\Delta v_1^2\right) = \frac{1}{2}\mathrm{abs}\left(-\overline{m}\left(v_1^0\right)^2\right) \tag{67}$$

$$E_2 = \mathrm{abs}\left(\int_0^t f_2\,\mathrm{d}s_2\right) = \frac{1}{2}\mathrm{abs}\left(\overline{m}_2\Delta v_2^2\right) = \frac{1}{2}\mathrm{abs}\left(-\overline{m}_2\left(v_2^0\right)^2\right) \tag{68}$$

$$E_3 = \mathrm{abs}\left(\int_0^t f_3\,\mathrm{d}s_3\right) = \frac{1}{2}\mathrm{abs}\left(\overline{m}_3\Delta v_3^2\right) = \frac{1}{2}\mathrm{abs}\left(\overline{m}_3\left(e^2-1\right)\left(v_3^0\right)^2\right) \tag{69}$$

b. Sliding case, $|\mu_n| > |\mu_0|$

If sliding occurs, we have

$$\mu_n = \mu_0 \tag{70}$$

One additional condition should be introduced to solve Eq. (18) in this case. It is assumed that the sticking case occurs tentatively, and we thus obtain μ_t according to the method described above. Therefore, with μ_0, μ_t and $\mathrm{d}v_3$, Eq. (18) is solved on the basis of Eqs. (57) and (58). The $\mathrm{d}v_i$ and $\mathrm{d}p_i$ ($i = 1,2$) are then established. According to Eq. (44), the dissipated energy for the sliding case is given by

$$E_1 = \mathrm{abs}\left(\int_0^t f_1 \,\mathrm{d}s_1\right) = \frac{1}{2}\mathrm{abs}\left(\overline{m}_1 \Delta v_1^2\right) = \frac{1}{2}\mathrm{abs}\left(\overline{m}_1 \,\mathrm{d}v_1\left(\mathrm{d}v_1 + 2v_1^0\right)\right) \tag{71}$$

$$E_2 = \mathrm{abs}\left(\int_0^t f_2 \,\mathrm{d}s_2\right) = \frac{1}{2}\mathrm{abs}\left(\overline{m}_2 \Delta v_2^2\right) = \frac{1}{2}\mathrm{abs}\left(\overline{m}_2 \,\mathrm{d}v_2\left(\mathrm{d}v_2 + 2v_2^0\right)\right) \tag{72}$$

$$E_3 = \mathrm{abs}\left(\int_0^t f_3 \,\mathrm{d}s_3\right) = \frac{1}{2}\mathrm{abs}\left(\overline{m}_3 \Delta v_3^2\right) = \frac{1}{2}\mathrm{abs}\left(\overline{m}_3\left(e^2 - 1\right)\left(v_3^0\right)^2\right) \tag{73}$$

5. Application to 2D collisions

5.1. Energy dissipation equations

In this section it is shown that the present method degrades to the 2D expressions. Obviously, we have

$$\beta' = 0 \tag{74}$$

$$\hat{r}_z = \hat{r}'_z = 0 \tag{75}$$

where $\hat{r}_z, \hat{r}'_z$ are the Z-axis components of the direction vectors $\hat{\mathbf{r}}, \hat{\mathbf{r}}'$ for ships A and B, respectively. The transformation matrices Eqs. (35) and (36) become

$$T_{lg} = \begin{bmatrix} \cos(\alpha) & -\sin(\alpha) & 0 \\ 0 & 0 & -1 \\ \sin(\alpha) & \cos(\alpha) & 0 \end{bmatrix} \tag{76}$$

$$T_{ab} = \begin{bmatrix} \cos(\theta) & \sin(\theta) & 0 \\ -\sin(\theta) & \cos(\theta) & 0 \\ 0 & 0 & 1 \end{bmatrix} \tag{77}$$

We have following solutions:

a. Sticking case, if $|\mu_n| \le |\mu_0|$

Based on Eqs. (64), (67) and (69):

$$E_1 = \frac{1}{2}\mathrm{abs}\left(\frac{-1}{m_{11}^{-1} + m_{13}^{-1}\frac{1}{\mu_n}}\left(v_1^0\right)^2\right) \tag{78}$$

$$E_3 = \frac{1}{2}\mathrm{abs}\left(\frac{e^2-1}{m_{31}^{-1}\mu_n + m_{33}^{-1}}\left(v_3^0\right)^2\right) \tag{79}$$

b. Sliding case, if $|\mu_n| > |\mu_0|$

Based on Eqs. (66), (71) and (73):

$$E_1 = \frac{1}{2}\mathrm{abs}\left(\frac{1}{m_{11}^{-1} + m_{13}^{-1}\frac{1}{\mu_0}}\mathrm{d}v_1\left(\mathrm{d}v_1 + 2v_1^0\right)\right) \tag{80}$$

$$E_3 = \frac{1}{2}\mathrm{abs}\left(\frac{e^2-1}{m_{31}^{-1}\mu_0 + m_{33}^{-1}}\left(v_3^0\right)^2\right) \tag{81}$$

Referring to Appendix A and Eq. (23), the 2D collision mechanics can be derived. Comparing to the work done by Pedersen and Zhang [1] (also see Section 2 in present paper), similar equations are obtained. The difference between these two methods is that they are formulated in different coordinate systems. Pedersen and Zhang derive the equations of motion in the global coordinate system, while the present method is in the local coordinate system. The new formulation method enables the possibility to expand to solve 3D collision problems.

5.2. Numerical analysis – case 1

This case was first analysed by Pedersen and Zhang [1]. Two identical supply vessels are sailing with a forward speed of $\widehat{V} = \widehat{V}' = 4.5$ m/s. Collisions take place with different impact angles and locations; see Fig. 8. The length of each vessel is 82.5 m, the breadth is 18.8 m, the draught is 7.6 m, and the displacement is 4000 t. The radius of inertia for yaw motion is 20.6 m. The added mass coefficients are the same as those used in the original paper. More data are given in Table 1. The results of the present method and that of the model of Pedersen and Zhang are presented in Fig. 9. The agreement is excellent. It is interesting to see that the energy ratio in most cases attains a maximum for midship collision locations because little kinetic energy is transferred into yaw motion. However, collisions with θ equal to 120° and 150° follow a different trend because of the effect of bow shape, as described by the waterline angle α. When the collision takes place forward of 0.2 d/L in these two cases, the collision becomes increasingly similar to a head-on collision.

6. 3D analysis

6.1. Numerical analysis – case 2

Case 1 in Section 5.2 is analysed again using the 3D method. The waterline angle is assumed to be $\alpha = 0$, and the normal frame angle is assumed to be $\beta' = 0$; refer to Fig. 10. In the 2D analysis, vertical

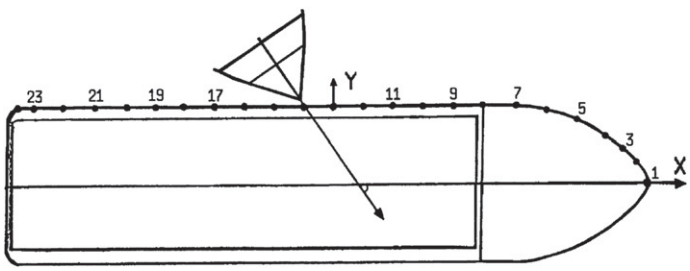

Fig. 8. Illustration for the numeric case 3, reprint from [1].

Table 1
Ship parameters – case 1.

Impact point	$\hat{r}_x$	$\hat{r}_y$	$\hat{r}_z$	$\hat{r}'_x$	$\hat{r}'_y$	$\hat{r}'_z$	α
1(bow)	40	0	0	41.25	0	0	90
2	38.5	2.6	0	41.25	0	0	45
3	36.6	4.1	0	41.25	0	0	37.5
4	34.6	5.6	0	41.25	0	0	32.5
5	30.8	7.5	0	41.25	0	0	21.7
6	27	9	0	41.25	0	0	14.4
7	23.1	9.4	0	41.25	0	0	7.3
8	19.3	9.4	0	41.25	0	0	0
9	15.4	9.4	0	41.25	0	0	0
10	11.6	9.4	0	41.25	0	0	0
11	7.7	9.4	0	41.25	0	0	0
12	3.9	9.4	0	41.25	0	0	0
13(mid)	0	9.4	0	41.25	0	0	0
14	−3.9	9.4	0	41.25	0	0	0
15	−7.7	9.4	0	41.25	0	0	0
16	−11.6	9.4	0	41.25	0	0	0
17	−15.4	9.4	0	41.25	0	0	0
18	−19.3	9.4	0	41.25	0	0	0
19	−23.1	9.4	0	41.25	0	0	0
20	−27	9.4	0	41.25	0	0	0
21	−30.8	9.4	0	41.25	0	0	0
22	−34.6	9.4	0	41.25	0	0	0
23	−38.5	9.4	0	41.25	0	0	0
24(stern)	−40	9.4	0	41.25	0	0	0

eccentricity was not considered, i.e., $\hat{r}_z = \hat{r}'_z = 0$ was implicitly assumed. When nonzero values of $\hat{r}_z$ and $\hat{r}'_z$ are taken into account, the roll motion of the ships is excited. The probable range of the collision point $\hat{r}_z$ is estimated to be from $0\hat{R}_{xx}$ to $1\hat{R}_{xx}$, where $\hat{R}_{xx}$ is the radius of gyration for the roll motion of ship A. This range is based on the assumption that the COG is located at a height of $T/2$ relative to the keel, where T is the draft, and the radius of gyration and added mass are as estimated in Appendices A and B. For ship B, $\hat{r}'_z$ is assumed to be $0.5\hat{R}'_{xx}$.

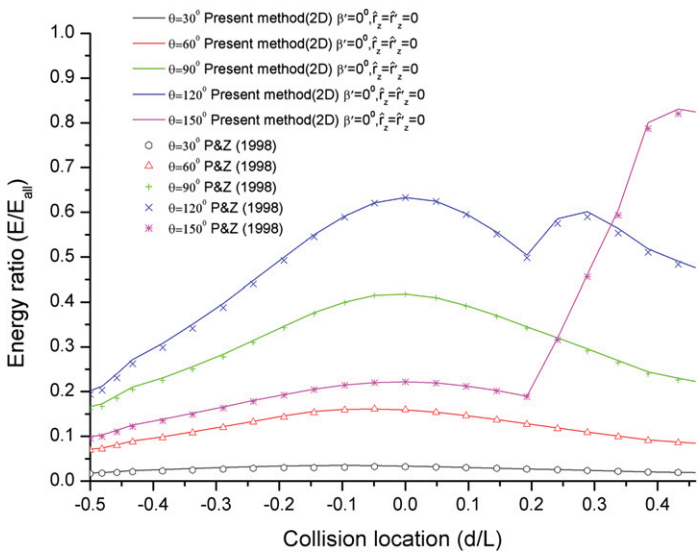

Fig. 9. Comparison of 2D numerical simulations.

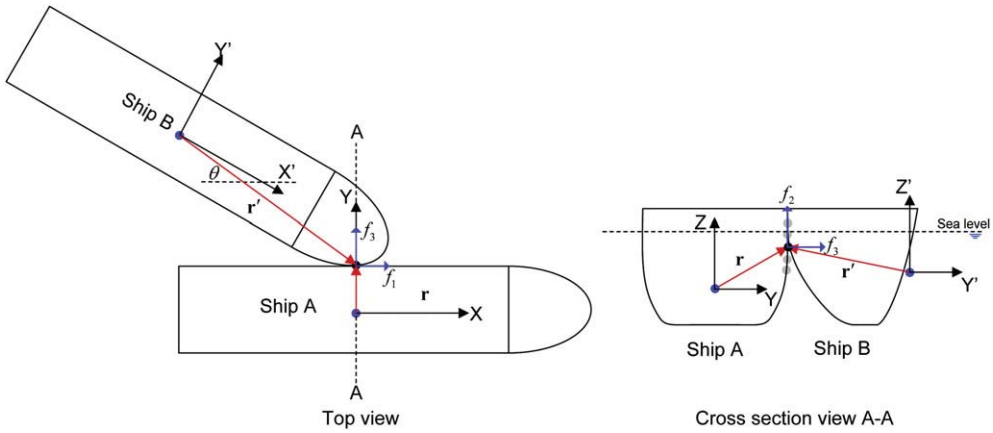

Fig. 10. Scenario of numerical example: case 2.

The results of the 3D analysis are presented in Fig. 11. It is interesting to see that the vertical eccentricity $\hat{r}_z$ has a significant influence on the dissipated energy, especially if the collision takes place amidships. In such cases, the roll motion (but not yaw motion) of ship A is excited, which takes a significant part of the total kinematical energy. If the collision is located close to the bow or the stern of ship, the longitudinal eccentricity exciting yaw motion becomes more important than the vertical eccentricity. In all cases, 3D analysis yields a smaller energy ratio than 2D analysis because the collision energy is allowed to transform into more kinetic energy components.

6.2. Numerical analysis – case 3

Recently, Tabri et al. [13] conducted model experiments on nonsymmetrical ship collisions; see Fig. 12. The collision point is controlled by adjusting the draft of the striking ship and the COG of the struck one, physical parameters of models are provided; see Tables 2 and 3.

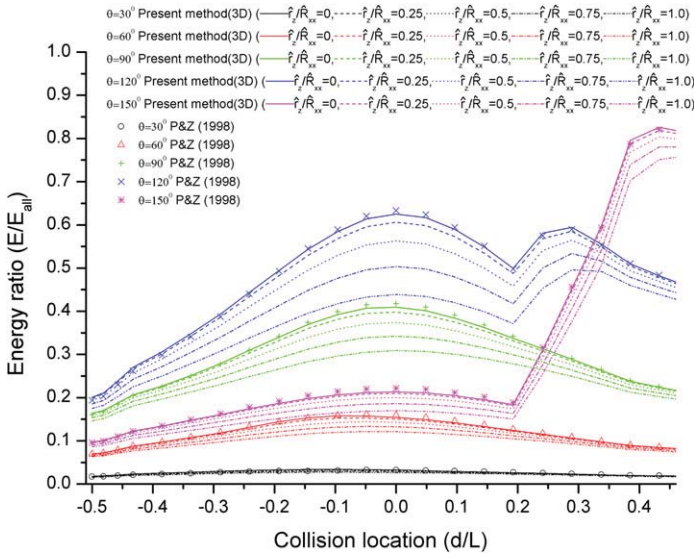

Fig. 11. Energy ratio of total dissipated energy with $\hat{r}_z/\hat{R}_{xx}$.

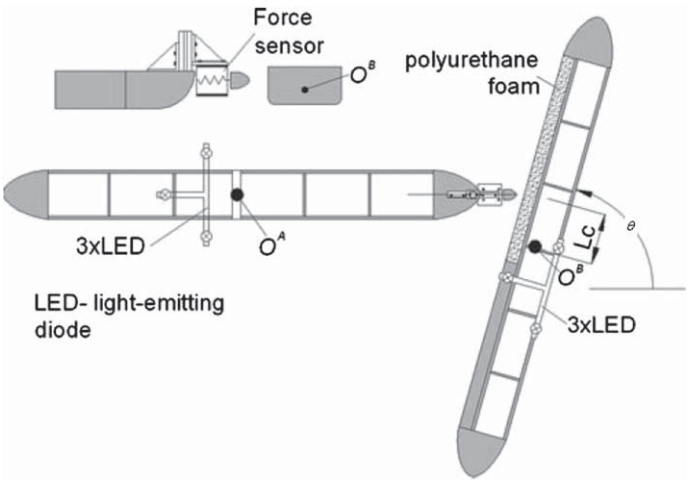

Fig. 12. General arrangement of the model tests, after Tabri et al. [13].

According to [13], the friction coefficient between the foam and the painted surface of the bulb was $\mu_0 = 0.15–0.2$. A value of 0.18 was adopted. In order to use the present method, the waterline angle α and the normal frame angle β' must be determined. The shape of the bulbs is an elliptic paraboloid. It is impossible to detect the exact collision point due to the deformation during the collision. However, the waterline angle and the frame angle can be estimated according to model information; see Table 4.

Generally, it is found that the recorded and predicted energy dissipation is in good agreement; see Fig. 13. Table 4 also lists all the components of the total dissipated energy. It was found that E_2 is quite small in most cases. The reason for this is that the relative position of COG with respect to the collision point varies little in most cases. Furthermore, the collision occurs at the tip of the bulbous bow where the frame angle is small (up to 20° as estimated). In this respect, most cases of the model tests are more relevant for 2D analysis.

6.3. Application to ship–iceberg collisions

The 3D (6DOF) model was then applied to the assessment of energy dissipation in a ship–iceberg collision. Because a ship–iceberg collision is most likely to take place at the shoulder area of the ship, a non-vertical contact surface can only be taken into account by the 3D method. In addition, the method also includes the 3D eccentricity of the iceberg in collision. A simplified iceberg shape is proposed to facility the 3D ship–iceberg impact analysis.

Generally, the dimensions of the above water part of iceberg are relatively easy to observe, but the submerged part is more difficult to see. An empirical equation could be used to estimate the mass of the iceberg based on the above water measurements, i.e.,

Table 2
Physical parameters of the models; see [13].

Model	Draft (cm)	Mass (kg)	KG (cm)	$\widehat{R}_{xx}$	$\widehat{R}_{yy}$	$\widehat{R}_{zz}$	$\widehat{m}_x$	$\widehat{m}_y$	$\widehat{m}_z$	$\widehat{j}_x$	$\widehat{j}_y$	$\widehat{j}_z$
Striking	4	20.5	7.4	19	70	70	0.05	0.17	3	0.12	2.20	0.14
Striking	6	285.	6.4	15	67	67	0.05	0.23	2.10	0.11	1.70	0.20
Striking	8	40.5	5.1	9	65	65	0.05	0.28	1.70	0.23	1.46	0.27
Struck	4	20.5	7.4	19	77	77	0.05	0.16	3.76	0.20	2.31	0.10
Struck	6	30.5	7.3	17	69	69	0.05	0.21	2.38	0.14	1.84	0.17
Struck	8	44.5	5.1	9	65	65	0.05	0.27	1.90	0.36	1.64	0.25

Table 3
Test matrix of model tests.

Tests	θ (deg)	L_c (m)	M (kg)	M' (kg)	$\hat{V}_x$ (m/s)	E (J)
201	90	0.82	28.5	30.5	0.87	3.91
202	90	0.83	28.5	30.5	0.71	2.36
203	90	0.83	28.5	30.5	0.38	0.75
204	90	0.45	28.5	30.5	0.91	6.3
205	90	0.48	28.5	30.5	0.91	6.3
206	90	0.38	28.5	30.5	0.38	0.95
207	90	0.8	28.5	20.5	0.9	4.2
208	90	0.41	28.5	20.5	0.89	4.92
301	120	0.37	28.5	20.5	0.87	4.2
302	120	0.32	28.5	20.5	0.3	0.51
303	120	0.3	28.5	44.5	0.84	6.5
304	120	0.38	28.5	44.5	0.37	1.01
305*	145	0.32	28.5	20.5	0.34	0.54
306*	145	0.44	28.5	20.5	0.87	3.91
307*	145	0.38	28.5	44.5	0.84	5.47
308	145	0.34	28.5	44.5	0.28	0.52
309*	145	0.46	28.5	20.5	0.87	3.19
310*	145	0.44	28.5	20.5	0.88	3.19
311	120	0.42	28.5	20.5	0.88	4.25
312	120	0.41	28.5	20.5	0.86	4.64
313	60	0.29	28.5	20.5	0.76	3.14
314	60	0.32	28.5	20.5	0.36	0.81
315	60	0.38	28.5	44.5	0.75	4.35
316	60	0.4	28.5	44.5	0.43	1.17

*Symbols denote “sliding”; see [13].

Table 4
Numerical calculation matrix.

Tests	α (deg)	β' (deg)	E (J)	E_1 (J)	E_2 (J)	E_3 (J)
201	90	0	5.63	0.00	0.00	5.63
202	90	0	3.75	0.00	0.00	3.75
203	90	0	1.07	0.00	0.00	1.07
204	90	0	6.33	0.00	0.00	6.33
205	90	0	6.32	0.00	0.00	6.32
206	90	0	1.11	0.00	0.00	1.11
207	90	0	4.79	0.00	0.00	4.79
208	90	0	4.88	0.00	0.00	4.88
301	30	10	2.48	0.65	0.05	1.78
302	30	10	0.30	0.08	0.01	0.21
303	30	10	3.67	0.93	0.06	2.68
304	30	10	0.71	0.18	0.01	0.52
305*	40	20	0.50	0.11	0.02	0.37
306*	40	20	2.98	0.66	0.12	2.21
307*	40	20	4.44	0.92	0.19	3.34
308	40	20	0.50	0.10	0.02	0.37
309*	40	20	2.97	0.65	0.12	2.20
310*	40	20	3.05	0.67	0.12	2.26
311	30	20	2.58	0.68	0.11	1.78
312	30	20	2.47	0.65	0.11	1.71
313	30	20	4.73	1.12	0.21	3.40
314	30	20	1.06	0.25	0.05	0.76
315	30	20	5.74	1.33	0.26	4.15
316	30	20	1.88	0.44	0.09	1.36

*Symbols denote “sliding”; see [13].

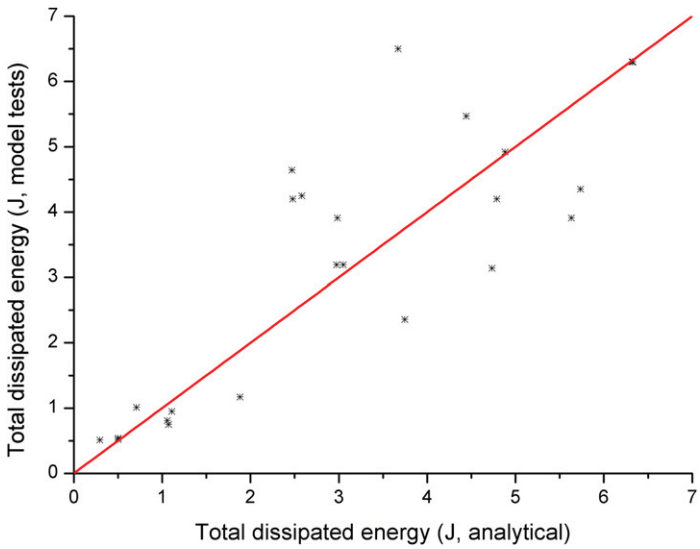

Fig. 13. Comparison of model tests and the analytical calculation of the total energy.

$$M_{iceberg} = \left(\frac{\rho_i \rho_w}{\rho_w - \rho_i}\right) f_b L_i W_i H_i \tag{82}$$

or

$$M_{iceberg} = a_i L_i^3 \tag{83}$$

where M_{iceberg} is the mass of iceberg, ρ_i, ρ_w are densities for the iceberg and sea water, respectively, f_b is the block coefficient for the above water part, which is dependent on the iceberg shape, L_i is the waterline length (the longest waterline dimension), W_i is the waterline width (the waterline dimension perpendicular to L_i), H_i is the maximum height above the water surface, and a_i is a shape coefficient, approximately 300 kg/m^3. Eq. (83) may be applied if only L_i is available, as discussed in reference [8]. The inertia properties of the iceberg can only be obtained if the underwater profile is known. A sonar system could be used to detect it, as shown in Fig. 14.

It may be convenient to define a simplified, equivalent iceberg shape first to investigate the ship–iceberg collision. A cone-shaped iceberg is proposed, in which only the waterline length and height are needed because these two parameters are quite easy to obtain by field measurements; see Fig. 15. The suggested shape consists of two cones, one for the above water part and one for the submerged volume.

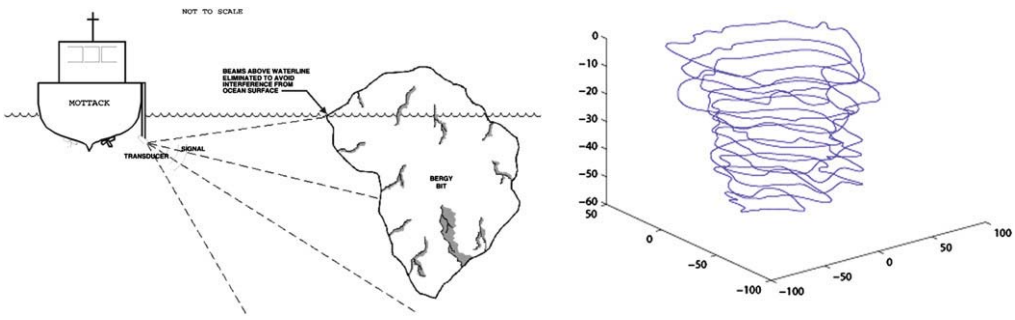

Fig. 14. Sonar mounting configuration (left) and underwater profiles of iceberg (right), after Ralph et al. [8].

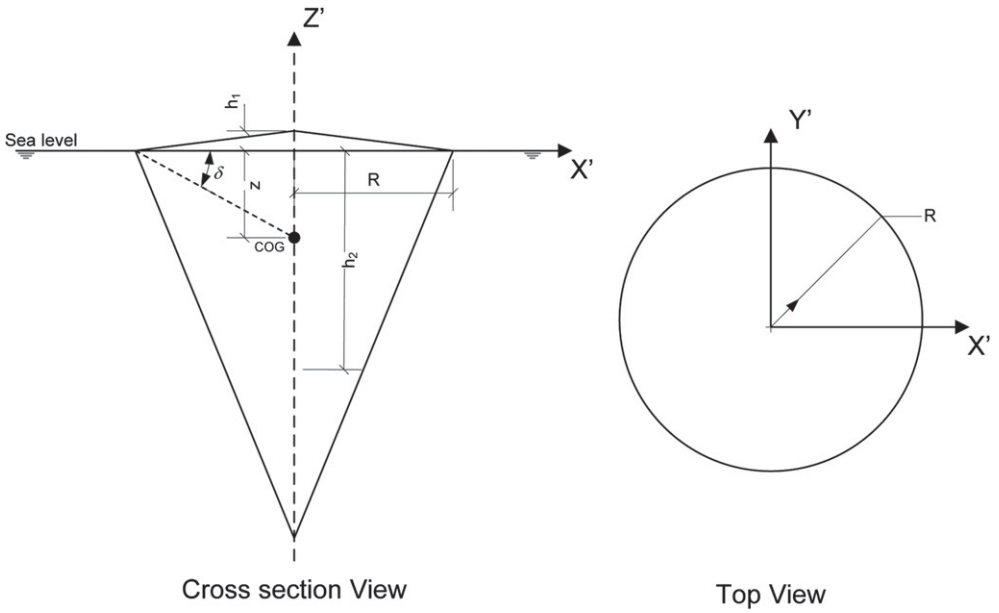

Fig. 15. Simplified iceberg shape.

For this shape the following relationships apply:

$$k = \frac{h_1}{h_2} = \frac{\rho_w - \rho_i}{\rho_i} \tag{84}$$

$$z = \frac{h_2 - h_1}{4} = \frac{h_1(1-k)}{4k} \tag{85}$$

$$\widehat{R}_{zz}^2 = \frac{3}{10}R^2 \tag{86}$$

$$\widehat{R}_{xx}^2 = \widehat{R}_{yy}^2 = \frac{3}{20(1+k)}\left(\left(k+1\right)R^2 + \frac{h_1^2}{4}\left(k+\frac{1}{k^2}\right)\right) + \frac{h_1^2}{16k} \tag{87}$$

where k is the ratio between the height h_1 and draft h_2 of the iceberg, z is the vertical distance from the COG to the waterline, $\widehat{R}_{xx}, \widehat{R}_{yy}, \widehat{R}_{zz}$ are the radii of gyration for the roll, pitch and yaw motions, respectively, and R is the radius of the cross section at sea level. The block coefficient of the present shape is given by $f_b = \pi/12 = 0.26$ according to Eq. (82), which is in agreement with reference [8]. It has to be noted that this simplified shape is not valid for dry-dock icebergs.

Assume an oil tanker collides with an iceberg with the shape defined above; see Fig. 16. The main dimensions are listed in Table 5. Appendix B shows the details for the added mass factors and inertial radii for the striking ship. The empirical equations for the assessment of the added mass of the iceberg are not available. In lieu of this an averaged value of 0.5 is adopted [14], and a further sensitivity study will be presented. The ship is assumed to travel with a speed of 4.5 m/s, while the iceberg has zero speed. The COG of the ship is assumed to be 8.5 m below the waterline, which is $\widehat{r}_z = 8.5$ m. The relative vertical distance from the collision point to the COG of the ship has a minor impact on the energy dissipation because the collision happens at the bow area, as discussed before. The COG of

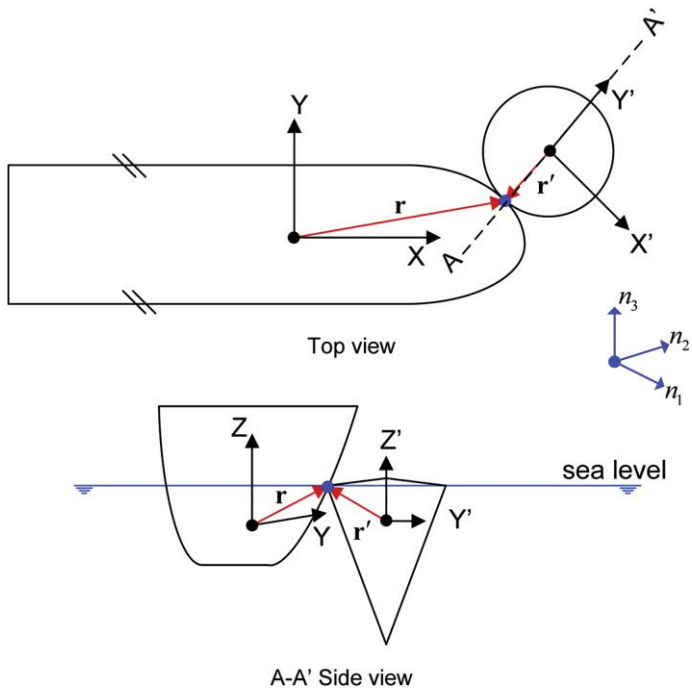

Fig. 16. Collision scenario and the main dimensions.

the iceberg is calculated as $\widehat{r}'_z = z = h_1(1-k)/4k$; see Eq. (85). The waterline angle obeys $\alpha = 30^\circ$ and $\theta = \alpha$; see Fig. 16. The friction between the ice and steel is set at 0.15. According to these settings, the calculated total dissipated energy is 5.06 MJ.

A sensitivity study is carried out for the uncertain added mass factor for the iceberg. κ is introduced to describe the relative magnitude of the parameter in question. The relative amount of energy dissipation is plotted in Fig. 17. It is observed that the added mass in the normal direction of tangential plane $\widehat{m}'_y$ influences the results considerably, while the other parameters have a moderate influence.

It is further interesting to see how the energy dissipation ratio depends on the normal frame angle β' as a function of the iceberg mass. According to McKenna [15], the following relationship between h_1 and R may be further assumed:

$$h_1 = \frac{1}{2}R \tag{88}$$

By letting R vary from 1.5 m to 15 m the mass increases from 3 t to 13,000 t, which is in the bergy bit size domain and is of great interest. In practice, the waterline angle α may typically be in the range of 30°, while the normal frame angle β' might vary considerably. The results are displayed in Fig. 18. The

Table 5
Main dimensions.

Ship		Iceberg	
Height	$H = 22$ m	Height over sea level	$h_1 = 3.75$ m
Length	$L = 256.50$ m	Radius	$R = 7.5$ m
Breadth	$B = 42.5$ m	Water density	$\rho_w = 1025$ kg/m^3
Draft	$T = 17$ m	Ice density:	$\rho_i = 900$ kg/m^3
Mass	$M_{ship} = 151{,}000$ t	Mass	$M_{iceberg} = 1630$ t

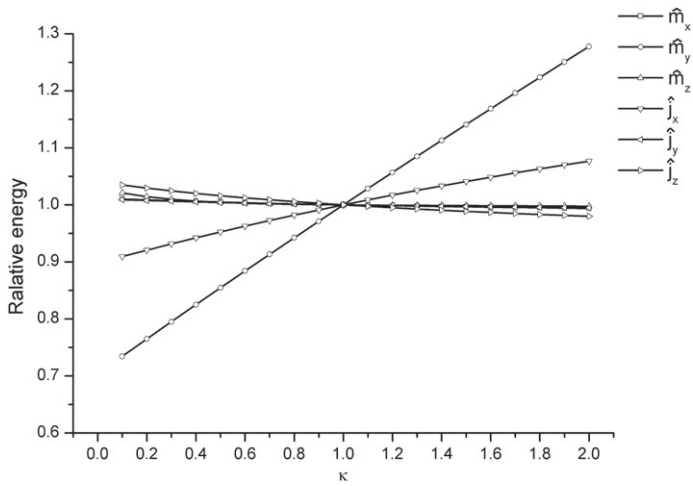

Fig. 17. Sensitivity of energy dissipation with respect to added mass values.

energy dissipation is normalised versus the maximum possible energy dissipation E_0, associated with a central, plastic impact as given in reference [16]:

$$E_0 = \frac{1}{2} M_{iceberg} \hat{v}_{ship}^2 \frac{\left(1 - \frac{\hat{v}_{ice}}{\hat{v}_{ship}}\right)^2}{1 + \frac{M_{iceberg}}{M_{ship}}} \tag{89}$$

where $\hat{v}_{\text{ship}}, \hat{v}_{\text{ice}}$ are velocities under the global coordinate system of ship and iceberg respectively, M_{ship} is the mass of ship. In Eq. (89) the masses include the appropriate added masses. The method from Pedersen and Zhang is also included in the figure. It is observed that a very large normal frame angle β' is favourable with respect to small energy dissipation for the given iceberg shape. As

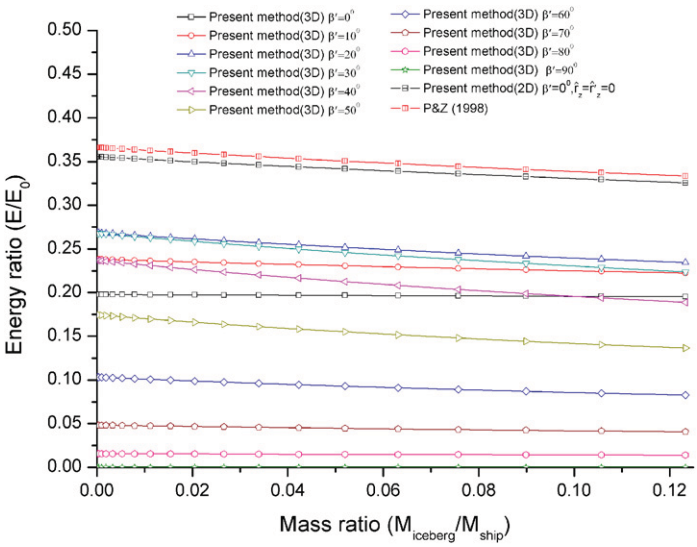

Fig. 18. Energy ratio and mass ratio relationship.

β' decreases, the energy dissipation increases and attains a maximum for $\beta' = 20^\circ$ to 30°. Fig. 18 shows that the 3D method produces a smaller energy ratio than the 2D method, which is expected because the 3D method allows transfer of the kinetic energy into motion components in all 6DOFs. The 2D method proposed by Pedersen and Zhang is quite conservative in this case.

The "worst" frame angle for the present scenario is between 20° and 30°. Eq. (49) shows that the "worst" angle is governed by the equivalent mass $\overline{m}_i$ and the change of the relative velocity squared Δv_i^2. The frame angle influences both parameters. The equivalent mass takes on a maximum value when the collision force is oriented through the COG and eliminates roll motion. Assuming the friction force to be small, the maximum value occurs when

$$\delta = a\tan\left(\frac{z}{R}\right) = a\tan\left(\frac{h_1(1-k)}{4Rk}\right) \tag{90}$$

According to Eq. (88) and Table 1, $\delta = 37.8^\circ \equiv \beta'$ is obtained. The change of relative velocity squared Δv_i^2 increases for decreasing frame angles, such that the combined effect of the two parameters produces the "worst" angle of 20° to 30°.

7. Conclusions

A new 3D formulation for the analysis of the external mechanics of ship collisions is presented, and it is successfully applied to the analysis of ship–iceberg and ship–ship collisions. The 3D method is compared with the 2D method proposed by Pedersen and Zhang for various collision cases. The conclusions are as follows:

- The present theory is capable of solving 2D problems. It degenerates to the 2D method by assuming the ship side to be vertical and neglecting the vertical eccentricity of the contact point with respect to the centre of gravity of the ship. In this case, only sway, surge and yaw motion are considered.
- Excellent agreement is obtained with the 2D method for ship–ship collisions when vertical eccentricity exciting roll motion is neglected.
- It is found that the energy ratio to be dissipated as strain energy is significantly influenced by vertical eccentricity when the collision takes place amidships. If the collision is located close to the ship's bow or stern, the influence is overshadowed by longitudinal eccentricity exciting yaw motion.
- Analysis of ship–iceberg collisions shows that the 2D theory may produce very conservative values for the energy ratio.
- The normal frame angle of the ship influences the energy ratio significantly. It is found that the "worst" frame angle for the iceberg collision scenario analysed is in the range of $20^\circ$to 30°.

Acknowledgement

The present work is carried out within the scope of the Strategic University Programme (SUP) "ScenaRisC&G" at the Norwegian University of Science and Technology (NTNU), which is funded by the Research Council of Norway (NFR). The authors wish to thank the Research Council of Norway for the funding of the study. The authors extend also their gratitude to Dr. McKenna and Prof. Daley in Canada for useful discussions.

Appendix A. Usage of the transformation matrix

Mass matrix

The mass matrices for objects A and B under the local coordinate system are obtained as follows:

$$M_{ij} = T_{lg}\widehat{M}_{ij}T_{lg}^T \tag{A.1}$$

$$M'_{ij} = T'_{lg}\widehat{M}'_{ij}T'^{T}_{lg} \tag{A.2}$$

where $\widehat{M}_{ij}$ and $\widehat{M}'_{ij}$ are the mass matrices for objects A and B in the global coordinate system, respectively. Taking the ships as an example, the mass matrices for the ships are

$$\widehat{M}_{ij} = \begin{bmatrix} 1+\widehat{m}_x & 0 & 0 \\ 0 & 1+\widehat{m}_y & 0 \\ 0 & 0 & 1+\widehat{m}_z \end{bmatrix} M,\ \widehat{M}'_{ij} = \begin{bmatrix} 1+\widehat{m}'_x & 0 & 0 \\ 0 & 1+\widehat{m}'_y & 0 \\ 0 & 0 & 1+\widehat{m}'_z \end{bmatrix} M'$$

where $\widehat{m}_x, \widehat{m}_y, \widehat{m}_z$ and $\widehat{m}'_x, \widehat{m}'_y, \widehat{m}'_z$ are the added mass factors, and M and M' are the masses for ship A and ship B, respectively.

Inertia matrix

The inertia matrices under the local coordinate system are obtained as follows:

$$I_{ij} = T_{lg}\widehat{I}_{ij}T^{T}_{lg} \tag{A.3}$$

$$I'_{ij} = T'_{lg}\widehat{I}'_{ij}T'^{T}_{lg} \tag{A.4}$$

For ships, the inertia matrices, $\widehat{I}_{ij}$ and $\widehat{I}'_{ij}$, under the global coordinate system might be written as follows due to symmetry.

$$\widehat{I}_{ij} = \begin{bmatrix} \left(1+\widehat{j}_{xx}\right)\widehat{R}^2_{xx} & 0 & -\widehat{I}_{13}/M \\ 0 & \left(1+\widehat{j}_{yy}\right)\widehat{R}^2_{yy} & 0 \\ -\widehat{I}_{13}/M & 0 & \left(1+\widehat{j}_{zz}\right)\widehat{R}^2_{zz} \end{bmatrix} M$$

$$\widehat{I}'_{ij} = \begin{bmatrix} \left(1+\widehat{j}'_{xx}\right)\widehat{R}'^2_{xx} & 0 & -\widehat{I}'_{13}/M \\ 0 & \left(1+\widehat{j}'_{yy}\right)\widehat{R}'^2_{yy} & 0 \\ -\widehat{I}'_{13}/M & 0 & \left(1+\widehat{j}'_{zz}\right)\widehat{R}'^2_{zz} \end{bmatrix} M'$$

where $\widehat{j}_{xx}, \widehat{j}_{yy}, \widehat{j}_{zz}$ (and $\widehat{j}'_{xx}, \widehat{j}'_{yy}, \widehat{j}'_{zz}$) are added mass factors, and $\widehat{R}_{xx}, \widehat{R}_{yy}, \widehat{R}_{zz}$ (and $\widehat{R}'_{xx}, \widehat{R}'_{yy}, \widehat{R}'_{zz}$) are the radii of gyration for roll, pitch and yaw, respectively. The only product of inertia that appears is $\widehat{I}_{13}(\widehat{I}'_{13})$, which will vanish if the ship has fore-and-aft symmetry and is small otherwise (see Salvesen et al. [9]).

Direction vector

$$\mathbf{r} = T_{lg}\widehat{\mathbf{r}} \tag{A.5}$$

$$\mathbf{r}' = T'_{lg}\widehat{\mathbf{r}}' \tag{A.6}$$

where $\widehat{\mathbf{r}}$ and $\widehat{\mathbf{r}}'$ are the direction vectors from the COG to the impact point in the global coordinate system for objects A and B, respectively, e.g., $\widehat{\mathbf{r}} = [\,\widehat{r}_x \quad \widehat{r}_y \quad \widehat{r}_z\,]^T$. $\boldsymbol{r}$ and $\mathbf{r}'$ are the corresponding direction vectors under the local coordinate system, e.g., $\mathbf{r} = [\,r_x \quad r_y \quad r_z\,]^T$.

Relative velocity

$$\mathbf{v} = T_{lg}\widehat{\mathbf{v}} \tag{A.7}$$

$$\mathbf{v}' = T'_{\mathrm{lg}}\widehat{\mathbf{v}}' \tag{A.8}$$

where $\widehat{\mathbf{v}}, \widehat{\mathbf{v}}'$ are the relative velocity vectors between objects A and B under the global coordinate system, respectively, e.g., $\widehat{\mathbf{v}} = [\,\widehat{v}_x \quad \widehat{v}_y \quad \widehat{v}_z\,]^T$. $\boldsymbol{v}, \boldsymbol{v}'$ are the corresponding relative velocity vectors under the local coordinate system, e.g., $\mathbf{v} = [\,v_x \quad v_y \quad v_z\,]^T$.

Appendix B. The empirical equation from Popov

In order to investigate the ice loads exerted on the ship structure, Popov et al. [5] derived a series of empirical equation to assess the added mass factor and radius of gyration for ships.

$$\widehat{m}_x = 0 \tag{B.1}$$

$$\widehat{m}_y = 2T/B \tag{B.2}$$

$$\widehat{m}_z = 2/3\left(BC_{wp}^2\right)/\left(TC_b\left(1+C_{wp}\right)\right) \tag{B.3}$$

$$\widehat{j}_{xx} = 0.25 \tag{B.4}$$

$$\widehat{j}_{yy} = B/\left(T\left(3-2C_{wp}\right)\left(3-C_{wp}\right)\right) \tag{B.5}$$

$$\widehat{j}_{zz} = 0.3 + 0.05L/B \tag{B.6}$$

$$\widehat{R}_{xx}^2 = C_{wp}B^2/(11.4C_m) + H^2/12 \tag{B.7}$$

$$\widehat{R}_{yy}^2 = 0.07C_{wp}L^2 \tag{B.8}$$

$$\widehat{R}_{zz}^2 = L^2/16 \tag{B.9}$$

where T is the height, B is the width, L is the length, C_{wp} is the water plane coefficient, C_{b} is the block coefficient, and C_{m} is midship section coefficient.

References

[1] Pedersen PT, Zhang S. On impact mechanics in ship collisions. J Mar Struct 1998;11(10):429–49.
[2] Cammaert AB, Tsinker GP. Impact of large ice floes and icebergs on marine structures. In: International conference on port and ocean engineering under Arctic conditions, Quebec; 1981.
[3] Matskevitch DG. Eccentric impact of an ice feature: linearized model. Cold Reg Sci Technol 1997;25(3):159–71.
[4] Matskevitch DG. Eccentric impact of an ice feature: non-linear model. Cold Reg Sci Technol 1997;26(1):55–66.
[5] Popov YN, Faddeev OV, et al. Strength of ships sailing in ice. Leningrad: Sudostroyeniye Publishing House; 1969. 227 pp.
[6] Johnston M, Timco GW, et al. Measuring global impact forces on the CCGS Terry Fox with an inertial measurement system called MOTAN. Reg Sci Technol 2008;52(1):67–82.
[7] Stronge WJ. Impact mechanics. Cambridge: Cambridge University Press; 2004. 304 pp.
[8] Ralph F, McKenna R, Gagnon R. Iceberg characterization for the bergy bit impact study. Cold Reg Sci Technol 2008;52(1):7–28.
[9] Salvesen N, Tuck EO, Faltinsen O. Ship motions and sea loads. In: The annual meeting of the society of naval architects and marine engineers, New York; 1970.
[10] DNV. Rules for classification of ships. Pt 5, Ch 1. In: Ships for navigation in ice. Høvik; 2009.
[11] Daley CG. Energy based ice collision forces. In: International conference on port and ocean engineering under Arctic conditions, Espoo; 1999.
[12] Johnson KL. Contact mechanics. Cambridge: Cambridge University Press; 1985. 468 pp.
[13] Tabri K, Varsta P, Matusiak J. Numerical and experimental motion simulations of nonsymmetric ship collisions. J Mar Sci Technol 2009;15(1):87–101.
[14] Bass DW, Sen D. Added mass and damping coefficient for certain `realistic' iceberg models. Cold Reg Sci Technol 1986;12(2):163–74.
[15] McKenna R. Refinement of iceberg shape characterization for risk to grand banks installations. PERD/CHC Report 20-77; 2005.
[16] Norsok Standard N-004. Design of steel structures, Appendix A, Design against accidental actions, Oslo, Norway; 2004. p. 88.

PAPER II

Liu Z., Amdahl J and Løset S.

Plasticity based material modelling of ice and its application to ship-iceberg impacts

Published in:

Cold Regions Science and Technology

Volume 65, Issue 3, Pages 326-334, 2011.

Cold Regions Science and Technology 65 (2011) 326–334

Contents lists available at ScienceDirect

Cold Regions Science and Technology

journal homepage: www.elsevier.com/locate/coldregions

Plasticity based material modelling of ice and its application to ship–iceberg impacts

Zhenhui Liu *, Jørgen Amdahl, Sveinung Løset

Norwegian University of Science and Technology, Trondheim, Norway

ARTICLE INFO

Article history:
Received 11 May 2010
Accepted 9 October 2010

Keywords:
Plasticity
Numeric simulation
Material modelling
Shared-energy design
Iceberg impacts

ABSTRACT

The present paper considers numerical modelling of ship–iceberg collisions with emphasis on material modelling. A material model is proposed for ice. The model is pressure-dependent and strain rate-independent. The so called *Tsai-Wu* yield surface envelop is adopted, and plastic flow theory is used to derive the constitutive relationships. The ice is assumed to be isotropic, the temperature profile of icebergs is considered in the present model, and the influence of strain rate is discussed. A user-defined failure criterion is proposed; the criterion is based on effective plastic strain and hydrostatic pressure and enables crack initiation and damage evolution. The material model has been simulated using the commercial code LS-DYNA. Both local and global contact pressures have been investigated. Numerical examples show that the present model produces reasonably good results. It is applied to integrated analysis of iceberg impacts for the Accidental Limit State. Results from simulations of a head-on collision between a ship bow and icebergs are presented and discussed with respect to validity.

1. Introduction

Due to climate change, the melting speed of large glaciers both in Arctic and Antarctic regions has been accelerating, which may cause increased glacial surge and thus higher iceberg production. Increased ship traffic in these waters enhances the probability of ship and iceberg collisions, which necessitates assessment of the consequences of these collisions. In the limit state design format, loads from rare iceberg impacts can be characterized as an *Abnormal Level Ice Event* (*ALIE*) (see ISO/CD 19906, 2010), which corresponds to the *Accidental Limit State* (*ALS*) in modern codes for offshore structures. As indicated by the *ALIE* (or *ALS*) format, gross damage may occur, but the structure shall survive, preventing a cargo spill and any associated pollution. According to the NORSOK code (NORSOK, 2004), when a structure is designed according to the *ALS* format there may be distinguished between three different strategies; *Ductility design*, *Shared-energy design* and *Strength design* (Fig. 1).

Strength design implies that the structure is capable of crushing the ice with moderate structural deformations. Hence, the structure must resist the maximum pressure the ice will apply over the contact area and leads typically to pressure–area relationships specified for *Ultimate Limit State* (*ULS*) design or *Extreme Level Ice Events* (*ELIE*). The designer is free to adopt this approach for *ALIE*, but this may often yield excessive structural dimensions.

Ductility design implies that the structure has to dissipate the required level of strain energy in the collision, whereas the iceberg remains undamaged and may be treated as a rigid body. This strategy simplifies the analysis largely, but it may place heavy demands on the deformability and ductility of the structure; for a tanker the breadth of the (ballast) wing tanks may have to be increased substantially to avoid penetration of cargo tanks.

Shared-energy design implies that both the structure and the iceberg dissipate strain energy by undergoing significant deformations. The approach is extremely challenging, because the deformation of the ship and iceberg depends of their mutual behaviour; the resistance of the structure at a given time step depends upon the load from the iceberg and vice verse. Generally, the "softer" of the ship and the iceberg will deform, and the relative strength may change significantly during the impact. In order to facilitate such analysis a realistic continuum mechanics model of the ice is required. The purpose of this paper is to develop and verify an iceberg material model to be adopted in *Shared-energy design*.

Since ice is a very complicated material the ambition is not to develop a material model which captures the behaviour of ice in "all" respects. If the model with simple inputs is capable of predicting reasonable pressure–area relationships in the case of *Strength design* it is considered to be sufficiently accurate to be used in *Shared-energy design*.

Ice material models for Finite Element Method (*FEM*) simulation are not well established. Carney et al. (2006) presented an ice model for high strain rate ice impacts that is designed for very high velocity collisions (in the order of 100 m/s). Gagnon (2008) simulated growler impacts to ships by using a so called '*crushable foam*' material model to simulate the ice behaviour; the model was developed by Hallquist (2007). However, input for the '*crushable foam*' model suffers from lack of physical explanation. Further, ice cracks and damage are not

* Corresponding author. Tel.: +47 735 50586; fax: +47 735 95528.
E-mail address: zhenhui.liu@ntnu.no (Z. Liu).

0165-232X/$ – see front matter © 2010 Elsevier B.V. All rights reserved.
doi:10.1016/j.coldregions.2010.10.005

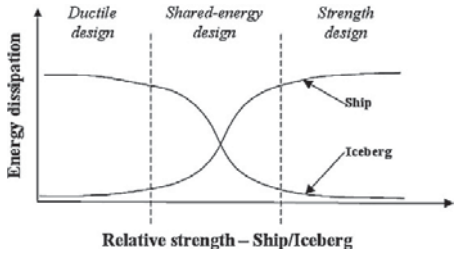

Fig. 1. Strength, ductility and shared-energy design in *ALS* design.

considered. In the present paper, a simple plastic model is proposed; this model is based on data from triaxial experiments and describes the material behaviour during iceberg impacts reasonably well.

In nature, ice exists at high temperature states (i.e., close to its melting point, where the homologous temperature is close to 1). The strain–stress behaviour of ice is strain rate- and temperature-dependent. Developing a complete ice material model that considers all scenarios of ice/structure interactions for all types of ice conditions is not realistic. In this study, application of the proposed ice model is limited to iceberg impact scenarios. Contrary to sea ice, iceberg ice may reasonably be considered as isotropic (Sanderson, 1988). The temperature and strain rate influence on iceberg strength are discussed. The difference in strength between the tensile and compression states is described by using a cut-off pressure p_{cut}.

The Lagrange finite method is considered here. A common way to simulate failure is to use the '*erosion*' technique. Elements violating the failure criterion are deleted. Erosion is an easy and efficient procedure and is employed in the present work. Prior experience has shown that '*erosion*' does not simulate elastic, brittle failure very well due to stress wave issues (Liu et al., 2009). Therefore, the ice is assumed to be elastic-perfect plastic. The yield surface is obtained by using curves fitting to the triaxial experimental data. An empirical, user-defined element failure criterion based on stress state and effective plastic strain is introduced. In this manner, a quasi-brittle material model is proposed and successfully simulated using the commercial code LS-DYNA 971.

2. Iceberg yield surface

According to elastic–plastic theory, the constitutive equations describing the strain–stress relationship can be derived from the yield surface formulation and the selected flow rule. The yield surface is usually formulated as an algebraic combination of the invariants of the stress tensor σ_{ij}. In the case of iceberg impact, ice particles in the center contact area are significantly confined from neighbouring particles. This means that the ice is in a triaxial stress state. In this sense, triaxial experiments should be carried out prior to adopting a suitable yield surface. The common method of *triaxial loading* experiments is to subject ice samples to a pressurized fluid and then to apply an additional axial load while holding constant the fluid pressure, e.g. Jones (1982), Durham et al. (1983), Rist and Murrell (1994), Gagnon and Gammon (1995), Sammonds et al. (1998) and Melanson et al. (1999). There are also other methods called *true triaxial loading*, as summarized in the book by Schulson and Duval (2009). The experiment data sets as mentioned are usually present in the formation of stress and strain or the differential stress and confining pressure relationship. In the present paper, only the data obtained by Gagnon and Gammon (1995) are picked up and discussed in following part of this paper.

Gagnon and Gammon (1995) carried out triaxial experiments with iceberg and glacier ice. Triaxial tests were conducted on cylindrical samples with strain rates ranging from $4\cdot10^{-5}s^{-1}$ to $2.7\cdot10^{-1}s^{-1}$ and confining pressure ranging from 0 to 13.8 MPa. Temperature was varied and chosen as −1, −6, −11, or −16 °C. Even though the available experimental data covered a limited span of hydrostatic pressures, an elliptical yield envelop for the iceberg (similar to that proposed by Nadreau) is proposed as by Derradji-Aouat (2000):

$$\left(\frac{\tau-\eta}{\tau_{\max}}\right)^2+\left(\frac{p-\lambda}{p_c}\right)^2=1 \tag{1}$$

where η, $\tau_{\max}$, λ, and p_c are constants,$\tau=\sqrt{\frac{s_{ij}:s_{ij}}{3}}$ is the octahedral stress s_{ij} is the deviatoric stress tensor and p is the hydrostatic pressure. Mathematically, the yield surface proposed by Derradji-Aouat (2000) is the same as the so called '*Tsai-Wu*' yield surface for the condition $\eta=0$ (see Appendix A). Fig. 9 shows the yield surface shape in $p-J_2$ space proposed by Derradji-Aouat for iceberg ice at a temperature of −11 °C. It has been used to model ice mechanics for years (Kierkegaard, 1993; Liukkonen and Kivimaa, 1991; Løset and Kvamsdal, 1994; Riska and Frederking, 1987). However, it has not been applied to integrated *FEM* simulation of ship–iceberg impacts. For an isotropic material, it is usually written in following form:

$$f(p,q)=q-\sqrt{a_0+a_1p+a_2p^2} \tag{2}$$

where $p=\frac{\sigma_{kk}}{3}=\frac{I_1}{3}$ is the hydrostatic pressure, $q=\frac{3}{2}\sqrt{s_{ij}:s_{ij}}$ is the Von Mises stress, and a_2, a_1, and a_0 are constants that require fitting to triaxial experimental data. In the present work, the elliptical yield surface is adopted to describe iceberg behaviour. In order to make the implementation convenient, the *Tsai-Wu* yield surface is rewritten in $p-J_2$ space as follows:

$$f(p,J_2)=J_2-\left(a_0+a_1p+a_2p^2\right)=0 \tag{3}$$

where J_2 is the second invariant of deviatoric stress tensor. Fig. 2 shows a comparison of the recommended inputs based on various data sources in $p-J_2$ space. It is seen that there are big differences existing which are due to the different data sources and the fitting methods used to approach the experimental data sets.

3. Temperature profile discussion

Løset (1993) has performed a comprehensive study on the temperature profile of icebergs. This study found that for icebergs at

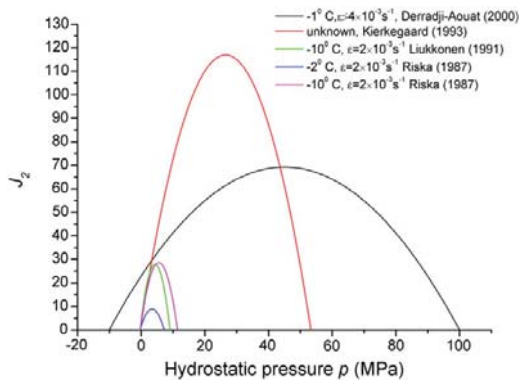

Fig. 2. Illustration of *Tsai-Wu* yield surface in $p-J_2$space.

sea, there is a temperature gradient from the surface to the core region due to the low thermal conductivity of ice. Within the submerged part of the iceberg, ablation during the late winter, spring and summer seasons gives rise to a steep gradient that reaches the core temperature approximately 3 m into the ice. The corresponding change in strength of the ice can be considered in the following way:

$$f(p,J_2) = J_2 - \left(a_0(T) + a_1(T)p + a_2(T)p^2\right) = 0 \tag{4}$$

where T is the temperature. Linear interpolation may be used for elements between the surface and core area. The temperature gradient consideration has been incorporated into the material model using the computer code LS-DYNA.

4. Strain rate effects

Gagnon and Gammon (1995) found that the iceberg strength increases with increasing strain rate (up to $5\cdot10^{-3}s^{-1}$). However, ice tested at a strain rate of $50\cdot10^{-3}s^{-1}$ has lower strength than ice tested at $5\cdot10^{-3}s^{-1}$. Derradji-Aouat (2000) concluded that the yield envelope of the iceberg under various strain rates expands to a maximum size and then contracts. This indicates that the strength of iceberg ice decreases at high strain rates (those larger than $3\cdot10^{-3}s^{-1}$). But it is not yet clear whether there is a limit or whether the iceberg strength will decrease indefinitely. More experimental data are needed to draw firm conclusions regarding this matter. There is perhaps a slight indication from the work performed by Jones (2007), even though this work only deals with the uniaxial compressive strength of iceberg ice. However, the data are too few and too scattered to draw any meaningful conclusion.

By using an explicit code such as LS-DYNA in conjunction with numerical simulation of a ship and iceberg impact, the strain rate may be calculated by the following equation:

$$\dot{\varepsilon}_v = \frac{d\varepsilon_v}{dt} \tag{5}$$

where $\dot{\varepsilon}_v$ is the volumetric strain rate, $d\,\varepsilon_v$ is the increase in volumetric strain and d t is the time step. d t is dependent on the element mesh size as well as sound wave speed (Hallquist, 2007) and d ε_v is dependent on the impact velocity and geometry of distorted elements. Trial numerical simulations show that the strain rate spans from $4\cdot10^{-3}s^{-1}$ to $4\cdot10^{-1}s^{-1}$ with impact velocities from 85 mm/s to 10 m/s for a mesh size of 50 mm × 50 mm × 50 mm. This indicates that the ship and iceberg impact probably involves high strain rates (those larger than $1\cdot10^{-3}s^{-1}$), where the ice should be in a brittle failure mode. This conclusion is in agreement with the suggestions given by Derradji-Aouat and Lau (2005), which is obtained through calculations based on an empirical equation. As discussed before, the lack of experimental data makes it impractical to consider the strain rate in the material model. Thus, the strain rate dependence has not been incorporated into the present model. In lieu of this, a yield envelope representative of high strain rates is used in the following numerical simulations.

5. Failure criterion and numerical examples

The *Tsai-Wu* yield surface has been incorporated into the explicit code LS-DYNA as a user-defined subroutine. The *Cutting Plane Algorithm* is used to map the stress back to the yield surface (Simo and Hughes, 1998). This execution enables introduction of a more advanced failure criterion based on the stress state. Ralston (1980) argued that the apparent stiffness of the ice sample will not change significantly until later in the loading process when the plastic limit load is approached. The key point to consider is how long the stress trajectory travels along the yield surface before failure occurs. Based on this hypothesis, an empirical failure criterion based on effective plastic strain and hydrostatic pressure is proposed here (see Fig. 3).

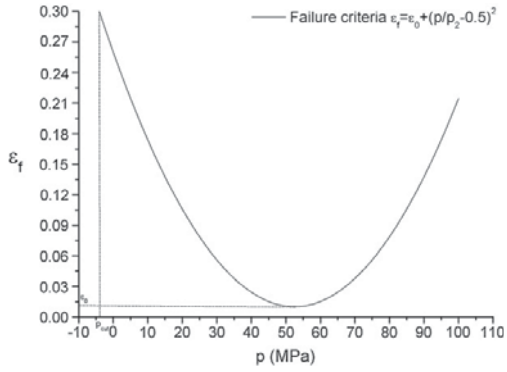

Fig. 3. Illustration of failure criteria curve ($p_2 = 100$ MPa).

$$\varepsilon^p_{eq} = \sqrt{\frac{2}{3}\varepsilon^p_{ij} : \varepsilon^p_{ij}} \tag{6}$$

$$\varepsilon_f = \varepsilon_0 + \left(\frac{p}{p_2} - 0.5\right)^2 \tag{7}$$

where ε^p_{eq} is the equivalent plastic strain, ε^p_{ij} is the plastic strain tensor, ε_f is the failure strain, $\varepsilon_0$is the initial failure strain, which should be adjusted according to experimental data, and p_2 is the larger root of the yield function. If $\varepsilon^p_{eq} > \varepsilon_f$ or the pressure is not greater than the cut-off pressure p_{cut}, erosion is activated. This failure criterion is based on trial and error simulations and is purely empirical. Only one input parameter (ε_0) is needed.

5.1. Numerical study — Case 1: Iceberg collision with rigid wall

This case concerns a conically shaped iceberg colliding with a rigid wall (see Fig. 4). The temperature gradient is not considered in this simulation. During crushing, the pressure–area relationship is recorded. This is performed by considering the average pressure over various contact areas at various stages of deformation. From an *ALS* perspective, this may be a direct measurement of the stiffness of the material model.

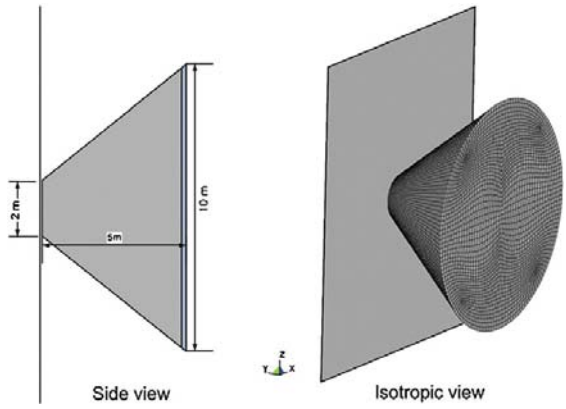

Fig. 4. Iceberg collision with a rigid wall.

Table 1
Input parameters for the iceberg material model.

Items	Derradji-Aouat (2000)	Kierkegaard (1993)	data 1 by Riska and Frederking (1987)	data 2 by Riska and Frederking (1987)
Constant a_0	22.93	2.588	1.60	3.1
Constant a_1	2.06	8.63	4.26	9.20
Constant a_2	−0.023	−0.163	−0.62	−0.83

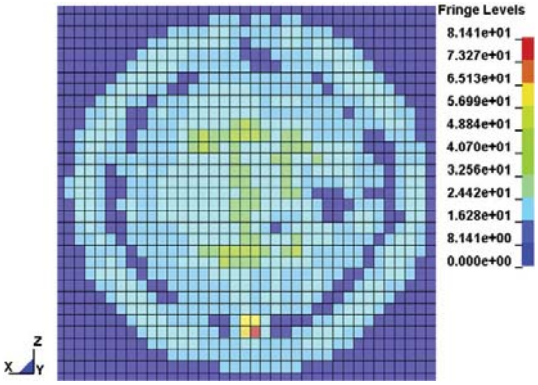

Fig. 5. Example of recorded contact pressure (MPa).

The mesh size for the iceberg is 50 mm × 50 mm × 50 mm. Various yield surfaces have been used and it is listed in Table 1; the initial failure strain is set as 0.01 (1%). The density is set to 900 kg/m^3, Poisson's ratio is 0.3, the elastic modulus is 9.5 GPa and the cut-off pressure for the tensile strength is set to −2 MPa. The corresponding strain rate is greater than $10^{-3}s^{-1}$. The purpose of the present simulation is to obtain the maximum contact pressure within various areas. As shown in Fig. 5, the instantaneous contact pressure varies from 81 MPa to 0 MPa per grid (100 mm × 100 mm).

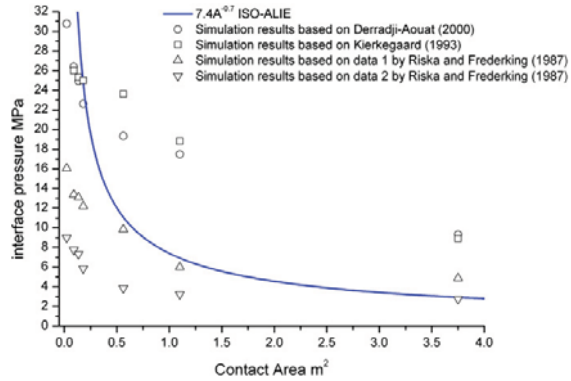

Fig. 7. Recorded maximum pressure versus contact area (based on various input parameters as given in Table 1).

Fig. 6 shows one example of the ice cracking and failure process during the collision simulation. Cracking and crushing evolutions develop in this simulation. Fig. 7 shows the recorded maximum contact pressure versus contact area based on various yield surface inputs (see Table 1). The design curve proposed by Masterson et al. (2007) is plotted for comparison, which is also recommended by the ISO code, ISO/CD 19906 (2010) for the ice loads in *ALIE*. This comparison shows that the yield surface derived by Derradji-Aouat (2000) and Kierkegaard (1993) produces values closest to the pressure curve recommended by ISO/CD 19906 (2010) when the contact area is less than 0.5 m^2. For larger areas, conservative interface pressure is obtained. The data provided by Riska (1987) shows the opposite trend. It should be noted that inputs 1 and 2 as shown in Fig. 14 by Riska and Frederking (1987) are derived from biaxial compression tests of multi-year ice for a temperature of −2 °C and −10 °C, respectively. The Derradji-Aouat (2000) data is recommended when considering the local deformation of ship structure during iceberg impacts. However, if the assessment focuses on global reactions, it is recommended to use inputs based on the Riska and Frederking (1987) data.

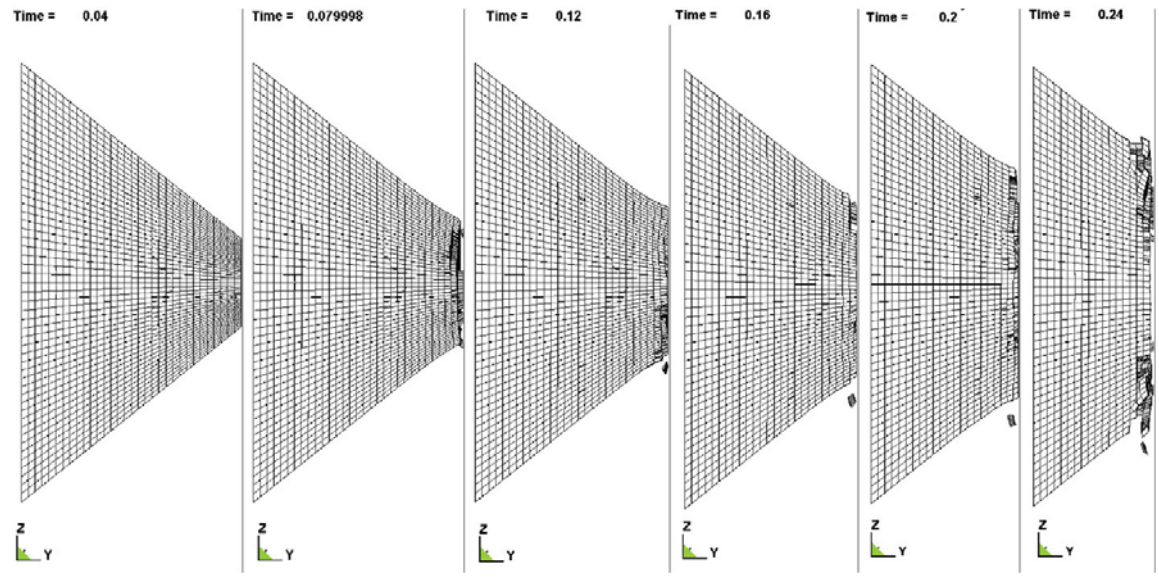

Fig. 6. Numeric simulation of crack and failure of iceberg during collision with rigid wall.

5.2. Numeric Case 2: pond inlet indentor tests

During the fall of 1983 and winter of 1984, a major research project was undertaken by the Hibernia Partners (Mobil, Chevron, Gulf and Petro-Canada) to simulate the results of an iceberg impacting an offshore structure. A total of 21 iceberg impact simulation tests were performed in four tunnels (3 m × 3 m × 15 m) that were dug into an iceberg grounded off the Hamlet of Pond Inlet, Nunavut. Five spherical indenter plates, each with a specified radius of curvature and maximum area of contact, were fabricated for the tests (see Fig. 8). The 3 m^2 test data are available (Daley, 1994).

The ice properties were also tested during the experiment, but no triaxial testing data are available. Therefore, the value proposed by Derradji-Aouat (2000) is used as a reference (see Fig. 9). The strain rate in the experiment was sufficiently high to produce crushing type ice failures in the brittle zone (Johnson, 1987). ε_0 is adjusted by trial and error simulations and set to 0.01 (1%) here. The other input parameters for the material model are the same as those in Case 1. It is not necessary to account for the temperature gradient in this simulation because the experiment is conducted deep within the iceberg.

The *FEM* model of the indenter is a rigid sphere, while the iceberg is modelled with solid elements with one integration point. The center contact area has a fine mesh (50 mm × 50 mm × 50 mm) (see Fig. 10). The denting velocity is controlled by a quarter cosine displacement curve, as used in the experiment. The contact algorithm must take into account the emerging surface that results from the eroded elements. Thus, the ERODING_SURFACE_TO SURFACE contact method with SOFT option 2 is used here (Hallquist, 2007).

The plasticity *flag* is shown in Fig. 11 (*flag* = 1 when yielding occurs, otherwise *flag* = 0). The erosion only occurs if the *flag* equals 1 and the failure criterion is met. Unlike the first example, the crack propagation in this case cannot be simulated since the ice is always well confined. The non-simultaneous failure mechanics are captured (Jordaan, 2001) and the load at various points in time is transmitted through several distinct points.

To investigate the local interface pressure during the denting process, two small patches are chosen which are located at the center bottom of the indentor. One patch is with the size of 100 mm × 100 mm and the other one is 400 mm × 400 mm. The interface pressure is recorded and plotted with denting distance, see Fig. 12. It is seen that the interface pressure can be as high as 35.5 MPa for the first patch and 29.2 MPa for the second. This is less than the results in first numerical case which is probably due to lower denting speed. The interface pressure for both patches is in the form of a sawtooth shape. These two figures show that the present material model is also capable of producing the high pressure zones in the local contact area. The variation in interface pressure may cause dynamic effects in the response of the structure. This has not been pursued in the present study.

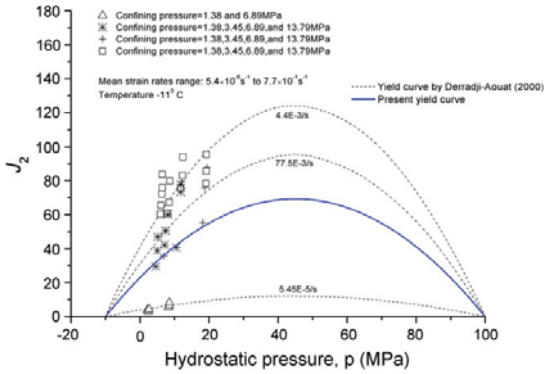

Fig. 9. Elliptical failure curves obtained by using the Gagnon and Gammon triaxial test results for iceberg ice in the $p - J_2$space (Derradji-Aouat, 2000).

Other results of the simulation are presented in terms of pressure versus nominal contact area. The pressure is calculated by dividing the contact force by the nominal contact area, which depends on the penetration distance. Good agreement between simulations and tests is obtained if the contact area is larger than 0.3 m^2 (see Fig. 13). Initially, the simulation predicts a significantly higher pressure than that recorded in the experiments (contact area less than 0.3 m^2). As discussed by Johnson (1987), significant noise in the experimental displacement curves caused difficulty in precisely locating the penetration distance in the beginning of interaction. This may explain the large discrepancies for small contact areas. However, the simple iceberg material model yields promising results and agrees reasonably with the ISO-ALIE design curve.

The mesh size sensitivity is investigated by using four mesh sizes in the center contact area: $100mm \times 100mm \times 100mm$, $80mm \times 80mm \times 80mm$, $50mm \times 50mm \times 50mm$ and $25mm \times 25mm \times 25mm$. Fig. 14 shows that the results from the last two mesh sizes are very close. The 25 mm mesh size is computationally demanding. A trade-off between computation time and accuracy supports a mesh size of $50mm \times 50mm \times 50mm$.

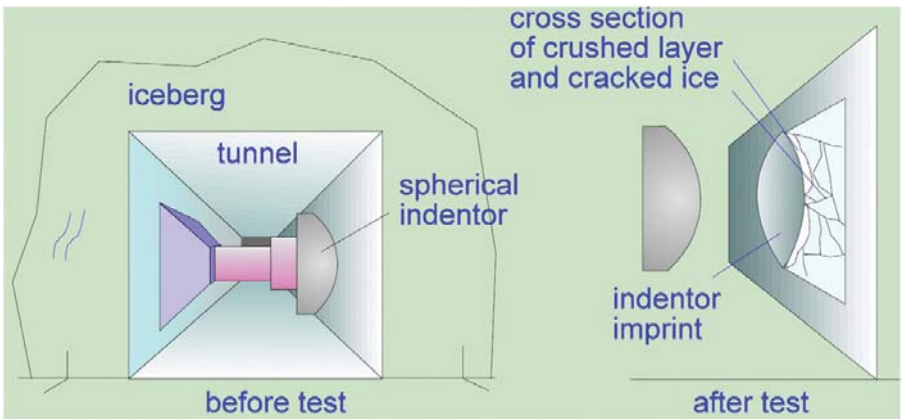

Fig. 8. Sketch of the test arrangement at Pond Inlet, (Daley, 1994).

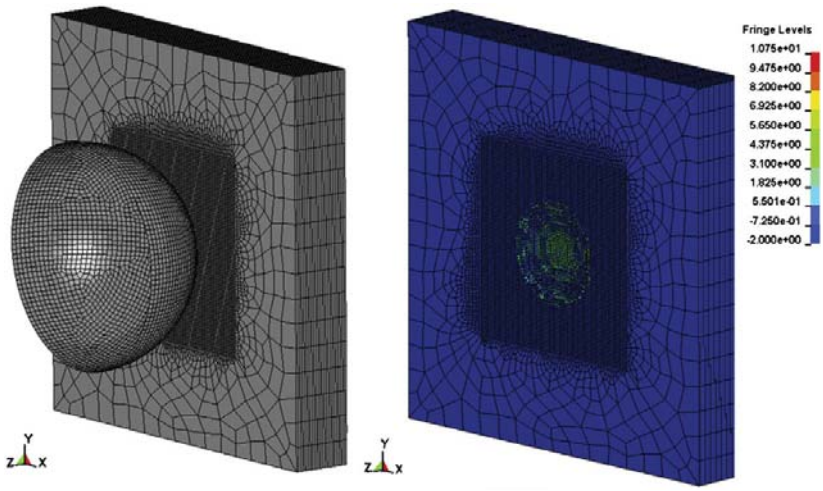

Fig. 10. Numerical model (left) and damaged iceberg with contour of pressure (right).

6. Application to ship bow–iceberg head-on collision

6.1. FEA model set-up

In this section, an integrated analysis of a ship bow–iceberg head-on collision scenario is carried out in order to investigate features of the material model. In the *ALS* design, it is convenient to split the collision scenarios into external mechanics and internal mechanics (Pedersen and Zhang, 1998).The coupling between the external and internal mechanics is the amount of kinetic energy to be dissipated as strain energy. Liu and Amdahl (2010) proposed a new formulation for calculating the ship–iceberg collision. It should be noted that:

$$E_0 = \frac{1}{2} M_{\text{iceberg}} \hat{v}_{\text{ship}}^2 \frac{\left(1 - \frac{\hat{v}_{\text{ice}}}{\hat{v}_{\text{ship}}}\right)^2}{1 + \frac{M_{\text{iceberg}}}{M_{\text{ship}}}} \tag{8}$$

where E_0 is the maximum dissipated energy associated with a central plastic impact, $\hat{v}_{\text{ship}}$ is the velocity of the ship, $\hat{v}_{\text{ice}}$ is the velocity of the

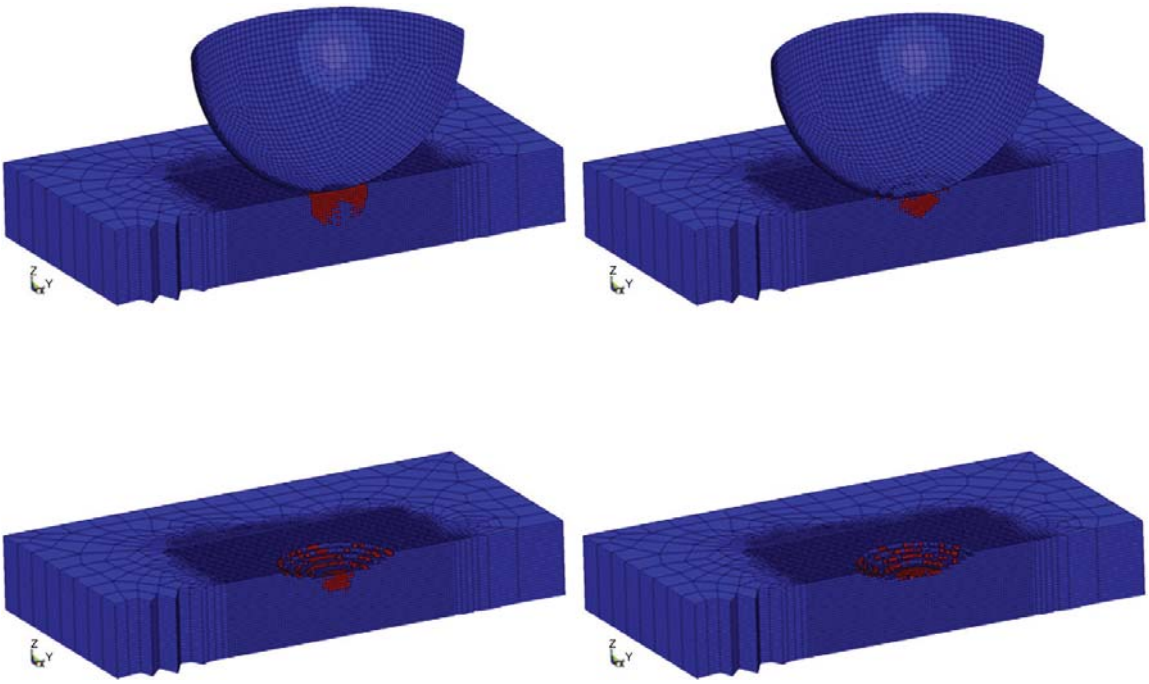

Fig. 11. Detailed numerical simulation at different time (read means *flag=1*).

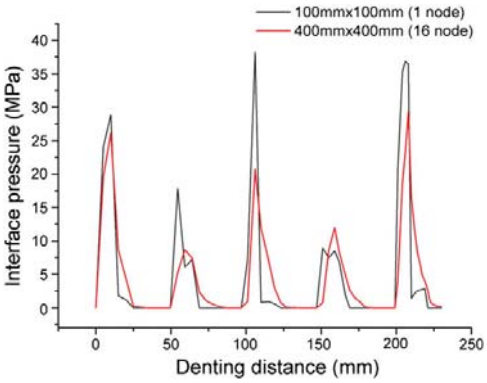

Fig. 12. Average local interface pressure for 100 mm × 100 mm and 400 mm × 400 mm patches.

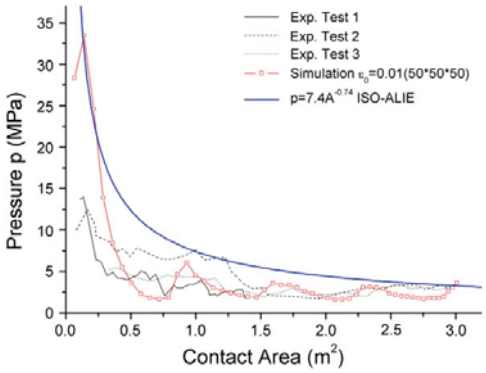

Fig. 13. Numerical results and experimental data (pressure with nominal contact area).

iceberg and $M_{iceberg}$ and M_{ship} are the mass properties of iceberg and ship, respectively. In principle, the added mass should be included, the added mass in surge for ship is set as 0.05 (Popov et al., 1969) and 0.5 for iceberg (Bass and Sen, 1986).

Fig. 15 shows that due to the vertical eccentricity of the contact force, the energy dissipation is slightly different than that of a central plastic impact. For example, consider two scenarios for which the ship

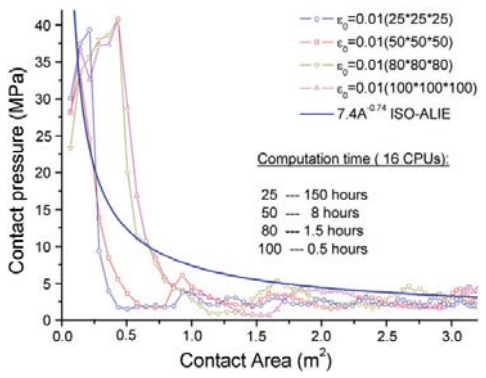

Fig. 14. Effects of mesh size.

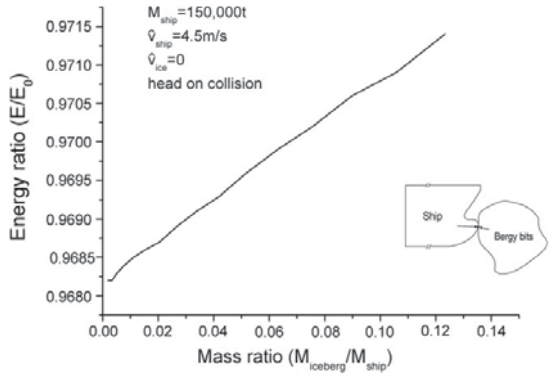

Fig. 15. Energy dissipation ratio versus mass ratio.

has a forward velocity of 4.5 m/s and the iceberg is assumed to be static.

- Scenario A: for a bergy bit with a mass of 1250 t, the dissipated energy is 18.2 MJ;
- Scenario B: for a bergy bit with a mass of 5400 t, the dissipated energy is 75.5 MJ.

Simulating the ship/iceberg collision is significantly simplified by splitting the problem into external and internal mechanics, which saves considerable computation. The integrated analysis concerns the internal mechanics. Only the parts directly involved and the adjacent structure are modelled.

The ship bow belongs to an ice strengthened shuttle tanker with the displacement of 150,000 t. Within the bow area, a detailed finite element model is created. An elastic–plastic kinematical hardening model is used for steel, with has a yield stress of 355 MPa. Fracture of the steel plating is not considered in the present case. The mesh size is typically 120 mm × 120 mm for shell elements of the ship, while the iceberg is meshed with solid elements of size $50mm \times 50mm \times 50mm$, as in the simulations described in the previous section. The temperature gradient has been considered in this case, and the temperature changes from −1 °C to −11 °C over a depth of 3 m (Løset, 1993). The ship bow is travelling with a speed of $4.5m/s$, while the iceberg has zero speed. Collision between the bow and a rigid wall is also carried out. The input parameters for the ice material model are the same as those for the numerical example 2 that was discussed in the previous section.

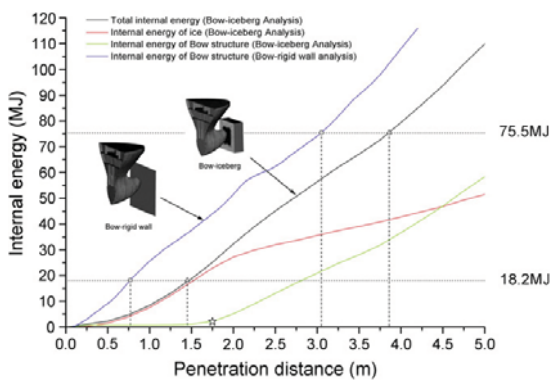

Fig. 16. Internal energy versus penetration distance.

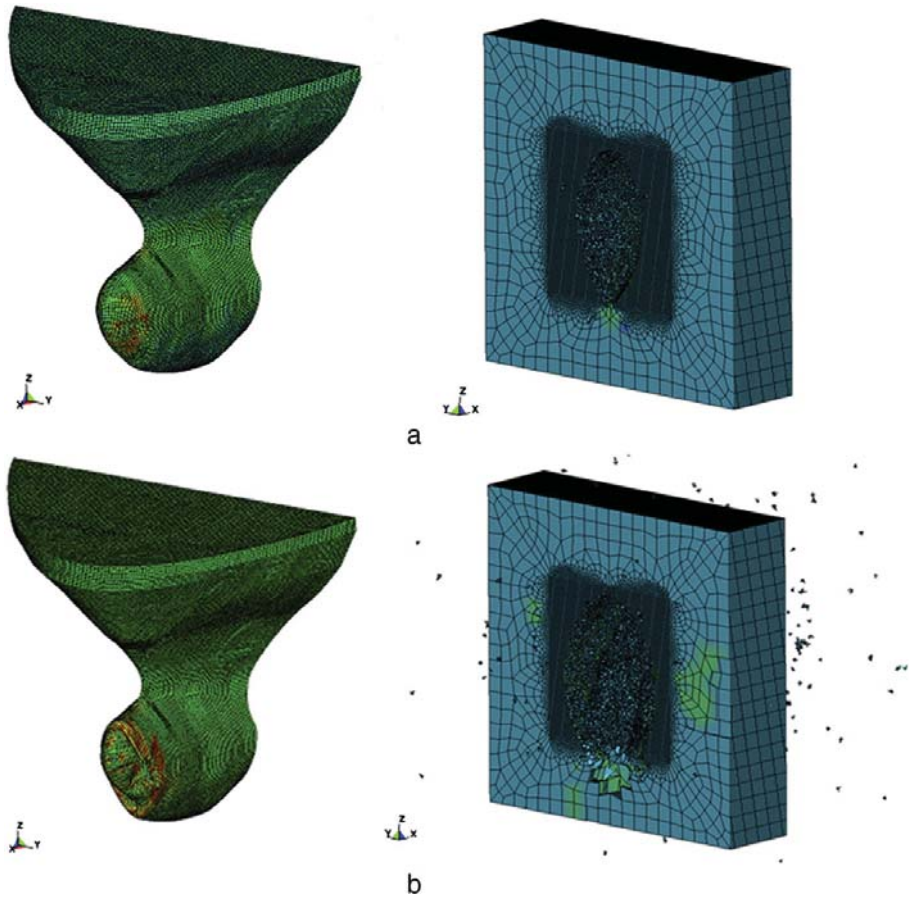

Fig. 17. Bow and iceberg deformation (penetration distance = 1.5 m (a), 3.9 m (b)).

7. Results

The simulation is carried out in the same environment as that used in the previous validations. Fig. 16 shows that the strain energy is dissipated in both the iceberg and the ship structure for the bow collision with iceberg and rigid wall. In scenario A, the penetration distance corresponding to an energy dissipation of 18.2 MJ is 1. 5 m; the ship structure undergoes minor plastic deformations while the iceberg dissipates most of the energy (see Fig. 17(a)). In other words, the ship bow structure is strong enough to crush the iceberg. For scenario B, 75.5 MJ is dissipated for a penetration distance of 3.9 m. Both the ship bow and the iceberg experience large plastic deformations. Ice particles have been eroded extensively (see Fig. 17(b)), and the bow is subjected to significant crushing behaviour. It is interesting to see that there is a 'maximum crushing distance' for the ship bow corresponding to the present ice material model. From this point, the bow structure begins to undergo significant permanent deformation (see the turning point symbol (☆) in Fig. 16). This takes place for a penetration of 1.7 m, which corresponds to an internal energy dissipation of 25 MJ. Using the results of the external mechanics calculations, the associated iceberg mass is estimated to be 1750 t. In other word, if the iceberg is heavier than 1750 t in the present scenario, the bow will be crushed. In future studies, a failure criterion will be included for the steel material so that tearing of the shell plating can be accounted for as well.

8. Conclusions

The present paper considers numerical modelling of ship–iceberg collisions with emphasis on material modelling. The most important results are as follows:

- a plastic material model is proposed;
- the material model consists of two parts: the elastic-perfectly plastic material model and the user-defined failure criterion, which is based on hydrostatic pressure and effective plastic strain;
- the material model is based on triaxial experimental data and the effects of a temperature gradient may be taken into account;
- numerical examples show that the present model yields good results; it undergoes mesh convergence and the computational time is acceptable. For instance, simulating one second of a bow–iceberg collision takes 12 h if 4CPU nodes are used;
- the material model is successfully applied to simulation of ship bow–iceberg collisions;
- separating the external and internal mechanics of ship–iceberg collision problems simplifies the numerical simulations significantly;

- during a collision, the ship bow and iceberg share the total dissipated energy. The iceberg dissipates most of the energy initially. In the scenario analysed here, the bow will be crushed if the iceberg is heavier than 1750 t.

The present model provides a useful tool for *ALS* design of ship structures with respect to iceberg impact loads. Ongoing work regarding integrated analysis of ship–iceberg collisions that account for fracture and crack propagation in ship shell plating will be presented in the near future.

Acknowledgements

This work was carried out within the collaboration of the Strategic University Programmes (SUP) "ScenaRisC&G" and "PetroArctic" at NTNU, both funded by the Norwegian Research Council. The authors wish to thank the Norwegian Research Council for supporting this research. The authors extend also their gratitude to Prof. O. Hopperstad and Prof. K. Høyland for constructive discussion on material modelling and ice mechanics.

Appendix A. Equivalent interpretation between Derradji-Aout and *Tsai-Wu* yield surface

The elliptical yield curve proposed by Derradji-Aouat (2000) is presented as following:

$$\left(\frac{\tau-\eta}{\tau_{\max}}\right)^2+\left(\frac{p-\lambda}{p_c}\right)^2=1 \tag{A.1}$$

where τ is the octahedral shear stress, $\tau_{\max}$ is the minor axis of the ellipse, η and λ are the center coordinates of the ellipse, p is the hydrostatic pressure, p_c is the major axis of the ellipse.

The *Tsai-Wu* yield curve for the isotropic material can be simplified as following:

$$f(p,J_2)=J_2-\left(a_0+a_1p+a_2p^2\right)=0 \tag{A.2}$$

Where $p$is the hydrostatic pressure, J_2 is the second invariant for deviatoric stress tensor, a_0,a_1,a_2 are constants.

Based on the definition, we have:

$$J_2=\frac{1}{2}s_{ij}:s_{ij} \tag{A.3}$$

where s_{ij} is the deviatoric stress tensor and $s_{ij}=\sigma_{ij}-\delta_{ij}\frac{\sigma_{kk}}{3}$.

The Von Mises stress q can be obtained through the following equation:

$$q=\sqrt{3J_2} \tag{A.4}$$

And the octahedral stress τ is as following:

$$\tau=\frac{\sqrt{2}}{3}q \tag{A.5}$$

If

$$\eta=0 \tag{A.6}$$

Eq. (A.1) could be equivalently transferred to Eq. (A.2) according to following:

$$a_0=\frac{3\tau_{\max}^2}{2p_c^2}\left(-\lambda^2+p_c^2\right) \tag{A.7}$$

$$a_1=\frac{3\tau_{\max}^2}{p_c^2}\lambda \tag{A.8}$$

$$a_2=\frac{-3\tau_{\max}^2}{2p_c^2} \tag{A.9}$$

References

Bass, D.W., Sen, D., 1986. Added mass and damping coefficient for certain 'realistic' iceberg models. Cold Reg. Sci. Technol. 12 (2), 163–174.
Carney, K.S., Benson, D.J., DuBois, P., Lee, R., 2006. A phenomenological high strain rate model with failure for ice. Int. J. Solids Struct. 43 (25–26), 7820–7839.
Daley, C., 1994. Compilation of medium scale ice indentation test results and comparison to ASPPR. Daley R&E, Ottawa, Canada.
Derradji-Aouat, A., 2000. A unified failure envelope for isotropic fresh water ice and iceberg ice. Proc. of the ETCE/OMAE-2000 Joint Conference, Energy for the New Millennium, New Orleans, USA, OMAE2000/P&A-1002.
Derradji-Aouat, A., Lau, M., 2005. Ice loads on electric power generating stations in the bell isle strait. Proc. Of 18th Int. Conf. on Port and Ocean Eng. Under Arctic Conditions, Potsdam, New York, pp. 387–398.
Durham, W.B., Heard, H.C., Kirby, S.H., 1983. Experimental deformation of polycrystalline H_2O ice at high pressure and low temperature: preliminary results. J. Geophys. Res. 88, B377–B392.
Gagnon, R., 2008. Analysis of data from bergy bit impacts using a novel hull-mounted external Impact Panel. Cold Reg. Sci. Technol. 52 (1), 50–66.
Gagnon, R.E., Gammon, P.H., 1995. Triaxial experiments on iceberg and glaciers ice. J. Glaciol. 41 (139), 528–840.
Hallquist, J.O., 2007. Ls-dyna Keyword User's Manual (version 971). Livermore Software Technology Corp, Livermore, USA.
ISO/CD 19906, 2010. Petroleum and Natural Gas Industries — Arctic Offshore Structures, ISO TC 67/SC 7/WG 8. Final Draft International Standard. International Standardisation Organization, Geneva, Switzerland. 434 pp.
Johnson, R.C., 1987. Iceberg impact strength, Proc. Of Int. Offshore Technology Conf., Houston, USA, pp. OTC 5599, pp. 417–423.
Jones, S.J., 1982. The confined compressive strength of polycrystalline ice. J. Glaciol. 28 (80), 171–177.
Jones, S.J., 2007. A review of the strength of iceberg and other freshwater ice and the effect of temperature. Cold Reg. Sci. Technol. 47 (3), 256–262.
Jordaan, I.J., 2001. Mechanics of ice-structure interaction. J. Eng. Fract. Mech. 68 (17–18), 1923–1960.
Kierkegaard, H., 1993. Ship Collisions with Icebergs. Doctoral thesis, Denmark Technology University, 149 pp.
Liu, Z., Amdahl, J., 2010. A new formulation of the impact mechanics of ship collisions and its application to a ship–iceberg collision. J. Mar. Struct. 23 (3), 360–384.
Liu, Z., Amdahl, J., Løset, S., 2009. Numeric simulation of collisions between ships and icebergs. 20th Int. Conf. on Port and Ocean Eng. under Arctic Conditions, Lulea, Sweden, POAC09-38.
Liukkonen, S., Kivimaa, S., 1991. FE-Modelling of Ice Failure Load During Ship Bow Indentation into Multi-Year Ice. Technical Research Center of Finland, Espoo, Finland.
Løset, S., 1993. Thermal energy conservation in icebergs and tracking by temperature. J. Geophys. Res. 98 (C6), 10001–10012.
Løset, S., Kvamsdal, T., 1994. Iceberg/structure interaction-effects of ice temperature on the impact force. Proc. Of the Int. Association for Hydro-Environment Eng. and Research (IAHR) Ice Symposium, Trondheim, Norway, pp. 205–218.
Masterson, D., Frederking, B., Wright, B., Karna, T., Maddock, W., 2007. A revised pressure area curve. 19th Int. Conf. on Port and Ocean Eng. Under Arctic Conditions, Dalian, China, June 26–29, pp. 305–314.
Melanson, P.M., Meglis, I.L., Jordaan, I.J., Stone, B.M., 1999. Microstructural change in ice: I. Constant-deformation-rate tests under triaxial stress conditions. J. Glaciol. 45, 417–455.
NORSOK, 2004. Design of steel structures. Appendix A: Design against Accidental Actions. Standards Norway, Oslo, Norway, p. 88.
Pedersen, P.T., Zhang, S., 1998. On impact mechanics in ship collisions. J. Mar. Struct. 11 (10), 429–449.
Popov, Yu., Faddeyev, O., Kheysin, D., Yakovlev, A., 1967. Strength of ships sailing in ice, Sudostroyeniye Publishing House, Leningrad. Technical translation, U.S. Army Foreign Science and Technology Center, FSTC-HT-23-96-68., 223 pp.
Ralston, T.D., 1980. Yield and plastic deformation in ice crushing failure. Proceeding of the Arctic Ice Dynamics Joint Experiment International Commission on Snow and Ice Symposium, pp. 234–245.
Riska, K., Frederking, R., 1987. Ice load penetration modelling. Proc. of the 9th Port and Ocean Eng. under Arctic Conditions Conf., Fairbanks, Alaska, USA, pp. 317–327.
Rist, M.A., Murrell, S.A.F., 1994. Ice triaxial deformation and fracture. J. Glaciol. 40, 305–318.
Sammonds, P.R., Murrell, S.A.F., Rist, M.A., 1998. Fracture of multi-year sea ice. J. Geophys. Res. 103, 21, 795–21, 815.
Sanderson, T.J., 1988. Ice Mechanics-Risks to Offshore Structures. Graham and Trotman, London. 253 pp.
Schulson, Erland M., Duval, Paul, 2009. Creep and Fracture of Ice. Cambridge University press. 401 pp.
Simo, J.C., Hughes, T.J.R., 1998. Computational Inelasticity. Springer. 392 pp.

PAPER III

Liu Z., Amdahl J and Løset S.

Integrated numerical analysis of an iceberg collision with a foreship structure

Published in:

Marine Structures

(In press)

.

Marine Structures xxx (2010) 1–19

Contents lists available at ScienceDirect

Marine Structures

journal homepage: www.elsevier.com/locate/marstruc

Integrated numerical analysis of an iceberg collision with a foreship structure

Zhenhui Liu*, Jørgen Amdahl, Sveinung Løset

Norwegian University of Science and Technology, Trondheim, Norway

ARTICLE INFO

Article history:
Received 5 February 2011
Received in revised form 25 March 2011
Accepted 11 May 2011

Keywords:
Numerical analysis
Iceberg
Ship
Collision

ABSTRACT

This paper presents results of integrated elasto-plastic analyses of ship-iceberg collisions based on continuum mechanics modelling of both bodies. The collision simulation was simplified by splitting the problem into external and internal mechanics, which are both discussed in detail. A simplified formulation was used to obtain the demand for energy dissipation in a ship-iceberg collision. The internal mechanics was assessed by means of the explicit non-linear code LS-DYNA 971. A new iceberg material model was used to simulate the iceberg behaviour during the impact. The foreship structure was modelled by shell elements. Rupture due to excessive straining was taken into account by a widely used steel fracture model. The relative strength of the ship and iceberg was varied by adjusting the stress-strain properties of the steel. Two iceberg shapes were investigated: a half-sphere with a radius of 2000 mm and another half-sphere with a radius of 1000 mm. The point of impact of the iceberg was assumed to be either the web frame or midway between web frames. The evolution of contact pressure and the distribution of damage to the foreship and crushing of the iceberg were studied comprehensively.

1. Introduction

The Arctic waters are becoming an attractive area due to its large reservoir of oil and gas. Explorations in such areas will meet with harsh environmental elements, such as ice loads and low temperatures. However, the sea ice extent and thickness have diminished over the past few years due

* Corresponding author.
E-mail address: zhenhui.liu@ntnu.no (Z. Liu).

0951-8339/$ – see front matter © 2011 Elsevier Ltd. All rights reserved.
doi:10.1016/j.marstruc.2011.05.004

to global warming. This diminishing ice may provide access to new sailing routes in these waters in the years to come. The probability of collisions between ships and icebergs may increase due to this increased activity. The assessment of the loads caused by iceberg impacts is an important issue for ship designers. In modern ship and offshore structure design, the design should always be carried out under the principle of the Ultimate Limit State (ULS) and further checked with the requirements for the Accidental Limit State (ALS).

Although it is not explicitly stated, the conventional design of ship structures is carried out in the ULS format. This design implies that the structure is only allowed to undergo small deformations with no or limited elasto-plastic behaviour. The task is then to determine the scantlings such that the structure can resist the maximum pressures and forces from the ice as the ice is being crushed by the ship. Consequently, the ice action is characterised as pressure versus contact area curves; the smaller the contact area, the larger is the indentation pressure. Substantial efforts have been invested over the past decades to determine pressure-area relationships for crushing ice. A variety of formulations can be found in ship classification codes and rules for arctic offshore structures, such as IACS [12] and ISO 19906 [13]. The return periods for the ice pressures are not always explicitly stated, but in general, vary from a few years to 100 years.

Pressure-area relationships are sometimes also given for very rare ice impact events, for example, for a return period of 10000 years. The intention is to use the pressure for design in the ALS format. Such pressure–area relationships are useful if the objective is to design the structure to be so strong that it can crush the ice with very moderate deformations, similar to the task in the ULS design. However, such a design will often lead to overly conservative design. In most codes, it is accepted that the structure may undergo substantial deformations in the ALS design; yielding, plastic mechanisms, buckling, et al., are allowed, but the integrity of the structure with respect to global stability shall not be put in jeopardy. For a ship or offshore structures carrying dangerous cargo, it is also normally required that a spill into the environment should not occur. For a double-hull tanker, this requirement implies that while gross deformation and fracture of the outer shell may be accepted, puncturing of the inner shell (cargo tank) should not occur. For this kind of design, pressure-area curves are meaningless; the pressures on the ice-structure interface will to a large extent be limited by the structural resistance.

For a realistic design against an accidental iceberg impact, we require knowledge about the iceberg shape and a continuum mechanics model of icebergs, in addition to iceberg mass and speed. Both issues are associated with substantial challenges.

Icebergs may take on a variety of shapes. A few attempts have been made to characterise the shapes, e.g., Sanderson [20] and McKenna [18], but so far, a common agreement on standard shapes to be used for ALS design has not been established. An alternative approach to characterisation of iceberg shapes on the basis of empirical surveys is to characterise the shapes in view of the structural resistance to iceberg impacts. In principle, a “spear-like” protrusion of an iceberg has a large puncturing potential. However, in such cases the side of the ship will simply crush the ice. A vertical, plane iceberg surface yields significant confinement of the ice, which may become virtually rigid compared to the structure. However, the associated large contact area yields a significant energy dissipation capability, and no penetration of the inner hull is likely (unless the iceberg kinetic energy is very large). An important objective of the present work is to evaluate iceberg shapes in terms of their damage potential. It will be shown that the demand for strain energy dissipation for collisions with bergy bits, icebergs and growlers up to 1000 tons is moderate. This observation implies that a relatively small part of the iceberg will be crushed and contribute to the energy dissipation. Consequently, it is not essential to have exact information about the overall shape of the iceberg, but instead, the local shape is important. Furthermore, the local shape should be evaluated in view of the structural configuration of the ship.

The physical properties of ice are complex, and relatively few continuum mechanics models exist. These limitations make the numerical simulation of ice-structure interactions a challenge. In the 1980’s, the typical numerical methodology to model iceberg ice was based on the use of simplified analytical equations and ice failure strength, e.g. Cammaert and Tsinker [3] and Arockiasamy et al. [2]. The crushing and crack of iceberg ice during impact were not considered at all. Gagnon has done extensive research on numerical simulation of iceberg impacts, e.g. Gagnon [8,9]. The so-called “crushable foam” material type was adopted to simulate ice crushing. It is a promising method for investigating structure and iceberg interactions. However, it has not yet been applied to integrated

Please cite this article in press as: Liu Z, et al., Integrated numerical analysis of an iceberg collision with a foreship structure, Marine Structures (2010), doi:10.1016/j.marstruc.2011.05.004

analysis. Liu et al. [15] presented a new material model for iceberg ice that is designed to facilitate simulation of ship structure and iceberg interactions. It is based on plasticity theory, and the "erosion" technique is employed to simulate the crushing of the iceberg. This model is adopted in the integrated analyses reported in the present paper.

The material model used is based on a simplified modelling of complex physical iceberg mechanisms. Hence, it is essential to verify that it yields a realistic description of iceberg-crushing behaviour. The structure-iceberg interface pressures obtained in the integrated analyses were, therefore, studied in detail in the present paper.

The demand for energy dissipation is another issue of importance. The iceberg with its associated added mass represents a kinetic energy, where the impact speed often is largely governed by the ship speed. Only a fraction of the kinetic energy must, however, be dissipated as strain energy. Depending on the collision geometry, a significant part of the impact energy will remain as kinetic energy. This determination is conveniently made by splitting the analysis into two tasks, namely, an assessment of i) external mechanics and ii) internal mechanics. The result of external mechanics is the demand for energy dissipation. This result provides a useful perspective on the amount of deformations that is to be expected in the structure and the ice. The distribution of damage and energy dissipation is determined in the integrated analysis of internal mechanics. A major objective of the present work is to study the distribution of damage in the ship and the iceberg as a function of the relative strength of the two structures. A further objective is to determine the size of iceberg impacts that a typical tanker can resist without jeopardising the acceptance criteria.

The integrated analysis of ship-iceberg collisions in the present paper means that the deformations of both ship and iceberg are taken into consideration in the non-linear finite element simulations. This analysis corresponds to the shared-energy design method in the ALS design stage. For simplicity, it is convenient to split the dynamics of ship-iceberg collisions into external and internal mechanics (see Fig. 1). The external mechanics deal with the global translational and rotational momentum balance for the ship and iceberg. It can be analysed by analytical methods (for more details refer the work done by Liu and Amdahl [14]. However, the internal mechanics focus on the local deformation of ship and iceberg. Non-linear finite element (NLFEA) methods are used in this paper to analyse the internal mechanics due to its geometry and mechanical complexity of both ship and iceberg. These two mechanics are coupled together by the dissipated energy level. The present paper will mainly describe the internal mechanics of a ship-iceberg collision.

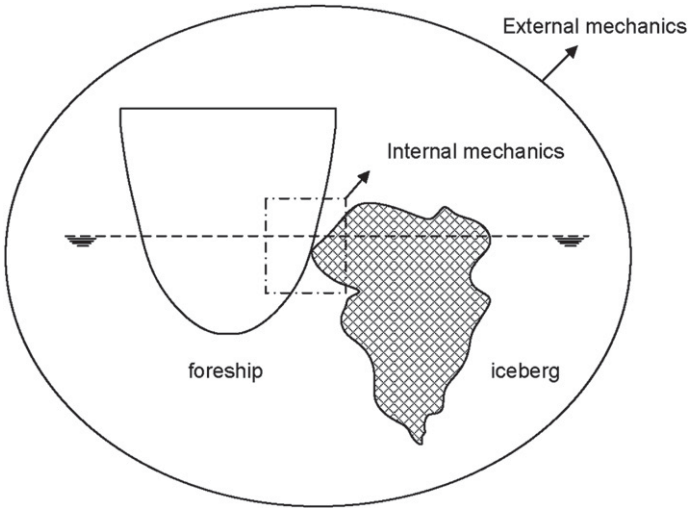

Fig. 1. Illustration of the external and internal mechanics.

Please cite this article in press as: Liu Z, et al., Integrated numerical analysis of an iceberg collision with a foreship structure, Marine Structures (2010), doi:10.1016/j.marstruc.2011.05.004

2. External mechanics

To put the energy level into a practical perspective, the demand for energy dissipation was first determined by calculating the external mechanics using the model developed by Liu and Amdahl [14]. The model depends on several factors, such as the iceberg mass, centre of gravity, added mass factors and collision angles. In general, such parameters are highly dependent on field data, which were not available during the study. The data are also associated with considerable uncertainties. These uncertainties may be considered within the framework of probabilistic analysis, see Fuglem et al. [7]. In this context, the following simplifying assumptions are introduced.

According to Liu and Amdahl [14], the maximum dissipated energy (E_0) in a collision between ship and iceberg is reached if the impact is purely plastic and central (collision force through the centre of gravity), which yields the following expression:

$$E_0 = \frac{1}{2} M_{iceberg} \hat{v}^2_{ship} \frac{\left(1 - \frac{\hat{v}_{ice}}{\hat{v}_{ship}}\right)^2}{1 + \frac{M_{iceberg}}{M_{ship}}} \tag{1}$$

Eq. (1) can be rewritten as the following expression:

$$E_0 = \frac{1}{2} \chi M_{iceberg} \Delta v^2 \tag{2}$$

where $M_{ship}$and $M_{iceberg}$ are the masses of the ship and iceberg, respectively. In general, the added mass factor should be considered (see the discussion in Liu and Amdahl [14]. However, for simplicity, it is neglected in the present discussion. $\chi = 1/(1 + M_{iceberg}/M_{ship}) = M_{ship}/(M_{ship} + M_{iceberg})$, and χ is usually close to 1 in this work because the focus is on growler or bergy bits collisions with ship structures. If a ship of mass 150000 tons collides with an iceberg of mass 1000 tons, then $\chi = 150/151$. $\Delta v = \hat{v}_{ship} - \hat{v}_{ice}$ is the relative velocity between the ship and iceberg. The demand for energy dissipation (E) in a ship-iceberg collision may therefore be expressed as follows:

$$E = \xi E_0 \tag{3}$$

where ξ is a factor that depends on a variety of parameters, such as the collision position, the water line angle, the frame angle of ship, the relative centre of gravity (COG) position and the velocity direction between the ship and iceberg. To quantify the value of ξ is a challenge. The work done by Fuglem et al. [7] sheds light on how to assess ξ. As to the iceberg and ship collision case, if we consider the iceberg collision with the foreship structure as the most likely scenario, a factor of 0.3 may be conservatively assumed based on previous study by Liu and Amdahl [14].

The demand for strain energy dissipation versus relative speed for foreship collisions with different iceberg sizes is plotted in Fig. 2. For example, if a 5000-ton iceberg collides with the foreship of a 150000-ton vessel with a relative velocity of 5 m/s, the estimated total dissipated energy is 18.2 MJ. If the iceberg size is 10000 tons, the demand for energy dissipation is then 35.2 MJ. These values are comparable to the present criteria for accidental collisions with platforms in the North Sea (14 MJ for supply vessels, 40–60 MJ for passing vessels, see Moan et al. [17]). However, a general conclusion regarding the energy level should be based on field data, such as the sizes, mass, shapes and velocities of both iceberg and ship, e.g. the work done by Liu et al. [16]. The required energy can be dissipated either as strain energy in the vessel or by crushing of the ice or by the crushing of the iceberg and the vessel. Such values give a direct measurement of the damage extent if we link it with the following internal mechanics analysis.

3. Internal mechanics

This section contains a detailed discussion about the internal mechanics during a ship and iceberg collision.

Please cite this article in press as: Liu Z, et al., Integrated numerical analysis of an iceberg collision with a foreship structure, Marine Structures (2010), doi:10.1016/j.marstruc.2011.05.004

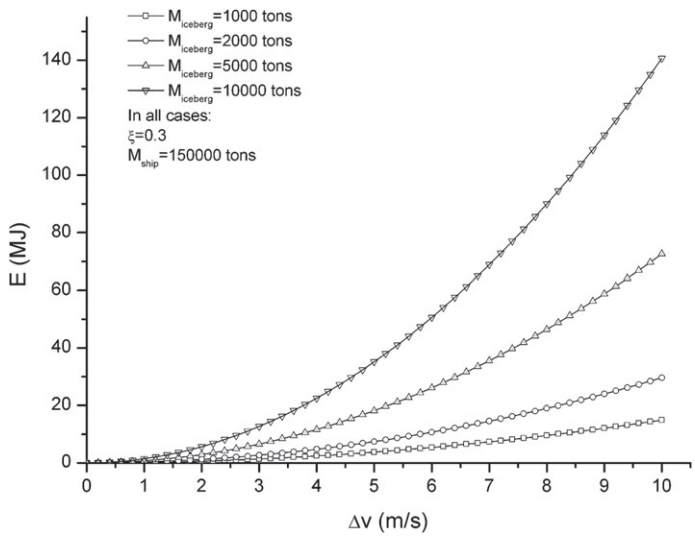

Fig. 2. *E* versus Δ*v*.

3.1. Ship model

The ship bow model is based on the drawing of an ice-strengthened FPSO structure (see Fig. 3(a)). The main dimensions are listed in Table 1.

The steel material model used was developed by Alsos et al. [1]. The material was assumed to have isotropic plastic properties and modelled using plane stress J_2 flow theory. The equivalent stress-strain relationship is represented by a modified power law formulation that includes the plateau strain:

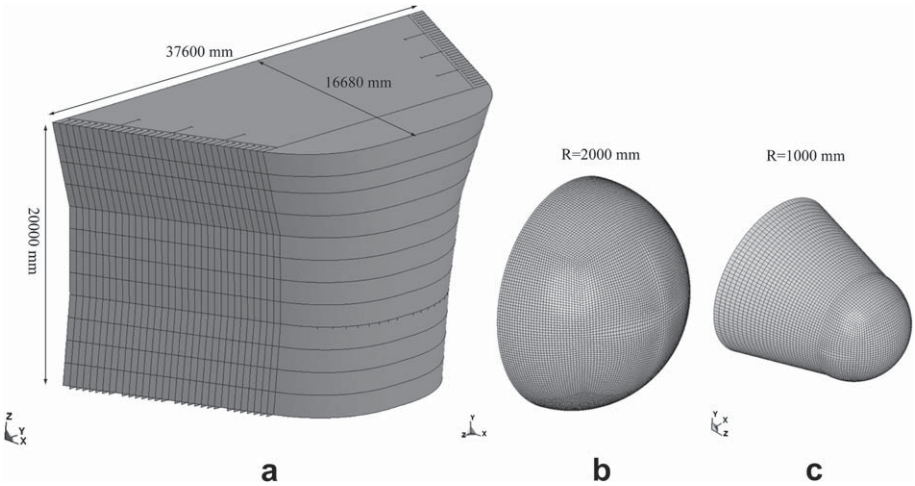

Fig. 3. (a) Foreship model, (b) Iceberg model $R = 2000$ mm, (c) Iceberg model $R = 1000$ mm. Notice that (a, b, c) are not at the same scale level.

Please cite this article in press as: Liu Z, et al., Integrated numerical analysis of an iceberg collision with a foreship structure, Marine Structures (2010), doi:10.1016/j.marstruc.2011.05.004

Table 1
Main dimensions of the bow structure.

Items	Dimension
Plating	35 mm
Stiffener spacing	400 mm
Stringer spacing	1650 mm
Stringer plating	20.5 mm
Web frame spacing	3200 mm
Stiffener	$400 \times 18 + 100 \times 11$ mm^2
Web frame	$3500 \times 12.5 + 200 \times 12.5$ mm^2
Stiffener of stringers	$1500 \times 200 \times 12$ mm^3

$$\sigma_{eq} = \begin{cases} \sigma_y & if\, \varepsilon_{eq} \le \varepsilon_{plat} \\ K(\varepsilon_{eq} + \varepsilon_0)^n & otherwise \end{cases} \tag{4}$$

where ε_{plat} is the equivalent plastic strain at the plateau exit and σ_y denotes the initial yield stress, K is strength index, n is the strain hardening index. The strain ε_0 at the intersection of the plateau and power law expression, (ε_{plat},σ_y), is given by the following expression:

$$\varepsilon_o = \left(\frac{\sigma_y}{K}\right)^{\frac{1}{n}} - \varepsilon_{plat} \tag{5}$$

The RTCL damage criterion was employed in the integrated analysis in the event that steel fracture and crack happened in the simulation. Detailed information can be found in the paper by Alsos et al. [1]. The key data for the steel model are listed in Table 2.

3.2. Iceberg model

It is a challenge to define real iceberg shapes. Nonetheless, two different iceberg shapes are proposed in the present study. The first is a half-sphere with a radius of 2000 mm. The second is a compositae shape comprising a half-sphere of radius 1000 mm in the front, a rounded platform of height 2000 mm, and top and bottom radii of 1000 mm and 1500 mm, respectively, in the back (see (b) and (c) in Fig. 3). The sphere-shaped iceberg simulates the contact area during the iceberg collision with the foreship. These shapes are highly idealised, and there are also other possibilities for the contact area shapes, which may be investigated later. The iceberg models are both modelled by hex-octahedron solid elements with a user-defined constitutive relationship.

The iceberg material model, which is based on the "Tsai-Wu" yield surface, was developed by Liu et al. [15]:

$$f(p,J_2) = J_2 - \left(a_0 + a_1 p + a_2 p^2\right) = 0 \tag{6}$$

where $p = \sigma_{kk}/3 = I_1/3$ is the hydrostatic pressure, $J_2 = 1/2 s_{ij} : s_{ij}$ is the second invariant for the deviatoric stress, and a_2, a_1, and a_0 are constants that require fitting to triaxial experimental data. A user-defined failure criterion was proposed as follows:

Table 2
Steel material model inputs.

Items	Value
Densityρ	7.89×10^3 kg/m^3
Young's modulus E	210 GPa
Poisson ratioν	0.3
Yields stress σ_y	285 MPa
Strength index K	740 MPa
Strain index n	0.24

Please cite this article in press as: Liu Z, et al., Integrated numerical analysis of an iceberg collision with a foreship structure, Marine Structures (2010), doi:10.1016/j.marstruc.2011.05.004

$$\varepsilon_{eq}^{p} = \sqrt{\frac{2}{3}\varepsilon_{ij}^{p} : \varepsilon_{ij}^{p}} \tag{7}$$

$$\varepsilon_{f} = \varepsilon_{0} + \left(\frac{p}{p_2} - 0.5\right)^2 \tag{8}$$

where $\varepsilon_{eq}^{p}\varepsilon_{eq}^{p}$ is the equivalent plastic strain, $\varepsilon_{ij}^{p}$is the plastic strain tensor, $\varepsilon_f$is the failure strain, ε_0 is the initial failure strain, which should be adjusted according to experimental data, and $p_2$is the larger root of the yield function. If $\varepsilon_{eq}^{p} > \varepsilon_f$ or the pressure is not greater than the cut-off pressure p_{cut}, erosion is activated. This failure criterion is based on trial and error and is purely empirical. Only one input parameter (ε_0) is needed.

The iceberg material model shows reasonably good behaviour in different numerical examples. More details are available in Liu et al. [15]. Different values for the yield surface parameters were tried, and it was concluded that the data obtained based on the work done by Derradji-Aouat [5] could be used for the simulation of the local structure deformation. The present paper contains a further investigation of the behaviour and validity of the iceberg material model. The data for the present iceberg material model are listed in Table 3. As discussed by Liu et al. [15], the data derived from Derradji-Aouat generally gives an upper bound of the iceberg impact loads.

3.3. Boundary conditions and collision positions

The end of the ship bow structure was fixed. The ship bow structure was big enough to minimise the influence of the boundary on the results. The iceberg was free to move against the ship bow with a velocity of 4000 mm/s. Collision positions were placed at the middle of two vertical stringers (side view in Fig. 4). Horizontally, two locations were considered: one was on the top of the web frame, and the other was located in the middle of two web frames (top view in Fig. 4).

4. Simulation results

The non-linear explicit finite element code LS-DYNA 971 was used to assess both the ship structure and the iceberg deformations. The simulations were run on a Xenon 64EMT Linux server with 8 CPUs. The simulation time for each case was approximately 20 h. Three groups of contacts and friction factors were defined as given in Table 4. The option *CONTACT_ERODING_SURFACE_TO_SURFACE was used to consider the contact between ship structure and the newly emerged surface of iceberg if the ice element is eroded. The option *CONTACT_AUTOMATIC_SINGLE_SURFACE was used to calculate internal contact between ship structural components. The command *CONTACT_ERODING_SINGLE_SURFACE enabled calculation of possible contact between ice elements. More information can be found in Hallquist [11].

Table 3
Iceberg material model inputs.

Items	Value [5]
Constant a_0	22.93 MPa^2
Constant a_1	2.06 MPa
Constant a_2	−0.023
Initial failure strain ε_0	0.01
Young's modulus E	9.5 GPa
Density ρ	900 kg/m3

Please cite this article in press as: Liu Z, et al., Integrated numerical analysis of an iceberg collision with a foreship structure, Marine Structures (2010), doi:10.1016/j.marstruc.2011.05.004

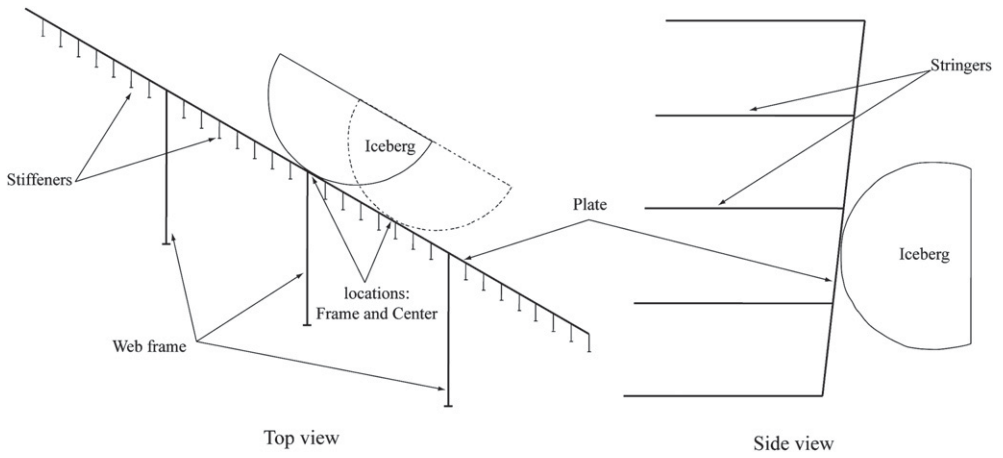

Fig. 4. Illustration of collision location.

4.1. Ice impact pressure

Prior to discussing how the deformation and energy dissipation are shared by the ice and the ship structure in the integrated analysis, it is interesting to investigate how ice pressures develop on the contact surface. The ice pressures were obtained by assessing the output data of contact pressure per node, which corresponds to a square mesh of size 0.014 m^2 (120 $\times$ 120 mm^2) in the present simulation (see Hallquist [11]). Gagnon [10] used a new impact panel to measure forces and pressures during collisions of a ship with bergy bits and small icebergs. It was concluded that the contact zones consisted of relatively small regions of hard ice (pressure in the range of 8–20 MPa for contact areas varying from 0.002 m^2 to 0.03 m^2) usually surrounded by a larger area of softer pulverised ice, where the pressure was around 2.5 MPa. To compare with this finding, the contact pressures in the numerical simulation were investigated. Screenshots of the contact pressure at time 0.005 s and 0.15 s are presented in Fig. 5(a, b). The contact pressure at the very beginning (at time 0.005 s) is in the range of 16–37 MPa. The maximum contact pressure at time 0.15 is 15.5 MPa (e.g. the red colour in Fig. 5(b)). The high contact pressure points in the range of 8–15.5 MPa at 0.15 s are distributed randomly within the contact surface. Several nodes are picked up for investigation; see Fig. 5(c). It is seen that the contact pressure in the centre area is generally higher than that in the area close to the edge. This is as expected since the ice at the centre area is well confined. The failure criterion embedded in the material model which determines the "erosion" of ice elements plays an important role on inducing such big variation of contact pressure as Fig. 5(b) presents. However, other reasons, e.g. the dynamic stress wave and the contact algorithm used by LS-DYNA may also exist. Anyway, the model that has been developed is capable of generating realistic impact forces and pressure distributions on the ship structure. (For interpretation of the references to colour in this figure legend, the reader is referred to the web version of this article.)

Table 4
Contact and friction definitions.

	Contact location	Contact algorithm	Friction
1	Ship structure and iceberg	*CONTACT_ERODING_SURFACE_TO_SURFACE	0.15
2	Ship structure	*CONTACT_AUTOMATIC_SINGLE_SURFACE	0.30
3	Iceberg	*CONTACT_ERODING_SINGLE_SURFACE	0.15

Please cite this article in press as: Liu Z, et al., Integrated numerical analysis of an iceberg collision with a foreship structure, Marine Structures (2010), doi:10.1016/j.marstruc.2011.05.004

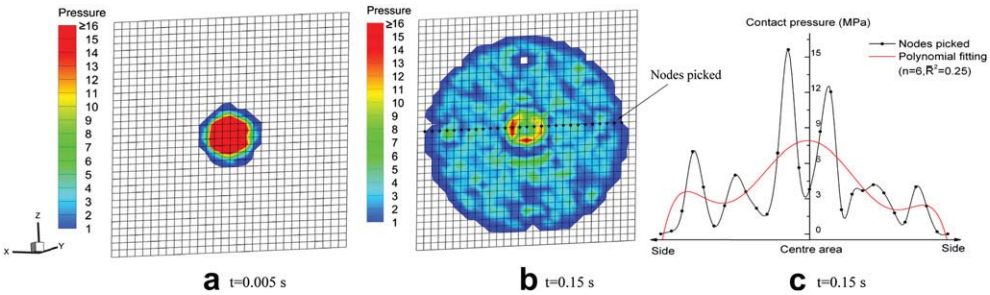

Fig. 5. (a, b) Contact pressure contour (unit: MPa) on the ship outer hull, at time 0.005 s and 0.15 s. (c) Contact pressure variation for nodes picked at time 0.15 s. A polynomial fitting curve is also plotted. Fitting degree $n = 6$, the adjusted R -square $\overline{R}^2 = 0.25$.

Further, three patches of different sizes were selected for the investigations. They are all located close to the centre contact area, see Figs. 6–8. The smallest area of 0.23 m^2 (16 nodes, 480 × 480 mm^2) was close to the square of the stiffener spacing, and was chosen because it is often the reference area used to design the local plate thickness (see Fig. 6). The second area of 0.9 m^2 (64 nodes, 960 × 960 mm^2) represented some intermediate situation where approximately two stiffener spaces were loaded directly (see Fig. 7). The largest area of 2.00 m^2 (143 nodes, 1320 × 1560 mm^2) represented a case where a complete plate field between stringers and web frames was loaded (see Fig. 8).

Interface pressures were recorded for a ship with basic material properties, see Table 2. In addition, pressures were monitored for the case that the ship was infinitely rigid. The results for the three areas are shown in Figs. 6–8.

Some interesting features are observed:

- For a rigid side, the largest pressures occurred in the early stages of contact. The pressures exhibited very large oscillations, especially for small contact areas. The oscillations were probably induced by the rapid change of stiffness for ice elements reaching the failure criteria;
- For realistic structure properties, the magnitude of the oscillations was considerably smaller, notably in the early stages of deformation. The peak pressures were significantly smaller. In the late

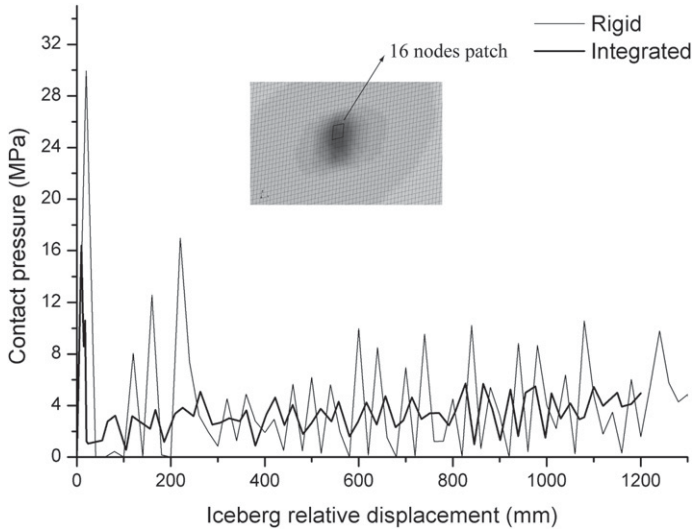

Fig. 6. Contact pressure for a loading patch of 16 nodes (0.22 m^2) located at the centre of the contact area. Rigid versus integrated.

Please cite this article in press as: Liu Z, et al., Integrated numerical analysis of an iceberg collision with a foreship structure, Marine Structures (2010), doi:10.1016/j.marstruc.2011.05.004

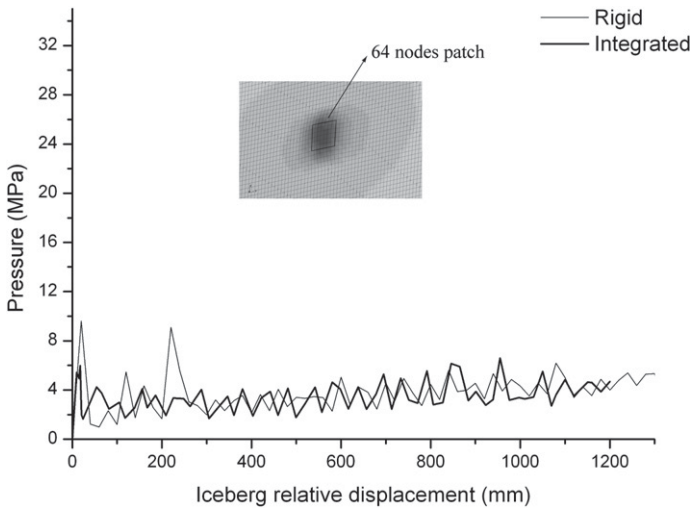

Fig. 7. Contact pressure for a loading patch of 64 nodes (0.9 m^2) located at the centre of the contact area. Rigid versus integrated.

stages of deformation, the difference in ice pressure experienced by the rigid and realistic structures was small, especially for the large contact area;

- The average contact pressures increased with increasing deformation (or time).

Based on Figs. 6–8, the maximum pressures experienced for the three areas for the rigid and realistic side structure are plotted in Fig 9 along with the ISO 19906 [13] specifications. The pressures lie above the design curve for the two smallest areas, whereas the pressures for the realistic structure fall below the curve. For the largest area, they are both virtually identical to the values given by the ISO-curve. Overall, the agreement with the design curve is good.

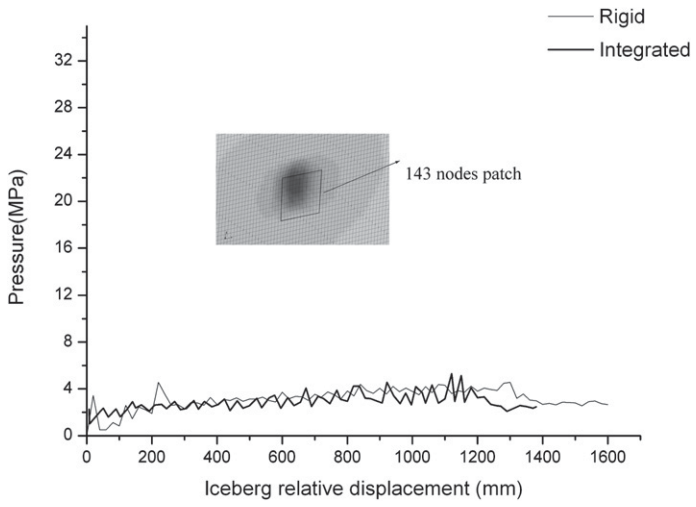

Fig. 8. Contact pressure for a loading patch of 143 nodes (2.0 m^2) located at the centre of the contact area. Rigid versus integrated.

Please cite this article in press as: Liu Z, et al., Integrated numerical analysis of an iceberg collision with a foreship structure, Marine Structures (2010), doi:10.1016/j.marstruc.2011.05.004

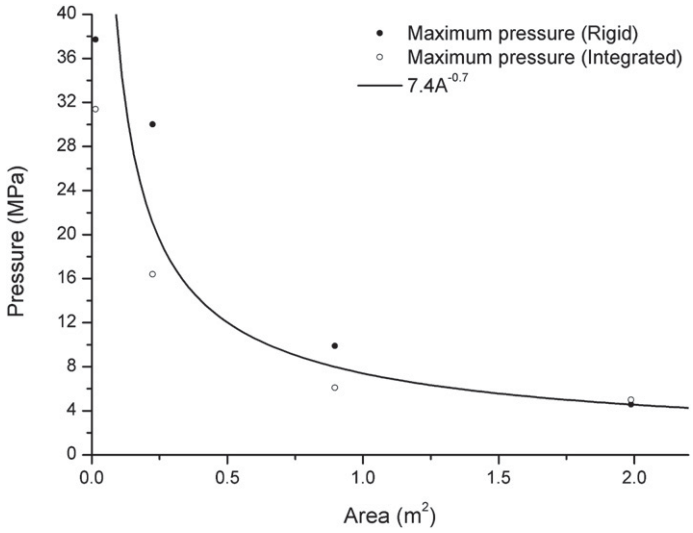

Fig. 9. Pressure-area relationship recorded during the rigid and integrated analysis.

These results demonstrate that the behaviour of the ice material model contained several favourable properties:

- The maximum pressures decreased with increasing area in the same manner as the accepted design curves. This feature is probably induced by the numerical method “erosion”, which is determined by the failure criterion embedded in the material model;
- The pressures oscillated significantly. We believe this behaviour to be the case for the pressures exerted by real ice;
- The magnitude of the oscillations decreased with increasing area. This behaviour is reasonable; due to the non-simultaneous failure at the contact surface, an increasing area should level out the oscillations;
- The reason that the peak pressures were smaller in the early stages of loading is due to the fact that the pressures are governed by the ship side resistance. The side of the ship was simply not strong enough to crush the ice initially. The strength of the side of the ship was limited by plastic deformation of the stiffeners. This behaviour is in agreement with the current practise for design of ship side structures; the plating possesses significant strength, while the stiffeners represent the “weak” link;
- When the contact area increased, the side of the ship became relatively stronger than the ice. Consequently, the ice began to be crushed, and the contact pressure for the rigid and realistic side became equal.
- The increase of the average pressure for a constant area with time seemed realistic; the total contact area increased, and the studied area experienced increasing confinement. The averaged contact pressure in all the path sizes was between 3.5 and 4 MPa, which agrees perfectly with the recommended value by Croasdale [4]. This agreement is expected because the iceberg impact loads from Croasdale and the present material model are both verified against the pond inlet tests (see Croasdale [4] and Liu et al. [15].

We emphasise that even if the maximum deformation of the hull of 137 mm is significant from a ULS design perspective, it constitutes very moderate damage from an ALS point of view. To conduct more thorough studies of the integrated analysis, it is necessary to change the relative strength of the ice and the side of the ship.

Please cite this article in press as: Liu Z, et al., Integrated numerical analysis of an iceberg collision with a foreship structure, Marine Structures (2010), doi:10.1016/j.marstruc.2011.05.004

4.2. Load-deformation curves

The structural and ice responses of the ship and iceberg can be formally represented as load-deformation relationships, as illustrated in Fig. 10 (also see reference NORSOK [19]. The strain energy dissipated by the ship and iceberg equals the total area under the load-deformation curves:

$$E = E_i + E_s = \int_0^{w_{i,max}} R_i dw_i + \int_0^{w_{s,max}} R_s dw_s \tag{9}$$

whereE_i,E_s are the dissipated strain energy by the iceberg and ship, respectively, $w_{i,\max}$,$w_{s,\max}$ are the maximum deformation for the iceberg and ship, respectively, R_i,R_s are the impact forces for the iceberg and ship, respectively, and dw_i,$dw_s$are the increments of the deformation for the iceberg and ship, respectively.

Depending on the relative strength of the ship and iceberg, the deformation and energy dissipation tend to be distributed to the weaker of the two "structures". The relative strength at a given time instant may vary significantly during the impact. Hence, the distribution of energy dissipation may exhibit different phases as illustrated in the principle sketch, Fig. 10. The curves show the various phases corresponding to the three ALS design principles defined in NORSOK [19], namely the ductile design, strength design and shared energy design. An important objective of the present work is to study the deformations and energy dissipation of the iceberg and ship structure when relative strength varies.

The most logical approach to adjust the relative strength of the iceberg and the ship is to either change the ship scantlings or let the ice material parameters vary. As the ice material has been calibrated to test data, changing the material parameters would introduce additional uncertainties (e.g. how the ice behaviour shall be interpreted?). It is easier to comprehend a variation in the ship strength. However, changing the scantlings of the ship side is cumbersome. Consequently, the ship strength was adjusted by simply scaling the yield strength. The yield stresses for the steel material for five different cases are presented in Fig. 11.

Integrated simulations of the iceberg-ship impacts were carried out for five different ship strength cases. The contact force versus deformation of the initial contact point of the ship and the ice are shown in Fig. 12.

The simulations show widely different behaviour depending on the relative strength. For example, for the weakest structure with a yield strength of σ_y=75 MPa, the iceberg behaved almost like a rigid

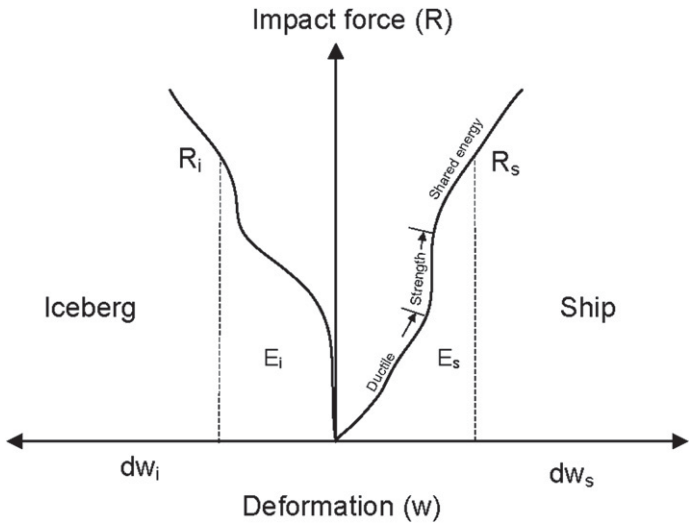

Fig. 10. Illustration of the load-deformation curve between the iceberg and ship.

Please cite this article in press as: Liu Z, et al., Integrated numerical analysis of an iceberg collision with a foreship structure, Marine Structures (2010), doi:10.1016/j.marstruc.2011.05.004

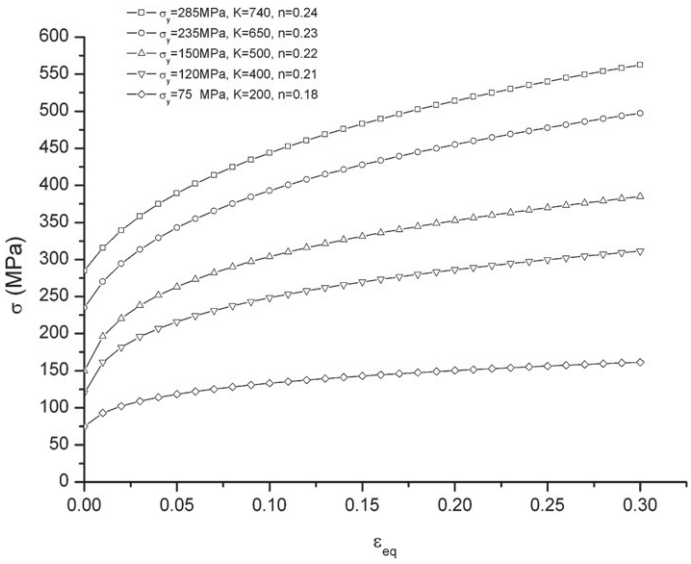

Fig. 11. The proposed stress-strain curves under different yield stresses.

body. It underwent only minor deformation, while the ship structure was damaged significantly and finally experienced ductile fracture (see Fig. 13a). With yield strengths of σ_y=120 MPa, 150 MPa, the iceberg ice and the ship structure had equal stiffness and shared the energy almost equally.

An interesting observation is that there was a "switch" in stiffness between the iceberg and the ship. Initially, the iceberg was strong enough to deform the side plating of the ship. As the side plating displaced, the centre of the contact area experienced increasing confinement, and the capacity of the ice increased. However, when the iceberg came into contact with the stringers, the tendency of the side plating to "wrap" around the iceberg was broken. At this stage, the "shoulders" of the iceberg in contact with the ship side experienced considerably less confinement, and the crushing resistance was reduced. At the same time, the resistance of the side structure increased due to the direct contact with the stringers. The combined effect was that the ship structure began to crush the iceberg. Once the iceberg began to be crushed, its strength was further reduced because of eroding elements. The significant increase of the contact area caused the stringers to buckle locally. Subsequently, the iceberg suffered most of the deformations (see Figs 13b and 14). We emphasise that the observations are based on the model adopted for the ice material. The "erosion" of elements technique adopted does not simulate any additional loads caused by the extrusion of crushed ice, which might play a role during the crushing. In spite of this limitation, we note that the pressures generated agree well with established pressure-area relationships (see Fig. 9). For the case of σ_y=235 MPa, 285 MPa, the ship underwent minor deformations compared to the iceberg (see Fig. 13c). The ship resisted the maximum pressures caused by the iceberg, except at the very beginning of contact.

The $\sigma_y = 75$ MPa or $\sigma_y = 120$ MPa, 150 MPa simulations represent the practical consequences when an impact occurs between an iceberg and ships that are not well strengthened for ice loads.

4.3. Iceberg shape considerations

The underwater shape of icebergs is often highly irregular. In particular, small icebergs may have small sections that protrude out of the main body. In principle, such protrusions may have a significant impact on the collision consequences. If the ship is not capable of crushing the protrusions, they may penetrate deep into the side structure and ultimately tear open the inner shell. To shed some light on

Please cite this article in press as: Liu Z, et al., Integrated numerical analysis of an iceberg collision with a foreship structure, Marine Structures (2010), doi:10.1016/j.marstruc.2011.05.004

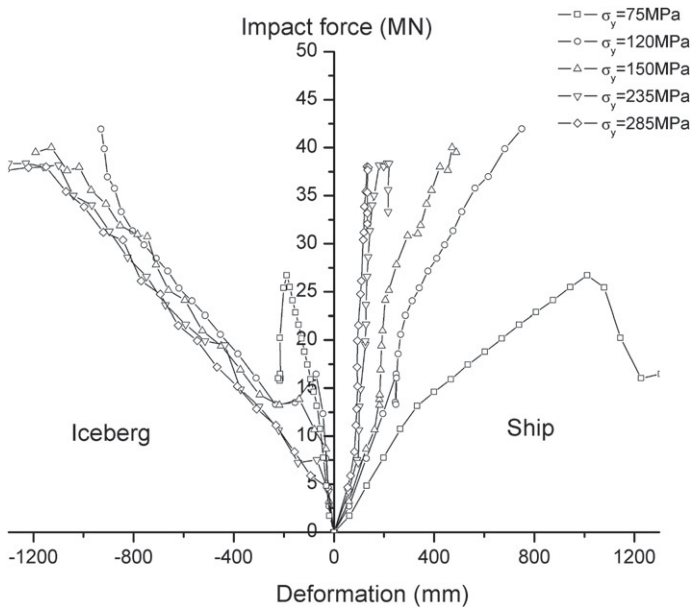

Fig. 12. Load-deformation curves, $R = 2000$ mm.

this issue, impacts with an iceberg with a smaller nose radius of 1000 mm were analysed (see Fig. 3(c)). The mesh size and velocity were identical to those of the iceberg with a nose radius of 2000 mm. The simulations were carried out for σ_y=75, 120 and 150 MPa.

The load deformation curves for the iceberg and the ship are plotted in Fig. 15 along with the corresponding curves for a nose radius of 2000 mm. The iceberg with the smaller nose radius of 1000 mm shows a similar but not exactly the same behaviour as the large radius iceberg. The iceberg force-deformation curves exhibit two peaks associated with direct contact with the iceberg on the upper and lower stringers. The non-simultaneous contact was caused by the inclined side hull of the bow. Compared to the iceberg with a nose radius of 2000 mm, the delay between the two peak forces was larger, and the averaged impact force was much smaller. The first effect was governed by the shape of the iceberg, and the second effect was governed by the resistance of the plating. Again, it is observed that the stiffeners constitute the weak link of the ship side; they cannot support the force level required

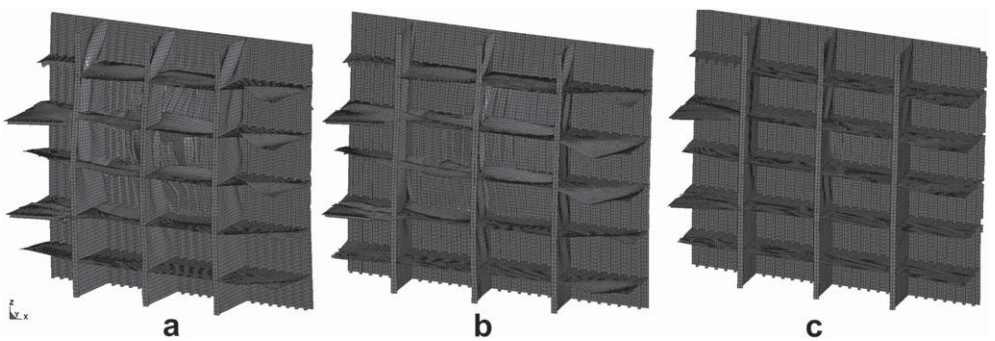

Fig. 13. Local view of structure damage in different cases (a,b,c).

Please cite this article in press as: Liu Z, et al., Integrated numerical analysis of an iceberg collision with a foreship structure, Marine Structures (2010), doi:10.1016/j.marstruc.2011.05.004

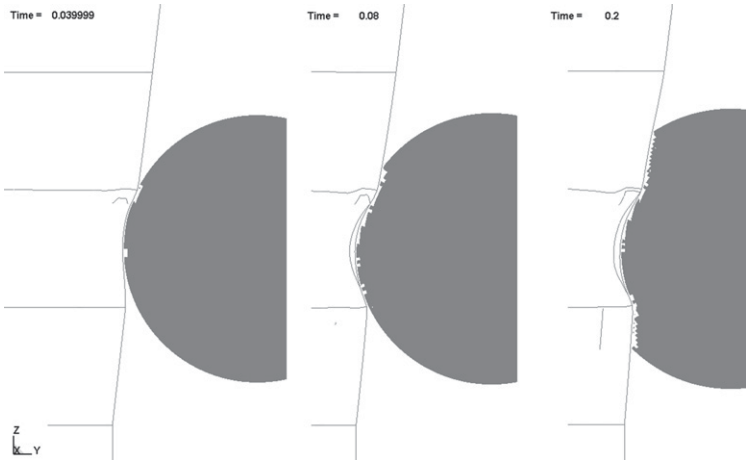

Fig. 14. Cross-sectional view (vertical) of the structure and iceberg interaction for $\sigma_y = 120$ MPa , $R = 2000$ mm. (Time unit: seconds)

to crush the ice. Consequently, in the first stages of contact, the iceberg with a nose radius of 1000 mm was capable of displacing the ship side by a greater extent compared with the large radius iceberg for the present range of steel strength. This observation is also evident by comparing the deformation pattern in Fig. 16. As seen in Fig. 15, the side of the ship was, therefore, more prone to rupture, although rupture did not take place except for the case where $\sigma_y = 75$ MPa. Once contact with the stringers was established, the ship began to crush the iceberg with a nose radius of 1000 mm, and the deformations in the side of the ship ceased for $\sigma_y = 120$ and 150 MPa.

For the case of $R = 2000$ mm and yield strength $\sigma_y = 120$ and 150 MPa, the deformation of the ship structure ceased for a short period after contact with the stringers was established and then began to increase again due to increased contact area and forces. The behaviour may be categorised as changing

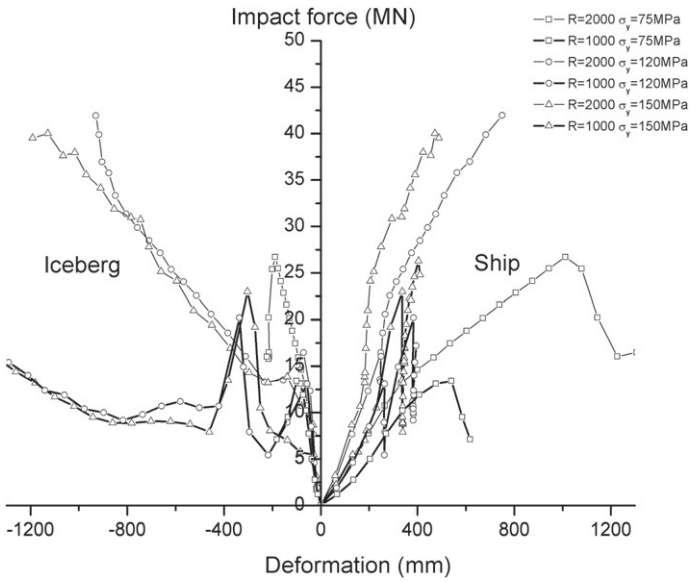

Fig. 15. Load-deformation curves, $R = 2000$, 1000 mm.

Please cite this article in press as: Liu Z, et al., Integrated numerical analysis of an iceberg collision with a foreship structure, Marine Structures (2010), doi:10.1016/j.marstruc.2011.05.004

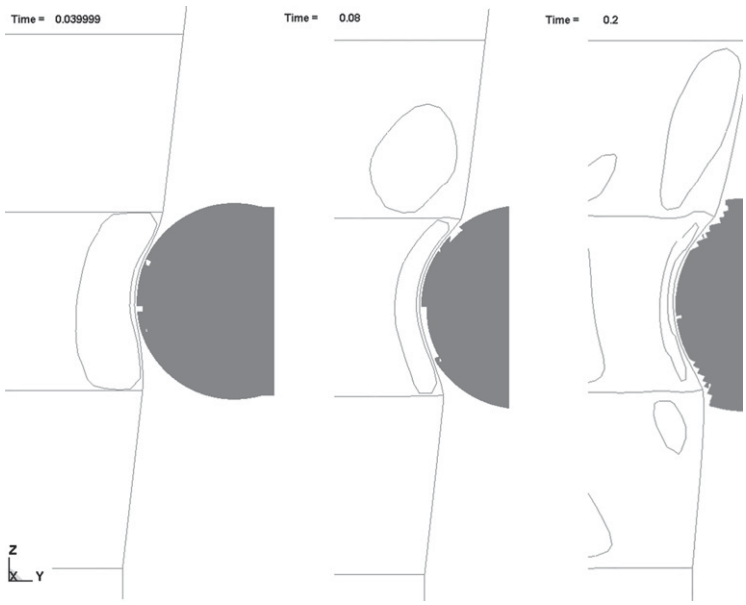

Fig. 16. Cross-sectional (vertical) view of the structure and iceberg interaction for σ_y =120 MPa, R=1000 mm., time unite: second. The envelops indicate the folding of frames.

from the "strength" to the "shared energy" domain, as annotated in Fig. 10. This observation may tell us that the ship structure was probably able to crush some types of icebergs, such as the R = 1000 mm case. If the strength of the side is increased to 285 MPa as defined previously, the simulation shows that the side will start to crush the ice with R = 1000 mm at an earlier stage, before the ice has contact with the stringers. However, the structure still undergoes moderate deformation before the deformation ceases and crushes the ice at a maximum deformation of around 170 mm.

How can the influence of iceberg shape be quantified? Fitzpatrick and Kennedy [6] proposed the aspect ratio (A_r) to describe the shapes' influence on iceberg impact loads. The aspect ratio is defined as follows:

$$A_r = \frac{H}{D} \tag{10}$$

where H,D are the height and diameter, respectively, of crushed ice at the leading edge, as defined by Fitzpatrick and Kennedy [6]. However, the parameterA_r is still difficult to assess because both H,Dcannot be easily obtained. Here, we adopted Fitzpatrick and Kennedy's concept and further assumed that A_r may be defined according to the structural configuration. We propose that the parameter$D$should be set equal to the spacing between strong structure components in a ship. In most cases, the stiffeners were too weak, and the natural choice was to set D as the spacing between stringers, frames, deck or bulkhead. The height H was then determined as illustrated in Fig. 17. In the present simulations, A_r equals 0.3 and 0.1 for R=1000 mm and 2000 mm, respectively; the larger the value ofA_r, the higher the potential of penetrating the inner shell. For large values ofA_r, the ice will start crushing while the structure remains intact or undergoes only moderate deformation. For small values ofA_r, the ship structure may endure most of the deformations.

4.4. Different locations

Two locations of the collision position were proposed for the iceberg with a radius of 2000 mm (see Fig. 4). The load-deformation curves are summarised in Fig. 18. As expected, the structure tended

Please cite this article in press as: Liu Z, et al., Integrated numerical analysis of an iceberg collision with a foreship structure, Marine Structures (2010), doi:10.1016/j.marstruc.2011.05.004

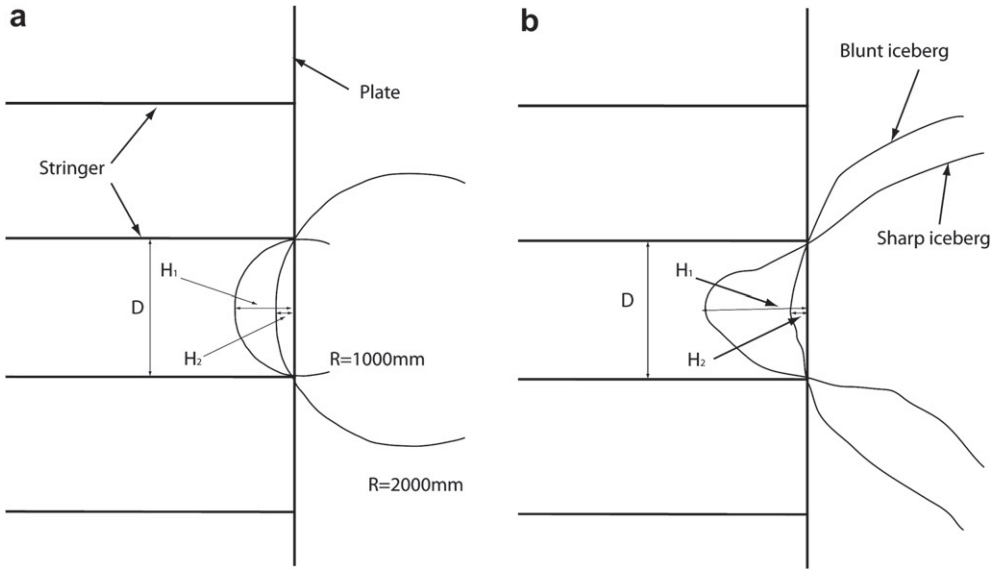

Fig. 17. Illustration of aspect ratio definition for (a) a sphere and (b) arbitrarily shaped iceberg profiles.

to deform more if the collision took place midway between web frames. An interesting observation is that the "switch" of the relative strength between the ship and iceberg was delayed in the centre collision case, which is obvious when $\sigma_y = 120$ MPa (see Fig. 18). For example, when $\sigma_y = 120$ MPa, the collision located in the centre deformed the stiffener immediately when the contact was established. The resistances for web frame contact and centre contact were virtually the same in the initial stages. In this stage, the contributions to the resistance from the web frame and the stiffener were almost the same. When the contact extended to the stringers, there was a noticeable difference

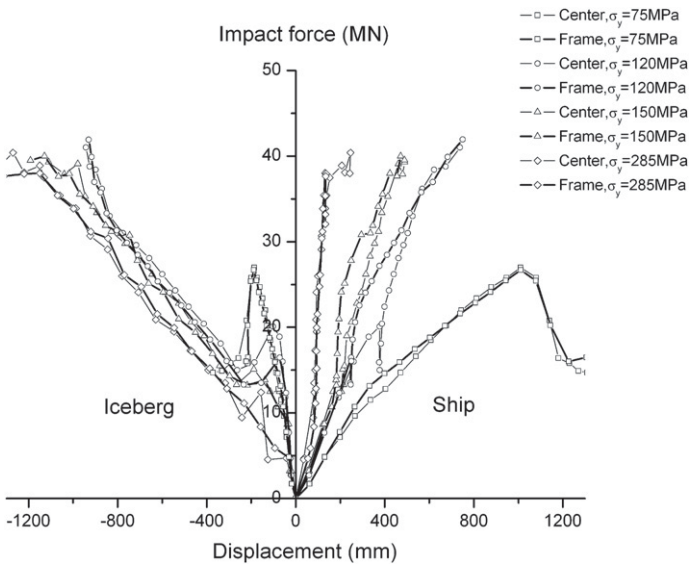

Fig. 18. Load-deformation curves for collisions at frame and centre, $R = 2000$ mm.

Please cite this article in press as: Liu Z, et al., Integrated numerical analysis of an iceberg collision with a foreship structure, Marine Structures (2010), doi:10.1016/j.marstruc.2011.05.004

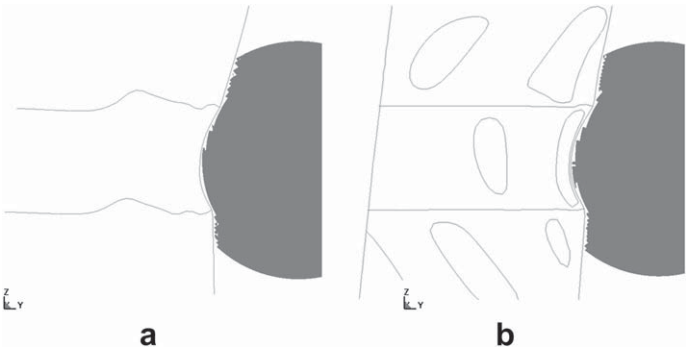

Fig. 19. Cross-sectional (vertical) view of simulations for (a) centre and (b) web frame, collisions at time 0.12 s, $R = 2000$ mm, and $\sigma_y = 120$ MPa. The envelops indicate the folding of frames.

for the web frame and centre collisions. For the web frame collision, the intersection between the stringer and the web frame was a hard spot that was sufficiently strong to crush the ice. Hence, the deformation in the side ceased. For the centre contact case, the resistance was slightly smaller due to the buckling of the stringer plate (see Fig. 19), and the side continued to deform until it reached a level at which the ice may be crushed.

5. Conclusions

The present work represents one of the first attempts to conduct truly integrated large deformation, elasto-plastic analyses of ship-iceberg collisions based on continuum mechanics modelling of both bodies. The properties of ice during crushing and its interaction with a deformable structure such as the steel ship are not well known and introduce significant uncertainties. In spite of these limitations, we believe that the results of the integrated analysis provide useful information and new perspectives on iceberg modelling aspects. Both external and internal mechanics were discussed in detail. A new developed material model for iceberg was successfully applied to simulate the iceberg and foreship collision. We took both iceberg and ship structure deformations into equal consideration in our numerical simulations. The major conclusions are the following:

- The demanded dissipated energy in an iceberg and foreship structure collision is mainly determined by the iceberg and ship masses and the relative velocity between them. A fully "plastic" impact represents an upper bound for the required energy dissipation. Based on typical foreship geometries, it has been found that the required energy dissipation is only 30% of the one represented by plastic impact. Thus, a significant amount of energy is transferred into kinetic energy by deflecting the iceberg.
- Large icebergs present the greatest damage potential. However, they are more likely to be detected by radar. Icebergs in the range of 5000–100000 tons represent probably the largest risk, taking into account the kinetic energy potential and detectability. If a 5000-ton iceberg collides with a ship with a mass of 150000 tons with a relative velocity of 5 m/s, the demand for energy dissipation is 18 MJ. This demand is not dramatic from an ALS point of view. The typical kinetic energy used for supply vessel collisions in the North Sea is 11–14 MJ. A FPSO has been shown to resist considerably larger energies before puncturing of the inner tank (see [17]).
- The ice material model proposed by Liu et al. [15] demonstrated many good features in our integrated analysis. It was able to provide reasonably good contact pressure values for various sizes of patches. The averaged contact pressure in the core area simulated was around 3.5–4 MPa;
- Impacts with icebergs with the modelled properties would not cause severe damage to the ice-strengthened foreship with a nominal yield strength of $\sigma_y = 285$ MPa studied. The maximum deflection of the side was 137 mm;

Please cite this article in press as: Liu Z, et al., Integrated numerical analysis of an iceberg collision with a foreship structure, Marine Structures (2010), doi:10.1016/j.marstruc.2011.05.004

- If a ship structure is not designed to be as strong as the present model, then an iceberg impact may cause severe damage to the side of the structure. Severe penetration and fracture were observed for the case when $\sigma_y = 75$ MPa;
- In all simulations, the stiffeners beneath the contact area were subjected to significant folding and cannot effectively support the forces created in the plating. If not directly hit, the stringers and web frames may support the membrane forces produced in the side when it undergoes finite deformations;
- If the iceberg has a sharp protrusion, it has the potential of puncturing the ship structure initially. However, the ship structure may crush such protrusions before that happens, as shown in the case of an iceberg with a half-sphere in the front with a radius of 1000 mm;
- Icebergs may take on infinitely many shapes, both on the macroscopic and local level. A few attempts have been made to characterise iceberg shapes, but accepted standards for iceberg shapes are far from being established by the engineering community, probably because the need for these standards has not been previously recognised. In an ALS analysis, the need to characterise iceberg shapes can no longer be circumvented. In lieu of relevant data, we propose to approach the iceberg shape issue from the ship scantlings' point of view. We also propose to use the aspect ratio A_r to describe the shapes of the leading edges of icebergs and further suggest that A_r can be defined from the structure damage point of view.

Acknowledgement

This work was carried out within the collaboration of the "ScenaRisC&G" and "PetroArctic" programmes at the NTNU, both funded by the Research Council of Norway. The authors wish to thank the Research Council of Norway for supporting this research.

References

[1] Alsos HS, Amdahl J, Hopperstad OS. On the resistance to penetration of stiffened plates, Part II: Numerical analysis. Int J Impact Eng 2009;36(7):875–87.
[2] Arockiasamy M, El-Tahan H, et al. Semisubmersible response to transient ice forces. J Ocean Eng. 1984;11(5):463–90.
[3] Cammaert AB, Tsinker GP. Impact of large ice floes and icebergs on marine structures. In: Proceedings of the 6th Int. Conf. on Port and Ocean Eng. under Arctic conditions. Quebec, Canada, vol. 2; 1981. 653–662.
[4] Croasdale KR. Local Ice Load Data Relevant to Grand Banks Structures. Tech. Report. K.R. Croasdale & Associates Ltd.; 2001. 208pp.
[5] Derradji-Aouat A. A Unified failure envelope for isotropic fresh water ice and iceberg ice. Feb. 14–17. In: Proceedings of the ETCE/OMAE-2000 Joint Conference, Energy for the New Millennium. New Orleans, USA: OMAE2000/P&A-1002; 2000.
[6] Fitzpatrick J, Kennedy K. Steel gravity-based structures for iceberg-infested waters. In: Proceedings of the 16th Int. Conf. on ocean, offshore and Arctic Eng, vol. 4. OMAE; 1997. Apr. 13–17, Yokohama, Japan377–391.
[7] Fuglem M, Muggeridge K, Jordaan I. Design load calculations for iceberg impacts. J Offshore and Polar Eng 1999;9(4): 298–306.
[8] Gagnon RE. A numerical model of ice crushing using a foam analogue. J Cold Regions Sci and Tech 2011;65(3):335–50.
[9] Gagnon RE. Results of numerical simulations of growler impact tests. J Cold Regions Sci and Tech. 2007;49(3):206–14.
[10] Gagnon RE. Analysis of data from bergy bit impacts using a novel hull-mounted external Impact Panel. J Cold Regions Sci and Tech 2008;52(1):50–66.
[11] Hallquist J. LS-DYNA keyword user's manual (version 971). Livermore software technology corporation (LSTC); 2007. 2206pp.
[12] IACS. Requirements concerning POLAR CLASS. International association of classification societies; 2007. 40pp.
[13] ISO 19906. Petroleum and natural gas industries - Arctic offshore structures. ISO TC 67/SC 7/WG 8. Geneva, Switzerland: International Standardization Organization; 2010. 434pp.
[14] Liu Z, Amdahl J. A new formulation of the impact mechanics of ship collisions and its application to a ship-iceberg collision. Marine Structures 2010;23:360–84.
[15] Liu Z, Amdahl J, Løset S. Plasticity based material modelling of ice and its application to ship-iceberg. J Cold Regions Sci and Tech 2011;65(3):326–33.
[16] Liu Z, Amdahl J, Løset S. Analysis of foreship and iceberg impact loads based on Bayesian networks. In: Proceedings of the 30th Int. Conf. on Ocean, Offshore and Arctic Engineering. OMAE2011–50028, June 19-24, Rotterdam, the Netherlands; 2011.
[17] Moan T., Amdahl J., et al. (2003). Risk assessment of FPSOs with emphasis on collision. In: Annual meeting of the Society of Naval Architects and Marine Engineers, p.307–338.
[18] McKenna R. Iceberg shape characterization. In: Proceedings of the 18th Int. Conf. on Port and Ocean Eng. under Arctic Conditions, vol. 2; 2005. p. 555–64.
[19] NORSOK. Design of Steel Structures, Appendix A: Design against Accidental Actions, Standards Norway. Lysaker, Norway: NORSOK STANDARD N-004; 2004. 287pp.
[20] Sanderson TJO. Ice mechanics and risks to offshore structures. Norwell, MA: Kluwer Academic Publishers; 1988. 272 pp.

Please cite this article in press as: Liu Z, et al., Integrated numerical analysis of an iceberg collision with a foreship structure, Marine Structures (2010), doi:10.1016/j.marstruc.2011.05.004

PAPER IV

Liu Z., Amdahl J. and Løset S.

Integrated numerical analysis of iceberg collision with ship side structures

Published in:

International Conference on Port and Arctic Engineering, 2011

POAC'11
Montréal, Canada

Proceedings of the 21st International Conference on
Port and Ocean Engineering under Arctic Conditions
July 10-14, 2011
Montréal, Canada

POAC11-004

Integrated numerical analysis of iceberg collisions with ship sides

Zhenhui Liu [1*], Jørgen Amdahl[2] and Sveinung Løset[3]

[1]Reinertsen AS, Trondheim, NORWAY

[2]Department of Marine Technology, Norwegian University of Science and Technology, Trondheim (NTNU), NORWAY

[3]Department of Civil and Transportation Engineering, Norwegian University of Science and Technology, Trondheim (NTNU), NORWAY

ABSTRACT

This paper deals with the integrated numerical analysis of iceberg collisions with ship sides. A nonlinear explicit commercial code LS-DYNA 971 was used in the analysis. The deformations and fracture of both the ship structure and iceberg are considered. The *RTCL* failure criterion is applied to simulate steel fracture, whereas the iceberg fracture model is simulated by a plastic strain and pressure-based empirical failure criterion. Material models for steel and iceberg are implemented in the commercial code through a user-defined subroutine. For simplicity, the ship-iceberg collision is split into external and internal mechanics. Thus, only part of the ship structure and iceberg is modelled in the numerical simulations. The ship structure is based on the drawings of an ice-strengthened FPSO, and only the side structure is modelled. The structure model has been enlarged to minimise boundary influences. Different shapes for the leading edges of the iceberg are proposed, namely so-called "sharp", "blunt" and "intermediate" icebergs. The iceberg shapes are simply represented by revolving a parabolic or circular profile line about its symmetry axis. Four profiles are proposed. Three different collision locations were simulated as well. Rigid analyses have also been performed. Finally, 24 numerical simulations have been carried out. The results for the maximum deflection of the outer and inner shells and the total internal energy are presented. Discussions and conclusions based on the results are provided as well.

Introduction

Arctic waters are attracting researchers and engineers due to the large reserves of oil and gas and the potential for new sailing routes through this area. It is expected that ship traffic will increase in this area in the near future. Thus, the probability of ship/iceberg collision increases, and it is necessary to investigate ship and iceberg collision problems in Arctic and sub-Arctic waters. This paper presents a study on the numerical simulation of iceberg collisions with ship sides.

---

[*] This work was conducted when the first author worked at NTNU as Ph.D. candidate.

To simplify the ship-iceberg collision, the division of external and internal mechanics is recommended; see Pedersen and Zhang [1]. The external mechanics describe translational and rotational momentum balance and energy dissipation. Recently, Liu and Amdahl [2] developed a new formulation for the external mechanics of ship-ship collisions. It is also applicable to ship-iceberg collisions. With the given information about the mass, velocities, added mass factors and ship/iceberg shape properties, the total dissipated energy for a ship-iceberg collision scenario can be efficiently obtained. On the other hand, the internal mechanics of ship-iceberg collision focus on the local deformations of both the ship and iceberg. *Nonlinear finite element analyses* (*NLFEA*) are always used to access the internal mechanics. Due to the large deformations, *NLFEA* should be able to handle the fracture of both steel and ice. The external and internal mechanics are linked to one another by the dissipated energy. By dividing the external and internal mechanics, models of the entire ship and iceberg are not required in the *finite element model (FEM).* The examples of this can be found in paper by Liu *et.al.* [3,4]. Figure 1 shows an illustration of this simplification. The computational time is significantly reduced by following this principle. More effort can then be focused on detailed studies of the internal mechanics.

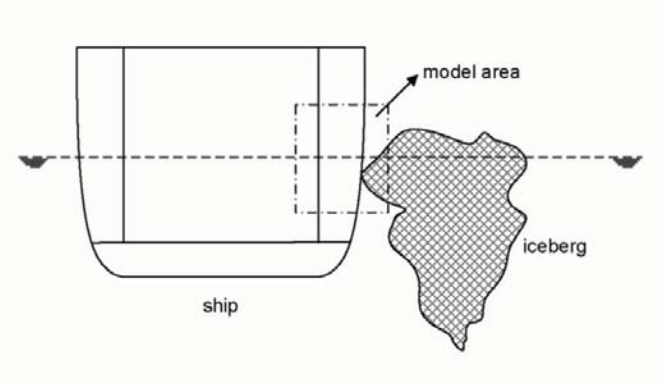

Figure 1. Illustration of side-ship and iceberg collision (cross-sectional view).

Ship and iceberg models

Ship structure

The ship structure model used in this study is based on the side scantlings of a FPSO tanker, which has been designed for ice loads. The main dimensions are listed in Table 1.

Table 1. Main dimensions.

Location	Stiffener/web Frame	Spacing [mm]	Frame/stringer spacing [mm]	Plate thickness [mm]	Material stiffener [MPa]	Material plating [MPa]
Side	250 x 12 BP	600	4430/2215	23	285	285
Inner	450 x 125 BP	825	4430	17	285	285

To minimise the influence of the boundary conditions set for the structural model, the model described above was arrayed into a 3 x 3 matrix as shown in Figure 2. The

boundary conditions are defined according to Table 2, where 1 denotes fixed and 0 indicates free (see also Figure 2).

Table 2. Boundary conditions.

Location	X	Y	Z	RX	RY	RZ
Boundary A	1	0	1	0	0	0
Boundary B	1	1	0	0	0	0

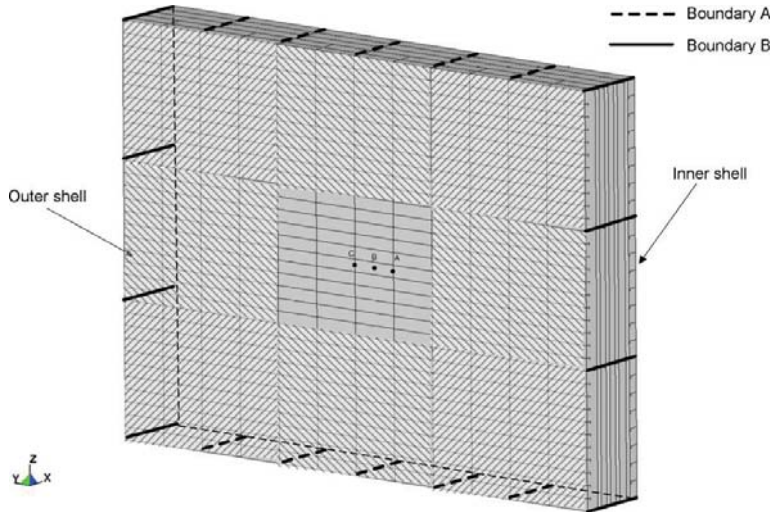

Figure 2. The side structure model with illustrations of the boundary conditions and collision locations.

The structure model was meshed by using a Belytschko-Tsay quadrangular mesh with a general mesh size of 120 mm × 120 mm. The material model for steel in this study should be able to predict the fracture and crack propagation of steel. Thus, the material model developed by Alsos et al. (2009) [5] is employed here. The power law expression was chosen to describe the stress-strain relationship. In this study, $\sigma_Y = 285$, $K = 740$, $n = 0.24$. The so-called *RTCL* (Rice–Tracey and Crockcroft–Latham) failure criterion was adopted in the material code for steel in which the triaxiality is considered; more information is provided in a paper by Alsos et al. [5].

Iceberg profile

As previously discussed, only the local area of contact with the iceberg is required in the numerical simulations. However, it is still a great challenge to model the correct shape of contact area. Similar problems have been discussed by Alsos and Amdahl [6] with respect to ship grounding They defined three categories of seabed topology on the basis of the extent of damage, namely rock, reef and shoal. Similarly, we may also consider categorising the iceberg profile based on the extent of structural damage.

Generally, two categories of iceberg profiles, “sharp” and “blunt”, are proposed. Both “sharp” and “blunt” can be simply represented by revolving a parabolic or a circle profile line about its symmetry axis. As shown in Figure 3, the iceberg profiles based on different parabolic or circular lines are created. The 3D iceberg shapes can be

easily obtained by revolving the profile lines 360° about the X-axis. In this paper, the iceberg shapes were modelled based on the parabolic line $X = -\frac{1}{500}Y^2$ and half-circle lines, $Y^2 + (X + r)^2 = r^2$, where r equals 1000 mm, 2000 mm and 3000 mm. All of the icebergs modelled have the same height of 2000 mm along the X-axis. Thus, a round platform was additionally attached to the half sphere when $r = 1000\,\text{mm}$ with an inclination angle of 25^0. The final iceberg shapes are presented in Figure 4.

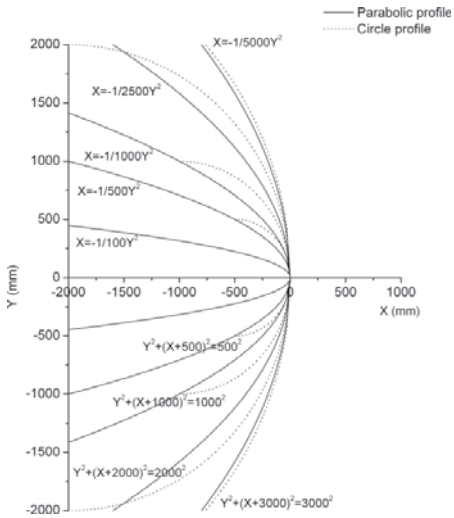

Figure 3. Iceberg profiles presented by parabolic and circle lines.

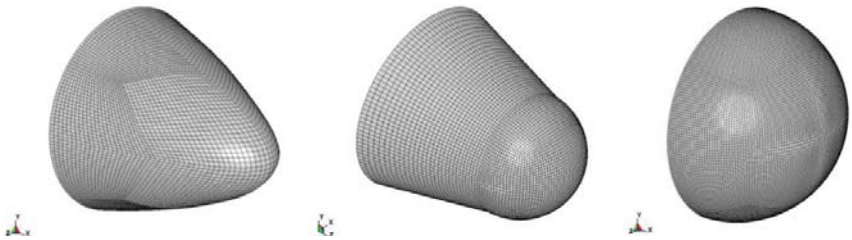
Figure 4. FEM models for local iceberg part (parabola, round platform plus half-sphere and sphere).

The 3D iceberg models were all meshed by hexahedral elements with mesh size of 50 mm x 50 mm x 50 mm. The material model used here is that presented by Liu et al. [6]. The inputs applied to the ice material model are: a_0 =22.93, a_1 =2.06, a_2 =-0.023, $p_{cut} = -2\,MPa$, $\varepsilon_0 = 0.01$, where a_0, a_1, a_2, p_{cut} and ε_0 are constants defining the material model. The iceberg material model was developed to facilitate the iceberg impact simulations by authors. It is based on the so called '*Tsai-Wu'* yield surface and a user-defined failure criterion. The failure is dependent on pressure and plastic strain of the elements; more information is available in a paper by Liu *et. al.* [7]. In addition to the integrated analysis, rigid icebergs are also included. For the rigid analysis, it is not necessary to use a solid-element mesh; the Belytschko-Tsay quadrangular mesh is used for the outer shell of the above icebergs' instead.

Collision location

The locations of initial contact during the ship-iceberg collision are assumed to be in the middle of the structure model; thus, the influence of the boundary conditions is minimised. Three typical locations are proposed, as seen in Figure 2. If we considered a grid (2215 mm × 600 mm) between the stringer/web frame and two longitudinal stiffeners, the three points A, B and C are distributed evenly along this grid.

Results

All of the simulations were carried out by the computer code LS-DYNA 971. There were three contacts defined in the simulations, as listed in Table 3. In total, 24 numerical cases are summarised in Table 4. The iceberg was simulated to move against the ship structure at a constant velocity of 4000 mm/s, and the maximum penetration was set to 2000 mm.

Table 3. Contact and friction definition.

	Contact location	Contact algorithm	Friction
1	Ship structure and iceberg	*CONTACT_ERODING_SURFACE_TO_SURFACE	0.15
2	Ship structure	*CONTACT_AUTOMATIC_SINGLE_SURFACE	0.30
3	Iceberg	*CONTACT_ERODING_SINGLE_SURFACE	0.15

Table 4. Summary of all numerical cases.

No.	Name	Integrated or Rigid analysis	Iceberg profiles	Location
1	I-P-500-A	Integrated	Parabolic line $X = -\frac{1}{500}Y^2$	A
2	R-P-500-A	Rigid	Parabolic line $X = -\frac{1}{500}Y^2$	A
3	I-C-1000-A	Integrated	Circle line $Y^2 + (X - 1000)^2 = 1000^2$	A
4	R-C-1000-A	Rigid	Circle line $Y^2 + (X - 1000)^2 = 1000^2$	A
5	I-C-2000-A	Integrated	Circle line $Y^2 + (X - 2000)^2 = 2000^2$	A
6	R-C-2000-A	Rigid	Circle line $Y^2 + (X - 2000)^2 = 2000^2$	A
7	I-C-3000-A	Integrated	Circle line $Y^2 + (X - 3000)^2 = 3000^2$	A
8	R-C-3000-A	Rigid	Circle line $Y^2 + (X - 3000)^2 = 3000^2$	A
9	I-P-500-B	Integrated	Parabolic line $X = -\frac{1}{500}Y^2$	B
…	…	…	…	…
24	R-C-3000-C	Rigid	Circle line $Y^2 + (X - 3000)^2 = 3000^2$	C

Figure 5 shows the iceberg damage patterns in the integrated analysis. The “sharp” (the first group, e.g., Figure 5(a) I-P-500-A) iceberg is mostly deformed, while the “blunt” (the last group, e.g. Figure 5(d) I-C-3000-A) iceberg is only slightly deformed. A moderate extent of deformation is observed for shapes intermediate between “sharp” and “blunt” (second and third group, e.g., I-C-1000-A and I-C-2000-A). The rigid analysis simulation was also carried out for the sake of comparison. Significant differences were observed, which point to the necessity of conducting integrated analyses of ship and iceberg collision scenarios. The following sections will present detailed results.

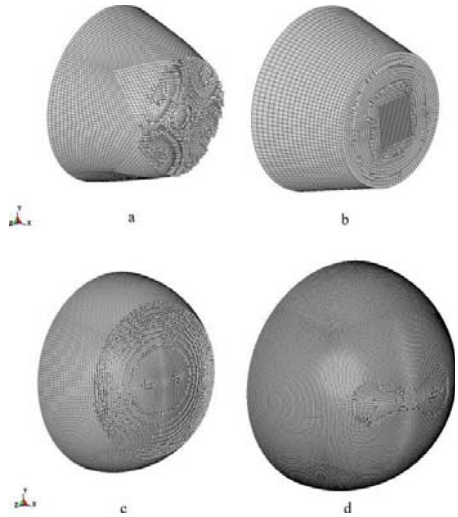

Figure 5. Iceberg damage patterns: a, Case 1, I-P-500-A, b, Case 3, I-C-1000-A, c, Case 6, I-C-2000-A, d, Case 9, I-C-3000-A.

Maximum deformation of outer and inner shell

The maximum deflections of the outer shell for all simulations are summarised in Figure 6. For the rigid analysis cases, the maximum deflection should be equal to the iceberg displacement; see the black line in Figure 6. In most cases, the integrated analyses are quite different from those corresponding to the rigid analyses. The difference becomes more obvious when the iceberg is "sharper", as the iceberg is quite easily crushed. The deflection of the structure in the integrated analyses is much smaller than that under the rigid analyses, e.g., cases I-P-500-A,B,C. It is interesting to note that the location of collision shows significant influence on the extent of damage of the side structure, e.g., cases I-C-1000-B and I-C-2000-B. The collision at location B in both cases produces much more damage to the side structure, while other two locations are less damaged. Location B is less supported than A and C, as shown in Figure 2. The detailed failure pattern in such cases is illustrated in Figure 7 for case I-C-1000-B. Initially, the iceberg is sufficiently stiff to crush the side structure; however, the relative stiffness changes when the iceberg is in contact with the web frame and the stringer. The support from the web frames and stringers increases the side structure's ability to crush the iceberg.

The differences between the integrated and rigid analyses for cases I-C-2000-A,B,C and I-C-3000-A,B,C are quite small. The side structure is not able to crush this size or shape of iceberg. Fracture is only observed in the first two groups of rigid analyses, e.g., R-P-500-A,B,C and R-C-1000-A,B,C. In cases R-P-500-A,B,C, the "sharp" iceberg penetrates the outer shell of the side structure during the early stage of collision (see the star symbol in Figure 6). For cases R-C-1000-A,B,C, the fracture is initiated when the iceberg penetration distance is approximately 1000 mm.

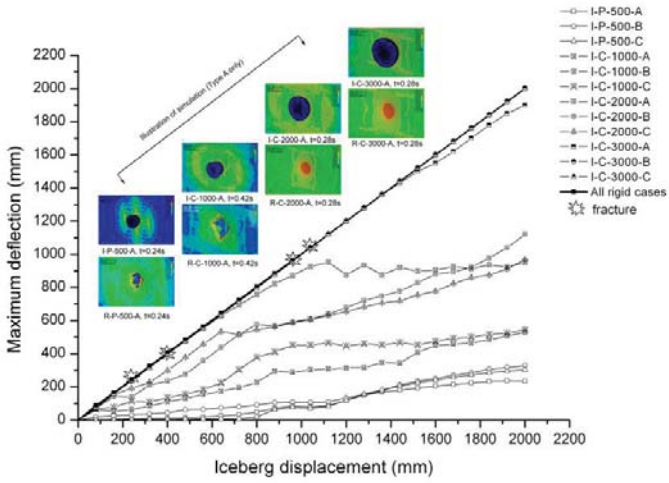

Figure 6. Maximum deflections of outer shell with iceberg displacement.

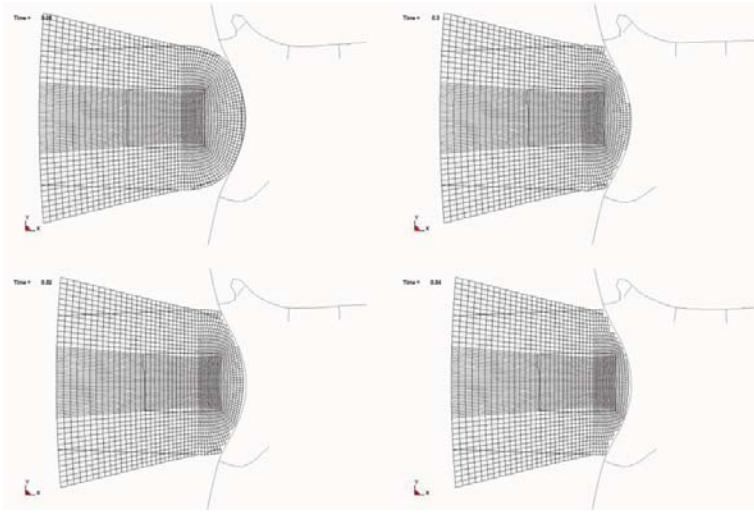

Figure 7. Horizontal cross-sections for case I-C-1000-B at different time frames.

The deflection of the inner shell is of great interest as it is an important criterion in judging a ship's survivability, especially for membrane-type LNG ships. The maximum deflection of the inner shell in the present research was only as high as 265 mm. Figure 8 summarises the maximum inner shell deflections for all cases. Only small differences are found between the integrated and rigid analyses in the first two groups (I-P-500-A,B,C, R-P-500-A,B,C and I-C-1000-A,B,C, R-C-1000-A,B,C), where fractures are observed. For the integrated analyses, the side structure crushes the iceberg ice and the inner shell experiences quite a small deflection, while for the rigid analyses, the side structure is penetrated by the iceberg, and large parts of the energy dissipation are focused in local areas where the rigid iceberg is in contact with it. Thus, the inner shell is still less influenced in such cases. However, it can be expected that the inner shell may be penetrated by the rigid iceberg if the iceberg displacement is sufficiently long. Another observation is that the deflection of the

inner shell in these two groups shows vibrations; this is due to the crushed ice that has been eroded in the simulation in the integrated cases and the fracture of the outer shell in the rigid cases. When the iceberg curvature becomes smaller, for example, in cases I-C-2000-A,B,C and R-C-2000-A,B,C, the difference is significant, as shown in Figure 8. For cases I-C-2000-A and I-C-2000-C, the collision is located where web frames and stringers are laid; the iceberg is crushed due to the strong support, and thus, the inner shell deflection is quite less than the deflections of the corresponding rigid analyses. The reason for this is the same as that discussed in the previous subsection. The differences between the integrated and rigid analyses for cases I-C-3000-A,B,C are quite small, indicating that the icebergs are sufficiently stiff to crush the side structure.

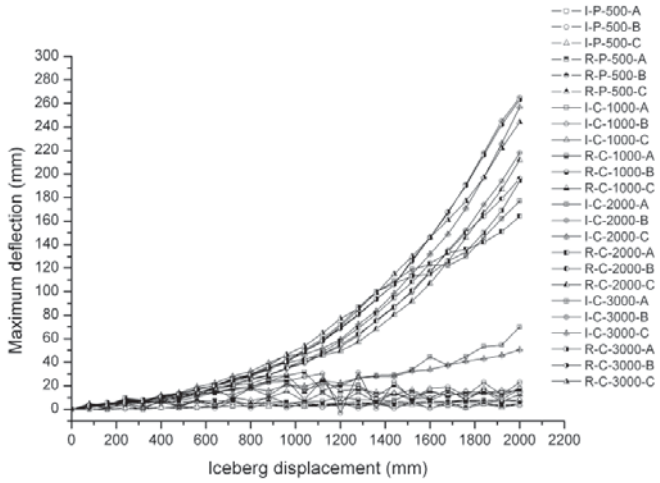

Figure 8. Maximum deflection of inner shell with penetration distance.

Energy dissipation ratio discussion

To illustrate the difference between the integrated and rigid analyses, the total internal energy dissipation during the collision was assessed. The total internal energy includes the eroded internal energy, as we have element erosion in most cases.

The total internal energy for the integrated analyses is normalised to that of the corresponding rigid analyses, as shown in Figure 9. The internal energy ratio in the first group (I-P-500-A,B,C) is far from being 1, which can only be described by the integrated analyses. The rigid analyses in such cases (“sharp”) may overestimate the internal energy and produce a design that is too conservative. The ratio in this group increases with the penetration distance, which indicates the increasing stiffness of the iceberg. The second and third group (I-C-1000-A,B,C and I-C-2000-A,B,C) show the same trend. The internal energy ratios for types A and C are smaller than 1 and almost equal to 1 for type B in both groups in which the points of collision are located in less-supported areas.

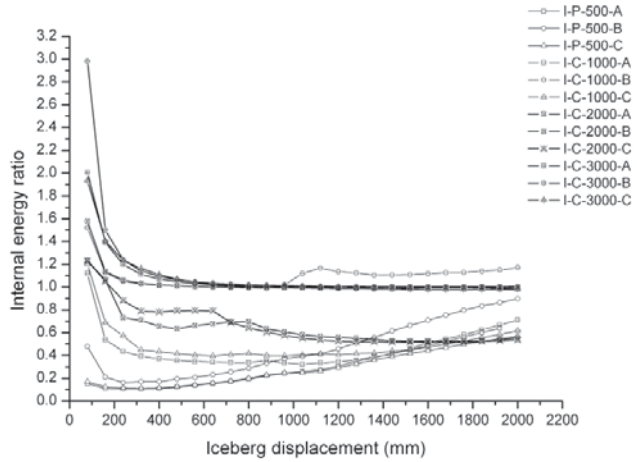

Figure 9. Internal energy ratio between the integrated and rigid analyses.

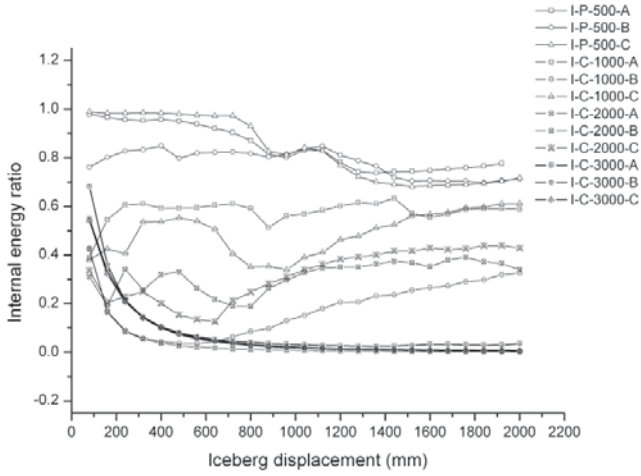

Figure 10. Internal energy ratio between icebergs and the total energy for integrated analyses.

Another interesting feature is shown in Figure 10. The internal energy ratio between the iceberg and the total energy is summarised for all of the integrated analyses. A ratio equal to 1 indicates that the internal energy goes to the iceberg, while the side structure is intact and has no contribution; on the contrary, if the ratio equals 0, then the side structure endures the deformation, while the iceberg remains stiff. It is shown that the internal energy ratio is close to 1 in the first group (I-P-500-A, B, C), where the iceberg is crushed, and the structure is kept intact. The influence of the collision location is also observed. The second group (I-C-1000-A,B,C) shows that the iceberg and the structure contribute almost equally to the total internal energy, except for case I-C-1000-B where the side structure is less supported. The ratio in the third group (I-C-2000-A, B, C) is smaller than 0.5, which means that the side structure contributes more than the iceberg to the internal energy. The iceberg is becoming stiff and more of

the structure is crushed. The iceberg in case I-C-2000-B is almost as stiff as it is rigid as the ratio is close to 0. The last group (I-C-3000-A, B, C) shows that the iceberg in this scenario is almost the same as that in the rigid case. All of the internal energy is contributed by the side structure.

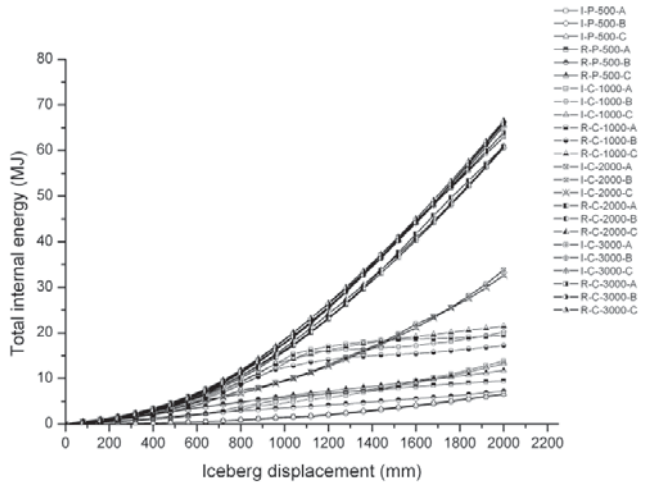

Figure 11. Total internal energy with the iceberg displacement for all cases.

Discussion and conclusions

The results presented previously show the details of the integrated and rigid analyses, which are mainly focused on the internal mechanics, local deformations and energy dissipation. To place the internal mechanics into a practical context, the introduction of the external mechanics is necessary. Figure 11 shows the values of the total internal energy for all cases analysed. Based on these results, we consider case I-P-500-B as an example. The total internal energy is 6.5 MJ at a displacement of 2000 mm. Based on the work by Liu and Amdahl [2], it can be estimated that roughly 40% of the maximum possible impact energy will be dissipated in this scenario, which yields 16.25 MJ. If we assume a ship with a size of 150,000 t, the corresponding iceberg size will be 1605 t. In such a case, the ship will mostly crush the iceberg, and no penetration will be initiated. The maximum deflections of the outer and inner shell are 328 mm and 7.5 mm, respectively, which are obtained based on Figures 6 and 8. Other scenarios may follow the same procedure to obtain the extents of damage.

Finally, the following conclusions can be highlighted based on the present numerical study:

- The steel model by Alsos et al.(2009) [5] and the iceberg model by Liu et al. [7] are successfully coupled to simulate the side-ship and iceberg collision;
- The iceberg profiles in the present study have been simplified by revolving a parabolic or a circular line about an axis. An iceberg with a parabolic profile ($y = 1/500\,x^2$) will be crushed by a ship, and an iceberg with a circular line profile ($Y^2 + (X - r)^2 = r^2, r = 3000$ mm) is sufficiently stiff to crush the side structure. When $r = 1000$, 2000 mm, the iceberg and side structure share the energy during the collision in the integrated analyses;

- In the rigid analyses, the "sharp" profiles, the first and second profiles ($y = 1/500\,x^2$ and $Y^2 + (X - 1000)^2 = 1000^2$), penetrate the side structure. In the integrated analyses, no fracture is observed in the side structure in all cases;
- The collision location shows significant influence when both the iceberg and side structure endure large deformation, for example, the second and third groups (I-C-1000-A,B,C and I-C-2000-A,B,C). The web frame and stringer provide support for types A and C and increases the side structure stiffness significantly compared to type B, where the location of collision is in the middle of the spacing;
- The integrated analyses differ very much from the rigid analyses in most cases. Moreover, the difference is highly dependent on the iceberg profiles. The iceberg with a "sharp" profile shows the greatest difference, while the "blunt" profile shows little difference. In the present study, when the radius of the circle profile is greater than 2000 mm, the iceberg will be as stiff as it is rigid; thus, the rigid analysis is valid in such cases.
- However, it is still quite difficulty to quantify the definitions of "sharp" and "blunt" icebergs. It is recommended to consider the damage of both ship and iceberg at the same time. More work is needed before a general conclusion is derived.

Acknowledgement

This work was carried out through the collaboration of the programmes "ScenaRisC&G" and "PetroArctic" at NTNU, both funded by the Norwegian Research Council. The authors wish to thank the Norwegian Research Council for supporting this research.

References:

[1] Terndrup Pedersen P. and S. Zhang, *On Impact mechanics in ship collisions.* Marine Structures, 1998. 11(10): p. 429-449.

[2] Liu Z. and J. Amdahl, *A new formulation of the impact mechanics of ship collisions and its application to a ship-iceberg collision.* Marine Structures, 2010. 23(2010): p. 360-384.

[3] Liu Z., J. Amdahl, and S. Løset. *Numeric simulation of collisions between ships and icebergs*. *International Conference on Port and Ocean Engineering Under Arctic Conditions*. 2009. Lulea, Sweden.

[4] Liu Z., J. Amdahl, and S. Løset. *Integrated numerical analysis of an iceberg collision with a foreship structure.* Marine Structures (in press).

[5] Alsos H.S., J. Amdahl, and O.S. Hopperstad, *On the resistance to penetration of stiffened plates, Part II: Numerical analysis.* International Journal of Impact Engineering, 2009. 36(7): p. 875 - 887.

[6] Alsos H.S. and J. Amdahl, *On the resistance of tanker bottom structures during stranding.* Marine Structures, 2007. 20(4): p. 218 - 237.

[7] Liu Z., J. Amdahl, and S. Loset, *Plasticity based material modelling of ice and its application to ship-iceberg.* Cold Regions Science and Technology, 2011. 65(3): p. 326-334.

PAPER V

Liu Z., Amdahl J.

Numerical and simplified methods for analysis of the residual strength of ship double bottoms

Submitted to:

Ocean Engineering

Numerical and simplified methods for analysis of the residual strength of ship double bottoms

Zhenhui Liu, Jøgen Amdahl

Department of Marine Technology, Norwegian University of Science and Technology, 7491, Trondheim, Norway

Abstract

This paper presents a numerical simulation and simplified methods for estimating the residual strength of a damaged double bottom. A typical double-bottom structure from a shuttle tanker was modelled. The structure was idealised to a small degree. Imperfections were introduced to the whole structure according to design rules. The most severe situation of the fully loaded condition was investigated. Hull girder bending was considered. Damage was caused by a variety of indenters that were specially designed to obtain a desired damage profile. A total of 16 numerical-calculation cases were investigated using the explicit commercial code *LS-DYNA 971*. A simplified method was derived. This method includes elastic plus rigid-plastic analyses of a 3-span, single-stiffener model. Unlike Smith's method, the present approach takes damaged stiffened panels into account in the residual strength assessment. The elastic and rigid-plastic analyses were combined to provide the load-end shortening curve for the damaged stiffeners. A simplified damage mechanism for the tripping of stiffeners is presented, as is a 3-span single stiffener model with proper boundary conditions. Both the analytical and single stiffener models were used to estimate the residual strength of a damaged double bottom. Both methods were validated with *Non-linear Finite Element Analysis* (*NLFEA*) simulation.

Keywords: residual strength, rigid-plastic analysis, shortening curve

1. Introduction

Ships are always at risk of encountering accidental loads during their service time, such as collision, grounding, and dropped objects. Whenever these accidents occur, the residual strength of the ship's structure becomes a key issue. In this study, the residual strength of a damaged double bottom was investigated.

No general consensus exists on how to characterise damage. The damage profile depends on the shape of the sea floor and the motion of the ship during grounding, as discussed by A.Hagbart and J.Amdahl (2007) [1]. Depending on the grounding scenario, a large part of the bottom may be subjected to damage. Damage in the form of the lateral denting of stiffeners and the associated plate flange between adjacent frames was studied in the present paper to minimise the number of variables. The dent depth was varied, as was the width of the dented area (i.e., the number of dented stiffeners). To preserve the plastic deformations and residual stresses generated during the denting phase, the entire process was analysed in two steps: the denting process and the subsequent compression phase.

The numerical analyses that were conducted were cumbersome. To establish a potential alternative simplified calculation model, a new analytical method and a 3-span, single stiffener model were established. Both methods were able to provide the load-end shortening characteristics for the damaged stiffened panels. Based on this, an effective and quick estimate of the residual strength of a damaged double bottom was achieved.

The method first proposed by Smith (1977)[2] and later developed by Yao and Nikolov (1991,1992) [3, 4] has been widely used to assess the residual strength of damaged ships. Smith and Dow (1981) presented a general review on how to calculate the residual strength of damaged ship structures and offshore platforms. Zhang et al. (1996)[5], Paik et al. (1996)[6] and Wang et al. (2002)[7] have all proposed analytical methods for calculating residual strength. Soares et al. (2008)[8] performed a benchmark study on the use of simplified structural codes to predict the ultimate strength of a damaged ship hull. They concluded that the simplified method based on Smith's assumption is valid for predicting residual strength. In any case, neglecting damaged structures when calculating the residual strength is not always acceptable, especially when the damage level is relatively small. In such cases, a damaged stiffened panel can still provide a significant contribution to the total strength. Based on the DNV ship rules (2009)[9], calculating the strength of hull girders should be based on the shortening curves of each structure element on the cross section and also on the location of the neutral axis.

As to intact stiffeners, significant amount of work has been conducted on the ultimate strength of intact single stiffeners with adjacent plate flanges by Faulkner (1975)[10], Soares and Gordo (1997)[11], and Paik and Kim (2002)[12], among others. By contrast, there have been few studies on the compressive resistance of damaged stiffened panels. The present paper is the first study on deriving the shortening curve for damaged stiffeners. The elastic and rigid-plastic methods are adopted as a simplified means for accessing the residual strength of damaged stiffeners. This method has been widely used by researchers, for example, see Murray (1973)[13], Louca and

Items	Value
total length	264.68m
length between pp	256.50m
breadth modeled:	42.5m
width modeled	22.0m
design draft	15.0m
scanting draft	15.65m
design dead weight	119.315 mt

Table 1: Main dimension of shuttle tanker

Harding (1994)[14], Paik and Pedersen (1995)[15], Cui and Mansour (1998)[16] and Amdahl (2004)[17].

The present method follows Amdahl's method (see Amdahl, 2004) and combines it with elastic analysis to obtain the shortening curve for damaged stiffeners. At the same time, a 3-span, single stiffener model with the proper boundary conditions was also investigated. Both of these results were validated through NLFEA simulations. In the simulations, both geometric and material nonlinearities were taken into account. Imperfections corresponding to the rule tolerance requirements were embedded in a finite element (FE) model of the entire double bottom model through a user-defined subroutine. The initial damage (dent) and associated residual stress were obtained through the CONTACT algorithm in the explicit computer code LS-DYNA 971, as in Hallquist (2006). Material hardening was modelled by means of Ludwik's formulation, as in Ludwik (1909). To illustrate this approach, a typical double bottom structure of an oil tanker was modelled and will be described in the following section.

2. Model Characteristics

The double bottom structure of a 140,000 m3 shuttle tanker is the subject of the present study.

The cross section is not perfectly symmetrical due to the centre bulkhead; this was neglected, however, and only the starboard side was modelled. A section of 4 frames from frames 65 to 68 in the drawing were modelled, as shown in Figure 1. This selection was considered large enough to allow the longitudinal redistribution of stress/strain after damage. The structure was slightly idealised compared to the structure as built; a longitudinal girder was shifted slightly to have an uneven number of stiffeners, and the double bottom height was constant. Initial analyses showed that transverse webs might buckle vertically due to the high loads transferred during the denting phase. This effect obscured the results; hence, the thicknesses of frames 66 and 67 in the middle were increased by 75% to avoid buckling. The main dimensions of the FE model and the profile of the stiffeners are shown in Figure 1.

The plastic behaviour was thoroughly considered in the material modelling. In this study, the true stress-strain relationship of the material in the plastic range was described by the Ludwik relation in the form of a power law, $\sigma = \sigma_0 + K(\epsilon^p)^n$, where σ_0 is the yield stress, and ϵ_p is the effective plastic strain. The following parameters were based on experimental test data: σ_0=275

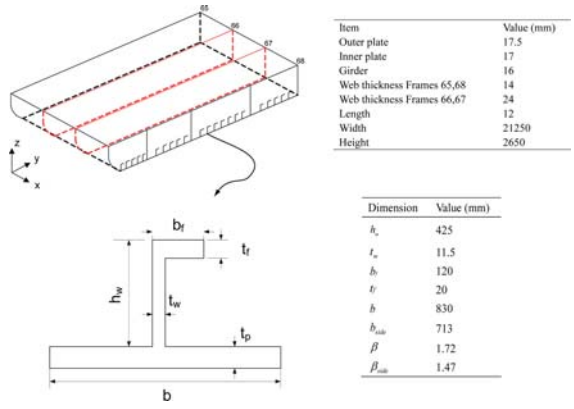

Item	Value (mm)
Outer plate	17.5
Inner plate	17
Girder	16
Web thickness Frames 65,68	14
Web thickness Frames 66,67	24
Length	12
Width	21250
Height	2650

Dimension	Value (mm)
h_w	425
t_w	11.5
b_f	120
t_f	20
b	830
b_{stiff}	713
β	1.72
β_{stiff}	1.47

Figure 1: Profile and dimensions of the double bottom model

MPa, K=740, and n=0.24. Ruptures were not taken into account (i.e., infinite strains were allowed, in principle).

2.1. Imperfections

Due to the manufacturing process, residual welding stresses and distortions are unavoidably introduced. Sherbourne (1960) examined the effect of imperfections and demonstrated an appreciable reduction in the maximum load capacity, even for small initial deflections. Hence, it was necessary to represent imperfections properly to achieve reliable results from the NLFEA. The actual shape of an initial defect is fabrication-dependent, complex and generally unknown.

For design purposes and for parametric studies of compressive strength, equivalent imperfections are frequently introduced. Due to a lack of data, the shape is assumed to be compatible with the critical buckling mode as far as possible, and the magnitude is typically equal to the fabrication tolerance. Figure 2 illustrates the imperfections used in this study for the following:

- the plate between stiffeners
- the stiffeners between the frames
- the panel between the transverse frames and longitudinal girders
- the tripping mode of the stiffeners and
- the plates between the stiffeners on girder

A 'sine curve' shape is generally assumed to represent the initial defect. Imperfections are introduced into the FE model by means of the following formulas:

$$f(z) = \sum w_{ij} \sin(\frac{m\pi}{a_i}x) \sin(\frac{n\pi}{b_j}y) \quad (1)$$

$$f(y) = \sum w_{ij} \sin(\frac{m\pi}{a_i}x) \sin(\frac{n\pi}{b_j}z) \quad (2)$$

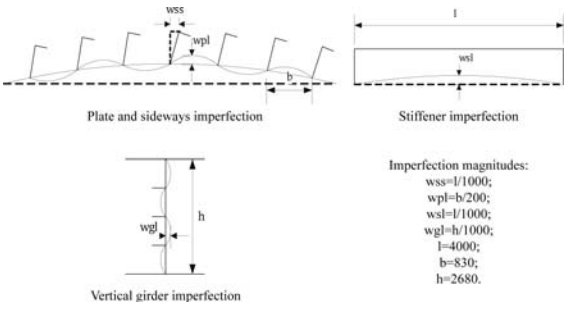

Figure 2: The imperfections and their magnitudes

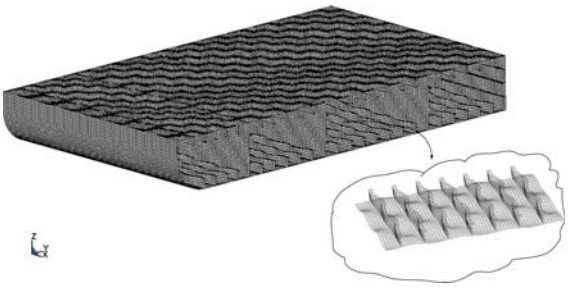

Figure 3: An illustration of imperfection in present FE model (scale factor 20)

where x, y, z are the coordinates of the nodes, m, n are the numbers of the half-waves, $f(z)$ is for the plates and stiffeners and $f(y)$ is for the girders. Here m, n were coincidently set as to the global buckling mode, and we set $m = 5$ for the plate- and girder- induced longitudinal imperfection. The value of n was always equals to 1, which causes asymmetrical waves transversely. The amplitudes are identical to those used by the PULS code (2001) [18], except that the amplitude for the girder was set according to the DNV(2004) rule [19]. The imperfections, although being nominal, are considered to represent the combined effects of the residual stresses and the initial distortions.

The global mesh size was 120mm and the elements used were the five integration points of quadrature element. The final finite element model is shown in Figure 3.

2.2. Loads

The tanker was assumed to be in the fully loaded condition. The corresponding draft was 15m and the oil-pressure height was 19m. Thus the water and oil pressures were set to 0.15 MPa and 0.161 MPa, respectively. The bottom damage caused by contact with the sea floor is created by rigid indenters, with given slopes in the transverse direction and the longitudinal directions. The indenter was 'stretched' in the transverse directions to allow 1,3,5,7 and 9 stiffeners to be damaged in Cases a,b,c,d and e, respectively (Case e has 2 girders). As seen from Fig. 4, the indenter has the same shape factors α, β if the denting depth $\delta$is the same. Specially, $\alpha = \arctan(\frac{\delta}{d})$ and $\beta = \arctan(\frac{\delta}{k})$, where $d = 800, k = 1500$. Three denting depths (δ), nominally

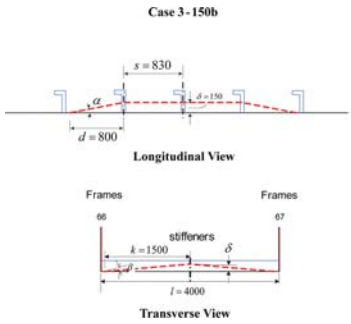

Target indentation	No. of damaged stiffeners	Notation
50	1	50a
50	3	50b
50	5	50c
50	7	50d
50	9	50e
100	1	100a
100	3	100b
100	5	100c
100	7	100d
100	9	100e
150	1	150a
150	3	150b
150	5	150c
150	7	150d
150	9	150e

Figure 4: An illustration of the indenter for Case 3-150b and the notations used in the present study.

50mm, 100mm and 150mm, were simulated. Additonally, the simulation contains a loading and unloading procedure. After the indentation process is finished, the indenter is unloaded from the model. Due to the elastic deformation caused by the indentation, some rebound took place; thus, the residual indentation depth generally differed from the target value by approximately 10%. The denting is conducted in the midsection between the adjacent transverse frames 66 and 67, as in Figure 4.

The indenter is placed 10 mm lower than the base plane in order to avoid of initial penetration .Contact between the indenter and the outer shell is obtained by means of the automatic surface contact algorithm in *LS-DYNA*[20]. Subsequent to the introduction of the damage, the double bottom is subjected to compression created by the forced inward displacement of the boundaries. The forced displacement should mimic the global bending of the hull girder. In pure bending and in the elastic phase the displacement will vary linearly over the double bottom height as illustrated, as illustrated in Figure 5.

The correct inward displacement, or rate of displacement, of the double bottom was obtained by introducing an angular rate of rotation w, in addition to the mean inward speed,V_0 , whic is given by:

$$\frac{V_0}{V_0 + wh/2} = \frac{H - h/2}{H} \tag{3}$$

so

$$w = \frac{2}{2H - h} V_0 \tag{4}$$

where H is the height of the neutral axis above the keel and h is the height of the double bottom.

2.3. Boundary Conditions

As shown in Figure 6, the boundary conditions are divided into three groups: the forward (FOR) frame, the afterward (AFT) Frame, and the centre nodes. The six-degree constraints for all three groups are found in Figure 6, in which 1 indicates fixed and 0 indicates free. The symmetry conditions were imposed on the center line nodes. The nodes for the AFT. and

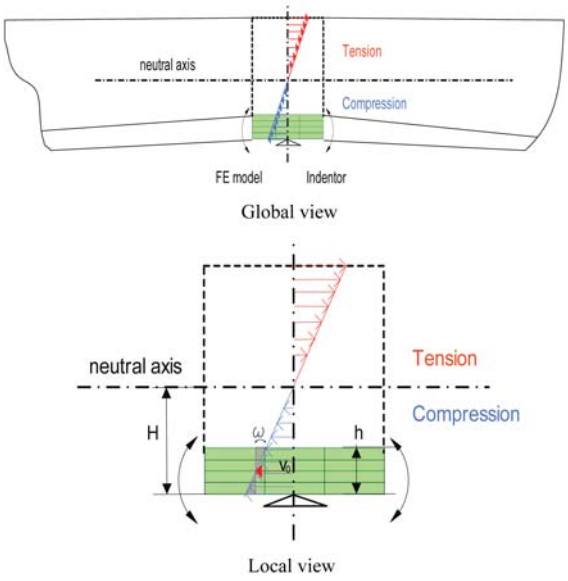

Figure 5: Simplification of the axial loads.

FOR. frames are rigidly connected and behaved as a rigid section. The nodes for the AFT. frame were fixed on the X,Y and Z displacements, and the rotation was free about the Y-axis. A bending moment was applied. The nodes on the FOR. frame had fixed displacement on the Y-axis and fixed rotation about the Z-axis. These conditions were due to the combined compression and bending loads added to these nodes in the simulation. These boundary conditions cause the membrane forces during the denting stage in the simulation to be balanced by the middle span of the total double bottom structure.

	X	Y	Z	RX	RY	RZ
AFT. Frame	1	1	1	1	0	1
FOR. Frame	0	1	1	1	0	1
Nodes Center	0	1	0	0	0	1

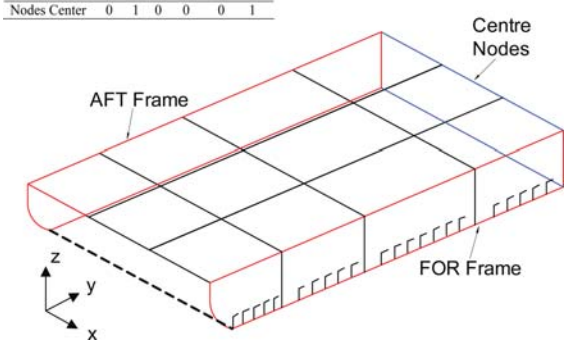

Figure 6: The boundary Conditions.

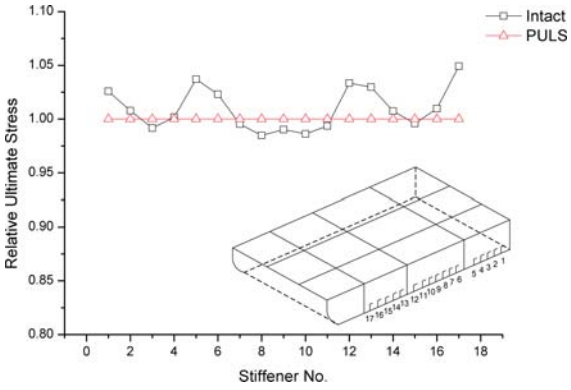

Figure 7: The relative ultimate strengths of the individual stiffeners as predicted by *LS-DYNA* and PULS' prediction for the intact case.

3. Simulation Results

The simulations were conducted using the explicit dynamic code LS-DYNA on Xeron 64 EMT platform servers running the Linux 2.4.21 OS. The average computation time was 5 hours for each case when using 4 CPUs. The detailed results will be presented in following subsections.

3.1. Comparison with PULS

According to DNV (2004b)[21], PULS is a recognized computer code for calculating the ultimate strength of stiffened plates and is an accepted tool for checking the design of ship panels. The PULS code is based on a series expansion of plate deformations combined with a numerical solution strategy. In the present work, a comparison with PULS for the intact case was made to verify that the LS-DYNA 971 simulations provide good estimates of the ultimate strength.

A target damaged stiffened panel in the outer bottom was selected for the comparison. Figure 7 shows the ultimate strength (i.e., the maximum stress level through each individual stiffener in the outer shell panel). The results from LS_DYNA 971 agree quite well with those from PULS. The stiffeners midway between the longitudinal girders (stiffeners 3, 9 and 15) have larger defects due to the effect of sea pressure. Thus, they attain a lower ultimate strength than those close to the longitudinal girders. This NLFA model proved to be capable of providing reasonable results.

3.2. The residual strength of the double bottom

The effect of damage to the stiffeners is to reduce their ability to sustain compressive forces. Due to the difference in the rate of inward displacement caused by global bending, the inner plate and outer plate will buckle non-simultaneously. Figure 8 shows a typical force-end shortening relationship for the double bottom. It consists of two peaks, denoted by A and B, which correspond to the buckling of the outer bottom plating and inner bottom plating, respectively. The distance between peaks A and B is dependent on the ratio between the height of the double

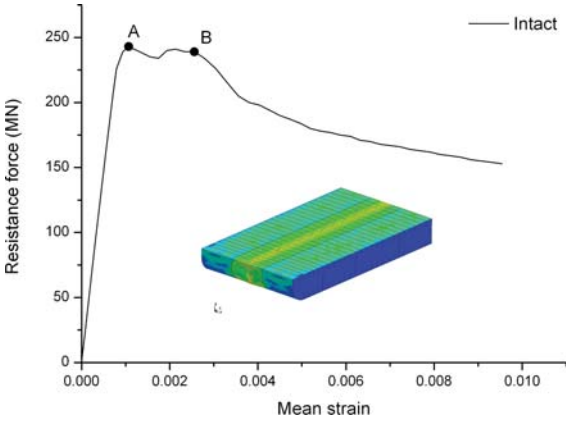

Figure 8: The resistance force and shortening relationship for Case1-Intact

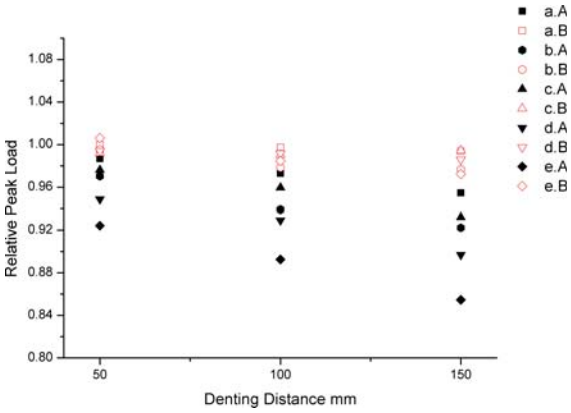

Figure 9: Peak load comparison for all the normalized cases versus the resistance in the intact condition (note that: a,b,c,d and e denote the indenter types and A,B denote the peak loads for A and B, respectively).

bottom h and the location of the neutral axis of the hull girder H. It is due to both h and H determining the shortening rate difference, $\Delta\dot{\epsilon}$, between the inner and outer bottoms. $\Delta\dot{\epsilon}$ can be expressed as follows:

$$\Delta\dot{\epsilon} = \frac{wh}{l} = \frac{1}{(\frac{H}{h} - 0.5)l} V_0 \tag{5}$$

where l is the stiffener length.

The two normalised peak loads are summarised in Figure 9. It is interesting to observe that for a given number of damaged stiffeners, the peak resistance B shows relatively low small sensitivity to the level of indentation, whereas the resistance A to the buckling of the outer panels is significantly more sensitive. In other words, the initial buckling is considerably influenced by the degree of denting, whereas the resistance of the damaged stiffeners, which are well into the post-collapse region at point B, depends only weakly on the degree of denting.

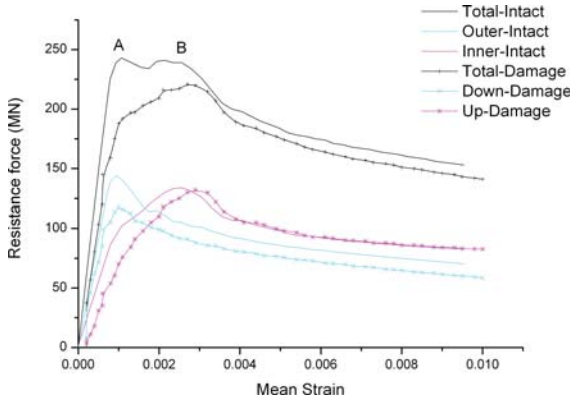

Figure 10: Ultimate strength of the bottom,Case intact and Case 150d

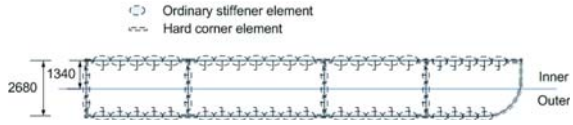

Figure 11: Configuration of ordinary stiffener element and hard corner element

The reason for this difference is the decreased degradation of the resistance in the post-buckling region at point B relative to the ultimate resistance at point A for the damaged stiffeners. This is illustrated in Figure 10 for the case intact and the case150d. This figure indicates that the residual strength of the double bottom is the sum of the inner bottom and outer bottom strengths. The different shortening rates for the inner and outer bottoms are evident. Although the ultimate strength of the double bottom may be attained at peak A in the intact case, (i.e. at the initiation of buckling of the stiffeners in the outer bottom), the maximum load on the damaged panel is more likely to be attained at peak B(i.e. when the inner bottom stiffeners buckle).

4. Prediction of the residual strength

The key point for predicting the residual strength of a damaged double bottom is obtaining the force end-shortening curve both for the intact and damaged stiffeners. As for the intact stiffeners, they are determined by the common structural rules for oil tankers, see DNV(2009) [9]. As illustrated in Figure 11, the double bottom model was divided into an ordinary stiffener element and a hard corner element. To illustrate the difference, the entire double bottom structure was categorized into two halves; the inner bottom and the outer bottom. The total strength of the double bottom was obtained by summing the resistances of all the elements of the inner and outer bottoms for a give strain.

The present case involved significant hydrostatic pressure that could not be ignored, see X.Wang (1997) [22]. Hence, the shortening-curve had to be adjusted to consider the pressure effects. A large number of stiffeners (all L shaped) have been investigated, see Figure 12.

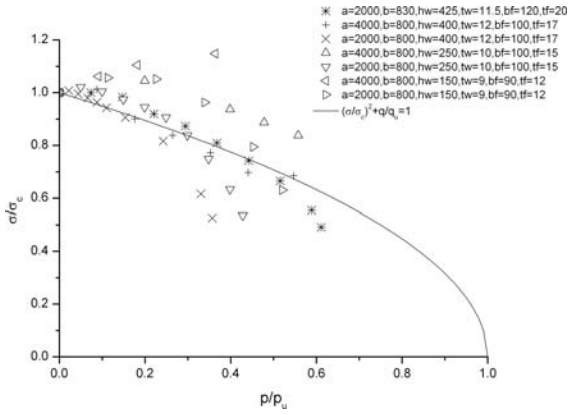

Figure 12: The study of pressure influence to the stiffener ultimate strength (plate thickness 17.5mm)

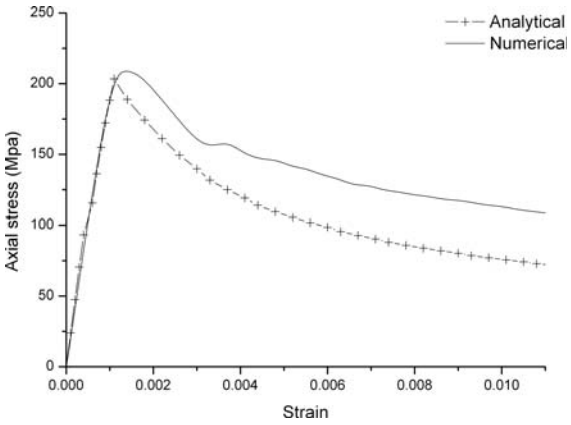

Figure 13: Prediction of the intact stiffener shortening curve based on DNV(2009)[9]

The simple interaction equation proposed by Faulkner (1979) [23] was adopted:

$$(\frac{\sigma_x}{\sigma_c})^2 + \frac{p}{p_u} = 1 \tag{6}$$

where σ_x is the axial stress, σ_c is the axial critical stress without pressure, p is the pressure and p_u is the ultimate pressure corresponding to the collapse load for the three hinge mechanism. The peak resistances in the analytical results agree quite well with those of the simulations. However, the post-buckling strength is underestimated by the analytical method relative to the numerical results, (Figure 13). Consequently, the analytical method gave a conservative prediction for the strength of the double bottom.

Obtaining the the shortening curve for damaged stiffeners is a challenge. First, it can be seen from the damage pattern shown in Figure 14 that a tripping mode of deformation is indicated by the relatively large lateral distortion. The tripping makes simplified analytical calculations difficult. Second, it can be seen

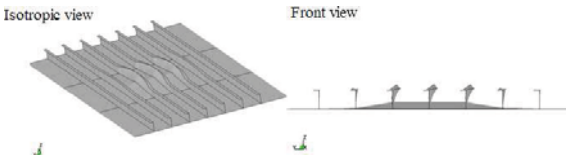

Figure 14: The damage pattern after the denting process (e.g. Case7_150b)

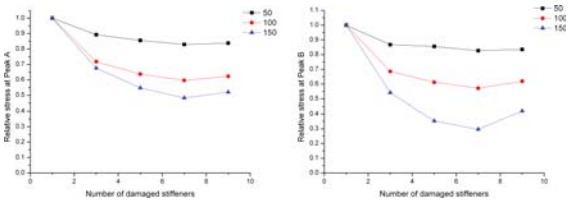

Figure 15: The ultimate stresses of stiffener 9 at Peak A (left) and Peak B (right)

from Figure 15, that the ultimate resistance and also the post-buckling strength of the double-bottom center stiffener (stiffener No.9 as defined in Figure 7) are virtually constant when at least five stiffeners are damaged. For Case a, in which only one stiffener is damaged, the two adjacent stiffeners strengthen the resistance of the centre stiffener. Case b is less influenced by the undamaged stiffeners but still shows similar strength, especially for the strength at Peak A. Based on this observation, it was assumed that the centre damaged stiffener would have the same ultimate strength in Cases b, c, d and e. Case a was not considered in the present approach.

4.1. The Elastic and Rigid-plastic method

To obtain the resistances of compression members, it is often useful to combine elastic analysis with the rigid-plastic analysis mentioned earlier. The resent approach is a further application of the method presented in Amdahl(2004) [17].

4.1.1. Elastic analysis

The end shortening in the elastic domain consists of one component due to axial straining and one due to bending:

$$\delta^e = \frac{Nl}{EA} + \frac{\pi^2}{l}\frac{\delta_0^2}{(1-\frac{N}{N_E})^2} \tag{7}$$

where $\delta^e$is the elastic axial shortening, N is the axial force, l is the length of stiffener,E is elastic modulus, $A$is the section area of the stiffener,$N_E$is the Euler column force and δ_0 is the imperfection amplitude. In the case of the denting of stiffeners, the elastic shortening curve should be corrected. The final shortening is:

$$\delta^e + \delta_0 \cong \delta^e + \frac{2w_0^2}{l} \tag{8}$$

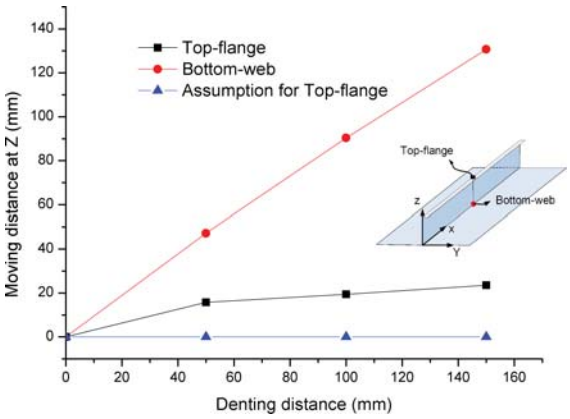

Figure 16: The damage shape of the stiffener.

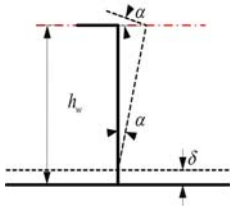

Figure 17: The simplified damage mechanics at the cross section of stiffener.

4.1.2. Rigid-plastic analysis

Assuming the material to be perfectly plastic, the $N-M$ relationship of the cross section of the stiffener can be derived (Appendix Appendix A). Four stages have been defined, depending on the magnitude of the axial force (Appendix Appendix A). A simplified mechanism based on observations from the simulations was used to take the tripping into consideration.

The plots in Figure 16, demonstrates that the top-flange is displaced very little in all of the denting cases. Hence, it is simply assumed that the top flange does not displace at all (see the blue line in Figure 16). Obviously, the assumption is incorrect if the denting distance exceeds the web height. The assumption is conservative for small dents, but yields more reasonable results if the denting distance is large

The model for a dented stiffener is shown in Figure 16.The following relations apply:

$$h_w^e = h_w - \delta \tag{9}$$

$$\cos(\alpha) = \frac{h_w^e}{h_w} \tag{10}$$

and

$$b_f^e = b_f \cos(\alpha) \tag{11}$$

where h_w^e, b_f^e are the effective web height and flange width after damage and α is the tripping angle. The effective web height and flange width are used instead of h, b when calculating the section properties in the $N-M$ relationship.

An additional equation is needed to solve the $N-M$ equation. The external equilibrium equation for the axial force and moment at the centre was based on rigid beam mechanism (Appendix Appendix B).

Finally, based on the above $N-M$ relationships, the axial force N can be obtained explicitly. Then the axial stress was obtained by:

$$\sigma = \frac{F}{A} = \frac{N\cos(\theta') + Q/2\sin(\theta')}{A} \tag{12}$$

where F is the axial force, A is the cross secion area of stiffener, Q is resultant force caused by hydrostatic pressure,θ' is the beam deflection angle, see Appendix Appendix B.

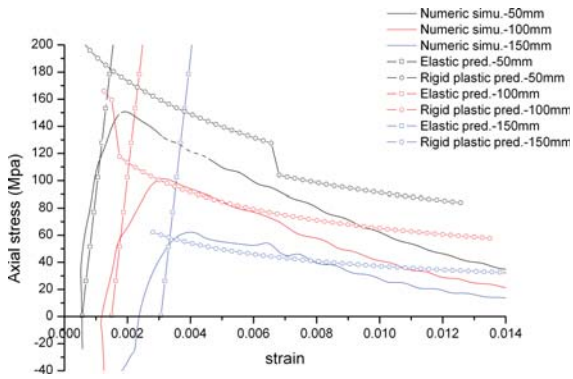

Figure 18: A comparison between elastic rigid-plastic and numeric analysis.

4.1.3. Validation

This elastic and rigid-plastic analysis was validated by comparing the numerical simulation with the analytical deviation (Figure 18).

Because of the previous denting stage, it can be seen that the average stress-strain curve for damaged stiffeners does not start from zero strain. Generally good results were obtained. As expected, the larger denting distance yielded better results than the smaller one. The residual strength of the damaged double bottom is calculated using the procedure for damaged stiffeners in combination with the methods described in DNV (2009) [9] for intact stiffeners..

4.2. Finite element analysis of 3-span single stiffener

A significant reduction in the computational effort is achieved if the force-end shortening curve for the damaged stiffeners can be predicted by simulating individual stiffeners. A key issue in this context is obviously the proper boundary conditions, notably with respect to the behaviour of the plate long edges and the rotational restraint of the stiffener at the boundaries.. A reasonable assumption may be to assume that the long edges are free to move but are constrained to be straight. The fixity of the stiffener at the boundaries depends heavily on the

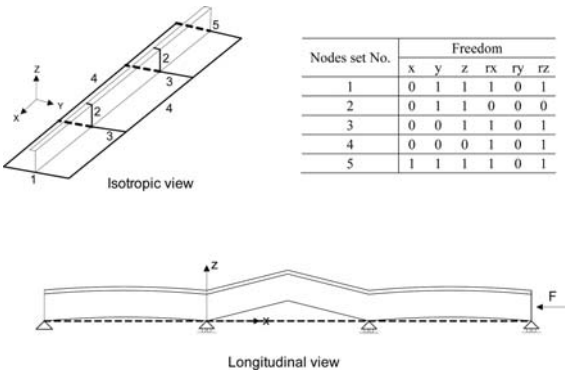

Nodes set No.	Freedom					
	x	y	z	rx	ry	rz
1	0	1	1	1	0	1
2	0	1	1	0	0	0
3	0	0	1	1	0	1
4	0	0	0	1	0	1
5	1	1	1	1	0	1

Figure 19: Illustration of the boundary conditions and the damage pattern for the single stiffener model.

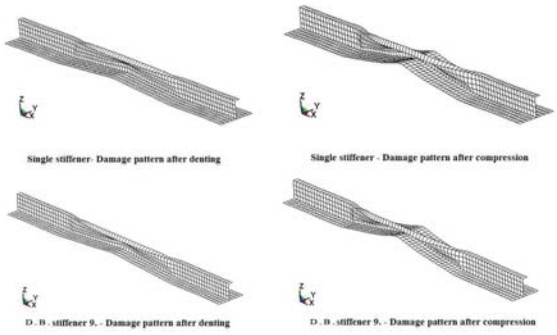

Figure 20: Comparison of the damage patterns of the single model and Case150c in D.B.

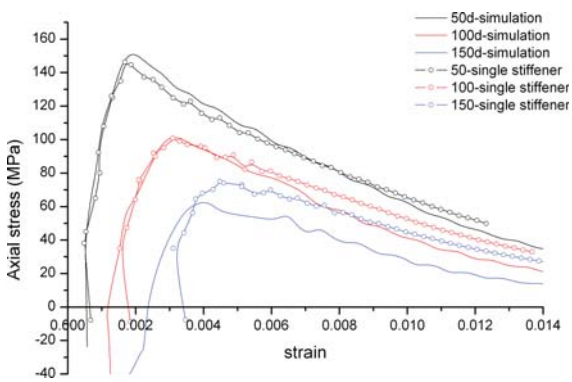

Figure 21: The single stiffener model and the numeric simulation

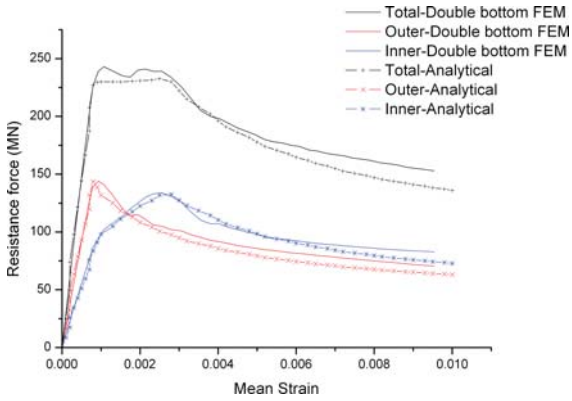

Figure 22: Prediction 1: the intact case

level of hydrostatic pressure. The uncertainty is significantly reduced by using a three-span model. The boundary settings as shown in Figure 19 were applied.

Figure 20 shows that the single stiffener model with the selected boundary conditions captures the damage mode of the double bottom model very well. As demonstrated the force-end shortening relationships in Figure 21,good agreement is obtained with the double bottom predictions, except for the denting distance of 150mm. For such large dents, the simplified boundary conditions do not represent the real deformations.

4.3. Application and validation

With the force-end shortening curves established by the two methods described above, the residual strength of the double bottom could be predicted. The total resistance of the double bottom is found by summation of the resistances of all the ordinary stiffener elements and hard-corner elements. The resistance of the intact stiffeners was based on the DNV (2009) [9], and the resistance of the damaged stiffeners was based on the elastic and rigid-plastic analysis or the single stiffener model. All of the damaged stiffeners are assumed to have the same shortening curve as the center stiffener (No.9). As mentioned, the strain-history relationship is simplified by the combination of angular velocity and axial displacement and the neutral axis location is assumed to be fixed. For example, the strain history for the outer bottom is $(V_0 + wh)/(3l)$ before the buckling occurs and is changed to $(V_0 + wh)/l$ after buckling is initiated. This simple expression agrees well with the numerical simulations. A computer code was developed for the elastic rigid-plastic analysis and the single-stiffener model. The analytical results were compared with the numerical simulations.

Figure 22 shows the intact case which also validates the shortening curves derived by the common structure code (see DNV(2009) [9]. Excellent agreement was obtained. For the damaged cases, the shortening curves are partly replaced by the elastic rigid-plastic analysis or the single stiffener model results. It is further assumed all of the damaged stiffeners have the same shortening curves. Again, good results were obtained for all the cases, as seen Figure 23-25.

5. Conclusions

On the basis of the numerical and analytical analyses, the following conclusions can be drawn.

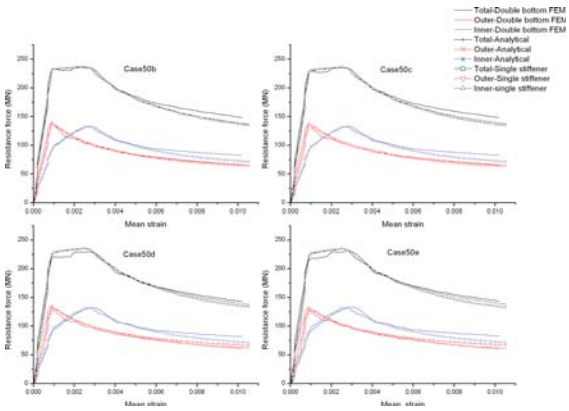

Figure 23: Prediction 2: the 50mm denting cases

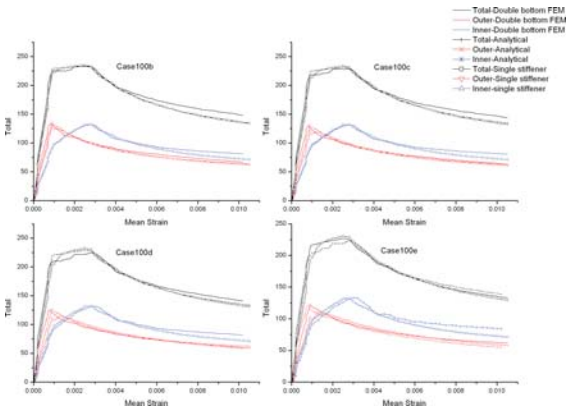

Figure 24: Prediction 3: the 100mm denting cases

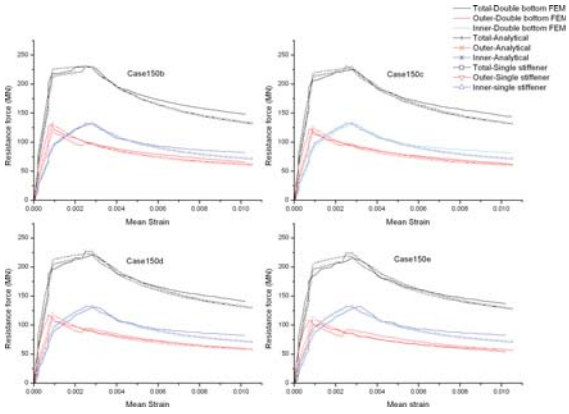

Figure 25: Prediction 4: the 150mm denting cases

- The damage caused by the indentation of the bottom stiffeners primarily affects the load-bearing capacity of the stiffeners that are directly subjected to the damage;
- The height of the double bottom and the location of the neutral axis have a substantial influence on the resistance force of the double bottom. This influence is because together they determine the difference in the end-shortening rate between the inner and outer bottoms;
- The peak resistance (buckling strength) of an individual stiffener is significantly affected by the indentation level, but the post-buckling resistance at the point of ultimate resistance of the entire double bottom is influenced significantly less;
- The method described in the DNV rules for obtaining the post-buckling strength of a ship's hull was verified to be effective and accurate;
- A simplified damaged mechanism for the tripping behaviour of stiffened plates was developed. Based on this mechanism, the force-end shortening curves can be obtained by means of an elastic and rigid-plastic analysis. This approach constitutes a quick and efficient method for assessing the residual strength of a ship's structure;
- A single stiffener FEM analysis model was proposed. The force-end shortening relationships obtained using the single-stiffener model agree well with those obtained using the double-bottom model;
- The results from the analytical and single-stiffener analysis may be used to effectively determine the residual strength of a double bottom with a large reduction in computation time.

6. Acknowledgements

The present work was conducted within the scope of the Strategic University Programme (SUP) 'ScenaRisC&G' at the Norwegian University of Science and Technology (NTNU), which is funded by the Research Council of Norway (NFR). The authors wish to thank the Research Council of Norway for funding the study. This work is also part of the EU 'Flagship' project. The authors also extend their gratitude to this project for its financial support.

Appendix A. The plastic axial force-bending moment interaction

The $N - M$ Interaction at the cross section, also see Amdahl(2004)[17].

Stage 1: $N \leq N^*$ and $N^* = (\frac{2A_p}{A} - 1)N_p$ (Figure A.1).

$$\frac{M}{M_p} = 1 \tag{A.1}$$

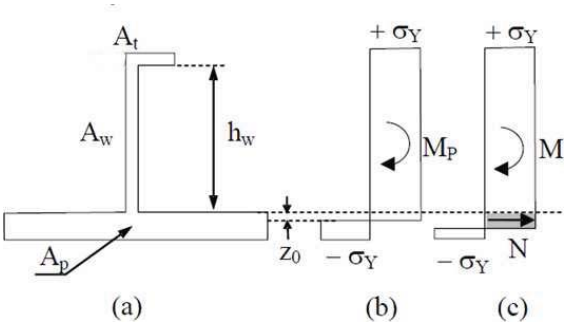

Figure A.1: The plastic stress distribution in stage 1

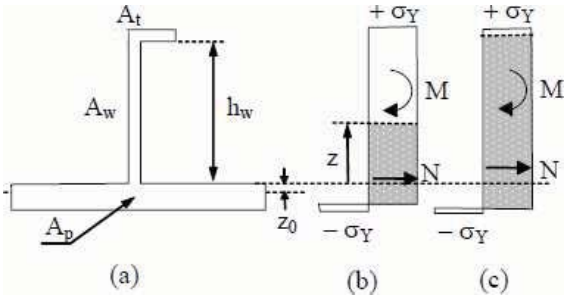

Figure A.2: The plastic stress distributions in stage 2

and

$$F = \frac{M}{M_p} + (\frac{N}{N_p})^{\alpha} - 1 = 0 \tag{A.2}$$

where α is a constant. Stage 2: $N^* < N \leq N^{**}$ and $N^{**} = (1 - \frac{2A_f}{A})N_p$ (Figure A.2).

$$F = \frac{M}{M_p} + (\frac{A}{2A_w})^2 \frac{1}{1 + 2\frac{A_f}{A_w}} (\frac{N - N^*}{N_p})^2 - 1 = 0 \tag{A.3}$$

Stage 3: $N^{**} < N < N_p$

$$F = \frac{M}{M^{**}} + \frac{N - N^*}{N_p - N^{**}} - 1 = 0 \tag{A.4}$$

where $M^{**} = \sigma_y A_f h_w$ Stage 4: $N = N_p$

$$F = 0 \tag{A.5}$$

Appendix B. Force equilibrium

The $N-M$relationship of the global balance equilibrium (Figure B.1).

$$\delta_0 = 2(\frac{l}{2} - \sqrt{\frac{l^2}{4} - w_0^2}) \cong l(1 - \sqrt{1 - (\frac{2w_0^2}{l})^2}) \cong \frac{2w_0^2}{l} \tag{B.1}$$

$$\cos(\theta_0) = \frac{\sqrt{\frac{l^2}{4} - w_0^2}}{l} = \sqrt{1 - \frac{4w_0^2}{l^2}} \tag{B.2}$$

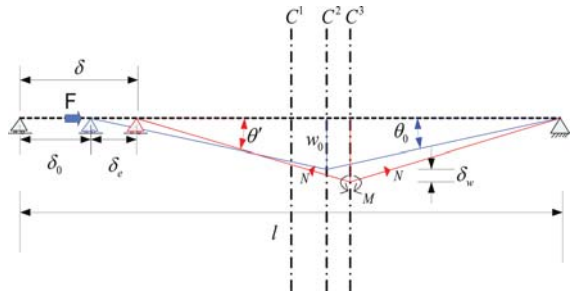

Figure B.1: The external balance mechanism for $N - M$

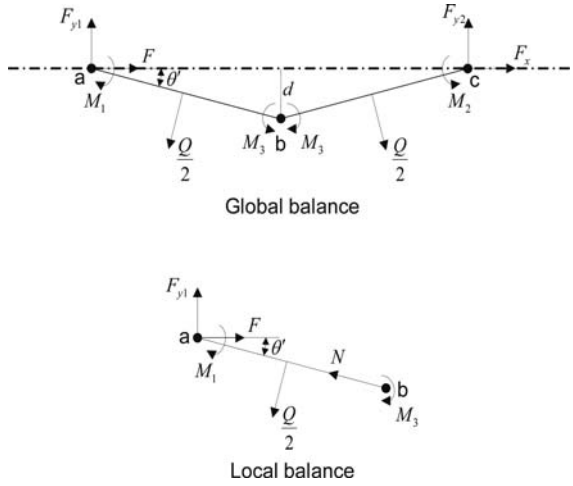

Figure B.2: A demonstration of force and momentum balance

and

$$\delta_w + w_0 = \sqrt{w_0^2 + \frac{\delta_e \sqrt{l^2 - 4w_0^2}}{2} - \frac{\delta_e^2}{4}} \tag{B.3}$$

where w_0 is the initial deflection (denting distance), δ_0 is the initial shortening due to the denting damage, θ_0 is the initial deflection angle, δ_w is the additional deflection, δ_e is the axial shortening and l is the length.

The equilibrium equation:

From the global balance:

$$F_{y1} + F_{y2} - \frac{Q}{2}\cos(\theta') \cdot 2 = 0 \tag{B.4}$$

where $F_{y1}, F_{y2}$are the reaction forces at both ends in the vertical direction and Q is the resultant force caused by the hydrostatic pressure, see Eq.B.9.

For the symmetry condition, we have

$$F_{y1} = F_{y2} = \frac{Q}{2}\cos(\theta') \tag{B.5}$$

From the local balance:

$$F - \frac{Q}{2}\sin(\theta') - N\cos(\theta') = 0 \tag{B.6}$$

where θ' is the deflection angle (Figure B.2). The moment balance to Point b in the local balance (Figure B.2) is:

$$F_{y1} \cdot \frac{l}{2} \cdot \cos(\theta') + F \cdot d - \frac{Q}{2} \cdot \frac{l}{4} = M_1 + M_3 \quad \text{(B.7)}$$

where d is the deflection. It is further assumed that:

$$M_1 = M_3 \quad \text{(B.8)}$$

and

$$Q = Pbl \quad \text{(B.9)}$$

where b is the spacing distance. Substituting Eqs. B.5,B.6, B.8 and B.9 to Eq. B.7, we have:

$$Nd\cos(\theta') + \frac{Pbl^2}{8}(2\cos^2(\theta') - 1) + \frac{Pbl}{2}d\sin(\theta') = 2M \quad \text{(B.10)}$$

Finally, the $N - M$ relationship is established as follows:

$$N(\delta_w + w_0)\cos(\theta') + \frac{Pbl^2}{8}(2\cos^2(\theta') - 1) + \frac{Pbl}{2}(\delta_w + w_0)\sin(\theta') = 2M \quad \text{(B.11)}$$

If $P = 0$, then we have the simplified equation:

$$N(\delta_w + w_0)\cos(\theta') = 2M \quad \text{(B.12)}$$

References

[1] H. S. Alsos, J. Amdahl, On the resistance of tanker bottom structures during stranding, Marine Structures 20 (2007) 218–237.

[2] C. S. Smith, Influence of local compressive failure on ultimate longitudinal strength of ship's hull, in: PRADS, 1977.

[3] T.Yao, P. Nikolov, Progressive collapse analysis of a ship's hull under longitudinal bending., J. Soc.Naval.Arch. of Japan 170 (1991) 449–461.

[4] T.Yao, P. Nikolov, Progressive collapse analysis of a ship's hull under longitudinal bending (2nd report)., J. Soc.Naval.Arch. of Japan 172.

[5] S.-K. Zhang, Q. Yu, Y. Mu, Semi-analytical method of assessing the residual longitudinal strength of damaged ship hull, vol. 4 of *Proceedings of the International Offshore and Polar Engineering Conference*, Los Angeles, CA, USA, 510–516, 1996.

[6] J. K. Paik, P. T. Pedersen, Grounding-induced sectional forces and residual strength of grounded ship hulls, vol. 4, Int Soc of Offshore and Polar Engineerns (ISOPE), Golden, CO, USA, Los Angeles, CA, USA, 517–522, 1996.

[7] G. Wang, Y. Chen, H. Zhang, H. Peng, Longitudinal strength of ships with accidental damages, Marine Structures 15 (2) (2002) 119–138.

[8] e. a. C. Guedes Soares, R.M. Luis, Benchmark study on the use of simplified structural codes to predict the ultimate strength of a damaged ship hull, Int. Shipbuilding Progress 55 (2008) 87–107.

[9] DNV, Common structural rules for double hull oil tankers with length 150 meters and above, Tech. Rep., Det Norske Veritas, 2009.

[10] D. Faulkner, A Review of Effective Plating for Use in The Analysis of Stiffened Plating in Bending and Compression, Journal of Ship Research 19 (1).

[11] C. Guedes Soares, J. M. Gordo, Design methods for stiffened plates under predominantly uniaxial compression, Marine Structures 10 (6) (1997) 465–497.

[12] J. K. Paik, B. J. Kim, Ultimate strength formulations for stiffened panels under combined axial load, in-plane bending and lateral pressure: a benchmark study, Thin-Walled Structures 40 (1) (2002) 45–83.

[13] N. Murray, Buckling of stiffened panels loaded axially and in bending, Struct. Engr. 51 (285).

[14] L. A. Louca, J. E. Harding, A plastic collapse mechanism for the tripping behaviour of flat-bar ring stiffeners in cylindrical shells subject to external pressure, International Journal of Mechanical Sciences 36 (3) (1994) 257–276.

[15] J. Paik, P. Pedersen, A simplified method for predicting ultimate compressive strength of ship panels., International Journal of Shipbuilding progress 43(434) (1995) 139–157.

[16] W. Cui, A. Mansour, Generalization of a simplified method for predicting ultimate compressive strength of ship panels, Int. Shipbuilding Progress 46(447) (1998) 291–303.

[17] J.Amdahl, Static resistance of stiffened plates to explosions, FABIG Newsletter No.38.

[18] K. w. E. Steen T.K.., E.Byklum, PULS User's manual, Tech. Rep., Det Norske Veritas, 2001.

[19] DNV, Fabrication and Testing of Offshore Structures, Tech. Rep., Det Norske Veritas, 2004.

[20] J. O. Hallquist, LS-DYNA Theory Manual, Tech. Rep., Livermore Software 2006, 2006.

[21] DNV, DNV-RP-C201, Tech. Rep., Det Norske Veritas, 2004.

[22] X. Wang, Ultimate strength analysis of stiffened panels in ships subjected to biaxial and lateral loading, Int. Journal of Offshore and Polar Engineering 1 (1997) 22.

[23] D. Faulkner, Design against collapse for marine structures, in: International symposium on Advances in Marine Technology, 1979.

Appendix B: Previous reports and doctorial theses list published at the Department of Marine Technology, Norwegian University of Science and Technology (NTNU)

R A P P O R T E R
UTGITT VED
INSTITUTT FOR MARIN TEKNIKK
(tidligere: FAKULTET FOR MARIN TEKNIKK)
NORGES TEKNISK-NATURVITENSKAPELIGE UNIVERSITET

Report No.	Author	Title
	Kavlie, Dag	Optimization of Plane Elastic Grillages, 1967
	Hansen, Hans R.	Man-Machine Communication and Data-Storage Methods in Ship Structural Design, 1971
	Gisvold, Kaare M.	A Method for non-linear mixed -integer programming and its Application to Design Problems, 1971
	Lund, Sverre	Tanker Frame Optimalization by means of SUMT-Transformation and Behaviour Models, 1971
	Vinje, Tor	On Vibration of Spherical Shells Interacting with Fluid, 1972
	Lorentz, Jan D.	Tank Arrangement for Crude Oil Carriers in Accordance with the new Anti-Pollution Regulations, 1975
	Carlsen, Carl A.	Computer-Aided Design of Tanker Structures, 1975
	Larsen, Carl M.	Static and Dynamic Analysis of Offshore Pipelines during Installation, 1976
UR-79-01	Brigt Hatlestad, MK	The finite element method used in a fatigue evaluation of fixed offshore platforms. (Dr.Ing. Thesis)
UR-79-02	Erik Pettersen, MK	Analysis and design of cellular structures. (Dr.Ing. Thesis)
UR-79-03	Sverre Valsgård, MK	Finite difference and finite element methods applied to nonlinear analysis of plated structures. (Dr.Ing. Thesis)
UR-79-04	Nils T. Nordsve, MK	Finite element collapse analysis of structural members considering imperfections and stresses due to fabrication. (Dr.Ing. Thesis)
UR-79-05	Ivar J. Fylling, MK	Analysis of towline forces in ocean towing systems. (Dr.Ing. Thesis)
UR-80-06	Nils Sandsmark, MM	Analysis of Stationary and Transient Heat Conduction by the Use of the Finite Element Method. (Dr.Ing. Thesis)
UR-80-09	Sverre Haver, MK	Analysis of uncertainties related to the stochastic modeling of ocean waves. (Dr.Ing. Thesis)
UR-81-15	Odland, Jonas	On the Strength of welded Ring stiffened cylindrical Shells primarily subjected to axial Compression

UR-82-17	Engesvik, Knut	Analysis of Uncertainties in the fatigue Capacity of Welded Joints
UR-82-18	Rye, Henrik	Ocean wave groups
UR-83-30	Eide, Oddvar Inge	On Cumulative Fatigue Damage in Steel Welded Joints
UR-83-33	Mo, Olav	Stochastic Time Domain Analysis of Slender Offshore Structures
UR-83-34	Amdahl, Jørgen	Energy absorption in Ship-platform impacts
UR-84-37	Mørch, Morten	Motions and mooring forces of semi submersibles as determined by full-scale measurements and theoretical analysis
UR-84-38	Soares, C. Guedes	Probabilistic models for load effects in ship structures
UR-84-39	Aarsnes, Jan V.	Current forces on ships
UR-84-40	Czujko, Jerzy	Collapse Analysis of Plates subjected to Biaxial Compression and Lateral Load
UR-85-46	Alf G. Engseth, MK	Finite element collapse analysis of tubular steel offshore structures. (Dr.Ing. Thesis)
UR-86-47	Dengody Sheshappa, MP	A Computer Design Model for Optimizing Fishing Vessel Designs Based on Techno-Economic Analysis. (Dr.Ing. Thesis)
UR-86-48	Vidar Aanesland, MH	A Theoretical and Numerical Study of Ship Wave Resistance. (Dr.Ing. Thesis)
UR-86-49	Heinz-Joachim Wessel, MK	Fracture Mechanics Analysis of Crack Growth in Plate Girders. (Dr.Ing. Thesis)
UR-86-50	Jon Taby, MK	Ultimate and Post-ultimate Strength of Dented Tubular Members. (Dr.Ing. Thesis)
UR-86-51	Walter Lian, MH	A Numerical Study of Two-Dimensional Separated Flow Past Bluff Bodies at Moderate KC-Numbers. (Dr.Ing. Thesis)
UR-86-52	Bjørn Sortland, MH	Force Measurements in Oscillating Flow on Ship Sections and Circular Cylinders in a U-Tube Water Tank. (Dr.Ing. Thesis)
UR-86-53	Kurt Strand, MM	A System Dynamic Approach to One-dimensional Fluid Flow. (Dr.Ing. Thesis)
UR-86-54	Arne Edvin Løken, MH	Three Dimensional Second Order Hydrodynamic Effects on Ocean Structures in Waves. (Dr.Ing. Thesis)
UR-86-55	Sigurd Falch, MH	A Numerical Study of Slamming of Two-Dimensional Bodies. (Dr.Ing. Thesis)
UR-87-56	Arne Braathen, MH	Application of a Vortex Tracking Method to the Prediction of Roll Damping of a Two-Dimension

		Floating Body. (Dr.Ing. Thesis)
UR-87-57	Bernt Leira, MK	Gaussian Vector Processes for Reliability Analysis involving Wave-Induced Load Effects. (Dr.Ing. Thesis)
UR-87-58	Magnus Småvik, MM	Thermal Load and Process Characteristics in a Two-Stroke Diesel Engine with Thermal Barriers (in Norwegian). (Dr.Ing. Thesis)
MTA-88-59	Bernt Arild Bremdal, MP	An Investigation of Marine Installation Processes – A Knowledge - Based Planning Approach. (Dr.Ing. Thesis)
MTA-88-60	Xu Jun, MK	Non-linear Dynamic Analysis of Space-framed Offshore Structures. (Dr.Ing. Thesis)
MTA-89-61	Gang Miao, MH	Hydrodynamic Forces and Dynamic Responses of Circular Cylinders in Wave Zones. (Dr.Ing. Thesis)
MTA-89-62	Martin Greenhow, MH	Linear and Non-Linear Studies of Waves and Floating Bodies. Part I and Part II. (Dr.Techn. Thesis)
MTA-89-63	Chang Li, MH	Force Coefficients of Spheres and Cubes in Oscillatory Flow with and without Current. (Dr.Ing. Thesis
MTA-89-64	Hu Ying, MP	A Study of Marketing and Design in Development of Marine Transport Systems. (Dr.Ing. Thesis)
MTA-89-65	Arild Jæger, MH	Seakeeping, Dynamic Stability and Performance of a Wedge Shaped Planing Hull. (Dr.Ing. Thesis)
MTA-89-66	Chan Siu Hung, MM	The dynamic characteristics of tilting-pad bearings
MTA-89-67	Kim Wikstrøm, MP	Analysis av projekteringen for ett offshore projekt. (Licenciat-avhandling)
MTA-89-68	Jiao Guoyang, MK	Reliability Analysis of Crack Growth under Random Loading, considering Model Updating. (Dr.Ing. Thesis)
MTA-89-69	Arnt Olufsen, MK	Uncertainty and Reliability Analysis of Fixed Offshore Structures. (Dr.Ing. Thesis)
MTA-89-70	Wu Yu-Lin, MR	System Reliability Analyses of Offshore Structures using improved Truss and Beam Models. (Dr.Ing. Thesis)
MTA-90-71	Jan Roger Hoff, MH	Three-dimensional Green function of a vessel with forward speed in waves. (Dr.Ing. Thesis)
MTA-90-72	Rong Zhao, MH	Slow-Drift Motions of a Moored Two-Dimensional Body in Irregular Waves. (Dr.Ing. Thesis)
MTA-90-73	Atle Minsaas, MP	Economical Risk Analysis. (Dr.Ing. Thesis)
MTA-90-74	Knut-Aril Farnes, MK	Long-term Statistics of Response in Non-linear Marine Structures. (Dr.Ing. Thesis)
MTA-90-	Torbjørn Sotberg, MK	Application of Reliability Methods for Safety

75		Assessment of Submarine Pipelines. (Dr.Ing. Thesis)
MTA-90-76	Zeuthen, Steffen, MP	SEAMAID. A computational model of the design process in a constraint-based logic programming environment. An example from the offshore domain. (Dr.Ing. Thesis)
MTA-91-77	Haagensen, Sven, MM	Fuel Dependant Cyclic Variability in a Spark Ignition Engine - An Optical Approach. (Dr.Ing. Thesis)
MTA-91-78	Løland, Geir, MH	Current forces on and flow through fish farms. (Dr.Ing. Thesis)
MTA-91-79	Hoen, Christopher, MK	System Identification of Structures Excited by Stochastic Load Processes. (Dr.Ing. Thesis)
MTA-91-80	Haugen, Stein, MK	Probabilistic Evaluation of Frequency of Collision between Ships and Offshore Platforms. (Dr.Ing. Thesis)
MTA-91-81	Sødahl, Nils, MK	Methods for Design and Analysis of Flexible Risers. (Dr.Ing. Thesis)
MTA-91-82	Ormberg, Harald, MK	Non-linear Response Analysis of Floating Fish Farm Systems. (Dr.Ing. Thesis)
MTA-91-83	Marley, Mark J., MK	Time Variant Reliability under Fatigue Degradation. (Dr.Ing. Thesis)
MTA-91-84	Krokstad, Jørgen R., MH	Second-order Loads in Multidirectional Seas. (Dr.Ing. Thesis)
MTA-91-85	Molteberg, Gunnar A., MM	The Application of System Identification Techniques to Performance Monitoring of Four Stroke Turbocharged Diesel Engines. (Dr.Ing. Thesis)
MTA-92-86	Mørch, Hans Jørgen Bjelke, MH	Aspects of Hydrofoil Design: with Emphasis on Hydrofoil Interaction in Calm Water. (Dr.Ing. Thesis)
MTA-92-87	Chan Siu Hung, MM	Nonlinear Analysis of Rotordynamic Instabilities in Highspeed Turbomachinery. (Dr.Ing. Thesis)
MTA-92-88	Bessason, Bjarni, MK	Assessment of Earthquake Loading and Response of Seismically Isolated Bridges. (Dr.Ing. Thesis)
MTA-92-89	Langli, Geir, MP	Improving Operational Safety through exploitation of Design Knowledge - an investigation of offshore platform safety. (Dr.Ing. Thesis)
MTA-92-90	Sævik, Svein, MK	On Stresses and Fatigue in Flexible Pipes. (Dr.Ing. Thesis)
MTA-92-91	Ask, Tor Ø., MM	Ignition and Flame Growth in Lean Gas-Air Mixtures. An Experimental Study with a Schlieren System. (Dr.Ing. Thesis)
MTA-86-92	Hessen, Gunnar, MK	Fracture Mechanics Analysis of Stiffened Tubular

		Members. (Dr.Ing. Thesis)
MTA-93-93	Steinebach, Christian, MM	Knowledge Based Systems for Diagnosis of Rotating Machinery. (Dr.Ing. Thesis)
MTA-93-94	Dalane, Jan Inge, MK	System Reliability in Design and Maintenance of Fixed Offshore Structures. (Dr.Ing. Thesis)
MTA-93-95	Steen, Sverre, MH	Cobblestone Effect on SES. (Dr.Ing. Thesis)
MTA-93-96	Karunakaran, Daniel, MK	Nonlinear Dynamic Response and Reliability Analysis of Drag-dominated Offshore Platforms. (Dr.Ing. Thesis)
MTA-93-97	Hagen, Arnulf, MP	The Framework of a Design Process Language. (Dr.Ing. Thesis)
MTA-93-98	Nordrik, Rune, MM	Investigation of Spark Ignition and Autoignition in Methane and Air Using Computational Fluid Dynamics and Chemical Reaction Kinetics. A Numerical Study of Ignition Processes in Internal Combustion Engines. (Dr.Ing. Thesis)
MTA-94-99	Passano, Elizabeth, MK	Efficient Analysis of Nonlinear Slender Marine Structures. (Dr.Ing. Thesis)
MTA-94-100	Kvålsvold, Jan, MH	Hydroelastic Modelling of Wetdeck Slamming on Multihull Vessels. (Dr.Ing. Thesis)
MTA-94-102	Bech, Sidsel M., MK	Experimental and Numerical Determination of Stiffness and Strength of GRP/PVC Sandwich Structures. (Dr.Ing. Thesis)
MTA-95-103	Paulsen, Hallvard, MM	A Study of Transient Jet and Spray using a Schlieren Method and Digital Image Processing. (Dr.Ing. Thesis)
MTA-95-104	Hovde, Geir Olav, MK	Fatigue and Overload Reliability of Offshore Structural Systems, Considering the Effect of Inspection and Repair. (Dr.Ing. Thesis)
MTA-95-105	Wang, Xiaozhi, MK	Reliability Analysis of Production Ships with Emphasis on Load Combination and Ultimate Strength. (Dr.Ing. Thesis)
MTA-95-106	Ulstein, Tore, MH	Nonlinear Effects of a Flexible Stern Seal Bag on Cobblestone Oscillations of an SES. (Dr.Ing. Thesis)
MTA-95-107	Solaas, Frøydis, MH	Analytical and Numerical Studies of Sloshing in Tanks. (Dr.Ing. Thesis)
MTA-95-108	Hellan, Øyvind, MK	Nonlinear Pushover and Cyclic Analyses in Ultimate Limit State Design and Reassessment of Tubular Steel Offshore Structures. (Dr.Ing. Thesis)
MTA-95-109	Hermundstad, Ole A., MK	Theoretical and Experimental Hydroelastic Analysis of High Speed Vessels. (Dr.Ing. Thesis)
MTA-96-110	Bratland, Anne K., MH	Wave-Current Interaction Effects on Large-Volume Bodies in Water of Finite Depth. (Dr.Ing. Thesis)

MTA-96-111	Herfjord, Kjell, MH	A Study of Two-dimensional Separated Flow by a Combination of the Finite Element Method and Navier-Stokes Equations. (Dr.Ing. Thesis)
MTA-96-112	Æsøy, Vilmar, MM	Hot Surface Assisted Compression Ignition in a Direct Injection Natural Gas Engine. (Dr.Ing. Thesis)
MTA-96-113	Eknes, Monika L., MK	Escalation Scenarios Initiated by Gas Explosions on Offshore Installations. (Dr.Ing. Thesis)
MTA-96-114	Erikstad, Stein O., MP	A Decision Support Model for Preliminary Ship Design. (Dr.Ing. Thesis)
MTA-96-115	Pedersen, Egil, MH	A Nautical Study of Towed Marine Seismic Streamer Cable Configurations. (Dr.Ing. Thesis)
MTA-97-116	Moksnes, Paul O., MM	Modelling Two-Phase Thermo-Fluid Systems Using Bond Graphs. (Dr.Ing. Thesis)
MTA-97-117	Halse, Karl H., MK	On Vortex Shedding and Prediction of Vortex-Induced Vibrations of Circular Cylinders. (Dr.Ing. Thesis)
MTA-97-118	Igland, Ragnar T., MK	Reliability Analysis of Pipelines during Laying, considering Ultimate Strength under Combined Loads. (Dr.Ing. Thesis)
MTA-97-119	Pedersen, Hans-P., MP	Levendefiskteknologi for fiskefartøy. (Dr.Ing. Thesis)
MTA-98-120	Vikestad, Kyrre, MK	Multi-Frequency Response of a Cylinder Subjected to Vortex Shedding and Support Motions. (Dr.Ing. Thesis)
MTA-98-121	Azadi, Mohammad R. E., MK	Analysis of Static and Dynamic Pile-Soil-Jacket Behaviour. (Dr.Ing. Thesis)
MTA-98-122	Ulltang, Terje, MP	A Communication Model for Product Information. (Dr.Ing. Thesis)
MTA-98-123	Torbergsen, Erik, MM	Impeller/Diffuser Interaction Forces in Centrifugal Pumps. (Dr.Ing. Thesis)
MTA-98-124	Hansen, Edmond, MH	A Discrete Element Model to Study Marginal Ice Zone Dynamics and the Behaviour of Vessels Moored in Broken Ice. (Dr.Ing. Thesis)
MTA-98-125	Videiro, Paulo M., MK	Reliability Based Design of Marine Structures. (Dr.Ing. Thesis)
MTA-99-126	Mainçon, Philippe, MK	Fatigue Reliability of Long Welds Application to Titanium Risers. (Dr.Ing. Thesis)
MTA-99-127	Haugen, Elin M., MH	Hydroelastic Analysis of Slamming on Stiffened Plates with Application to Catamaran Wetdecks. (Dr.Ing. Thesis)
MTA-99-128	Langhelle, Nina K., MK	Experimental Validation and Calibration of Nonlinear Finite Element Models for Use in Design of Aluminium Structures Exposed to Fire. (Dr.Ing.

		Thesis)
MTA-99-129	Berstad, Are J., MK	Calculation of Fatigue Damage in Ship Structures. (Dr.Ing. Thesis)
MTA-99-130	Andersen, Trond M., MM	Short Term Maintenance Planning. (Dr.Ing. Thesis)
MTA-99-131	Tveiten, Bård Wathne, MK	Fatigue Assessment of Welded Aluminium Ship Details. (Dr.Ing. Thesis)
MTA-99-132	Søreide, Fredrik, MP	Applications of underwater technology in deep water archaeology. Principles and practice. (Dr.Ing. Thesis)
MTA-99-133	Tønnessen, Rune, MH	A Finite Element Method Applied to Unsteady Viscous Flow Around 2D Blunt Bodies With Sharp Corners. (Dr.Ing. Thesis)
MTA-99-134	Elvekrok, Dag R., MP	Engineering Integration in Field Development Projects in the Norwegian Oil and Gas Industry. The Supplier Management of Norne. (Dr.Ing. Thesis)
MTA-99-135	Fagerholt, Kjetil, MP	Optimeringsbaserte Metoder for Ruteplanlegging innen skipsfart. (Dr.Ing. Thesis)
MTA-99-136	Bysveen, Marie, MM	Visualization in Two Directions on a Dynamic Combustion Rig for Studies of Fuel Quality. (Dr.Ing. Thesis)
MTA-2000-137	Storteig, Eskild, MM	Dynamic characteristics and leakage performance of liquid annular seals in centrifugal pumps. (Dr.Ing. Thesis)
MTA-2000-138	Sagli, Gro, MK	Model uncertainty and simplified estimates of long term extremes of hull girder loads in ships. (Dr.Ing. Thesis)
MTA-2000-139	Tronstad, Harald, MK	Nonlinear analysis and design of cable net structures like fishing gear based on the finite element method. (Dr.Ing. Thesis)
MTA-2000-140	Kroneberg, André, MP	Innovation in shipping by using scenarios. (Dr.Ing. Thesis)
MTA-2000-141	Haslum, Herbjørn Alf, MH	Simplified methods applied to nonlinear motion of spar platforms. (Dr.Ing. Thesis)
MTA-2001-142	Samdal, Ole Johan, MM	Modelling of Degradation Mechanisms and Stressor Interaction on Static Mechanical Equipment Residual Lifetime. (Dr.Ing. Thesis)
MTA-2001-143	Baarholm, Rolf Jarle, MH	Theoretical and experimental studies of wave impact underneath decks of offshore platforms. (Dr.Ing. Thesis)
MTA-2001-144	Wang, Lihua, MK	Probabilistic Analysis of Nonlinear Wave-induced Loads on Ships. (Dr.Ing. Thesis)
MTA-2001-145	Kristensen, Odd H. Holt, MK	Ultimate Capacity of Aluminium Plates under Multiple Loads, Considering HAZ Properties. (Dr.Ing. Thesis)

MTA-2001-146	Greco, Marilena, MH	A Two-Dimensional Study of Green-Water Loading. (Dr.Ing. Thesis)
MTA-2001-147	Heggelund, Svein E., MK	Calculation of Global Design Loads and Load Effects in Large High Speed Catamarans. (Dr.Ing. Thesis)
MTA-2001-148	Babalola, Olusegun T., MK	Fatigue Strength of Titanium Risers – Defect Sensitivity. (Dr.Ing. Thesis)
MTA-2001-149	Mohammed, Abuu K., MK	Nonlinear Shell Finite Elements for Ultimate Strength and Collapse Analysis of Ship Structures. (Dr.Ing. Thesis)
MTA-2002-150	Holmedal, Lars E., MH	Wave-current interactions in the vicinity of the sea bed. (Dr.Ing. Thesis)
MTA-2002-151	Rognebakke, Olav F., MH	Sloshing in rectangular tanks and interaction with ship motions. (Dr.Ing. Thesis)
MTA-2002-152	Lader, Pål Furset, MH	Geometry and Kinematics of Breaking Waves. (Dr.Ing. Thesis)
MTA-2002-153	Yang, Qinzheng, MH	Wash and wave resistance of ships in finite water depth. (Dr.Ing. Thesis)
MTA-2002-154	Melhus, Øyvin, MM	Utilization of VOC in Diesel Engines. Ignition and combustion of VOC released by crude oil tankers. (Dr.Ing. Thesis)
MTA-2002-155	Ronæss, Marit, MH	Wave Induced Motions of Two Ships Advancing on Parallel Course. (Dr.Ing. Thesis)
MTA-2002-156	Økland, Ole D., MK	Numerical and experimental investigation of whipping in twin hull vessels exposed to severe wet deck slamming. (Dr.Ing. Thesis)
MTA-2002-157	Ge, Chunhua, MK	Global Hydroelastic Response of Catamarans due to Wet Deck Slamming. (Dr.Ing. Thesis)
MTA-2002-158	Byklum, Eirik, MK	Nonlinear Shell Finite Elements for Ultimate Strength and Collapse Analysis of Ship Structures. (Dr.Ing. Thesis)
IMT-2003-1	Chen, Haibo, MK	Probabilistic Evaluation of FPSO-Tanker Collision in Tandem Offloading Operation. (Dr.Ing. Thesis)
IMT-2003-2	Skaugset, Kjetil Bjørn, MK	On the Suppression of Vortex Induced Vibrations of Circular Cylinders by Radial Water Jets. (Dr.Ing. Thesis)
IMT-2003-3	Chezhian, Muthu	Three-Dimensional Analysis of Slamming. (Dr.Ing. Thesis)
IMT-2003-4	Buhaug, Øyvind	Deposit Formation on Cylinder Liner Surfaces in Medium Speed Engines. (Dr.Ing. Thesis)
IMT-2003-5	Tregde, Vidar	Aspects of Ship Design: Optimization of Aft Hull with Inverse Geometry Design. (Dr.Ing. Thesis)

IMT-2003-6	Wist, Hanne Therese	Statistical Properties of Successive Ocean Wave Parameters. (Dr.Ing. Thesis)
IMT-2004-7	Ransau, Samuel	Numerical Methods for Flows with Evolving Interfaces. (Dr.Ing. Thesis)
IMT-2004-8	Soma, Torkel	Blue-Chip or Sub-Standard. A data interrogation approach of identity safety characteristics of shipping organization. (Dr.Ing. Thesis)
IMT-2004-9	Ersdal, Svein	An experimental study of hydrodynamic forces on cylinders and cables in near axial flow. (Dr.Ing. Thesis)
IMT-2005-10	Brodtkorb, Per Andreas	The Probability of Occurrence of Dangerous Wave Situations at Sea. (Dr.Ing. Thesis)
IMT-2005-11	Yttervik, Rune	Ocean current variability in relation to offshore engineering. (Dr.Ing. Thesis)
IMT-2005-12	Fredheim, Arne	Current Forces on Net-Structures. (Dr.Ing. Thesis)
IMT-2005-13	Heggernes, Kjetil	Flow around marine structures. (Dr.Ing. Thesis
IMT-2005-14	Fouques, Sebastien	Lagrangian Modelling of Ocean Surface Waves and Synthetic Aperture Radar Wave Measurements. (Dr.Ing. Thesis)
IMT-2006-15	Holm, Håvard	Numerical calculation of viscous free surface flow around marine structures. (Dr.Ing. Thesis)
IMT-2006-16	Bjørheim, Lars G.	Failure Assessment of Long Through Thickness Fatigue Cracks in Ship Hulls. (Dr.Ing. Thesis)
IMT-2006-17	Hansson, Lisbeth	Safety Management for Prevention of Occupational Accidents. (Dr.Ing. Thesis)
IMT-2006-18	Zhu, Xinying	Application of the CIP Method to Strongly Nonlinear Wave-Body Interaction Problems. (Dr.Ing. Thesis)
IMT-2006-19	Reite, Karl Johan	Modelling and Control of Trawl Systems. (Dr.Ing. Thesis)
IMT-2006-20	Smogeli, Øyvind Notland	Control of Marine Propellers. From Normal to Extreme Conditions. (Dr.Ing. Thesis)
IMT-2007-21	Storhaug, Gaute	Experimental Investigation of Wave Induced Vibrations and Their Effect on the Fatigue Loading of Ships. (Dr.Ing. Thesis)
IMT-2007-22	Sun, Hui	A Boundary Element Method Applied to Strongly Nonlinear Wave-Body Interaction Problems. (PhD Thesis, CeSOS)
IMT-2007-23	Rustad, Anne Marthine	Modelling and Control of Top Tensioned Risers. (PhD Thesis, CeSOS)
IMT-2007-24	Johansen, Vegar	Modelling flexible slender system for real-time simulations and control applications
IMT-	Wroldsen, Anders Sunde	Modelling and control of tensegrity structures. (PhD

2007-25		Thesis, CeSOS)
IMT-2007-26	Aronsen, Kristoffer Høye	An experimental investigation of in-line and combined inline and cross flow vortex induced vibrations. (Dr. avhandling, IMT)
IMT-2007-27	Gao, Zhen	Stochastic Response Analysis of Mooring Systems with Emphasis on Frequency-domain Analysis of Fatigue due to Wide-band Response Processes (PhD Thesis, CeSOS)
IMT-2007-28	Thorstensen, Tom Anders	Lifetime Profit Modelling of Ageing Systems Utilizing Information about Technical Condition. (Dr.ing. thesis, IMT)
IMT-2008-29	Berntsen, Per Ivar B.	Structural Reliability Based Position Mooring. (PhD-Thesis, IMT)
IMT-2008-30	Ye, Naiquan	Fatigue Assessment of Aluminium Welded Box-stiffener Joints in Ships (Dr.ing. thesis, IMT)
IMT-2008-31	Radan, Damir	Integrated Control of Marine Electrical Power Systems. (PhD-Thesis, IMT)
IMT-2008-32	Thomassen, Paul	Methods for Dynamic Response Analysis and Fatigue Life Estimation of Floating Fish Cages. (Dr.ing. thesis, IMT)
IMT-2008-33	Pákozdi, Csaba	A Smoothed Particle Hydrodynamics Study of Two-dimensional Nonlinear Sloshing in Rectangular Tanks. (Dr.ing.thesis, IMT)
IMT-2007-34	Grytøyr, Guttorm	A Higher-Order Boundary Element Method and Applications to Marine Hydrodynamics. (Dr.ing.thesis, IMT)
IMT-2008-35	Drummen, Ingo	Experimental and Numerical Investigation of Nonlinear Wave-Induced Load Effects in Containerships considering Hydroelasticity. (PhD thesis, CeSOS)
IMT-2008-36	Skejic, Renato	Maneuvering and Seakeeping of a Singel Ship and of Two Ships in Interaction. (PhD-Thesis, CeSOS)
IMT-2008-37	Harlem, Alf	An Age-Based Replacement Model for Repairable Systems with Attention to High-Speed Marine Diesel Engines. (PhD-Thesis, IMT)
IMT-2008-38	Alsos, Hagbart S.	Ship Grounding. Analysis of Ductile Fracture, Bottom Damage and Hull Girder Response. (PhD-thesis, IMT)
IMT-2008-39	Graczyk, Mateusz	Experimental Investigation of Sloshing Loading and Load Effects in Membrane LNG Tanks Subjected to Random Excitation. (PhD-thesis, CeSOS)
IMT-2008-40	Taghipour, Reza	Efficient Prediction of Dynamic Response for Flexible amd Multi-body Marine Structures. (PhD-thesis, CeSOS)
IMT-2008-41	Ruth, Eivind	Propulsion control and thrust allocation on marine vessels. (PhD thesis, CeSOS)

IMT-2008-42	Nystad, Bent Helge	Technical Condition Indexes and Remaining Useful Life of Aggregated Systems. PhD thesis, IMT
IMT-2008-43	Soni, Prashant Kumar	Hydrodynamic Coefficients for Vortex Induced Vibrations of Flexible Beams, PhD thesis, CeSOS
IMT-2009-43	Amlashi, Hadi K.K.	Ultimate Strength and Reliability-based Design of Ship Hulls with Emphasis on Combined Global and Local Loads. PhD Thesis, IMT
IMT-2009-44	Pedersen, Tom Arne	Bond Graph Modelling of Marine Power Systems. PhD Thesis, IMT
IMT-2009-45	Kristiansen, Trygve	Two-Dimensional Numerical and Experimental Studies of Piston-Mode Resonance. PhD-Thesis, CeSOS
IMT-2009-46	Ong, Muk Chen	Applications of a Standard High Reynolds Number Model and a Stochastic Scour Prediction Model for Marine Structures. PhD-thesis, IMT
IMT-2009-47	Hong, Lin	Simplified Analysis and Design of Ships subjected to Collision and Grounding. PhD-thesis, IMT
IMT-2009-48	Koushan, Kamran	Vortex Induced Vibrations of Free Span Pipelines, PhD thesis, IMT
IMT-2009-49	Korsvik, Jarl Eirik	Heuristic Methods for Ship Routing and Scheduling. PhD-thesis, IMT
IMT-2009-50	Lee, Jihoon	Experimental Investigation and Numerical in Analyzing the Ocean Current Displacement of Longlines. Ph.d.-Thesis, IMT.
IMT-2009-51	Vestbøstad, Tone Gran	A Numerical Study of Wave-in-Deck Impact usin a Two-Dimensional Constrained Interpolation Profile Method, Ph.d.thesis, CeSOS.
IMT-2009-52	Bruun, Kristine	Bond Graph Modelling of Fuel Cells for Marine Power Plants. Ph.d.-thesis, IMT
IMT 2009-53	Holstad, Anders	Numerical Investigation of Turbulence in a Sekwed Three-Dimensional Channel Flow, Ph.d.-thesis, IMT.
IMT 2009-54	Ayala-Uraga, Efren	Reliability-Based Assessment of Deteriorating Ship-shaped Offshore Structures, Ph.d.-thesis, IMT
IMT 2009-55	Kong, Xiangjun	A Numerical Study of a Damaged Ship in Beam Sea Waves. Ph.d.-thesis, IMT/CeSOS.
IMT 2010-56	Kristiansen, David	Wave Induced Effects on Floaters of Aquaculture Plants, Ph.d.-thesis, IMT/CeSOS.
IMT 2010-57	Ludvigsen, Martin	An ROV-Toolbox for Optical and Acoustic Scientific Seabed Investigation. Ph.d.-thesis IMT.
IMT 2010-58	Hals, Jørgen	Modelling and Phase Control of Wave-Energy Converters. Ph.d.thesis, CeSOS.

IMT 2010- 59	Shu, Zhi	Uncertainty Assessment of Wave Loads and Ultimate Strength of Tankers and Bulk Carriers in a Reliability Framework. Ph.d. Thesis, IMT.
IMT 2010-60	Shao, Yanlin	Numerical Potential-Flow Studies on Weakly-Nonlinear Wave-Body Interactions with/without Small Forward Speed, Ph.d.thesis, IMT.
IMT 2010-61	Califano, Andrea	Dynamic Loads on Marine Propellers due to Intermittent Ventilation. Ph.d.thesis, IMT.
IMT 2010-62	El Khoury, George	Numerical Simulations of Massively Separated Turbulent Flows, Ph.d.-thesis, IMT
IMT 2010-63	Seim, Knut Sponheim	Mixing Process in Dense Overflows with Emphasis on the Faroe Bank Channel Overflow. Ph.d.thesis, IMT
IMT 2010-64	Jia, Huirong	Structural Analysis of Intect and Damaged Ships in a Collission Risk Analysis Perspective. Ph.d.thesis CeSoS.
IMT 2010-65	Jiao, Linlin	Wave-Induced Effects on a Pontoon-type Very Large Floating Structures (VLFS). Ph.D.-thesis, CeSOS.
IMT 2010-66	Abrahamsen, Bjørn Christian	Sloshing Induced Tank Roof with Entrapped Air Pocket. Ph.d.thesis, CeSOS.
IMT 2011-67	Karimirad, Madjid	Stochastic Dynamic Response Analysis of Spar-Type Wind Turbines with Catenary or Taut Mooring Systems. Ph.d.-thesis, CeSOS.
IMT - 2011-68	Erlend Meland	Condition Monitoring of Safety Critical Valves. Ph.d.-thesis, IMT.
IMT – 2011-69	Yang, Limin	Stochastic Dynamic System Analysis of Wave Energy Converter with Hydraulic Power Take-Off, with Particular Reference to Wear Damage Analysis, Ph.d. Thesis, CeSOS.
IMT – 2011-70	Visscher, Jan	Application of Particla Image Velocimetry on Turbulent Marine Flows, Ph.d.Thesis, IMT.
IMT – 2011-71	Su, Biao	Numerical Predictions of Global and Local Ice Loads on Ships. Ph.d.Thesis, CeSOS.
IMT – 2011-72	Liu, Zhenhui	Analytical and Numerical Analysis of Iceberg Collisions with Ship Structures. Ph.d.Thesis, IMT.
IMT – 2011-73	Aarsæther, Karl Gunnar	Modeling and Analysis of Ship Traffic by Observation and Numerical Simulation. Ph.d.Thesis, IMT.
Imt – 2011-74	Wu, Jie	Hydrodynamic Force Identification from Stochastic Vortex Induced Vibration Experiments with Slender Beams. Ph.d.Thesis, IMT.
Imt – 2011-75	Amini, Hamid	Azimuth Propulsors in Off-design Conditions. Ph.d.Thesis, IMT.